Nanoconfinement of ammonia borane in titania aerogels for accelerated hydrogen release

Justin Driver MEng(Hons), AMIChemE

Department of Chemical & Biological Engineering,
Faculty of Engineering, University of Sheffield,
United Kingdom, September 2019

Thesis submitted in partial fulfilment of the requirements for the degree of Doctor of Philosophy

Acknowledgements

The author gratefully acknowledges the invaluable supervision of Prof. Peter Styring and Dr. James McGregor, as well as the support from many other researchers, technicians and support staff within the Department of Chemical & Biological Engineering at the University of Sheffield. Thanks are also due to Dr. María Dolores Bermejo Roda and Dr. Miriam Rueda at the High Pressure Processes Group for arranging my visit to the Universidad de Valladolid. Finally, but undoubtedly not least, I am indebted to the unwavering support from family, friends and loved ones during these past years – this thesis is as much a result of their efforts as it was mine.

Abstract

The combustion of fossil hydrocarbons to meet global energy demand is widely considered unsustainable and there is substantial motivation to transition toward renewable energy sources. Nevertheless, increasing integration of these renewable sources is challenged by their intermittency, which necessitates the installation of robust energy storage systems. In this context, hydrogen is an advantageous energy vector but current technologies offer insufficient storage performance. Ammonia borane (AB) offers potential as a candidate storage material but is nonetheless challenged by the need for (i) accelerated release of hydrogen, (ii) reduction of gaseous contaminants, and (iii) formation of polymeric residues that enable regeneration. This research sought to resolve these issues by nanoconfinement of AB within highly porous titania aerogels. Initially, titania aerogels were prepared and characterised, with the effect of several synthesis conditions understood. The best performing of these materials exhibited excellent surface area (S_{BET} = 660 m^2/g), pore volume (V_P = 1.17cm^3/g) and mesoporosity (d_P = 17 nm) that were among the highest reported for such materials. Importantly, it was found that extraction with carbon dioxide resulted in the formation of titania with surface bicarbonate functionality. The preparation of such functionalised materials typically requires the inclusion of carboxylic acids during synthesis, meaning this discovery represents a distinct route toward high performance materials. One titania aerogel was then studied for the nanoconfinement of AB for application as a hydrogen storage candidate, with the composite material designated AB/TA(L). Compared to bulk AB, the nanoconfined AB/TA(L) demonstrated distinct release characteristics including lowered onset temperatures (101 to 25 ^oC), reduced activation energy (171 to 85 kJ/mol), altered release kinetics, increased contaminants and reduced quantity of hydrogen. The cause of these fundamental changes was believed to be strong destabilisation induced by the aforementioned surface bicarbonate functionality, the amphoteric nature of which was speculated to mediate proton exchange. In contrast to trends in literature, this result directly implicates amphoteric materials as deserving further research. Whilst many of these changes prohibited application of AB/TA(L) toward storage applications, the findings highlighted new opportunities for nanoconfinement of AB. Additionally, the release mechanisms from bulk AB and nanoconfined AB/TA(L) were interrogated using two-dimensional infrared spectroscopy. These studies found the borane functionality of bulk AB was crucially involved in the release mechanism(s), with evidence to support the occurrence of counterintuitive homopolar interactions. Although such interactions have been reported before, this result appears to be the first evidence that confirms their existence without the possibility of hydrogen exchange.

Contents

List of Figures

List of Tables

Research Collaborators

This research was conducted in collaboration with the High Pressure Processes group located in the Department of Chemical Engineering and Environmental Technology within the University of Valladolid, Spain. The correspondence details for principal investigator in the group has been included below. One research area of the group is the application of elevated pressures for the preparation of high-performance, functionalised materials. In particular, the group has several publications that outline the preparation of silica aerogels using high-pressure carbon dioxide for solvent extraction. One application of these aerogels is the nanoconfinement of ammonia borane within the silica, effectively producing a material functionalised for hydrogen storage. Over a number of years, the High Pressure Processes group have optimised the preparation and application of these silica aerogel materials and reported their results in several publications.

Dr. María Dolores Bermejo Roda
Email: mdbermejo@gmail.com,
Tel: +34 983423174
Address: High Pressure Processes Group, Departamento de Ingeniería Química y Tecnología del Medio Ambiente, Escuela de Ingenierías Industriales, Sede Mergelina, Universidad de Valladolid, Valladolid – 47011, España

Despite this, new understanding in literature suggests aerogels based on other metal oxides may offer improved performance, effectively forming the basis of this research. To this end, the author spent around six weeks at the University of Valladolid as a visiting researcher (for the duration of October/November 2017). During this time, the author synthesised a variety of aerogels using the high-pressure solvent extraction equipment developed by the High Pressure Processes group. The resulting aerogels (some of which contained nanoconfined ammonia borane) were then promptly delivered by airfreight to the University of Sheffield, wherein the author conducted subsequent characterisation and analyses. Hence, the author specifically acknowledges the High Pressure Processes group for granting access to the high-pressure solvent extraction equipment as a valued contribution to this research.

1.0 Introduction

1.1 Research Motivation

Over the course of the nineteenth and twentieth centuries, technological advancement and subsequent industrialisation allowed explosive growth in the global population. In the UK, the population grew from a pre-industrial value of approximately 11 million in 1800, through 50 million in 1950 to a recent value of 66 million in 2017, as seen in Figure 1.1. Current projections for the UK estimate continued growth to 74 million in 2050 and upward to 83 million by 2100, with similar trends expected globally (ONS, 2018). This population growth has been accompanied by drastic changes in lifestyle, as commercialisation has enabled widespread access to modern conveniences such as electrical power, domestic heating, petroleum vehicles, *etc*. These technologies greatly improved the average global standard of living, one metric of which is the gross domestic product (GDP) per capita. For the UK, growth in GDP per capita (as inlaid on Figure 1.1) (World Bank, 2018), has increased from $1400 to $39,700 in the period from 1960 to 2017 indicating considerably improved living standards. While widespread access to these modern conveniences has undoubtedly had positive social and economic impacts, it has also fuelled unprecedented global demand for material resources and energy (World Bank, 2018).

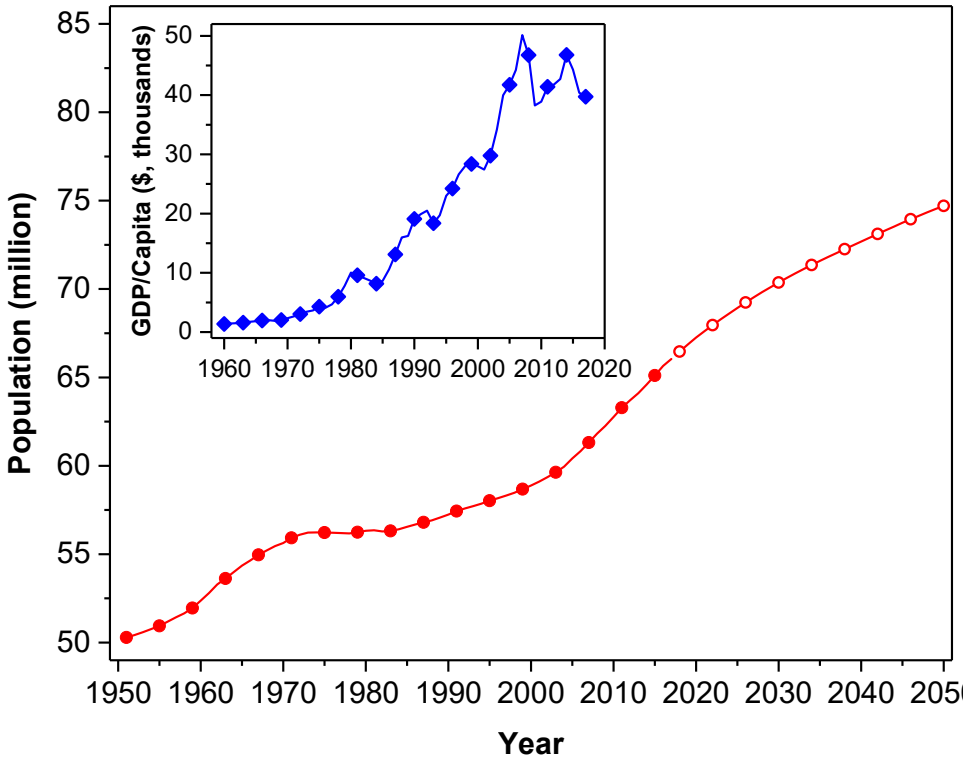

Figure 1.1: Historical population (●) from 1950-2017, and projected population (○) until 2050 of the UK (ONS, 2018)**. Inlaid: GDP per capita (◆) from 1960-2017 of the UK** (World Bank, 2018)**.**

Regarding energy, this demand has been predominantly fulfilled by the combustion of hydrocarbon fossil fuels, mostly consisting of coal, oil and natural gas (Hook, Sivertssen and Aleklett, 2010). However, a number of considerable disadvantages challenge long-term reliance on fossil fuels. Principal amongst these is that their combustion is associated with significant emissions of so-called greenhouse gases (GHGs). These include carbon dioxide (CO_2), methane (CH_4), nitrous oxide (N_2O) and others, which are emitted to the atmosphere from both static point sources (*e.g.* power stations) and mobile sources (*e.g.* petroleum vehicles) (IPCC, 2018). Emission of these GHGs is of serious concern since they are a major contributor toward anthropogenic climate change phenomena and associated catastrophic environmental events (*e.g.* global warming, glacial melting, desertification, ocean acidification). Consequently, these events are known to cause significant damage to global ecosystems, which will likely have disastrous humanitarian implications (*e.g.* displaced populations, famine, droughts) (IPCC, 2018).

As such, there has been strong international motivation to reduce emission of GHGs to the atmosphere. For example, the formation of the Intergovernmental Panel on Climate Change (IPCC), The Kyoto Protocol (UN, 1998), The Copenhagen Agreement (UN, 2010), and The Paris Agreement (UN, 2015), all of which culminated in international commitments to reduce GHG emissions. Recently, a specific target has been to limit global temperature rise from the so-called Greenhouse Effect to 1.5 ^{o}C (IPCC, 2018), which would help to avoid the aforementioned catastrophes. To achieve this, there is a particular emphasis on abatement of CO_2 emissions since, despite exhibiting the lowest global warming potential, it constitutes the largest share of GHG emissions by volume (IPCC, 2007). Evidentially, from a pre-industrial value of approximately 280 ppm, atmospheric concentration of CO_2 has risen to 410 ppm in 2017 and, at present rates of emission, is expected to reach 750 ppm by 2100 (effecting a global temperature increase of 4.5 ^{o}C compared to 1990) (IPCC, 2018). To limit this increase to 1.5 ^{o}C, net emissions of anthropogenic CO_2 need to be reduced by 45% by 2030 and be net zero by 2050 (relative to 2010) (IPCC, 2018).

In addition to the immediate concerns regarding GHG emissions, continued reliance on fossil fuels into the long-term is also challenged by their finite abundance and restricted geographical distribution (Hook, Sivertssen and Aleklett, 2010). It is predicted that as the limited worldwide reserves of fossil fuels are gradually depleted, the security of supply for these hydrocarbons will become increasingly endangered (Speight, 2019). For instance, as easily accessible fossil reserves are exhausted, production would be forced to move to more difficult reserves, effectively driving up the cost of extraction and the subsequent price of energy (Soetaert and Vandamme, 2009). Furthermore, remaining reserves would be geographically concentrated in fewer countries (*e.g* Venezuela, Saudi Arabia, Iran, Canada, Iraq, *etc.*) (OPEC, 2018), meaning supply of these fuels would be vulnerable to geopolitical

factors and price instability (Vakulchuk, Overland and Scholten, 2020). Disconcertingly, some estimates based on consumption rates and proven reserves predict depletion of fossil fuels between 50- 200 years (Soetaert and Vandamme, 2009). Hence, reliance on fossil fuels in the long-term future is ultimately unsustainable and poses a considerable threat to the national energy security of the UK and many other countries worldwide.

With consideration of the above, the scenario for the UK is shown in Figure 1.2(a)-(b), which respectively present the final primary energy consumption by source (DBEIS, 2018) and the net GHG emissions by species (DBEIS, 2019) between 1990-2017. For discussion, the energy sources have been categorised as either 'fossil' or 'alternative' (the summation of fossil and non-fossil sources respectively). As seen in Figure 1.2(a), the UK has made earnest progress toward reducing reliance on fossil sources, which constituted approximately 91% of final energy consumption in 1990, but only 80% of consumption in 2017 (DBEIS, 2018). Figure 1.2(b) highlights reductions in GHG emissions over the same period, particularly for emissions of CO_2 which were reduced from approximately 600 to 400 $MtCO_2$ (DBEIS, 2019). These achievements have been realised by several changes, including; use of less carbon-intense fossil fuels (*i.e.* decommissioning of coal-fired power plants), higher efficiency generation (*i.e.* commissioning of combined-cycle gas turbine power plants), better system efficiencies (*e.g.* improved domestic insulation), and larger generation alternative energy sources which are less carbon-intense (CarbonBrief, 2019).

With regard to the latter, the final primary energy consumption from alternative sources has more than doubled in the UK from approximately 9% to 20% between 1990-2017, with targets for 32% by 2030 (EU, 2018). In the UK, principal alternative energy sources include nuclear, wind, solar, biomass, hydroelectric and pumped, which are often used to generate secondary energy (*i.e.* electricity) (Gridwatch, 2019). Such sources may have the potential to meet the UK's energy demands, whilst simultaneously reducing emission of GHGs. Furthermore, most of these sources with the exception of nuclear are renewable and geographically abundant meaning short-term abatement of the aforementioned concerns regarding security of supply, geopolitical factors and price instability (Hache, 2018). However, increasing integration of alternative energy sources presents further challenges. To illustrate this, Figure 1.3(a)-(b) presents a selection of UK grid data on arbitrary dates (Gridwatch, 2019), averaged on an hourly and quarterly basis respectively (with fossil sources omitted for visual clarity). Note, this figure concerns demand for secondary energy and does not account for primary energy in other areas (*e.g.* domestic heating, transport fuels, industry). Nevertheless, subsequent discussion is relevant to these areas since elimination of fossil energy will prompt transition to replacement technologies. For example, the UK aims to ban sales of new petroleum and diesel cars by 2040 (Department for Transport, 2018), which will increase movement toward electric and other fuel-cell vehicles.

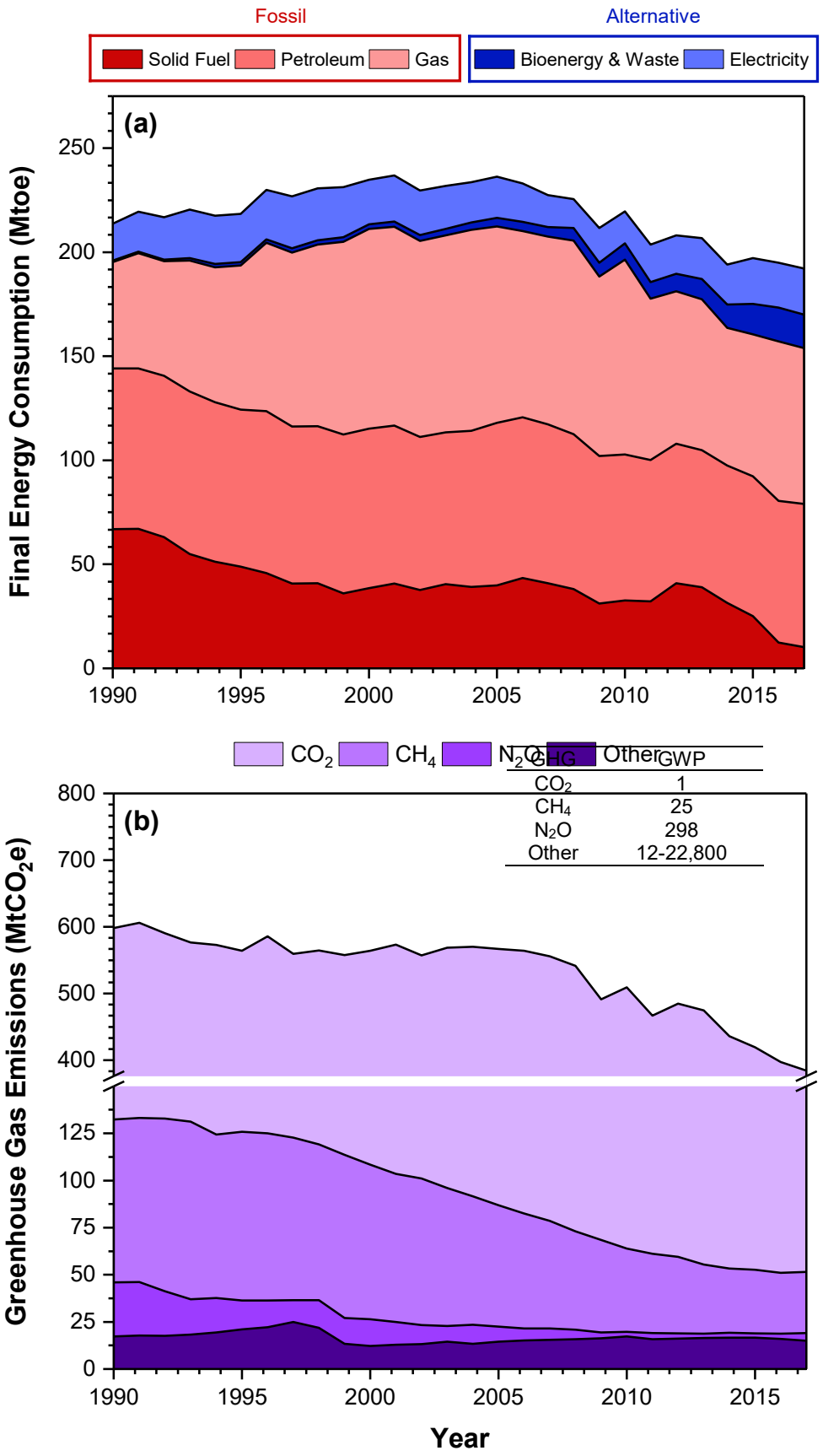

Figure 1.2: Estimated values for (a) final energy consumption by source, and (b) greenhouse gas emissions by type, of the UK between 1990-2017 (DBEIS, 2018), (DBEIS, 2019)

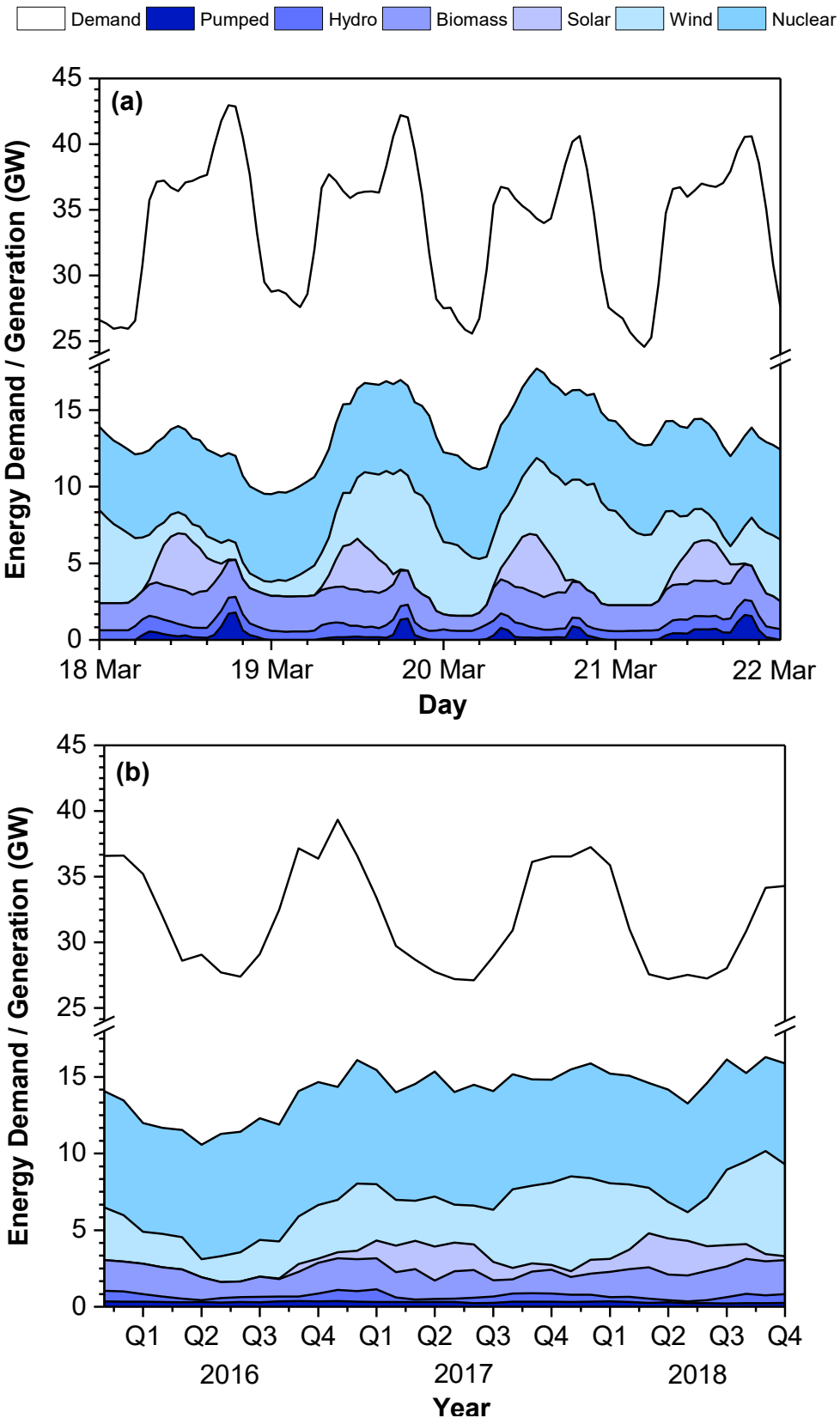

Figure 1.3: Variation in average energy demand and alternative energy generation in the UK on (a) hourly basis in March 2018, and (b) monthly basis for 2016-2018 respectively (Gridwatch, 2019)**.**

From Figure 1.3(a)-(b) it is immediately evident that the secondary energy demand of the UK changes over both an hourly and monthly basis, with demand highest during daytime hours and winter months. This variable demand is easily supplied by conventional plants that generate power from combustion of fossil fuels, which can adjust their output within a designed turndown range and/or undergo start-up upon demand (Gridwatch, 2019). Conversely, many alternative energy sources are ultimately limited by temporal availability, meaning they typically offer intermittent and unreliable power generation (Lovins, 2017). For instance, Figure 1.3(a) shows how generation from wind and solar can vary greatly over an hourly basis, with output ranging between approximately 0.8-7.1 GW and 0-3.8 GW respectively. Moreover, Figure 1.3(b) shows this variability extends over a monthly timeframe, variability of approximately 1.2-6.7 GW and 0-2.3 GW for wind and solar respectively. Whilst other alternative energy sources (namely nuclear, biomass, hydroelectric and pumped power) can offer more consistent and/or reliable generation, they are challenged by other issues that are beyond the scope of this introduction (Vakulchuk, Overland and Scholten, 2020).

Hence, it has long been apparent that increasing integration of alternative energy is challenged by the intermittent and unreliable nature of the respective energy sources. Variable energy generation introduces uncertainty and significantly complicates both the design and operation of national energy infrastructure (Lovins, 2017). On one hand, if generation unexpectedly falls below installed capacity, the resulting undersupply would result in energy shortages. On the other hand, should generation exceed demand the resulting oversupply would overload networks and result in curtailment. This underscores the critical need for the integration of energy storage systems alongside alternative energy (Vakulchuk, Overland and Scholten, 2020). With such systems, surplus energy produced when generation exceeds demand can be stored and discharged later when demand has surpassed generation, serving to balance the infrastructure and avoid under/oversupply. For the UK, alongside increasing alternatives to 32% by 2030 (EU, 2018), the installed energy storage capacity is predicted to more than double from its current value of 3 GW in 2017 to approximately 6-10 GW by 2030, and onward to 27-50 GW by 2050 (National Grid, 2018). This highlights a growing demand for efficient and economical energy storage systems, which has prompted research into a wide range of technologies based on storage of gravitational, kinetic, thermal, physicochemical, electrochemical or chemical energy (Gur, 2018).

1.2 The Hydrogen Economy

Hydrogen (H_2) is an alternative fuel and promising energy storage candidate that has been proposed as a replacement for fossil hydrocarbons (Moradi and Groth, 2019). Hydrogen demonstrates excellent specific energy density (120 MJ/kg) compared to hydrocarbons (*e.g.* 44 MJ/kg) (US DOE, 2019), meaning large amounts of energy can be stored in its constituent chemical bond. This energy is easily released by combustion and unlike hydrocarbons the sole product of these reactions is water (H_2O), effectively eliminating emission of aforementioned GHGs (Moradi and Groth, 2019). Furthermore, hydrogen is environmentally benign in the case of accidental releases since it is non-toxic and readily dissipates into the atmosphere. Additionally, its elemental abundance means hydrogen can be produced globally from a diverse range of sustainable feedstocks (Ball and Weeda, 2015), meaning greater long-term sustainability and security of supply. The widespread of use of hydrogen requires systems for its production, distribution, storage and utilisation, which has widely been referred to as the 'Hydrogen Economy' (Niaz, Manzoor and Pandith, 2015).

1.2.1 Hydrogen Production

Hydrogen can be produced from a range of processes that use a large number of chemical feedstocks and energy sources (Nikolaidis and Poullikkas, 2017). Predominant feedstocks include fossil hydrocarbons (*e.g.* natural gas) as well as sustainable feedstocks that are renewable and locally abundant (*e.g.* biomass, algae, water). This also applies to energy inputs, which can be from either fossil or alternative energy sources, as discussed above. A selection of these processes are shown in Table 1.1 (Nikolaidis and Poullikkas, 2017), followed by a brief summary of some notable examples. Note this discussion is not intended to be exhaustive and only serves to illustrate the diverse routes for production of hydrogen.

Currently, hydrogen is primarily derived from the steam reformation of fossil hydrocarbons (Dincer and Acar, 2014). The most common feedstock is natural gas, which is treated to remove contaminants (*e.g.* SO_2, H_2S), before proceeding several intensive reactions that form a syngas (Holladay *et al.*, 2009). This syngas is primarily composed of H_2, CH_4, CO and CO_2 and considerable processing is required to obtain pure hydrogen and recycle unreacted CH_4 and CO components for further conversion, which ultimately form large quantities of CO_2 (estimated at 8.6 tonnes(CO_2)/tonne(H_2))(EPA, 2008). This process benefits from low production costs, high efficiencies, existing infrastructure and technological maturity, but is nonetheless challenged by high capital, maintenance, and energy costs, as well as costly pre-treatment and purification (Nikolaidis and Poullikkas, 2017). Moreover, pressure to reduce GHGs could force retrofitting of carbon capture and storage (CCS) facilities to avoid emission of CO_2, which would add cost and complication to operations (Bui *et al.*, 2018).

A notable alternative to steam reformation is electrolysis, which achieves hydrogen production by electrochemical water splitting (Dincer and Acar, 2014). Fundamentally, upon application of electrical current through electrodes, water will dissociate to form constituent hydrogen and oxygen gases at the anode and cathode respectively (Niaz, Manzoor and Pandith, 2015). Electrolysers have undergone extensive development with several variants at or nearing commercial availability, namely alkaline, polymer exchange membrane, and solid oxide electrolysers (Holladay *et al.*, 2009). Using water as the feedstock is a substantial advantage since it is cheap, environmentally benign, naturally abundant and inexpensive pre-treatment is required (Nikolaidis and Poullikkas, 2017). Moreover, purification of the hydrogen product is easier since hydrogen formation at the anode can be physically isolated from oxygen formation by a membrane, meaning ultra-high purities (99.999%) can easily be achieved at reduced cost (Dincer and Acar, 2014). However, electrolysis is challenged by its extremely high energy demand (Nikolaidis and Poullikkas, 2017), which means its environmental impact is fundamentally linked to the source of the electricity used. This has led many to suggest electrolysis run by surplus alternative energy (*e.g.* wind-powered electrolysis) as a convenient method of generating hydrogen without emission of GHGs (Lovins, 2017)(Bennoua *et al.*, 2015). Such integration is conceptually advantageous since electrolysis is fundamentally an electrochemical process, and the relatively low heating requirements means production can be rapidly adjusted to match variable power inputs.

Another alternative similar reformation is biomass pyrolysis and/or gasification, which are based on the partial oxidation of biomass fuels (*e.g.* agricultural waste streams, municipal solid waste or energy crops) (Nikolaidis and Poullikkas, 2017). These biomass fuels undergo thermal processing to produce a syngas similarly composed of H_2, CH_4, CO and CO_2, with the H_2 being separated and purified and the unreacted fractions being recycled (Yamada, 2006). Biomass pyrolysis and gasification plants are technologically mature and have been commercially operated at an industrial scale (Holladay *et al.*, 2009). The benefits of the feedstock include that it is relatively cheap, geographically abundant, sustainable, environmentally benign, and processing results in reduced net GHG emissions due to CO_2 uptake during biomass growth (Dincer and Acar, 2014). However, similar to conventional reformation, biomass pyrolysis and gasification plants exhibit relatively high capital, operational and energy costs, as well as the need for considerable hydrogen purification (Nikolaidis and Poullikkas, 2017). Additionally, whilst the biomass feedstock offers many advantages it also presents additional costs due to the need for intensive pre-treatment (*e.g.* sourcing, blending, drying, grinding, feeding, *etc.*). Overall, despite the above challenges, biomass pyrolysis and gasification offer a reliable and achievable method of producing hydrogen with reduced net emission of GHGs (Dincer and Acar, 2014).

Fermentative techniques are another notable option for hydrogen production. This process relies on the anaerobic fermentation of a biomass feedstock by specialised bacteria to produce a biogas (typically composed of H_2, CH_4, CO_2, *etc.*) (Nikolaidis and Poullikkas, 2017). Careful control of the fermentation conditions is required to maintain the bacteria culture, prevent growth of competing bacteria (*e.g*. methanogens which produce CH_4), and maintain growth conditions that promote selective formation of hydrogen (Kapdan and Kargi, 2006). There are two types fermentation processes conducted in either the presence or absence of light, referred to as photo fermentation and dark fermentation respectively. Dark and photo fermentation are often conducted successively, together demonstrating efficient conversion of the feedstock biomass to hydrogen (Kapdan and Kargi, 2006). The aforementioned advantages and challenges of biomass feedstocks equally apply to fermentation. However, additional pre-treatment is required to hydrolyse cellulosic materials (which are indigestible) into fermentable sugars, adding complexity and cost to the overall process (Holladay *et al.*, 2009). Furthermore, the relatively low selectivity to hydrogen means more digestion units are required and a high capital cost value. Despite this, fermentation has been studied as a means of forming hydrogen from streams of agricultural waste with reduced GHG emissions (Nikolaidis and Poullikkas, 2017).

Table 1.1: A selection of hydrogen production processes, including characteristics such as energy source, feedstock, efficiency and generalised reaction. Adapted from (Nikolaidis and Poullikkas, 2017)

Process	Energy	Feedstock	Efficiency (%)	Generalised Reaction
Steam Reformation[a]	Fossil	Natural Gas	74-85	$CH_4 + 2H_2O \rightarrow CO_2 + 6H_2$
Dark Fermentation	-	Biomass	60-80	$C_6H_{12}O_6 + 2H_2O \rightarrow 2CH_3CO_2H + 2CO_2 + 4H_2$
Partial Oxidation[a]	Fossil	Coal	60-75	$CH_4 + ½O_2 \rightarrow CO + 2H_2$
Autothermal Reformation[a]	Fossil	Natural Gas	60-75	$CH_4 + ½H_2O + ¼O_2 \rightarrow CO + 2½H_2$
Electrolysis	Electrical[b]	Water	40-60	$H_2O \rightarrow ½O_2 + H_2$
Biomass Pyrolysis	Steam	Biomass	35-50	$C_xH_yO_z \rightarrow CH_4 + CO_2 + CO + \ldots + H_2$
Biomass Gasification	Steam	Biomass	35-50	$C_xH_yO_z + H_2O \rightarrow CH_4 + CO_2 + CO + \ldots + H_2$
Thermolysis	Thermal[b]	Water	20-45	$H_2O \rightarrow ½O_2 + H_2$
Bio-Photolysis	Solar	Algae	10	$C_xH_yO_z + 12H_2O \rightarrow 6CO_2 + 12H_2$
Photo Fermentation	Solar	Biomass	0.1	$CH_3CO_2H + 2H_2O \rightarrow 2CO_2 + 4H_2$
Photolysis	Solar	Water	0.06	$H_2O \rightarrow ½O_2 + H_2$

[a] Efficiency values do not include an integrated carbon capture and storage (CCS) process.
[b] Electrical can include fossil, nuclear, wind, solar (photovoltaic); heat can include fossil, nuclear and solar (thermal).

1.2.2 **Hydrogen Distribution**

A distribution network is required to transport hydrogen from centralised production locations to either stationary applications (*e.g.* chemical refineries, power plants, domestic properties) or refuelling stations for use in mobile applications (*i.e.* fuel-cell electric vehicles) (Moradi and Groth, 2019). The efficiency of distribution is believed to principally depend on the amount of hydrogen and the delivery distance, as well as specific circumstances such as local geography (Moliner, Lázaro and Suelves, 2016). For small amounts and/or short

distances (≤ 200 km), cylinders of hydrogen are preferred due to their simplicity, flexibility and lower capital cost. However, larger amounts and/or longer distances (> 200 km) are better suited to distribution by a network of pipelines, which offer reliable, low cost delivery but considerably higher capital cost (Moliner, Lázaro and Suelves, 2016). Conceptually, this cost could be reduced using existing natural gas networks to instead distribute hydrogen (Moradi and Groth, 2019). Conversely, as previously detailed, there is considerable interest toward using local alternative energy sources for decentralised production of hydrogen (Apostolou and Enevoldsen, 2019). Such an arrangement means hydrogen production can be conducted close to the point of use, effectively meeting local demand whilst minimising capital and operational costs. For instance, wind-powered electrolysis could provide hydrogen (or hydrogen-derived) fuel to a remote rural community without the cost of long distance connection to a centralised production plant (Morgan, Manwell and McGowan, 2014) (Frattini *et al.*, 2016). Whilst this prospect demonstrates potential, the challenges with intermittency of alternative energy highlight the critical need for hydrogen storage in such an arrangement (as discussed in *1.1 Research Motivation*)(Lovins, 2017).

1.2.3 **Hydrogen Conversion**

Hydrogen can be consumed in a variety of applications, with some notable examples given below. An established market for hydrogen is as a feedstock to the chemical industry where it is used in the production of a range of commodity chemicals (*e.g.* ammonia, methanol, hydrocarbons)(Ball and Weeda, 2015). Additionally, a growing market is within fuel-cell electric vehicles where hydrogen fuel is oxidised and generates electrical power to drive a motor. These fuel-cells are not limited in the same way as traditional heat engines and so exhibit greater efficiencies than typical internal combustion engines (approximately 60% versus 22-45% respectively (Niaz, Manzoor and Pandith, 2015)). Even more attractive is that the only product from oxidation is water, meaning fuel-cell electric vehicles do not result in mobile emissions of GHGs. In the UK, this market is expected to grow considerably in coming decades, since current targets are to end the UK sale of new petroleum and diesel cars in the UK by 2040 (Department for Transport, 2018). A recent study suggested hydrogen from surplus alternative energy (*e.g.* wind-powered electrolysis) was already commercially viable in the above areas (Ball and Weeda, 2015).

Another possible market for hydrogen is as an industrial or domestic fuel (Ball and Weeda, 2015). Industrially, a long-term option is to retrofit or replace conventional power generation with plants that instead combust hydrogen. For domestic fuel, one possibility is to blend hydrogen into the existing natural gas network for consumption (*e.g.* heating, cooking), however blending is currently limited to 5-20% due to the design of consumer systems (*e.g.*

domestic boilers) (Moliner, Lázaro and Suelves, 2016). In the long-term, consumer systems could be redesigned but this would require significant investment. Conversely, hydrogen could be supplied to a methanation process and the resulting synthetic natural gas blended into the existing network, avoiding the need for alteration to consumer systems. However, the above study found renewable hydrogen was not viable in these areas, since its current production cost exceeded the allowable cost of the market (Ball and Weeda, 2015).

1.3 Hydrogen Storage

However, transition toward a functional Hydrogen Economy is crucially challenged by the need for commercially viable hydrogen storage systems (Ren *et al.*, 2017). Conceptually, such systems are a practical necessity to account for latency between production and eventual consumption. The significance of storage is even more apparent when examined in the context of increasing generation from alternative energy sources (and the challenges posed by their intermittency and unreliability), as described previously (Lovins, 2017).

1.3.1 Storage Targets

The most widely accepted targets for hydrogen storage materials are those set by the United States Department of Energy (US DOE, 2017), which are specifically for hydrogen fuel in light-duty vehicles. These targets encompass a range of performance parameters, which include aspects such as the storage capacity, system cost, system operability and charging-discharging characteristics. To provide general context for this work, a selection of these performance targets are presented in Table 1.2 and discussed below (US DOE, 2017).

A critical parameter is the storage capacity of a material, for which there are two distinct metrics. Volumetric capacity describes the mass of stored hydrogen within a specific volume, whereas gravimetric capacity describes the mass of stored hydrogen relative to the total mass of the material (US DOE, 2017). Candidate storage materials must demonstrate sufficient values for both volumetric and gravimetric capacities, as these reflect storage efficiency with regard to space and weight respectively (US DOE, 2017). Additionally, candidate materials must be robust across a range of ambient temperatures and perform efficiently for many cycles over their lifetime. Throughout operation, candidate materials must be able to deliver hydrogen of temperature, pressure and purity suitable for downstream processing, with delivery suitably rapidly and with sufficient flowrate to meet downstream demand. Finally, candidate storage materials must achieve this performance within an economical cost that is able to compete with traditional fuels. Ongoing development of hydrogen storage materials must satisfy these targets to produce a candidate that is commercially viable (US DOE, 2017).

Table 1.2: A selection of performance parameter targets for hydrogen storage in light-duty vehicles, as recommended by United States Department of Energy (US DOE, 2017)

Parameter	Target		
	2020	**Ultimate**	**Units**
Capacity			
Gravimetric	5.5	7.5	wt%(H_2)
Volumetric	40	70	g/L
Cost			
System	400	266	\$/kg(H_2)
Operability			
Ambient Temperature	-40/60	-40/60	^oC
Delivery Temperature	-40/85	-40/85	^oC
Delivery Pressure	5/12	5/12	bar, abs
Delivery Purity	99.97	99.97	%(H_2)[a]
Operational Lifetime	1,500	1,500	cycles
System Efficiency	90	90	%
Charging/Discharging			
Charging Time	3/5	3/5	min/5 kg(H_2)
Minimum Flowrate	1.5	2.0	kg(H_2)/min
Start-Up Time	5	5	s

[a] **ISO 14687-2, Contaminant** (µmol/mol(H_2)): **He** (300), **N_2/Ar** (100), **O_2** (5), **H_2O** (5), **CO_2** (2), **C_xH_y** (2), **CO** (0.2), **HCCOH** (0.2), **NH_3** (0.1), **X** (0.05), **CH_2O** (0.01), **S** (0.004)

1.3.2 **Compression & Cryogenic**

The simplest storage method is compression of hydrogen gas to high pressures (≤ 700 bar) to increase the physical density of the gas (Zhang *et al.*, 2016). Whilst conceptually simple, compression exhibits insufficient performance with regard to the storage capacity (US DOE, 2017). Furthermore, pressurised storage of an explosive gas represents a considerable hazard and costly alloys are required to combat hydrogen embrittlement of the tank material (Moradi and Groth, 2019). Thus, continued work is predominantly toward the development of high strength tank materials that allow compression to higher pressures (whilst remaining cost-effective) (Barthelemy, Weber and Barbier, 2017). Alternatively, the physical density of the hydrogen can be increased by cooling to cryogenic temperatures (-253^{o}C) such that condensation occurs to form liquid hydrogen (Zhang *et al.*, 2016). Whilst better storage capacities are realised compared to compression (and the hazards of pressurised storage are avoided), condensation is incredibly energy intensive and storage tanks require considerable insulation (Barthelemy, Weber and Barbier, 2017). The current technological challenges are mostly toward implementing high performance, cost-effective insulation materials and reducing the cost of condensation (Moradi and Groth, 2019).

1.3.3 **Physical Adsorption**

Another process by which hydrogen can be stored is physical adsorption (also referred to as physisorption) (Ren *et al.*, 2017). In this phenomenon, molecules of hydrogen associatively adsorb to a porous support material where they remain weakly bonded to the surface by electrostatic attractions (typically $\Delta H_{ads} \approx$ -4 to-10 kJ/mol) (Bastos-Neto *et al.*, 2012). Because of this, desorption of the hydrogen from the support surface can be achieved by subjecting the material to heating or pressure reduction (known as temperature-swing and pressure-swing adsorption/desorption respectively) (Zhang *et al.*, 2016). Desorption of hydrogen from the surface effects bulk release whilst simultaneously regenerating the surface of the adsorbent for further storage. The mainstay of current research is toward the development and characterisation of high performance adsorbents that demonstrate high surface area and storage capacity, whilst maintaining low release temperatures and material cost (Ren *et al.*, 2017). A wide range of materials have been studied including activated carbon, graphene, zeolites, metal-organic frameworks (MOFs), covalent organic frameworks (COFs) and many other highly porous materials (Bastos-Neto *et al.*, 2012)(Moradi and Groth, 2019).

1.3.4 **Chemical Hydrides**

Hydrogen can be also be stored within the bonds of a chemical compound (*e.g.* C-H, O-H, N-H) (Moradi and Groth, 2019). The release of this hydrogen is a chemical reaction that necessarily decomposes the hydrogen-containing molecule into subsequent decomposition products. In most respects, this discussion is analogous to that for hydrogen production (as seen in *1.2.1 Hydrogen Production*) (Nikolaidis and Poullikkas, 2017), since hydrogen is 'stored' within the bonds of the feedstock and 'released' by production reaction (*e.g.* storage within the C-H bonds of CH_4 and release by the aforementioned reformation reactions). In contrast to the relatively weak bonding in physisorption, chemical hydrides usually require more energy to effect hydrogen release (typically $\Delta H_r \approx$ -40 to -100 kJ/mol) (Ren *et al.*, 2017), reflecting the increased strength of chemical bonds. Some of the most studied chemical hydrides include water (H_2O), methanol (MeOH), formic acid (CHOOH), formaldehyde (CH_2O), ammonia (NH_3), hydrazine (N_2H_4), carbohydrates $(CH_2O)_x$ and many other hydrocarbons (C_xH_y) (Moradi and Groth, 2019). Research is predominantly toward the development of catalysts that proceed hydrogen release at lower temperatures (Torrente-murciano, 2016), and the production of hydrides from abundant sustainable feedstocks (*e.g.* agricultural wastes)(Yamada, 2006).

1.3.5 **Metal Hydrides**

At elevated conditions of temperature and pressure many metals (M) are able to react with hydrogen to form metal hydrides (MH_X), storing the hydrogen in the subsequent metal hydride bonds (M-H) (Ren *et al.*, 2017). When required, the material can be heated to release this hydrogen and simultaneously regenerate the active sites on the metal for further storage. A variety of different hydrides have been studied for storage applications including complex metal hydrides (*e.g.* $NaBH_4$, $LiAlH_4$), metallic hydrides (*e.g.* LiH, MgH_2, TiH_2, PdH_x), and intermetallic metal hydrides (*e.g.* Mg_2NiH_4) (Zhang *et al.*, 2016). The material properties and storage characteristics of these hydrides vary considerably based on the metals present (Wietelmann, Felderhoff and Rittmeyer, 2016). In general, however, metal hydrides are crucially challenged by the requirement for high release temperatures (McWhorter *et al.*, 2012). Ongoing research aims to tackle this by using novel processing methods (*e.g.* ball-milling, micronisation, nanoscaling) (Lang and Huot, 2011) and including catalysts, both of which accelerate low temperature release without the need for expensive platinum group metals (Ren *et al.*, 2017). Another issue for some metal hydrides is their violent decomposition upon exposure to oxygen or moisture, which presents considerable process hazards (Wietelmann, Felderhoff and Rittmeyer, 2016).

1.3.6 **Comparison of Storage Methods**

There have been several performance reviews of hydrogen storage candidates reported in the literature, predominantly comparing their volumetric and gravimetric capacities (Torrente-murciano, 2016)(McWhorter *et al.*, 2012). One such review, has been shown in in Figure 1.4, which has been adapted to include the updated 2020 and Ultimate storage capacity targets referenced in Table 1.2 (Torrente-murciano, 2016) (US DOE, 2017). It should be noted, this comparison is not intended to be exhaustive and its purpose is simply to compare the storage capacities of the candidate materials discussed in the preceding section. Following this comparison, a candidate material that exhibited the most potential for cost effective hydrogen storage could be justified as the topic of this research.

To this end, Figure 1.4 shows how the storage candidates tend to display characteristic advantages and disadvantages with regard to capacity (Torrente-murciano, 2016). Storage by compression or cryogenic cooling of hydrogen (*e.g.* H_2 @ 350 bar) occupies an unfavourable position, exhibiting low values for both volumetric and gravimetric capacities that are insufficient to meet the target for 2020 (US DOE, 2017). Despite this, the simplicity of compressed and cryogenic storage offer undeniable advantages with regard to several other performance criteria in Table 1.2 (Zhang *et al.*, 2016). Both methods are fundamentally robust and capable of many charge-discharge cycles over the lifetime of the storage system

with minimal loss of efficiency (Moradi and Groth, 2019). Furthermore, the hydrogen released by these methods exhibit excellent purity, whilst the rate of release is both responsive and easily controllable (Zhang *et al.*, 2016). Nevertheless, the options for further research are rather limited and mostly confined to developing stronger tank materials that allow safer compression to higher pressures whilst remaining relatively cheap (Moradi and Groth, 2019)(Barthelemy, Weber and Barbier, 2017).

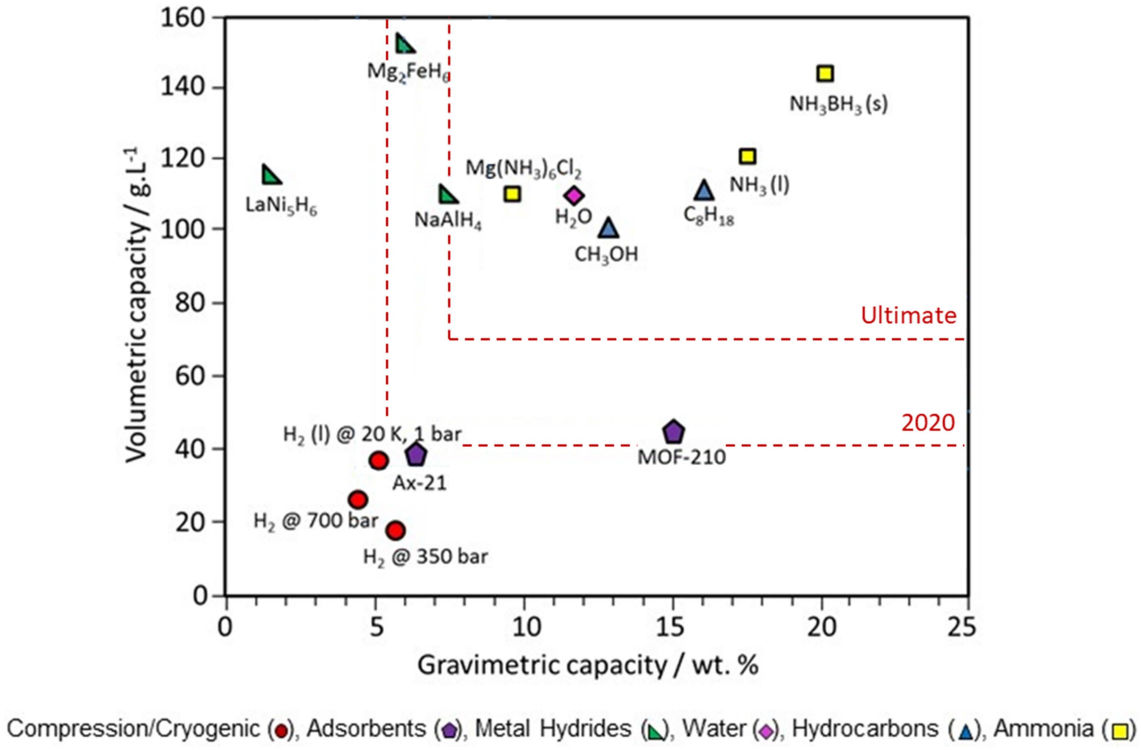

Figure 1.4: Performance comparison of a selection of hydrogen storage candidates according to volumetric and gravimetric capacities, illustrated against 2020 and Ultimate targets. Adapted from (Torrente-murciano, 2016) **to include updated targets set by** (US DOE, 2017)

This is in contrast to metal hydrides (*e.g.* Mg_2FeH_6), which tend to offer excellent volumetric capacity from the high density of the bulk metal alloy, but relatively poor gravimetric capacity due to the high mass of the constituent metallic atoms (effectively reducing volume and increasing weight respectively) (Wietelmann, Felderhoff and Rittmeyer, 2016). On the other hand, adsorbents (*e.g.* MOF-210) tend to exhibit the opposite trend; their extreme porosity means fewer heavy metallic atoms are needed, however their consequently low density means they occupy a large volume for a given capacity (Bastos-Neto *et al.*, 2012). This relationship appears to highlight a compromise between volumetric and gravimetric capacity driven by the mass/density of the storage material, and is a plausible reason why these materials occupy positions at opposing boundaries of the target for 2020 (Torrente-murciano, 2016). With regard to other performance criteria, metal hydrides and adsorbents

offer mixed results. Both candidates can typically deliver quite pure hydrogen due to the relative absence of other volatile components, however the high and low temperatures required for loading of metal hydrides and adsorbents respectively mean reduced overall efficiency (Zhang *et al.*, 2016). Furthermore, most of these materials have undergone little-to-no testing to determine their operational lifetimes after large numbers of charge-discharge cycles. Such testing is important since existing reports show these materials can experience substantial losses in efficacy after only a moderate amount of cycles (*e.g.* loss of 23% capacity after 264 cycles) (McWhorter *et al.*, 2012). Despite this, there is considerable scope for further research to solve these challenges by developing better storage materials with a range of advantageous material properties (Zhang *et al.*, 2016)(Ren *et al.*, 2017).

Conversely, chemical hydrides (*e.g.* H_2O, CH_3OH, NH_3) generally occupy favourable positions on Figure 1.5, offering an excellent balance between gravitational and volumetric capacities (Torrente-murciano, 2016). Presumably, this is because there are less heteroatoms and the mass of these heteroatoms are considerably lighter (where the term heteroatom is used to define a non-hydrogen atom). For instance, N accounts for only 25 mol% of NH_3 whereas Mg_2Fe accounts for 33 mol% of Mg_2FeH_6, and moreover the mass of these heteroatoms are 14 g/mol and 104 g/mol respectively. Overall, most chemical hydrides generally meet the 2020 and Ultimate targets for storage capacity (US DOE, 2017), however they are significantly challenged by their performance against other criteria. The presence of heteroatoms promotes the release contaminants alongside hydrogen that negatively affects downstream processes (Zhang *et al.*, 2016). Furthermore, as was discussed above, the relatively high temperature required to effect release reduces the overall efficiency achieved during storage (Zhang *et al.*, 2016). Similar to the above, the majority of research is toward finding high performance chemical hydrides and subsequently developing catalysts that accelerate low temperature release of hydrogen (Ren *et al.*, 2017).

In particular, ammonia borane (*i.e.* NH_3BH_3) represents a remarkable chemical hydride that exhibits exceptional storage capacities far in excess of the target requirements (Torrente-murciano, 2016). Indeed, explicitly with regard to storage capacity, ammonia borane is arguably the highest performing candidate currently known. Nevertheless, like many chemical hydrides, its performance in storage applications is insufficient against many of the hydrogen storage criteria (US DOE, 2017). However, examination of the relevant literature shows there is considerable scope to address these challenges, which if successful could realise ammonia borane as a viable hydrogen storage candidate (Demirci, 2017a). Hence, based on its current potential and the opportunities for further improvement, ammonia borane was justified as the topic of this research. As such, a detailed review of the research concerning ammonia borane has been provided in the subsequent literature review, specifically seen in section *2.1 Ammonia Borane.*

1.4 Summary of Introduction

To summarise, continuing to meet the global energy demand by combustion of fossil hydrocarbons is unsustainable for a number of reasons. Principal amongst these are the emissions of GHGs that result from their combustion, which are associated with anthropogenic climate change phenomena that could lead to environmental catastrophes and humanitarian disasters. Thus, there is strong international motivation to reduce reliance on fossil hydrocarbons, and instead generate power from alternative energy sources that produce fewer GHGs. However, increasing integration of alternatives is challenged by their unreliability and intermittency, which necessitates the installation of robust energy storage systems. Hydrogen is an attractive option for energy storage and alternative fuel for a number of reasons. Despite this, widespread adoption of hydrogen fuel requires a functional 'Hydrogen Economy' with commercially viable methods for the production, distribution, utilisation and storage of hydrogen. Current hydrogen storage methods offer insufficient performance against internationally recognised targets, and there is an incentive to develop more effective storage materials. One candidate is the chemical hydride ammonia borane, which offers exceptional performance in some regards but is severely limited in others. Despite this, there is considerable scope to resolve these issues and advance the application of ammonia borane in hydrogen storage, forming the overarching objective of this research.

2.0 Literature Review

Having qualitatively justified research into ammonia borane, a review of the available literature was conducted. The purpose of this review was to outline current knowledge in the field and identify scope for further understanding, from which specific hypotheses were formulated and examined in this research. Accordingly, the subsequent section familiarises the reader with literature relevant to this research, particularly in the areas of ammonia borane, modification by nanoconfinement, applications of titania, and aerogels.

2.1 Ammonia Borane

2.1.1 Properties and Functionality

Ammonia borane (NH_3BH_3, AB) is a molecule composed of ammonia (NH_3) and borane (BH_3) constituents bonded by a coordinate covalent bond originating from the lone pair of electrons on the nitrogen atom (Li *et al.*, 2014). AB is isoelectronically analogous to ethane (CH_3CH_3) but exhibits drastically different characteristics, as seen from the selection of chemical and physical properties included in Table 2.1 overleaf (Demirci, 2017a). Considering these characteristics, it is apparent why AB has high potential as a hydrogen storage candidate. The low molecular mass (M_w = 30.8 g/mol), coupled with relatively high density (ρ = 0.78 gcm^{-3}) and hydrogen content (6 mol_H/mol_{AB}) result in a remarkable gravimetric hydrogen capacity (19.6 wt%) (Wietelmann, Felderhoff and Rittmeyer, 2016). Moreover, AB exhibits somewhat unusual stability. Unlike ethane, which is a gas at ambient conditions, AB is a solid that demonstrates a considerably larger volumetric capacity (146 g/L) (Demirci, 2017a). Another consequence of this stability is that AB is relatively benign (Sigma-Aldrich, 2018a), unlike many other aforementioned hydride materials (*e.g.* LiH, NaH, $LiAlH_4$)(Wietelmann, Felderhoff and Rittmeyer, 2016). For instance, AB is stable in air and although it undergoes acid-catalysed hydrolysis upon exposure to atmospheric moisture, this reaction is non-violent and proceeds slowly (Zhang *et al.*, 2011). In many regards, this is desirable for storage applications since it reduces the hazards associating with handling and storage the material, however it also means hydrogen release from AB requires relatively high temperatures (which has energetic and economic impacts).

The stability of AB originates with the properties of its constituent atoms. The difference in electronegativity (χ) between the component hydrogen, nitrogen and boron atoms (χ_N = 3.04, χ_B = 2.04, χ_H = 2.20) produces varying polarisation in the adjacent bonds (Moireau and Veillard, 1968). The high electronegativity of nitrogen ($\chi_N > \chi_H$) withdraws electrons from the surrounding hydrogens, resulting in them exhibiting protic ($H^{\delta+}$) character. In contrast, boron has a lower electronegativity ($\chi_B < \chi_H$) and does not withdraw electrons, resulting in the

surrounding hydrogens exhibiting hydridic ($H^{\delta-}$) character (Li *et al.*, 2014). In this way, there exists a charge distribution across the AB molecule with the positive and negative charges predominating around the $-NH_3$ and $-BH_3$ moieties respectively (Li *et al.*, 2014). The intra- and intermolecular interaction of these protic and hydridic hydrogens are fundamental in explaining the properties of AB. For instance, consider the structure of AB as shown in Figure 2.1 in its staggered and eclipsed conformations (Demirci, 2017a). For most structurally analogous species, the staggered conformer is known to be more stable due to minimised electron-electron repulsions. However, attractions between opposing protic and hydridic hydrogens form intramolecular dihydrogen bonds ($H^{\delta+}\cdots H^{\delta-}$) which adjust the conformation such that these atoms are aligned. Hence, the eclipsed conformer is observed to be more stable than the staggered (Penner, Chang and Hutzal, 1999), in contrast to isoelectronic analogues such as ethane (Demirci, 2017a). Nevertheless, the staggered conformation is observed due to contributions from intermolecular interactions, as discussed below.

Table 2.1: Comparison for a selection of properties of AB and Ethane

Identification[a]				
Name	Ammonia borane		Ethane	
CAS number	13774-81-7		74-84-0	
Physical form	White solid		Colourless gas	
Properties[a],[b]				
Formula	BNH_6	-	C_2H_6	-
Molecular mass (M_w)	30.8	g/mol	30.1	g/mol
Melting point (T_m)	97-102	°C	-172	°C
Boiling point (T_b)	- [c]	°C	-88	°C
Density (ρ)	0.78	g/cm^3	0.362	g/cm^3
Gravimetric hydrogen capacity	19.6	wt%	20.1	$wt\%_H$
Volumetric hydrogen capacity	146	g/L	<0.3	g_H/L

[a] **Identification**: (Demirci, 2017a), (Sigma-Aldrich, 2018a)
[b] **Properties**: All property values reported at ambient conditions
[c] **Boiling Point**: Does not boil, typically sublimates and/or decomposes

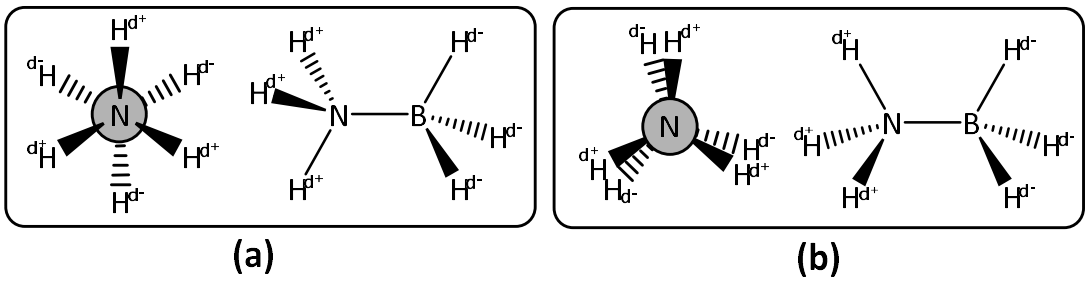

Figure 2.1: Structure of AB in (a) staggered, and (b) eclipsed conformations. Due to intramolecular bonding ($H^{\delta+}\cdots H^{\delta-}$) the eclipsed conformation is typically favoured, with isomerisation to the staggered inhibited by an energy barrier (Demirci, 2017a)

Similarly, attraction between protic and hydridic hydrogens on adjacent AB molecules are fundamental to intermolecular dihydrogen bond formation (Crabtree *et al.*, 1996), with modelling of such interactions predicting polymeric AB ranging from dimers up to pentamers (Zapata-Escobar *et al.*, 2016)(Merino, Bakhmutov and Vela, 2002). For example, Figure 2.2 shows an AB dimer in the head-to-tail configuration, illustrating the formation of four dihydrogen bonds (N-$H^{\delta+}\cdots H^{\delta-}$-B) between the protic and hydridic atoms on respective AB monomers (V. S. Nguyen *et al.*, 2007). These intermolecular bonds are relatively strong and contribute significantly to the stability of AB (Zapata-Escobar *et al.*, 2016), as evidenced by the selection of properties in Table 2.1. Nevertheless, in order to release of hydrogen from storage, the molecules of AB must be destabilised to prompt subsequent dehydrogenation reactions and disruption of intra- and intermolecular dihydrogen bonds is believed to be pivotal achieving this (Kulkarni, 1999)(V. S. Nguyen *et al.*, 2007)(as discussed in section *2.1.3 Hydrogen Release by Thermolytic Dehydrogenation*).

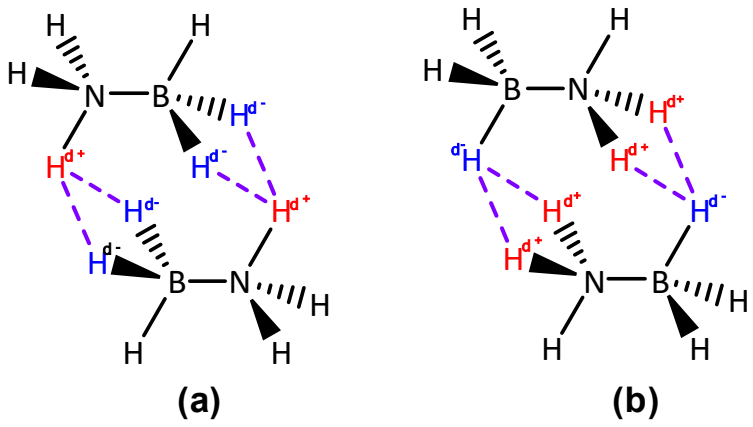

Figure 2.2: Examples of dimers formed by molecules of AB in the head-to-tail configuration, showing intermolecular dihydrogen bonding (N-$H^{\delta+}\cdots H^{\delta-}$-B) between protic (red) and hydridic (blue) atoms (Crabtree *et al.*, 1996) (Demirci, 2017a)**.**

2.1.2 Production of Ammonia Borane

An important factor to consider for AB as a hydrogen storage candidate is the difficulty and cost of production. Prohibitively difficult and/or expensive production would diminish the economic viability of AB irrespective of its technical performance (US DOE, 2017). As such, the following is a brief summary of the two predominant syntheses of AB (although other methods are known to exist). The first method of production is a double-displacement reaction between an ammonium salt ($[NH_4^+][X^-]$) and metal borohydride (MBH_4, M = Li, Na) (Equation 1.1a) (Heldebrant *et al.*, 2008). The resultant ammonium borohydride ($[NH_4^+]$ $[BH_4^-]$) intermediate is unstable above -40°C and rapidly undergoes dehydrogenation to yield AB and evolve H_2 (Equation 1.1b) (Heldebrant *et al.*, 2008). Typically, this reaction

takes place in an organic solvent (*e.g.* diethyl ether, dimethylformamide, dioxane, tetrahydrofuran, toluene) that is held between 0-45°C (Heldebrant *et al.*, 2008). Alternatively, lower temperatures can be used to stabilise the ammonium borohydride intermediate before further reaction (Zou, Tao and Chen, 2011). For instance, near quantitative yields (99%) of AB have been achieved reacting a nickel ammonia complex ($Ni(NH_3)_6Cl_2$) with sodium borohydride at -78°C, followed by extraction of the ammonium borohydride and warming to ambient temperature (Zou, Tao and Chen, 2011). This effectively decouples the synthesis into distinct steps (Equations 1.1a and 1.1b), resulting in nearly quantitative conversion (Zou, Tao and Chen, 2011). The second method utilises a base displacement reaction, whereby ammonia (NH_3) displaces a ligand (L) on the borane precursor ($L{\cdot}BH_3$) (Equation 1.2) (Chen *et al.*, 2012). Desirable ligands have lower basicity relative to ammonia (*e.g.* dimethyl ether, tetrahydrofuran, dimethyl sulphide) (Chen *et al.*, 2012). Conditions for this reaction are similar to the above, with the reaction being conducted in an organic solvent at approximately the same temperatures (Zou, Tao and Chen, 2011). In addition to the above, a selection of specific methods for production of AB are discussed in section *2.1.6 Regeneration of Depleted Residues* due to the relevance of their precursors in regenerating spent AB.

$$[NH_4]^+[X]^- + MBH_4 \xrightarrow[0\text{-}45\ ^oC]{\text{Solvent}} [NH_4]^+[BH_4]^- + MX \qquad \textbf{1.1(a)}$$

$$[NH_4]^+[BH_4]^- \xrightarrow[0\text{-}45\ ^oC]{\text{Solvent}} NH_3BH_3 + H_2 \qquad \textbf{1.1(b)}$$

$$NH_3 + BH_3{\cdot}L \xrightarrow[-78\ ^oC,\ 20\ ^oC]{\text{Solvent}} NH_3BH_3 + L \qquad \textbf{1.2}$$

The heat of reaction (ΔH_r) for syntheses of AB are seldom reported (Demirci, 2017b). Nevertheless, an approximate baseline can be assumed by considering the heat of formation (ΔH_f) of AB, as reported in literature (Kondrat'Ev *et al.*, 2015)(Autrey, Bowden and Karkamkar, 2011)(Matus *et al.*, 2007)(Shaulov, Shmyreva and Tubyanskaya, 1966). The mean average of these values (ΔH_f = -154.1 kJ/mol) suggests the synthesis of AB is moderately exothermic. This prompts justifiable concerns about the overall storage efficiency with AB due to energy loss during processing (*i.e.* synthesis, hydrogen release, regeneration), reducing the net energy storage capacity (Zhang *et al.*, 2016). This is an area of ongoing research with particular interest in the regeneration of spent residues of AB (Summerscales and Gordon, 2013), as discussed in *2.1.6 Regeneration of Depleted Residues.* Nevertheless, the facile routes reported above do not necessarily eliminate the potential of AB as a hydrogen storage material (Heldebrant *et al.*, 2008; Chen *et al.*, 2012). Whilst the thermal requirements of these reactions are severe, the reactions themselves proceed near-quantitative yields (Zou, Tao and Chen, 2011), drastically improving the atom economy and efficiency of the synthesis.

2.1.3 **Hydrogen Release by Thermolytic Dehydrogenation**

Hydrogen release from AB can occur by two principal mechanisms. The first mechanism is thermolytic dehydrogenation (*i.e.* 'thermolysis'), where heating destabilises molecules of AB causing them to decompose and proceed the evolution of H_2 (Demirci, 2017a). This process consists of a complex network of reactions, which have been generalised in Figure 2.3. The first hydrogen release is known to occur between 95-132 ^{o}C evolving approximately 1 mol of H_2 by intramolecular and/or intermolecular reactions (Kulkarni, 1999)(Baitalow *et al.*, 2002)(Bowden *et al.*, 2006). In the intermolecular case, this reaction eliminates H_2 and simultaneously proceeds polymerisation to form polyaminoborane (-$[H_2N{-}BH_2]_n$-, PAB) (Reaction 1)(Baitalow *et al.*, 2002)(Bowden *et al.*, 2006). This is in contrast to the intramolecular case, wherein H_2 is eliminated to form a monomeric aminoborane intermediate ($H_2N{=}BH_2$, MAB) (Reaction 1a), which is followed by a separate polymerisation reaction to form PAB (Reaction 1b)(Kulkarni, 1999). The PAB produced from these reactions progressively form linear-, branched- and cyclic-chained polymeric structures, for example the cyclic trimer cyclotriborazane ($B_3N_3H_{12}$, TBZ) (Al-kukhun, Hwang and Varma, 2012).

Subsequently, PAB then proceeds a second hydrogen release between 132-200^{o}C to yield polyiminoborane (-$[HN{=}BH]_n$-, PIB) (Reaction 2) with a second evolution of approximately 1 mole of H_2 (Baitalow *et al.*, 2002). PIB is similarly characterised by a range of polymeric structures, however specific products commonly reported include borazine ($B_3N_3H_6$, BZ), o-polyborazylene (PBZ) and cross-linked graphitic polymers (Demirci, 2017a) (Al-kukhun, Hwang and Varma, 2012). Generally, the thermolytic residues at this stage are considered to consist exhibit an empirical formula of NBH_x (where $x \leq 2$) (Frueh *et al.*, 2011). Further heating of NBH_x ($x \leq 2$) residues result in a third hydrogen release, with the evolution of approximately 1 mol of H_2 occurring between 1150-1500^{o}C to form hexagonal boron nitride (-$[B{=}N]_n$-, hBN) (Reaction 3) (Frueh *et al.*, 2011). For storage applications, this hydrogen is usually deemed unrecoverable due to the elevated temperature required for release. Furthermore, the extreme thermal and chemical stability of hBN is undesirable since it inhibits regeneration of spent AB, as discussed in *2.1.6 Regeneration of Depleted Residues*.

The heat of reaction (ΔH_r) values for the thermolytic dehydrogenation of AB have been summarised in Table 2.2. The consensus amongst these studies is that the progressive dehydrogenation of AB to PAB and PIB is exothermic at each stage of reaction (averaging at $\Delta H_r(1)$ = -21.1 kJ/mol, $\Delta H_r(2)$ = 20.0 kJ/mol respectively) (Kondrat'Ev *et al.*, 2015)(Wolf *et al.*, 2000). As discussed previously, the loss of heat during the release of hydrogen is widely accepted to cause reduced overall storage efficiency. In theory, released heat could be used autothermally to accelerate dehydrogenation or integrated within other storage processes (*e.g.* synthesis, regeneration). Nevertheless, whether such heat integration is technically feasible at large scale remains unclear (Andersson and Grönkvist, 2019).

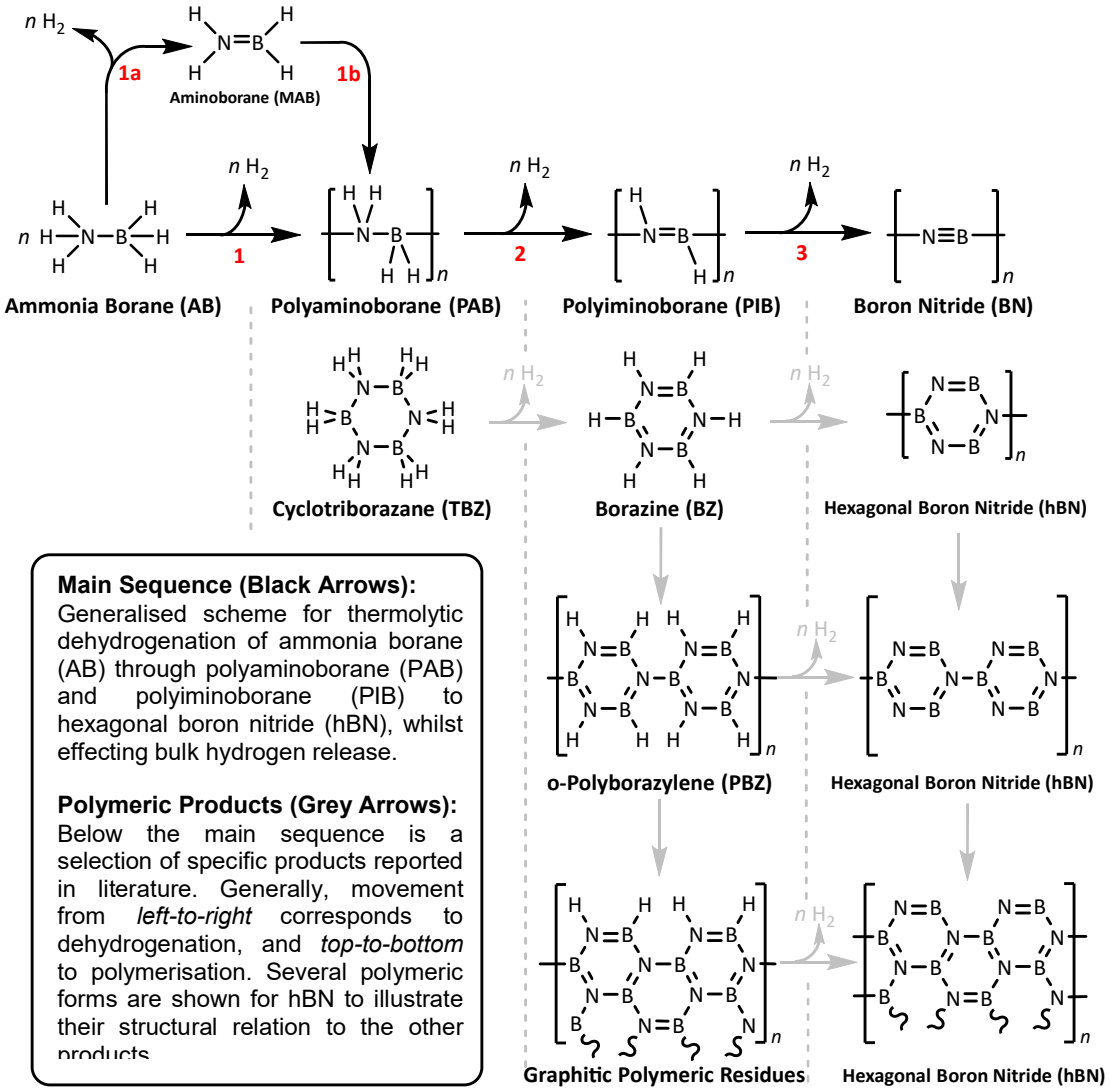

Figure 2.3: Generalised scheme for non-isothermal thermolytic dehydrogenation of AB, effecting H_2 evolution and bulk hydrogen release. Adapted from (Demirci, 2017a)

Table 2.2: Heats of reaction for thermolytic dehydrogenation of AB to PAB and PIB [a]

Reference	Heat of Reaction, ΔH_r (kJ/mol)	
	AB $\xrightarrow{-H_2}$ PAB	PAB $\xrightarrow{-H_2}$ PIB
(Kondrat'Ev *et al.*, 2015)	-24.9 ± 2.3	-
(Kang *et al.*, 2008)	-21.0	-
(Wolf *et al.*, 2000)	-21.7 ± 1.2	-
(Gutowska *et al.*, 2005)	-21.0 ± 1.0	-
(Neiner *et al.*, 2009)	-21.6	-33.3
(Benzouaa *et al.*, 2010)	-16.6	-7.4
(Matus *et al.*, 2007)	-25.0	-4.0
(Baumann, Baitalow and Wolf, 2005)	-	-23.9 ± 2.4
(Baumann, Baitalow and Wolf, 2005)	-	-15.4 ± 1.2
Average (Mean)	**-21.1**	**-20.0**
Average (Median)	**-21.3**	**-20.0**

[a] Dehydrogenation: Generalised to account for various polymeric forms of PAB and PIB.

In contrast to the above, hydrogen release from AB is often conducted isothermally (Palumbo *et al.*, 2010)(Bowden and Autrey, 2011), since this arrangement is more representative of commercial hydrogen storage systems. Isothermal thermolysis demonstrates distinctive characteristics that have provided a valuable mechanistic insight into the fundamental reactions occurring within AB (Gutowska *et al.*, 2005). The release profile exhibited during isothermal thermolysis is sigmoidal, characterised by an extended induction period followed by rapid evolution of H_2 until stabilisation at a final release value (Bowden *et al.*, 2006). The sigmoidal profile has been attributed to nucleation and growth kinetics, where rapid hydrogen release occurs only after a critical nucleation event (Bowden *et al.*, 2006). This event was believed to occur by intermolecular heteropolar ($N\text{-}H^{\delta+}\cdots H^{\delta-}\text{-}B$) interactions (Wolstenholme *et al.*, 2012)(Al-kukhun, Hwang and Varma, 2012)(Petit and Demirci, 2018), with one proposed mechanism shown in Figure 2.4, interpreted from a summary by (Demirci, 2017a). The figure has been generalised as the reaction of AB with R_nBH_3 where $R_n = (NH_2BH_2)_nNH_3$ given in terms of the number of cycles (n) increasing with integer values from zero. As such, the initial species is AB ($n = 0$, $R_0 = NH_3$) and successive cycles ($n = 1, 2, 3$, *etc.*) show polymerisation and growth of PAB accordingly (*e.g.* $n = 2$, $R_2 = (NH_2BH_2)_2NH_3$). For clarity, only a linear-chain has been considered, but progressive formation of branched- and eventually cyclic-chained PAB is believed to occur over the course of thermolysis (eventually forming PIB, PBZ and/or hBN) (Al-kukhun, Hwang and Varma, 2012).

The first step of this mechanism is believed to be thermal destabilisation of AB, which weakens the network of intermolecular dihydrogen bonds ($N\text{-}H^{\delta+}\cdots H^{\delta-}\text{-}B$) and induces relaxation within clusters of AB molecules (V. S. Nguyen *et al.*, 2007). This relaxation lengthens the B-N bond from 1.607 to 1.665 Å, which is accompanied by a decrease in the N-B-H angle from 108.4° to approximately 105° for the tetramer and monomer respectively (Merino, Bakhmutov and Vela, 2002). These changes reportedly allow formation of a 'mobile phase' of AB (Reaction 1) (Shaw *et al.*, 2010), observed as an exothermic event that precedes both melting and subsequent hydrogen release. The increased reactivity of this mobile AB prompts heteropolar ($N\text{-}H^{\delta+}\cdots H^{\delta-}\text{-}B$) interactions that lead to an isomerisation reaction between $\text{-}NH_3$ and $\text{-}BH_3$ groups on adjacent AB molecules to a transient intermediate (Reaction 2) (Bowden and Autrey, 2011). This intermediate is then believed to reversibly isomerise to diammoniate of diborane ($[NH_3BH_2NH_3^+][BH_4^-]$, DADB) (Reaction 3) (Shaw *et al.*, 2010). This reaction is believed to be the critical nucleation event that proceeds evolution of H_2 and polymerisation to form PAB (Reaction 4), since DADB is known to be more reactive than AB (Shaw *et al.*, 2010). This was strongly evidenced by (Bowden and Autrey, 2011) who doped AB with 5 wt% of DADB and observed immediate hydrogen release with complete elimination of the induction period seen with undoped AB.

Recently, conventional understanding that hydrogen release occurs exclusively through heteropolar (N-$H^{\delta+}\cdots H^{\delta-}$-B) interactions was challenged and found to be inaccurate (Wolstenholme *et al.*, 2012) (Al-kukhun, Hwang and Varma, 2012) (Petit and Demirci, 2018). Experimental investigations using deuterium labelled AB (ND_3BH_3 or NH_3BD_3) and analyses with ^{1}H-, ^{2}H-, ^{11}B- or ^{15}N-NMR spectroscopy have revealed the additional occurrence of homopolar (N-$H^{\delta+}\cdots H^{\delta+}$-N and B-$H^{\delta-}\cdots H^{\delta-}$-B) interactions between molecules of AB (Bowden and Autrey, 2011; Al-kukhun, Hwang and Varma, 2012; Wolstenholme *et al.*, 2012; Kobayashi *et al.*, 2014; Petit and Demirci, 2018). In general, these investigations agree that a significant portion of evolved H_2 is derived from intuitive heteropolar (N—$H^{\delta+}\cdots H^{\delta}$—B) interactions, however they report conflicting results with regard to unexpected homopolar interactions. Simulations proposed the reaction of BH_3 with AB to form a hydride-bridged intermediate (NH_3BH_2(μ-H)BH_3, AaDB), which then underwent reaction with NH_3 to either reform AB or form DADB (Chen *et al.*, 2011) (M. T. Nguyen *et al.*, 2007). This was supported by experiments that found such homopolar (B—$H^{\delta-}\cdots H^{\delta}$—B) interactions preceded the onset of hydrogen release, leading to the suggestion that BH_3 (from cleavage of AB) acts as a Lewis acid catalyst (Al-kukhun, Hwang and Varma, 2012). These findings support the importance of DADB, as discussed previously, however the mechanism for its formation would be somewhat different, as seen in Figure 2.5 overleaf (Chen *et al.*, 2011).

Alternative proposals include that this AaDB intermediate does not react to form DADB and instead forms μ-aminodiborane (μADB), monoaminoborane (MAB) and/or diborane (DB) (Al-kukhun, Hwang and Varma, 2012). Regardless of the precise mechanism, these studies generally found the amount of H_2 evolved from homopolar (B-$H^{\delta-}\cdots H^{\delta}$—B) interactions was significant, especially during the second release during thermolysis (from PAB to PIB at around 130 ^{o}C) (Wolstenholme *et al.*, 2012). Contrastingly, some authors report the occurrence of significant homopolar (N-$H^{\delta+}\cdots H^{\delta+}$-N) interactions but negligible homopolar (B-$H^{\delta-}\cdots H^{\delta}$—B) interactions (Petit and Demirci, 2018). These conflicting results highlight the need for further research to clarify the evidently complicated role of heteropolar and homopolar interactions in the hydrogen release mechanism from AB. Nevertheless, in spite of this lack of precise understanding, there is a general consensus that thermolysis of AB proceeds through PAB followed by PIB, to effect thermolytic residues with empirical structure of NBH_x ($x \leq 2$), as summarised in Figure 2.3 (Frueh *et al.*, 2011)(Demirci, 2017a).

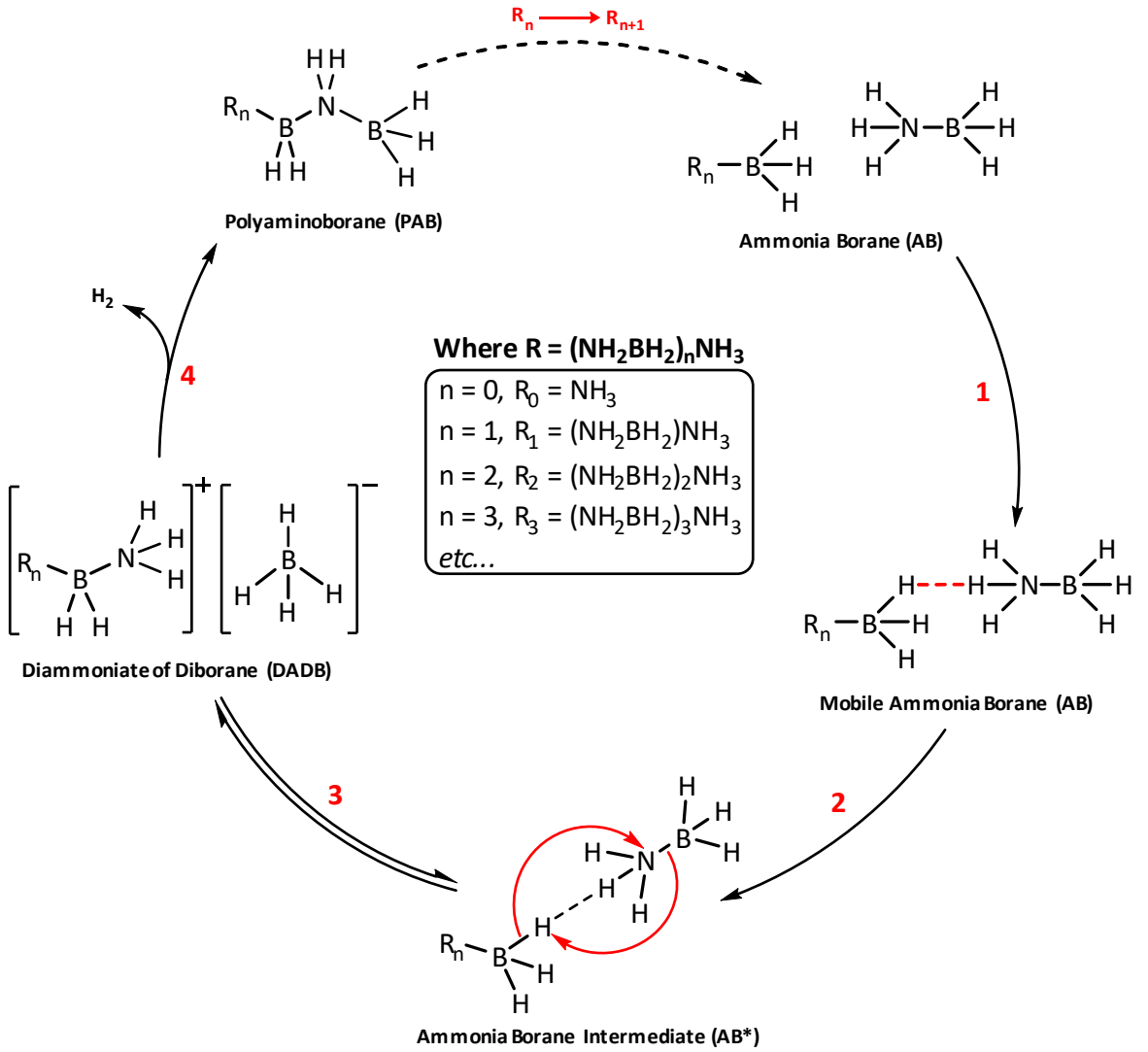

Figure 2.4: Proposed mechanism for the isothermal thermolytic dehydrogenation of AB by heteropolar (N-H$^{\delta+}$···H$^{\delta-}$-B) interactions, including (1) destabilisation to form a mobile phase of AB, (2) heteropolar interactions forming an intermediate, (3) isomerisation to form DADB, and (4) dehydrogenation of DADB to form PAB and evolve H_2. Adapted from (Demirci, 2017a)**.**

2.1.4 Hydrogen Release by Hydrolytic Dehydrogenation

Conversely, hydrogen release from AB can also occur by hydrolytic dehydrogenation (*i.e.* 'hydrolysis') where AB reacts with H_2O groups resulting in the formation of by-products and the evolution of H_2 (Sanyal *et al.*, 2011). This is typically conducted with AB dissolved in a protic solvent alongside a catalyst in a technique is known as solubilisation (as discussed in *2.1.8 Modification Techniques*) (Sanyal *et al.*, 2011). The reaction occurs between the protic atoms (O-H$^{\delta+}$) of the H_2O and the hydridic atoms (B-H$^{\delta-}$) of the dissolved AB, resulting in the evolution of H_2 which is removed from solution. This reaction decomposes the -BH_3 group of dissolved AB to produce compounds including boric acid (H_3BO_3), metaboric acid hydrate (HBO_2·H2O) metaborate anions (BO_2^-), tetrahydroborate anions ($B(OH)_4^-$), as well as various

other borates (Zhan, Zhu and Xu, 2016). Dehydrogenation of the -NH_3 moiety of AB is relatively difficult, with these molecules typically retained in solution as either dissolved NH_3 or NH_4^+ (Equations 2.1 to 2.3) (Sanyal *et al.*, 2011). Experiments using deuterium-labelled AB have confirmed this by evaluating the composition of evolved H_2, which was found to consist of equimolar amounts of atoms originating from the AB and H_2O (Sanyal *et al.*, 2011). Generally, hydrolysis proceeds with a more exothermic release (ΔH_r = -156 kJ/mol) compared to thermolysis, due to the greater stability of the resulting B-O bond (Demirci, 2017a). Importantly, hydrolysis can occur alongside thermolysis, where AB reacts with hydroxyl groups present on the surface of the support material (*e.g.* Si-OH) (Gutowska *et al.*, 2005). This effect contributes toward the acceleration of hydrogen release observed during nanoconfinement, as discussed in *2.1.8 Modification Techniques*.

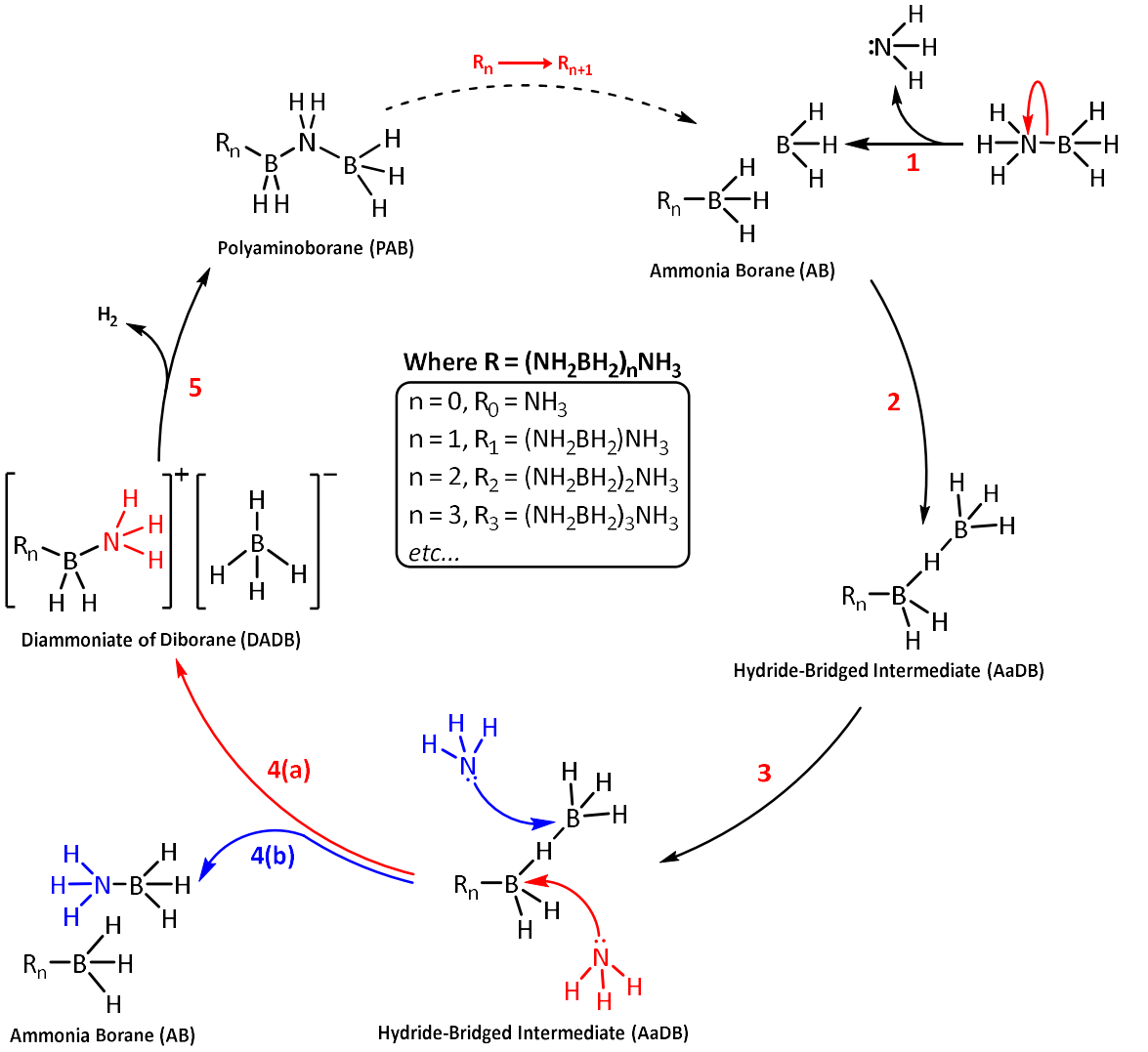

Figure 2.5: Proposed mechanism for the isothermal thermolytic dehydrogenation of AB by homopolar (B-H$^{\delta-}\cdots$H$^{\delta-}$-B) interactions, including (1) heterolytic cleavage of AB forming BH_3, (2) homopolar interaction of AB and BH_3 to form a hydride-bridged intermediate (AaDB), (3) reaction of NH_3 and AaDB leading to (4a) formation of DADB, followed by (5) dehydrogenation of DADB to form PAB and evolve H_2. Alternatively, (4b) reformation of AB without evolving H_2. Constructed based on (Chen *et al.*, 2011)

$$NH_3BH_3 + 3H_2O \longrightarrow NH_3 + B(OH)_3 + 3H_2 \quad \textbf{2.1}$$

$$NH_3BH_3 + 3H_2O \longrightarrow [NH_4]^+ + [B(OH)_4]^- + 3H_2 \quad \textbf{2.2}$$

$$NH_3BH_3 + 2H_2O \longrightarrow [NH_4]^+ + [BO_2]^- + 3H_2 \quad \textbf{2.3}$$

2.1.5 **Volatilisation of Gaseous Contaminants**

Previous discussions regarding the release of hydrogen during thermolysis of AB (as seen in Figure 2.4 and Figure 2.5) have exclusively considered the evolution of pure H_2. This discussion was idealised, since in practise a several nitrogen- and boron-containing species are volatilised alongside H_2 (Babenko *et al.*, 2017)(Kang *et al.*, 2008)(Zhao et al., 2010). These volatilised species contaminate the released H_2, leading problems such as decreased conversion efficiency (*i.e.* less selectivity to H_2), problems for downstream processing (*e.g.* poisoning of fuel cells) and reductions in overall efficiency (*i.e.* reduced potential for regeneration of spent AB) (US DOE, 2019)(Demirci, 2017a). These contaminants are of concern for systems that utilise hydrogen, as reflected by the contaminant targets specified by in Table 1.2 (US DOE, 2017). For instance, these guidelines recommend below 0.1 μmol(NH_3)/mol(H_2), corresponding to a concentration of 1 x10^{-5} mol% of NH_3 (US DOE, 2017). Hence, for many candidate storage materials (and particularly chemical hydrides) the purity of the released hydrogen remains a significant technical challenge (US DOE, 2017).

Experimental investigations have revealed the thermolysis of AB results in the volatilisation of several species of varying quantities (Babenko *et al.*, 2017)(Wood *et al.*, 2017)(Geanangel and Rabalais, 1985). These include many of the volatile species previously identified, such as BH_3, NH_3, DB, MAB, TB, μADB, ADB, BZ, as well as sublimated AB (Babenko *et al.*, 2017). Furthermore, other species have been detected whose structures are comparatively poorly defined, generally referred to by their empirical formula (*e.g.* NBH_x, NB_2H_x, $N_2B_2H_x$, $N_2B_3H_x$) (Babenko *et al.*, 2017). For clarity, the molecular structures for each of these contaminant species have been illustrated in Figure 2.6 overleaf alongside their respective molecular mass (M_W) values for consideration in Figure 2.7 (Demirci, 2017a). The quantity of volatilised species is complicated and reportedly dependent on many factors including the temperature, heating rate, extent of dehydrogenation, and the presence of impurities within the AB (Petit, Miele and Demirci, 2016).

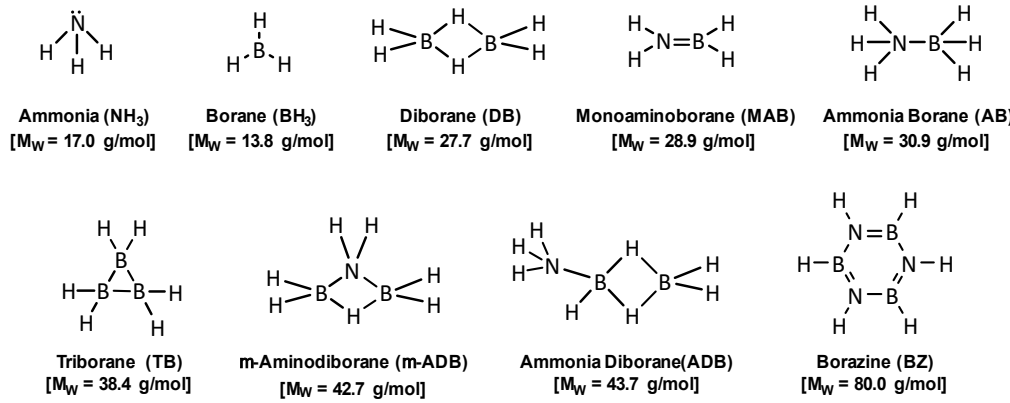

Figure 2.6: Molecular structures for volatilised species detected alongside evolved H_2 during thermolytic dehydrogenation of AB. Adapted from (Demirci, 2017a)**.**

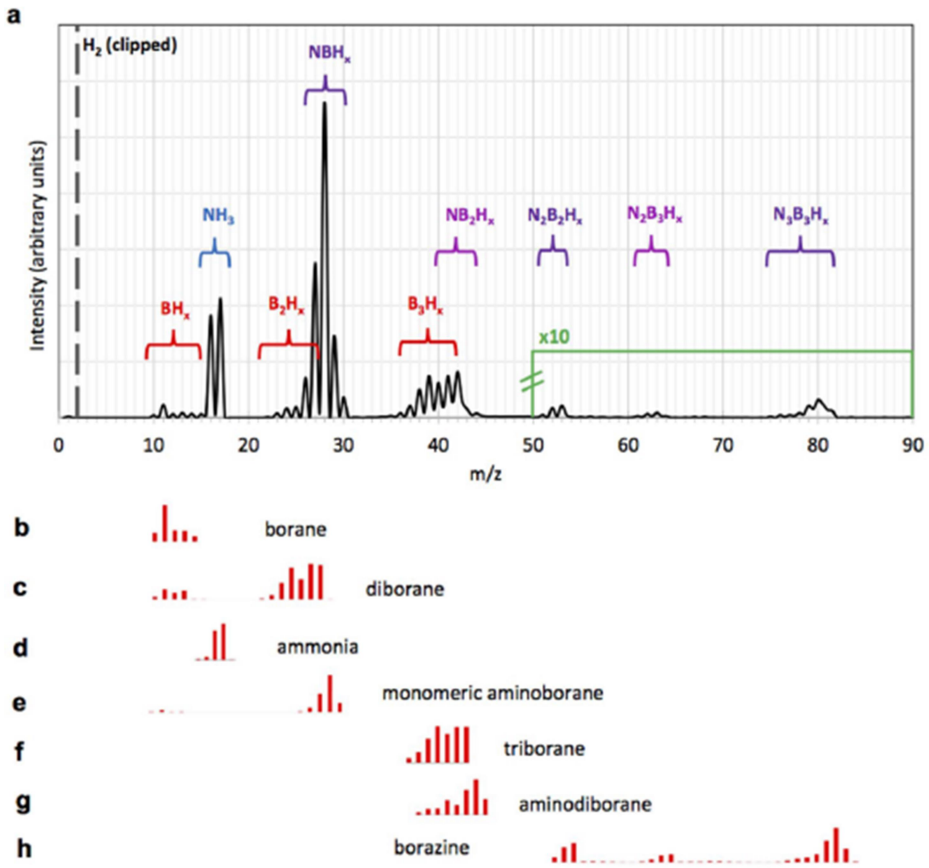

Figure 2.7: Mass spectrometry analysis of AB heated to 100 °C in H_2 showing (a) detected spectrum, and deconvoluted peaks and assignments including (b) borane, (c) diborane, (d) ammonia, (e) monomeric aminoborane, (f) triborane, (g) aminodiborane and (h) borazine. As reported by (Babenko *et al.*, 2017)**.**

For instance, with regard to heating rate, these contaminants have been observed in appreciable quantities at moderate rates (β = 1-5 °C/min), but decrease to below detectable quantities at slow rates (β = 0.15 °C/min) (Baitalow *et al.*, 2006). Furthermore, the volatilisation of these species occurs unequally during each stage of reaction (Babenko *et al.*, 2017). Evidentially, of the total volatilisation of BZ during thermolysis of AB, significantly less occurred during the first hydrogen release compared to the second hydrogen release (evaluated at ~7% and ~93%, between 95-132 °C and 132-200 °C respectively) (Benzouaa *et*

al., 2010). The volatilisation of these contaminants can be reduced and even completely eliminated by carefully controlling conditions during thermolysis or by modification of the AB (Baitalow et al., 2006) (Li, Zhu, et al., 2010). Various techniques have been employed to alter the characteristics of the molecules of AB, change the dehydrogenation mechanism and/or otherwise inhibit volatilisation (discussed in *2.1.8 Modification Techniques*).

2.1.6 **Regeneration of Depleted Residues**

Following release, the spent AB requires regeneration to restore the hydrogen content of the molecules for further storage cycles (Summerscales and Gordon, 2013). However, this is challenged by thermodynamic limitations that prevent direct rehydrogenation of spent AB with H_2 (Equation 2.4), meaning regeneration must instead proceed indirectly by reaction with other chemical feedstocks (Li *et al.*, 2014). However, the success of these reactions strongly depends on the precise composition of the spent AB (Ramachandran and Gagare, 2007)(Sutton, 2014). After preceding thermolysis, the resultant NBH_x ($x \leq 2$) residues show highly variable compositions that inhibit efficient conversion to AB (Summerscales and Gordon, 2013). Of the specific polymers within NBH_x ($x \leq 2$), the conversion of polyborazylene (PBZ) to AB by reaction with hydrazine (N_2H_4) in liquid NH_3 (Equation 2.5) has been demonstrated with a yield of 92% (Sutton, 2014). This strongly exothermic reaction proceeds with a large release of heat (ΔH_r = -271 kJ/mol) (Sutton, 2014). Hence, the selective formation of PBZ within the thermolytic residues of AB is highly desirable since the constituent B=N bonds are amenable regeneration (Summerscales and Gordon, 2013). In contrast, the only method currently reported for regeneration of PAB/PIB is by methanolysis to form dissolved ammonium tetramethylborate ($NH_4B(OCH_3)_4$) (Equation 2.6), which can then be reduced with ammonium chloride (NH_4Cl) and lithium aluminium hydride ($LiAlH_4$) (Equation 2.7) (Ramachandran and Gagare, 2007). As above, these reactions are exothermic and proceed the release of a substantial amounts of heat (evaluated experimentally at ΔH_r = -227 kJ/mol and ΔH_r = -23.4 kJ/mol respectively) (Stephens, Pons and Baker, 2007) (Demirci, 2017a). Although regeneration has been demonstrated, the products from methanolysis of AB are disadvantaged by the stability of the resulting B-O bonds, requiring more energetic reducing agents to achieve reduction (Li *et al.*, 2014).

2.4

2.5

2.6

2.7

As discussed previously, the release of heat during regeneration is widely held to reduce the overall efficiency of storage (Andersson and Grönkvist, 2019). Since the above reactions are both conducted at refrigerated temperatures (T ≈ -77 °C) (Sutton, 2014) (Ramachandran and Gagare, 2007), their released heats of reaction must be removed to maintain the overall reaction temperature. Thus, unless this heat can be integrated into other storage processes, the use of AB as a hydrogen storage candidate is indirectly challenged (US DOE, 2017). Furthermore, the systematic exothermic reactions (*i.e.* during synthesis, release and regeneration) strongly suggest an equivalent endothermic demand to complete the storage cycle, presumably 'hidden' within the reagents used for regeneration (*e.g.* $LiAlH_4$, NH_3, N_2H_4).

2.1.7 **Technical Challenges**

To reiterate, whilst AB demonstrates several remarkable performance characteristics there are a number of technical challenges that hinder its application as a hydrogen storage material (Demirci, 2017a). These challenges can be contextualised against the performance criteria specified for hydrogen storage materials in Table 1.2 (US DOE, 2017). Firstly, the temperatures required to effect dehydrogenation are relatively high and the release mechanism proceeds through a complex set of reactions with slow kinetics (particularly apparent during isothermal dehydrogenation) (Bowden *et al.*, 2006). These negatively affect target parameters such as system efficiency, minimum flowrate and start-up time. Secondly, the purity of hydrogen released from AB is compromised by the evolution of nitrogen- and boron-containing contaminants (Babenko *et al.*, 2017). The volatilisation of these species reduces delivery purity, but also adversely affects efficiency and operational lifetime due to the loss of unevolved hydrogen and regenerable material. Finally, there are also serious challenges regarding the synthesis and regeneration of AB. Several robust syntheses of AB have been demonstrated, however these reactions typically require intense temperatures and strong reagents (Heldebrant *et al.*, 2008), raising concerns about the overall system efficiency. Furthermore, regeneration of spent polymeric residues is complex since direct rehydrogenation with hydrogen gas is not thermodynamically possible (Stephens, Pons and Baker, 2007). Other regeneration routes have been reported, but ideally require the exclusive formation of specific polymeric residues (Sutton, 2014). Unless economic regeneration is realised, AB cannot be considered for reversible storage and would be limited to single-use storage. To summarise, the technical challenges inhibiting application of AB are:

i) **Hydrogen release**: Complex release reactions with slow kinetics and high temperature
ii) **Hydrogen purity**: Evolution of gaseous contaminants alongside released hydrogen
iii) **Regeneration**: Formation of varied polymeric residues that complicate regeneration

2.1.8 **Modification Techniques**

In order to resolve these technical challenges, a number of modification techniques have been applied to AB, namely solubilisation, solid-state doping, nanoconfinement, and chemical modification (Demirci, 2017a). These can be seen schematically illustrated in Figure 2.8 below, followed by a brief summary for each, with particular emphasis on nanoconfinement.

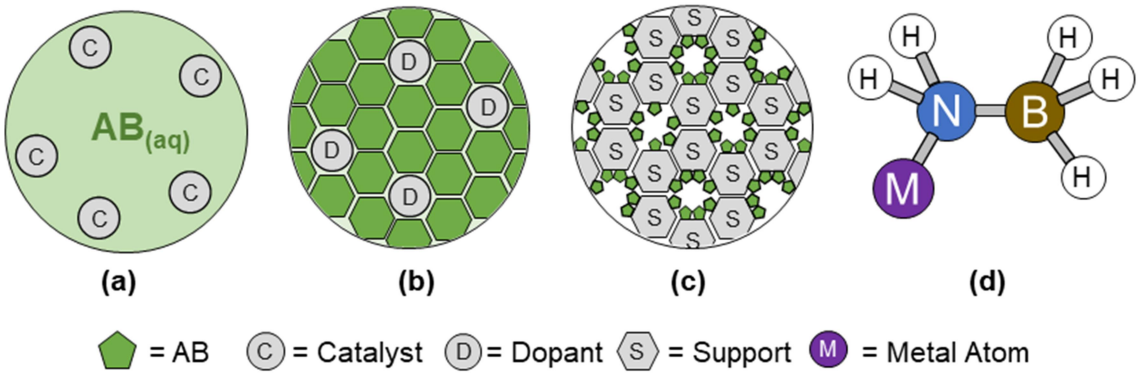

Figure 2.8: Modification techniques for destabilisation of AB, namely (a) solubilisation, (b) solid-state doping, (c) nanoconfinement, and (d) chemical (Demirci, 2017a)

Solubilisation involves dissolution of bulk AB within a solvent typically containing a catalyst, with dissolution acting to disrupt the intermolecular dihydrogen ($N\text{-}H^{\delta+}\cdots H^{\delta-}\text{-}B$) bonding that otherwise stabilises molecules of AB (Kostka *et al.*, 2012). This destabilisation allows a catalyst to facilitate dehydrogenation of AB in either protic (*e.g.* ammonia, water, ethanol) or aprotic (*e.g.* diglyme, tetrahydrofuran, diethyl ether) solvents (Benzouaa *et al.*, 2010) (Sanyal *et al.*, 2011). With regard to catalysts, a number of systems have been investigated with a wide variety reported for both homogeneous or heterogeneous catalysts (Zhan, Zhu and Xu, 2016). Those based on noble metals (*e.g.* Au, Ir, Pd, Pt, Rh, Ru) are highly active toward dehydrogenation of AB and greatly accelerate the release of hydrogen at lower temperatures, however the cost of these metals has also prompted research into cheaper catalysts based on transition metals (*e.g.* Fe, Ni, Cu, Co) (Zhan, Zhu and Xu, 2016). In the case of heterogeneous systems, these catalysts have been supported on a variety of materials including metal oxides (*e.g.* SiO_2, CeO_2, TiO_2, *etc.*), activated carbon (*e.g.* graphene, graphene oxide, carbon nanotubes), as well as MOFs (*e.g.* MIL-101) (Zhan, Zhu and Xu, 2016). One proposed mechanism involves the adsorption of AB and H_2O on the catalyst surface wherein a rate-limiting reaction with hydroxyl (OH^-) groups forms BH_3OH and NH_3 (Qu *et al.*, 2019). These species then recombine to form $BH_2OH\text{-}NH_3$ and a hydride (H^-). This hydride reacts with adsorbed H_2O to eliminate H_2 and regenerate OH^- for further reaction, which is repeated twice more to form borate ($B(OH)_3$) species and complete hydrolysis of AB (Qu *et al.*, 2019).

Alternatively, modification can be by a technique known as solid-state doping, wherein bulk AB is mixed with a dopant material that causes destabilisation and accelerates the release of hydrogen (Demirci, 2017a). A broad range of dopant materials have been examined including metal chlorides (*e.g.* $PtCl_3$, $NiCl_2$, $CuCl_3$) (He *et al.*, 2009), supported and unsupported metal nanoparticles (*e.g.* Pt, Ni, Al, Cu, Mg, Si) (Sun, Li and Wang, 2015), metallic hydrides (*e.g.* LiH, TiH_2, ZrH_2, MgH_2, CaH_2) (Kang *et al.*, 2009), metal oxides (*e.g.* SiO_2, Al_2O_3, MgO, TiO_2) (Simagina *et al.*, 2017), various inorganics (*e.g.* CaF_2, NH_4Cl, Zeolites) (Bowden and Autrey, 2011) (Simagina *et al.*, 2017) and organics (*e.g.* polyethylene oxide, mannitol, methyl cellulose) (Nathanson *et al.*, 2015), as well as many others. Due to their greatly differing properties, the proposed mechanisms by which these dopants operate are necessarily varied. However, the majority are accounted for by interactions of AB with sites that either exhibit Brønsted acidity (*e.g.* R-OH), Lewis basicity (e.g. M-O-M) or nucleation sites (*e.g.* B=N), as reviewed by (Demirci, 2017a). These are detailed later in subsequent discussion.

A further method for destabilisation of AB is chemical modification, in which AB is reacted to form a new species with distinct physical characteristics (Rossin and Peruzzini, 2016). Typically, this modification is by reaction of AB with a metal hydride (MH_n) to afford metallic aminoboranes ($M(NH_2BH_2)_n$, typically either alkali, alkali-earth or transition-block metals (*e.g.* Li, Na, Ca, Mg, *etc.*) (Demirci, 2017a). In addition to aminoboranes, other similar species have been reported including metallic amides, borohydrides, ammoniated borohydrides and alanates (Nakagawa *et al.*, 2014). The inclusion of the metal atom into the molecular structure disrupts the intermolecular dihydrogen ($N\text{-}H^{\delta+}\cdots H^{\delta-}\text{-}B$) bonding and effectively destabilises the AB (Rossin and Peruzzini, 2016). This might be explained by the different electronegativity of the incorporated metals, which alter the lengths of the constituent bonds and affect the protic ($H^{\delta+}$) and hydridic ($H^{\delta-}$) character of the hydrogen atoms.

Nevertheless, a further technique for modification of AB is nanoconfinement (Demirci, 2017a). This involves the deposition of AB within a porous support material, such that a highly dispersed layer of AB is formed within the pores of the support (Rueda, Sanz-moral and Martín, 2018). Unlike bulk AB, these crystallites are nanosized and relatively isolated, meaning they exhibit higher surface area and are more able to interact with the surface of pores (Wahab, Zhao and Yao, 2012). As above, these cause disruption of the intermolecular dihydrogen ($N\text{-}H^{\delta+}\cdots H^{\delta-}\text{-}B$) bonding, achieving destabilisation of the nanoconfined AB and accelerating hydrogen release. A comparative review of bulk and nanoconfined AB has been presented in Table 2.3, adapted and updated from (Rueda, Sanz-moral and Martín, 2018). This includes details on the type of support material, respective material properties, and information on the gases evolved upon heating. This includes the surface area (S_{BET}), pore volume (V_P) and average pore diameter (D_P), the activation energy (E_A) for hydrogen release, as well as the peak temperature for release of hydrogen and volatilised contaminants.

The variety of materials that have been used as supports for nanoconfinement of AB can be seen in Table 2.3, including forms of silica, metal-organic frameworks, carbon, organic polymers and other substances (Rueda, Sanz-moral and Martín, 2018). The potential of nanoconfinement is apparent in Table 2.3, with many finding substantially reduced activation energy, lower temperature for hydrogen release, and suppression of contaminants (Rueda, Sanz-moral and Martín, 2018). Evidentially, mesoporous silica supports were widely observed to reduce the activation energy from ~180 to 67 kJ/mol for bulk and nanoconfined AB respectively (Gutowska *et al.*, 2005). This was broadly observed to effect a reduction in hydrogen release temperature from ~110 ^{o}C to around 69 ^{o}C, improving the efficiency of release and evidencing the strength of nanoconfinement effects (Gutowska *et al.*, 2005) (Rueda *et al.*, 2017)(Lai *et al.*, 2012)(Paolone *et al.*, 2009). Alternatively, other materials appear to offer modest reductions in activation energy, but are able to suppress volatilisation of contaminants. For instance, some metal-organic frameworks (*e.g.* JUC-32) were able to completely eliminate the evolution of all measured contaminants (Li, Zhu, *et al.*, 2010).

Conceptually, the surface properties of support materials are fundamental in determining the subsequent nanoconfinement effects (Rueda, Sanz-moral and Martín, 2018). It is widely accepted that ideal supports exhibit high values for both surface area and pore volume, which increase the loading capacity and potential for surface interactions (Wahab, Zhao and Yao, 2012). Contrastingly, the effects of pore diameter are somewhat disputed with many proposing that small pore diameters (*i.e.* micropores) are ideal since they increase the strength of nanoconfinement effects and help to eliminate entrainment of contaminants into the evolved gas (Lai *et al.*, 2012). This is consistent with the understanding that nanoconfinement occurs at the support surface, where larger pore diameters necessarily exhibit a more internal volume and less surface contact. In spite of this, many authors report the preparation of supports with larger pore diameters (*i.e.* mesopores) to improve loading capacity (Rueda *et al.*, 2017) (Gutowska *et al.*, 2005) (Sepehri and Cao, 2009).

The predominant mechanisms for dehydrogenation of nanoconfined AB are divided between sites that exhibit Lewis basicity (*e.g.* Si-O-Si, C=O and B-N), sites that exhibit Brønsted acidity (*e.g.* Si-OH, C-OH and COOH), and nucleation sites (*e.g.* B-N) (Demirci, 2017a). These have been schematically illustrated in Figure 2.9(a)-(e), adapted from (Lai *et al.*, 2012). Firstly, Figure 2.9(a) shows nanoconfined AB that is within the volume of the pore but not in contact with the surface of the support. Conceptually, hydrogen release from these molecules of AB follow the heteropolar and/or homopolar mechanisms previously identified (Figures 2.4 and 2.5) due to the absence of strong interactions with the surface (Wolstenholme *et al.*, 2012) (Al-kukhun, Hwang and Varma, 2012) (Petit and Demirci, 2018). Nevertheless, even in the absence of support interactions, the physical nanoscaling of AB crystallites has been found to moderately accelerate release (Rueda *et al.*, 2017).

Table 2.3: Review of a selection of bulk AB and nanoconfined AB composites reported in literature. Adapted from (Rueda, Sanz-moral and Martín, 2018)

Reference	Support Material	Properties[a]					Temperature of Gases Evolved[b], T_p (°C)					Proposed Mechanism[c]
		S_{BET} (m_2/g)	V_P (cm_3/g)	D_P (nm)	L (wt% AB)	E_A (kJ/mol)	H_2	NH_3	BH_3	DB	BZ	
Bulk AB												
(Roy, Hajari, Manna, *et al.*, 2018)	-	-	-	-	100	-	129, 170	130, 185	-	173	167	-
(Frueh *et al.*, 2011)	-	-	-	-	100	-	110, 130	-	-	-	110, 130	-
(Li, Guo, *et al.*, 2010)	-	-	-	-	100	138	110, 154	-	-	-	-	-
(Li, Zhu, *et al.*, 2010)	-	-	-	-	100	-	114, 150	118,155	-	155	155	-
(Zhao *et al.*, 2010)	-	-	-	-	100	-	106, 154	n.d	-	170	175	-
(He *et al.*, 2009)	-	-	-	-	100	129	100, 160	-	-	-	-	-
(Li *et al.*, 2009)	-	-	-	-	100	184	105, 140	105	-	-	n.d	-
(Kang *et al.*, 2008)	-	-	-	-	100	183	114, 153	-	-	153	153	-
(Sepehri, Garcia and Cao, 2008)	-	-	-	-	100	160	115, 150	-	-	-	-	-
(Gutowska *et al.*, 2005)	-	-	-	-	100	184	110, 155	-	-	-	160	-
Nanoconfined AB												
(Rueda *et al.*, 2017)	Mesoporous Silica (Aerogel)	890	1.9	9	13, 30, 60	-	69, 109	-	-	-	-	Interaction with surface Si-OH and/or Si-O-Si
(Lai *et al.*, 2012)	Mesoporous Silica (MCM-41)	1009	0.85	3	50	-	113, 146	100		120	153	Interaction with surface Si-OH and/or Si-O-Si
(Lai *et al.*, 2012)	Mesoporous Silica (SBA-15)	817	1.13	6	50	-	116, 151	102		150	151	Interaction with surface Si-OH and/or Si-O-Si
(Paolone *et al.*, 2009)	Mesoporous Silica (MCM-41)	-	-	-	33, 50	-	-	-	-	-	-	-
(Wang *et al.*, 2009)	Mesoporous Silica (MCM-41)	900	0.75	-	33, 50, 75	-	-	-	-	-	-	-
(Gutowska *et al.*, 2005)	Mesoporous Silica (SBA-15)	900	1.2	8	50	67	95	-	-	-	140	Interaction with Si-OH, Defect sites in crystallites of AB
(Autrey *et al.*, 2004)	Mesoporous Silica (SBA-15)	1000	-	3	50	-	-	-	-	-	-	-
(Li *et al.*, 2015)	Metal-Organic-Framework (MOF-5)	1032	0.57	-	50	68	84	84	-	n.d	n.d	Interaction with unsaturated coordinated metal sites
(Gadipelli *et al.*, 2012)	Metal-Organic Framework (MOF-74)	1100	-	-	26	-	102	102	-	103	102, 140	Interaction with unsaturated coordinated metal sites
(Zhong *et al.*, 2012)	Metal-Organic Framework (ZIF-8)	1253	0.3-1.2	-	6-90	-	82, 133	-	-	-	-	Interaction with metal sites and/or organic ligands
(Li, Zhu, *et al.*, 2010)	Metal-Organic-Framework (JUC-32)	659	0.27	-	8	-	84	n.d	n.d	n.d	n.d	Interaction with unsaturated coordinated metal sites
(Yang *et al.*, 2017)	Mesoporous Carbon Framework (CEMC)	1652	0.87	1	-	75	86	n.d	n.d	-	-	-
(Moussa *et al.*, 2012)	Activated Carbon	716	0.36	-	50	64	110	150	-	-	120	Interaction with surface COOH
(Sepehri and Cao, 2009)	Activated Carbon (Cryogel, BN-doped)	446	0.96	16	50, 60	115	103	-	-	-	-	Presence of B and N, Interaction with surface C-OH
(Li *et al.*, 2009)	Activated Carbon (CMK-3, 5% Li)	1150	1.5	-	50	98	95	95	-	-	n.d	Interaction with surface COOH and/or C-OH, Catalysis by Li
(Sepehri, Garcia and Cao, 2008)	Activated Carbon (Cryogel)	350-500	0.69-0.97	2-50	33, 50	150	101	-	-	-	-	-
(Sepehri *et al.*, 2007)	Activated Carbon (Cryogel)	500	0.7	2-20	40	150	-	-	-	-	-	Interaction with surface C-OH
(Feaver *et al.*, 2007)	Activated Carbon (Cryogel)	300	0.7	2-20	24	-	90	-	-	-	n.d	Interaction with surface COOH
(Tang *et al.*, 2012)	Carbon (Graphene Oxide)	104-391	0.65-2.85	4-10	30, 50	30	99, 125	n.d	-	n.d	n.d	Presence of B and N, Interaction with surface C-OH
(Li, Guo, *et al.*, 2010)	Carbon Nanotubes (CNT, 10% Pt)	169	-	-	50	106	108, 150	-	-	-	n.d	Catalysis by Pt/CNT
(Alipour, Shoushtari and Kaflou, 2015)	Polymer (Polymethacrylate-CNT)	-	-	-	5-25	-	80	-	-	-	-	Interaction with surface C=O
(Zhao *et al.*, 2010)	Polymer (Polymethacrylate)	-	-	-	20/80	-	95	120	-	n.d	n.d	Interaction with surface C=O
(Salameh *et al.*, 2018)	Mesoporous Boron Nitride (BN)	584-728	0.75-0.93	4	-	-	118	-	-	-	-	Presence of B and N
(Roy, Hajari, Manna, *et al.*, 2018)	Aluminium Phosphate ($AlPO_4$)	201	-	-	11-50	-	109	111	-	n.d.	170	Promotion of homopolar ($B\text{-}H^{\delta-}\cdots H^{\delta}\text{-}B$) interactions
(Roy, Manna, *et al.*, 2018)	Porous Clay (Bentonite)	42	-	-	50	121	120, 150	-	-	n.d.	n.d.	-

[a] Properties: S_{BET} = surface area (m^2/g), V_P = pore volume (cm^3/g), D_P = pore diameter (nm), L = loading (wt%), E_A = activation energy (kJ/mol)
[b] Gases Evolved: H_2 = hydrogen, NH_3 = ammonia, BH_3 = borane, DB = diborane, BZ = borazine, n.d. = measured but not detected
[c] Proposed Mechanism: vague explanations have been omitted due to their unspecific insight (*e.g.* “destabilisation of AB due to disruption of intermolecular dihydrogen bonding”)

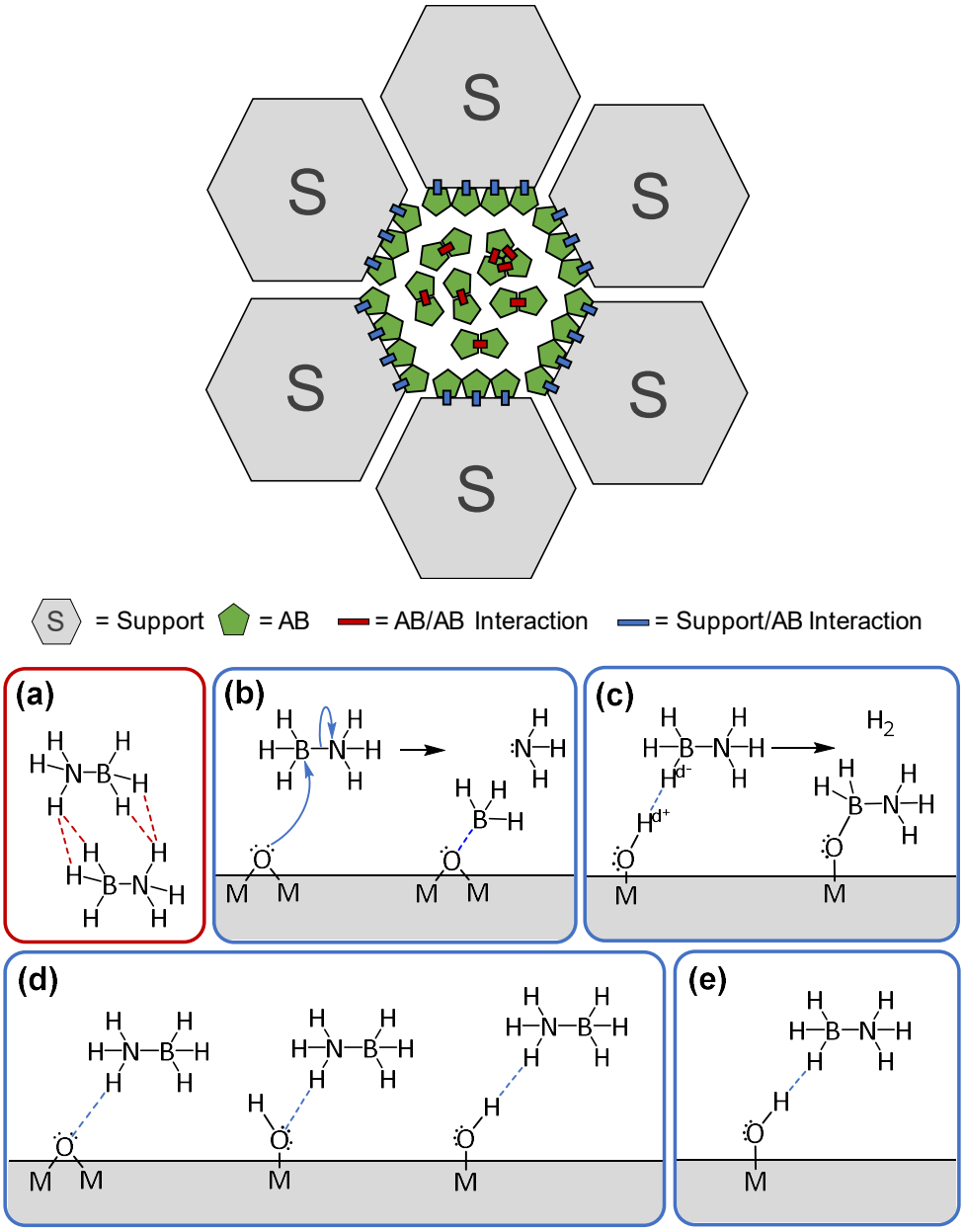

Figure 2.9: Potential mechanisms for the promotion of hydrogen release from nanoconfined AB, including (a) intermolecular dihydrogen (N-H$^{\delta+}$···H$^{\delta-}$-B) bonding between molecules of AB. Alternatively, interactions between molecules of AB and the support surface, namely (b) M-O-M sites with Lewis basicity, (c) M-OH sites with Brønsted acidity, (d) M-O-M and/or M-OH sites hydrogen bonding to NH_3, and (e) M-OH sites hydrogen bonding to -BH_3. Adapted from (Lai *et al.*, 2012), (Moussa *et al.*, 2012)

Conversely, Figure 2.9(b) shows the interaction of AB with M-O-M sites that exhibit strong Lewis basicity (Lai *et al.*, 2012). The free electrons of this surface group are able to form a coordinate bond with the –BH_3 group of AB, causing cleavage of the coordinate B-N bond and displacing NH_3 (Lai *et al.*, 2012). Conceivably, the facile generation of this BH_3 species might then proceed the homopolar formation of DADB (according to Figure 2.5) (Chen *et al.*, 2011), greatly lowering the activation energy and accelerating dehydrogenation whilst forming

PAB/PIB. For some examples, the transition of nanoconfined AB to DADB has been confirmed using X-ray diffraction, although the homopolar mechanism of its formation remains speculative (Rueda *et al.*, 2017). Furthermore, this hydrogen release by this mechanism conveniently explains the large quantities of volatilised NH_3 observed experimentally by some authors, despite apparent suppression of other contaminants (Lai *et al.*, 2012).

Alternatively, Figure 2.9(c) shows the interaction of AB with sites that exhibit Brønsted acid characteristic (Lai *et al.*, 2012). In this mechanism, protic ($H^{\delta+}$) hydrogen atoms from surface hydroxyl or carboxyl species react with the hydridic hydrogens ($H^{\delta-}$) in the $-BH_3$ group of AB in a heteropolar manner analogous to that for bulk AB (as shown in Figure 2.9(a)) (Rueda *et al.*, 2017) (Li *et al.*, 2009). Initially, the greater protic character in these surface species (relative to $-NH_3$ of AB) might explain lowered activation energy and spontaneous isomerisation to form DADB (Moussa *et al.*, 2012). However, it is not clear how subsequent polymerisation to progressively form PAB and PIB would be accelerated since these steps do not obviously benefit from surface interactions. Nonetheless, the anticipated formation of B-O bonds between surface groups and AB has been experimentally confirmed for a number of thermolytic residues (Rueda *et al.*, 2017).

Otherwise, Figure 2.9(d) and (e) show similar mechanisms that occur through the formation of hydrogen and/or dihydrogen bonds between surface species and the $-NH_3$ or $-BH_3$ groups of AB respectively (Lai *et al.*, 2012). Plausibly, these might arise from weaker acidic/basic sites that are unable to directly react as in Figure 2.9(a) or (b), but might enable indirect isomerisation to DADB by disrupting the intermolecular bonding otherwise present in bulk AB (Lai *et al.*, 2012). Finally, the inclusion of B and N atoms appears to act as nucleation sites for polymerisation of PAB/PIB, which facilitates dehydrogenation with lower activation energy (Salameh *et al.*, 2018)(Tang *et al.*, 2012) (not shown in figure).

2.2 Titania

2.2.1 Properties of Titania Catalysts

Titania has been widely applied as a heterogeneous catalyst support in a range of reactions including deoxygenation, hydrogenation, dehydrogenation, methanation, reduction and various other photocatalytic reactions (Bagheri *et al.*, 2014; Oi *et al.*, 2016). Its successful application in these areas has been facilitated by its advantageous properties including physical and chemical stability, surface acidity/basicity, electronic interactions, and wide band gap (Bagheri *et al.*, 2014). In particular, titania is one of few reducible supports that easily forms corresponding suboxides (*e.g.* Ti_2O_3, Ti_3O_5, Ti_5O_7) (Xu *et al.*, 2016), which then

enhance the reactivity of supported metals (*e.g.* Pt, Rh, Ru, Ni, *etc.*) through strong metal-support interactions (SMSI) (Pan *et al.*, 2017) (Schneider and Baiker, 1997). This reduction is accompanied by charge transfer between the suboxide and supported metal, which results in migration of the support atoms such that they form an overlayer above the supported metal atoms (Cai and Feng, 2016). Such layering drastically changes the interaction of these metal sites with adsorbates often leading to greater reactivity as predicted by the *d*-band centre model (Ruban *et al.*, 1997). Indeed, for a variety of reactions employing supported metal catalysts (*i.e.* M/TiO_2 where M = Pt, Rh, Ru, Ni, *etc.*), SMSI effects have often been attributed to observations of greater reactivity and selectivity (Oi *et al.*, 2016). In the absence of supported metals and induced SMSI effects, interactions with adsorbates are believed to be driven by the surface acid-base characteristic of titania, as seen on Figure 2.10 (Manriquez *et al.*, 2004). Titania usually exhibits weak surface acidity in the form of Brønsted ($Ti\text{-}OH^{\delta+}$) or Lewis acid (Ti) sites, however surface basicity has also been reported with corresponding Lewis base (M-O-M) sites (Oi *et al.*, 2016). The surface characteristic of titania materials are determined during their preparation relative to the isoelectric point (IEP = 2.8), with acidic and basic character predominating at lower (pH ≤ 2.8) and higher (pH ≥ 2.8) conditions respectively (Hanaor *et al.*, 2011).

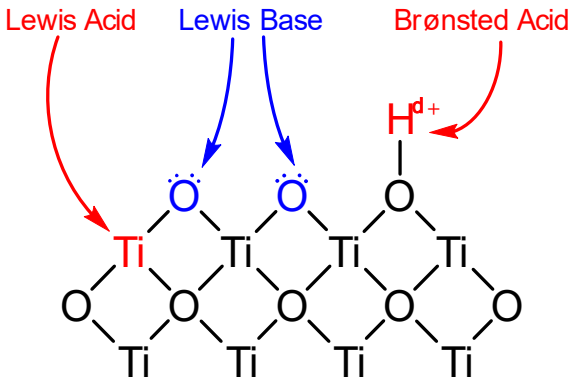

Figure 2.10: Schematic illustration of surface acidity-basicity exhibited by titania

2.2.2 Application to Dehydrogenation of AB

Relative to other catalysts, dopants and/or support materials, comparatively little research has been conducted principally examining the effect of titania on dehydrogenation of AB (Akbayrak and Ozkar, 2018). In contrast, Table 2.4 summarises a selection systems where titania is nonetheless included albeit in a secondary role. Of this research, the vast majority has studied the use of crystalline titania as a support in M/TiO_2 catalysts which was applied to the hydrolysis of AB (Mori, Miyawaki and Yamashita, 2016). Experiments comparing the

effect of different metal oxide supports found Ru/TiO_2 demonstrated superior activity compared to Ru/Al_2O_3, Ru/ZrO_2 and Ru/MgO and Ru/HfO_2, being surpassed only by Ru/CeO_2 (Mori, Miyawaki and Yamashita, 2016) (Akbayrak and Ozkar, 2018). This suggests the excellent catalytic activity of Ru/TiO_2 and Ru/CeO_2 are derived from aforementioned SMSI effects since both are well known as reducible supports (Akbayrak and Ozkar, 2018). In addition to accelerating the rate of release, Table 2.4 also shows how M/TiO_2 catalysts were widely able to quickly effect complete dehydrogenation of AB by release of the third stoichiometric equivalent of H_2 (normally requiring elevated temperature, as in Figure 2.3) (Ma *et al.*, 2017)(Zhou and Xu, 2017)(Khalily *et al.*, 2016). In comparison, the effect of bulk titania (without supported metal) on hydrolysis of AB is unsurprisingly subdued since it possess neither metallic active sites nor any SMSI effects (Simagina *et al.*, 2017)(Yousef, Barakat and Yong, 2013)(Nirmala *et al.*, 2012).

Table 2.4: Review of a selection of titania catalysts applied to dehydrogenation of AB

Reference	Catalyst	Properties				H_2 Release[c] (mol / min)
		Phase[a]	S_{BET} (m^2/g)	E_A (kJ/mol)	TOF[b] (min^{-1})	
Hydrolysis						
(Wang *et al.*, 2018)	$CuNi/B\text{-}TiO_2$	A	-	36	16	2.7, 4 [d]
(Ma *et al.*, 2017)	$Ru/B\text{-}TiO_2$	A	-	46	303	3.0 / 2
(Zhou and Xu, 2017)	PtTi	-	-	39	51	3.0 / 8
(Simagina *et al.*, 2017)	TiO_2	A	-	-	-	0.9 / 240
(Mori, Miyawaki and Yamashita, 2016)	Ru/TiO_2	A	338	-	455	2.9 / 16
(Mori, Miyawaki and Yamashita, 2016)	Ru/TiO_2	A, R	40	38	604	2.9 / 16
(Mori, Miyawaki and Yamashita, 2016)	Ru/TiO_2	R	40	-	510	2.9 / 16
(Mori, Miyawaki and Yamashita, 2016)	$RuNi/TiO_2$	A, R	40	28	914	2.9 / 11
(Khalily *et al.*, 2016)	Pt/TiO_2	-	45	-	310	3.0
(Tonbul, Akbayrak and Ozkar, 2016)	Pd/TiO_2	A	-	-	7	2.8 / 23
(Li, Zeng and Fan, 2015a)	$RuCo/Ti_3C_2X_2$	C	-	31	896	3.0 / 1
(Li, Zeng and Fan, 2015b)	$RuNi/Ti_3C_2X_2$	C		26	825	2.8 / 2
(Akbayrak, Tanyıldızı, *et al.*, 2014)	Ru/TiO_2	A	-	70	241	3.0 / 5
(Akbayrak, Gençturk, *et al.*, 2014)	Rh/TiO_2	A	11	66	260	3.0 / 8
(Rakap, 2014)	$Co\text{-}P/TiO_2$	A, R	-	48	-	3.0 / 4
(Yousef, Barakat and Yong, 2013)	CuO/TiO_2	R, A	-	45	-	3.0 / 23
(Yousef, Barakat and Yong, 2013)	TiO_2	R, A	-	54	-	1.1 / 110
(Nirmala *et al.*, 2012)	TiO_2	R, A	-	-	-	1.4 / 120 [d]
(Nirmala *et al.*, 2012)	Ni/TiO_2	R, A	-	-	-	1.7 / 120 [d]
Thermolysis						
(Komova *et al.*, 2011)	TiO_2	A, R	74	-	-	-
(Komova *et al.*, 2013)	TiO_2	A, R	74	-	-	1.2 / 100
(Simagina *et al.*, 2017)	TiO_2	A	243	-	-	1.4 / 150

[a] Phase: (-) = amorphous, A = anatase, B = brookite, R = rutile, C = Unspecified crystalline
[b] Properties: S_{BET} = surface area (m^2/g), E_A = activation energy (kJ/mol), TOF = turnover frequency (min^{-1})
[c] H_2 Release: Conditions reported for maximum release quantity of H_2 regardless of reaction conditions.
[d] Photocatalysis: Dehydrogenation conducted under presence of UV/Vis light

Even less research has examined the effect of titania on the thermolysis of AB. Nevertheless, preliminary results for solid-state doping of AB with bulk titania ($AB\text{-}TiO_2$) appear relatively promising, as illustrated in Figure 2.11 (Simagina *et al.*, 2017). The doping of AB with SiO_2, TiO_2, Al_2O_3, MgO, HY (Zeolite) and CaF_2 showed slight differences in performance, where AB-HY, $AB\text{-}TiO_2$ and $AB\text{-}Al_2O_3$ generally exhibited better performance than corresponding

mixtures of AB-SiO_2 and AB-MgO (Simagina *et al.*, 2017). In the case of AB-TiO_2, the detection of B-O functionality in the resulting thermolytic residues evidenced the involvement of TiO_2 (Komova *et al.*, 2011), which the authors asserted was due to Brønsted acid sites derived from surface hydroxyls (Ti-OH) (Komova *et al.*, 2013). This was evidenced by the greater activity of humidified AB-TiO_2 (with greater presence of surface hydroxyls) as opposed to mixtures of AB with freshly calcined TiO_2 (with less surface hydroxyls) (Komova *et al.*, 2013).

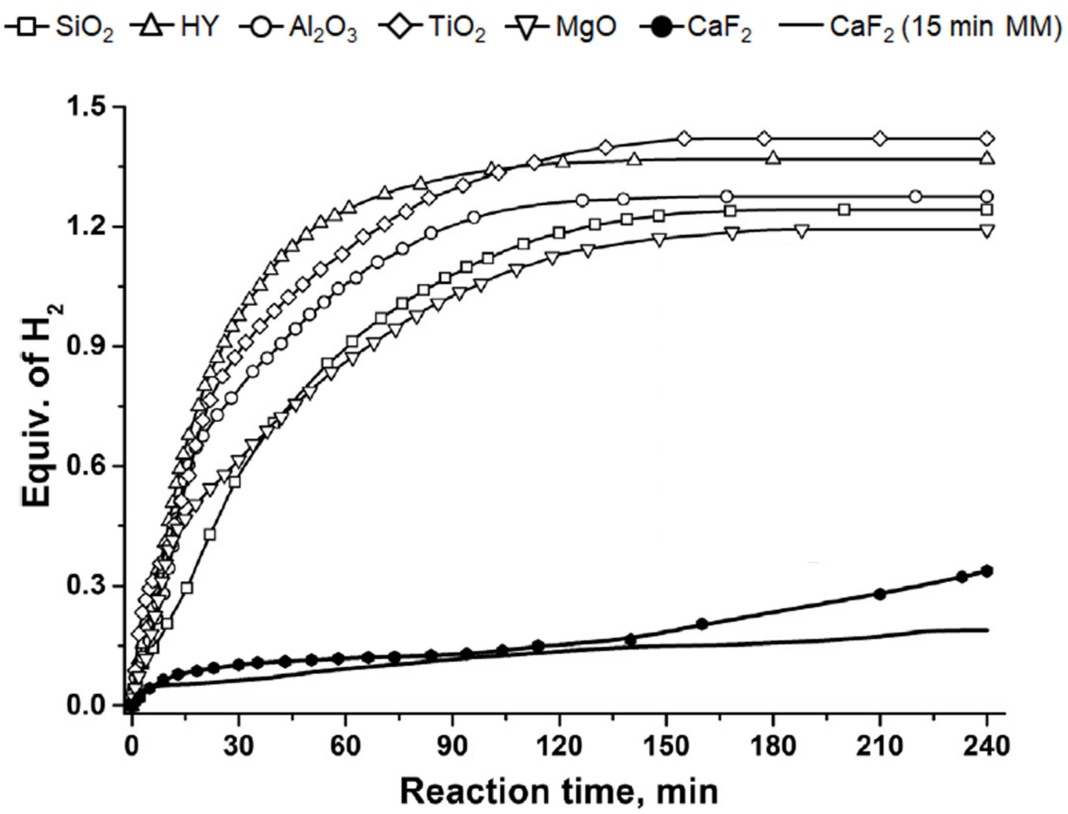

Figure 2.11: Effect of solid-state dopants on thermolysis of AB (Simagina *et al.*, 2017)

Interestingly, the observed performance did not correlate with the reported acidity trend for these metal oxides, which increased from MgO < Al_2O_3 < TiO_2 < SiO_2 (with IEP ≈ 10.3, 7.7, 4.4 and 3.4 respectively) (Carre, Roger and Varinot, 1992). The authors observed the most acidic (*i.e* SiO_2) and basic (*i.e.* MgO) metal oxide dopants to perform worse compared to the more moderate oxides (*i.e.* TiO_2, Al_2O_3) (Simagina *et al.*, 2017). This appears to conflict with the previously described role of surface acidity and basicity in accelerating dehydrogenation of AB proposed by (Lai *et al.*, 2012; Moussa *et al.*, 2012) (as summarised in Figure 2.9). This clearly highlights the need for more research to clarify the role of surface characteristic toward accelerating the dehydrogenation of AB.

2.3 Aerogels

2.3.1 Characteristics of Aerogels

Aerogels are materials that exhibit a number of advantageous characteristics compared to substances from conventional methods (*e.g.* precipitation, hydrothermal, spray-drying) (Pajonk, 1991). Aerogels often demonstrate outstanding surface properties including exceptional porosity (≥95 %), remarkably high surface areas (≤2000 cm^2/g) and large pore volumes (≥1 cm^3/g) (Vareda, Lamy-Mendes and Durães, 2018). Careful control during syntheses can effect well-defined pore geometries with narrow size distributions, either in the mesoporous (2-50 nm) or microporous (<2 nm) ranges (Vareda, Lamy-Mendes and Durães, 2018). Furthermore, due to their high porosity, aerogels often exhibit low density (≤0.5 g/cm^3) which then effects correspondingly low thermal conductivity (<0.05 W/mK) (Pajonk, 1991). Moreover, aerogels often demonstrate robust thermal and chemical stability exhibiting minimal degradation during use, meaning the aforementioned surface properties are better retained over time (Rafael *et al.*, 2015). Finally, the manner of aerogel preparation allows the potential for pre-forming of structures (*e.g.* monoliths), reducing the need for forming processes (*e.g.* milling, shaping, extrusion) which can negatively impact surface properties (Smirnova and Gurikov, 2018). On the other hand, relative to other materials, aerogels are challenged by poor mechanical properties (*i.e.* fragility), their complexity of formation, and the intensive conditions required for drying (Rafael *et al.*, 2015).

2.3.2 Applications of Aerogels

Because of these properties, aerogels have been applied to a number of different fields, with their application to heterogeneous catalysis being particularly notable (Rafael *et al.*, 2015). Since heterogeneous catalysis occurs on active sites at the surface of the catalyst, the overall activity is highly sensitive to the surface properties of the material (Lloyd, 2011). Hence, relative to catalysts prepared by conventional methods, aerogel catalysts offer great potential due to their remarkable surface characteristics (Smirnova and Gurikov, 2018). The high surface area of aerogels present a greater number of active sites on which catalysis can occur, conceptually increasing the overall catalytic activity (Lloyd, 2011). Similarly, their high porosity means a greater fraction of material is exposed on the catalyst surface as opposed to within the bulk (which is inaccessible to reagents and so catalytically inactive) (Pajonk, 1991). As such, conventional understanding would suggest lower catalyst loadings can be used without decreasing catalytic activity, which subsequently reduces material costs (particularly for catalysts based on rare and expensive elements) (Lloyd, 2011). Likewise, their chemical and thermal stability means catalyst deactivation phenomena (*e.g.* sintering)

are minimised over long durations of use (Pajonk, 1991), typically translating to extended catalyst lifetimes and reduced costs (Lloyd, 2011). Aside from catalysis, the excellent properties of aerogels have seen them applied as filtration media, chemical adsorbents, thermal insulators, gas sensors and in optical equipment (Smirnova and Gurikov, 2018), all of which are nonetheless outside the scope of this literature review.

2.3.3 **Preparation of Aerogels**

The properties of aerogels are a direct result of the manner in which they are prepared (Rafael *et al.*, 2015). A typical procedure for the preparation of a metal oxide aerogel from a metal alkoxide (M-OR) precursor is shown in Figure 2.12 (Rafael *et al.*, 2015). The initial steps are comprised of hydrolysis and polymerisation reactions collectively known as the sol-gel process (Debecker *et al.*, 2018). Initially, the alkoxide undergoes acid- or base-catalysed hydrolysis to produce the metal hydroxide (M-OH) and eliminate the corresponding alcohol (R-OH) (Equation 2.8) (Debecker *et al.*, 2018). Next, a condensation reaction proceeds between hydroxides and/or alkoxide, resulting in polymerisation and the formation of oxygen-bridged species (M-O-M) (Equations 2.9 and 2.10 respectively)(Debecker *et al.*, 2018). As hydrolysis and condensation reactions continue, an alcogel develops consisting of a three-dimensional network of metal oxide species (Pajonk, 1991), with this alcogel as the fundamental precursor to the subsequent aerogel (Vareda, Lamy-Mendes and Durães, 2018). The three-dimensional metal oxide network is the basis for the eventual porosity and so many of the final aerogel properties are determined by synthesis conditions employed at this stage of preparation (Smirnova and Gurikov, 2018).

$$\text{M-OR} + \text{H}_2\text{O} \xrightarrow{\text{Acid / Base}} \text{M-OH} + \text{R-OH} \qquad \textbf{2.8}$$

$$\text{M-OH} + \text{HO-M} \xrightarrow{\text{Acid / Base}} \text{M-O-M} + \text{H}_2\text{O} \qquad \textbf{2.9}$$

$$\text{M-OH} + \text{RO-M} \xrightarrow{\text{Acid / Base}} \text{M-O-M} + \text{R-OH} \qquad \textbf{2.10}$$

The interstitial volume within the incipient alcogel is occupied by the reaction mixture (Vareda, Lamy-Mendes and Durães, 2018). This solution predominantly consists of solvent but conceivable must also contain contaminants (*e.g.* unreacted reagents, catalyst, templating agents, dispersants) which require removal before further processing (Pajonk, 1991). These are removed by washing the alcogel with fresh solvent, such that the concentration gradient

of contaminants causes diffusion from within the alcogel into the bulk solvent (Smirnova and Gurikov, 2018). The contaminated solvent is then removed and the above procedure usually repeated to achieve multiple washing cycles. The same process can be used for solvent exchange, wherein alcogels are transferred to a solvent other than that used during synthesis, which causes the original solvent to be removed alongside contaminants (Vareda, Lamy-Mendes and Durães, 2018). Simultaneously, whilst in solution the alcogel undergoes an ageing process, which helps to promote complete hydrolysis and strengthen the metal oxide network formed during condensation (Rafael *et al.*, 2015). Usually a minimum ageing duration is necessary for full development of the alcogel, after which further ageing has diminishing effect due to complete of hydrolysis of the alkoxide precursor (Iswar *et al.*, 2017).

Following ageing, the final step toward the preparation of aerogels is the removal of solvent from the alcogel (Vareda, Lamy-Mendes and Durães, 2018). Conceptually, the most convenient option for this is by evaporative drying, which can be achieved by heating such that the solvent evaporates out of the metal oxide network. However, this is complicated by the occurrence of surface tension at the liquid-gas phase boundary, which induces capillary forces that act on the metal oxide network (Rafael *et al.*, 2015). Over the course of evaporation these capillary forces increase in magnitude, eventually resulting in structural damage and pore collapse in the incipient material (Rafael *et al.*, 2015). Necessarily, this adversely affects the surface properties of the final material, often resulting in lower surface area, smaller pore volume and compromised pore structure (Rafael *et al.*, 2015). Materials produced by evaporative drying of alcogels are often referred to as xerogels (Pajonk, 1991). Incidentally, conventional materials (*e.g* precipitated solids) are also prepared by evaporative drying, resulting in similar surface properties due to identical pore collapse phenomena.

Despite this, these capillary forces can be circumvented by using supercritical solvent extraction (*i.e.* 'supercritical drying'), such that solvent within the metal oxide network is removed by an extractant at supercritical conditions (Vareda, Lamy-Mendes and Durães, 2018). Contacting the alcogel with a miscible extractant causes the solvent within the network to dissolve into the extractant (in an identical manner to aforementioned washing and solvent exchange processes) (Vareda, Lamy-Mendes and Durães, 2018). After sufficient contact time, the solvent is effectively removed from the metal oxide network and entirely replaced by extractant. However, subsequent removal of the extractant does not occur across the liquid-gas phase boundary since no such boundary exists in the supercritical region (Maleki, 2016). Thus, the extractant moves from the supercritical phase directly to the gas phase, avoiding the aforementioned capillary forces, structural damage and pore collapse (Maleki, 2016). Materials prepared in this manner are referred to as aerogels, and it is fundamentally because of method of preparation that they demonstrate such remarkable

properties (Pajonk, 1991). By preserving the structure of the metal oxide network developed during the sol-gel process, aerogels exhibit exceptional surface properties compared to xerogels and other conventional materials (Smirnova and Gurikov, 2018).

Another option for removal is by freeze-drying, where the solvent in the metal oxide network is frozen and removed by sublimation (Pajonk, 1991). Freezing causes the solvent to transition to the solid phase, after which the application of a vacuum prompts sublimation directly to the gas phase (Vareda, Lamy-Mendes and Durães, 2018). This removal occurs across the solid-gas phase boundary and so avoids the aforementioned capillary forces (a phenomenon specifically associated with the liquid phase), as well as the associated structural damage and pore collapse (Maleki, 2016). Materials prepared in this manner are often referred to as cryogels (Maleki, 2016). Similar to aerogels, the above preparation retains the structure of the metal oxide of the alcogel, meaning cryogels exhibit excellent surface properties (Maleki, 2016). Nevertheless, despite their competitive material properties a detailed discussion of cryogels is beyond the scope of this review.

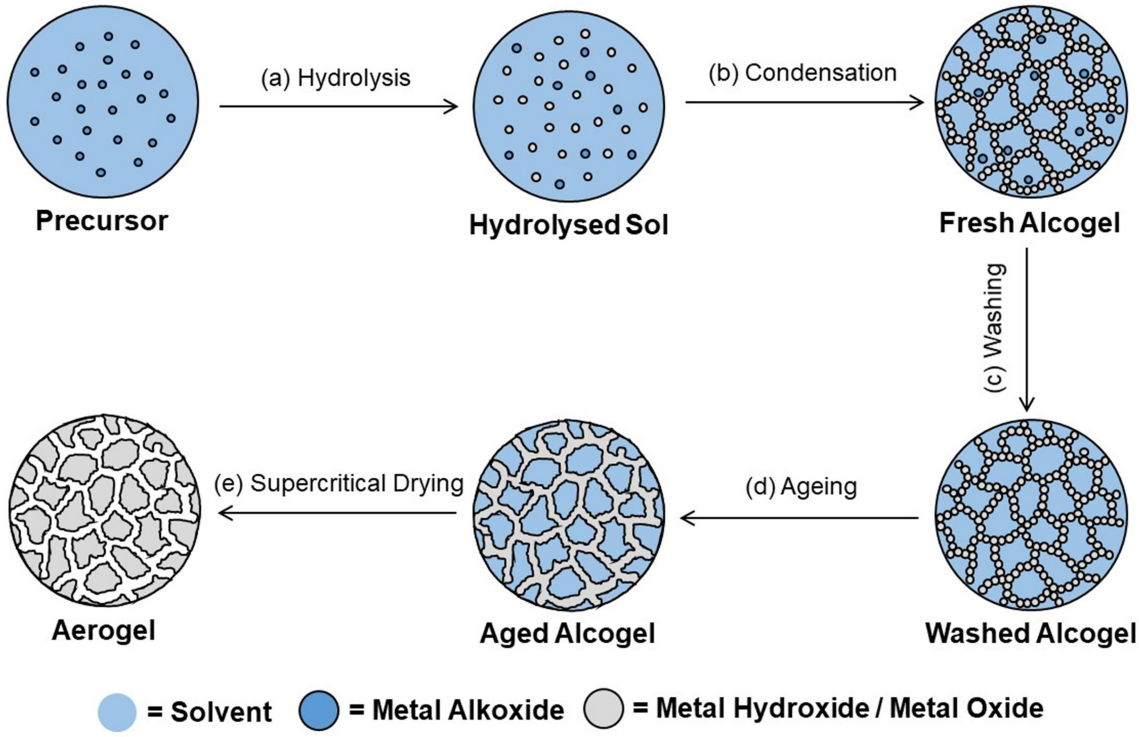

Figure 2.12: Illustration of a typical procedure for preparation of aerogels, including (a) hydrolysis and (b) condensation reactions of the sol-gel process, followed by (c) washing, (d) ageing, and finally (e) supercritical drying.

2.3.4 **Review of Titania Aerogels**

The generalised preparation method detailed above can make use of a wide variety of metal precursors to form aerogels of the corresponding metal oxide, with procedures reported for aerogels of silica, alumina, titania, magnesia, chromia, zirconia, molybdena and vanadia, to name a few (Rafael *et al.*, 2015) (Vareda, Lamy-Mendes and Durães, 2018) (Pajonk, 1991). Furthermore, these precursors can be used simultaneously to prepare aerogels of mixed metal oxides, typically either as binary- or ternary-mixtures (Pajonk, 1991). Separately, preparations using exclusively organic precursors can be used to produce aerogels based on carbon or organic polymers (Vareda, Lamy-Mendes and Durães, 2018). In light of previous discussion and the scope of this research, a selection of procedures reported for the preparation of titania aerogels have been presented in Table 2.5 overleaf, as well as the mean and media average conditions for these preparations. This principally includes the conditions used during each respective synthesis, ageing and drying processes, as well as the surface properties of the titania aerogels produced, including the reported surface area (S_{BET}), pore volume (V_P) and average pore diameter (D_P). Subsequent discussion focusses on the impact of these parameters toward the surface properties of the final titania aerogel. For comparison, Table 2.55 also includes the surface properties of *Degussa P25 Evonik*, a commonly used titania material composed of highly uniform crystalline particles that are produced by rapid flame-hydrolysis (Raj and Viswanathan, 2009).

For the preparation conditions highlighted in Table 2.5, several general trends have been widely reported across literature (Aguado-Serrano and Rojas-Cervantes, 2006)(Schneider and Baiker, 1997). Firstly, the selection of titanium precursor, solvent and catalyst is reported to influence the properties of the incipient alcogel by controlling the hydrolysis and condensation reactions in the sol-gel process (Simonsen and Søgaard, 2010) (Aguado-Serrano and Rojas-Cervantes, 2006). This was evidenced by alcogels prepared with different combinations of these components demonstrating different properties, with differences between acidic (*e.g.* HNO_3) and basic (*e.g.* NH_4OH) catalysts being the most significant (Simonsen and Søgaard, 2010). Nevertheless, whilst the selection of components must fundamentally influence the properties of the subsequent aerogels, examination of Table 2.5 shows no single combination of these components offers definitively superior performance.

This can be seen in Table 2.5, where aerogels prepared with identical precursor, solvent and catalyst often demonstrate varying properties, highlighting the sensitivity of the sol-gel process to the relative amounts of these components. For example, the surface areas reported by (Dagan and Tomkiewicz, 1994) and (Cerhová *et al.*, 2018) (S_{BET} = 316 and 634 m^2/g respectively) vary greatly despite using identical reagents. Of these, the relative amount of water is believed to be critical (Aguado-Serrano and Rojas-Cervantes, 2006). Small quantities

Table 2.5: Review of a selection of methods for the preparation of titania aerogels and subsequent surface properties

Reference	Form[a] (P/M)	Precursor[b] (Pr)	Solvent[c] (S)	Catalyst[d] (C)	Molar Ratio[e] (Pr:	S:	C:	W)	Ageing (h)	Drying[f] (Ex)	S_{BET} (m^2/g)	V_P (cm^3/g)	d_P (nm)
Degussa P25 (Evonik)													
(Raj and Viswanathan, 2009)	P	-	-	-	-	-	-	-	-	-	56	0.25	17.5
Aerogel													
(Desario *et al.*, 2019)	P	Ti-iPr	EtOH	HNO_3	1	19	0.10	2.5	16	CO_2	130-150	0.6	4-30
(Lermontov *et al.*, 2018)	M	Ti-iPr	iPrOH	HCl	1	16	2.75	-	>24	CO_2	150	-	-
(Lermontov *et al.*, 2018)	M	Ti-iPr	MEO	HCl	1	16	2.75	-	>24	CO_2	>500	-	-
(Cerhová *et al.*, 2018)	M	Ti-iPr	iPrOH	HNO_3	1	10	0.05	0.01	72	CO_2	634	-	-
(Choi *et al.*, 2018)	P	Ti-nBu	MeOH	HNO3	1	37	0.14	7.9	24-72	CO_2	590-685	1.7-2.4	11-16
(Moussaoui, Elghniji and Elaloui, 2017)	P	Ti-iPr	iPrOH	CH_3COOH	1	4	-	0.5	12	iPrOH	89	-	-
(Sadrieyeh and Malekfar, 2017)	M	Ti-iPr	EtOH	HNO_3	1	21	0.08	7.4	960	CO_2	639	2.3	14
(Zirakjou, Aghdam and Soorbaghi, 2015)	M	Ti-iPr	iPrOH	HNO_3	1	20	0.86	4.0	24	CO_2	-	-	-
(Zu *et al.*, 2015)	M	Ti-nBu	EtOH	HNO_3	1	11	0.03	0.8	48	EtOH	361	1.5	11
(Rafael *et al.*, 2015)	P	$TiCl_4$	C_6H_6	-	1	24	-	-	24	CO_2	510	-	18
(Kong, Shen and Cui, 2014)	M	Ti-tBu	EtOH	HNO_3	1	30	0.33	2.8	24	EtOH	110	1.5	-
(Kong, Shen and Cui, 2013)	M	Ti-tBu	EtOH	HNO_3	1	27	0.33	2.6	24	CO_2	519	2.9	-
(Lv, Qin and Wei, 2013)	P	Ti-nBu	EtOH	CH_3COOH	1	-	-	-	-	EtOH	39-242	0.1-0.4	7-11
(Brown, Anderson and Carroll, 2012)	M	Ti-nBu	MeOH	HNO_3	1	40	0.01	4	24	-	127-188	0.5-0.7	10-15
(Shimoyama *et al.*, 2010)	P	Ti-nBu	$(CH_3)_2CO$	CH_3COOH	1	-	5.50	-	24	CO_2	190	-	-
(Wang and Lin, 2008)	P	Ti-tBu	EtOH	-	1	4.8	-	-	-	EtOH	75.9	-	-
(Stengl, Bakardjieva and Szatmary, 2006)	P	$TiOSO_4$	iPrOH	NH_3	1	-	-	-	24	CO_2	1085	3.4	20-80
(Dagan and Tomkiewicz, 1994)	P	Ti-iPr	iPrOH	HNO_3	1	20	0.08	3.8	720	CO_2	316	1.09	5.8
(Campbell, Na and Ko, 1992)	P	Ti-tBu	MeOH	HNO_3	1	40	0.13	4.0	2	CO_2	650	2.1	2-10
(Ayen *et al.*, 1988)	M	Ti-iPr	iPrOH	HCl, HF	1	-	-	-	-	CO_2	600-750	1.9-3.6	15-18
Average	**P**	**Ti-iPr**	**iPrOH**	**HNO_3**	**1**	**21**	**0.94**	**3.3**	**121**	**CO_2**	**412**	**1.8**	**16**
Median	**P**	**Ti-iPr**	**iPrOH**	**HNO_3**	**1**	**20**	**0.14**	**3.2**	**24**	**CO_2**	**431**	**2.1**	**14**

[a] Form: P = Particles, M = Monolith
[b] Precursor: Ti-iPr = Titanium isopropoxide, Ti-tBu = Titanium butoxide, $TiCl_4$ = Titanium chloride, $TiBr_4$ = Titanium bromide
[c] Solvent: iPrOH = Isopropanol, EtOH = Ethanol, MeOH = Methanol, tBuOH = Butanol, MEO = Methoxyethanol, $(CH_3)_2CO$ = Acetone
[d] Catalyst: HNO_3 = Nitric Acid, CH_3COOH = Acetic Acid, H_2SO_4 = Sulphuric Acid
[e] Molar Ratio: Precursor : Solvent : Catalyst : Water (Pr : S : C : W)
[f] Drying: CO_2, S = Supercritical Carbon Dioxide, EtOH, S = Supercritical Ethanol, iPrOH, S = Supercritical Isopropanol

of water effect insufficient hydrolysis, inhibiting the formation of the alcogel (Schneider and Baiker, 1997). Conversely, excessive water helps to ensure complete hydrolysis, but this occurs very rapidly and prompts precipitation instead of forming the alcogel (Aguado-Serrano and Rojas-Cervantes, 2006). Necessarily, this strongly affects the surface properties of the final aerogel. Generally, the optimum amount of water for surface properties appears to be slightly below the stoichiometric equivalent for complete hydrolysis (*e.g.* for Ti-iPr this corresponds to Ti-iPr:H_2O of 1:4) (Dagan and Tomkiewicz, 1994), as seen in Table 2.5. Similarly, sufficient acid catalyst is crucial for stabilising the alcogel but excessive acid then results in destabilisation and weakening (Aguado-Serrano and Rojas-Cervantes, 2006). Nevertheless, the relative amount is not as well defined as that for water with a wide range of values reported in literature (*e.g.* Ti-iPr:HNO_3 between 1:0.01 to 0.86), also seen in Table 2.5. Conversely, the amount of solvent is not explicitly reported to have a strong effect, presumably since change in the relative amount simply changes the absolute rate by dilution and so does not fundamentally alter the underlying reactions.

Other fundamental differences between the preparations in Table 2.5 included whether the alcogels were allowed to form a single monolith or disrupted to form particulates. There is little literature that explicitly compares these forms of aerogel. Nevertheless, examination of Table 2.5 appears to show monolithic aerogels demonstrate superior surface properties, however this should not detract from several comparable particulate aerogels. Presumably, this is because during formation of the monolith the sol-gel reactions are able to produce a three-dimensional metal oxide network, whereas in particulates the disruptive action prevents full development of such a network (Debecker *et al.*, 2018). A similar effect exists for ageing conditions (*e.g.* duration, solvent, acidity, temperature, *etc.*) which are known to affect the development of the metal oxide network and so the surface properties of the final aerogel (Iswar *et al.*, 2017) (Choi *et al.*, 2018). Further effects are reported regarding the conditions during drying, most notable of which is that the choice of extractant can affect the crystalline properties of the final aerogel (Vareda, Lamy-Mendes and Durães, 2018). For instance, preparations in Table 2.5 that used either supercritical EtOH or iPrOH effected crystalline titania aerogels in the anatase phase. Conversely, the application of either liquid (LCO_2) or supercritical (SCO_2) carbon dioxide effected amorphous titania aerogels with differing surface properties. Likewise, the conditions during drying are also reported to affect the surface properties of the resultant aerogels, with higher temperatures and pressures effecting greater extraction (Shimoyama *et al.*, 2010).

2.4 Summary & Research Hypotheses

2.4.1 Summary of Literature Review

To summarise, ammonia borane has many characteristics that make it an ideal hydrogen storage candidate. Nevertheless, there are several technical challenges that require resolution in order to satisfy both current and future hydrogen storage targets. These include accelerating the release kinetics of hydrogen at lower temperatures, reducing the volatilisation of gaseous contaminants, and promoting selective formation of polymeric residues that enable facile regeneration. To resolve these technical challenges, research has applied a number of modification techniques to bulk ammonia borane including solubilisation, solid-state doping, chemical modification and nanoconfinement.

Nanoconfinement involves the deposition of ammonia borane within a porous support material. Previous research has studied various support materials including porous forms of carbon, metal oxides, aerogels, metal-organic frameworks and polymers. Nanoconfined ammonia borane demonstrates considerably improved performance toward the aforementioned technical challenges compared to bulk ammonia borane. Generally, it is agreed that the material properties including surface acidity and/or basicity are important for inducing destabilisation and accelerating hydrogen release from ammonia borane. However, there is considerable uncertainty about the precise mechanism and pathway of the dehydrogenation reactions, particularly due to the complicated role of intermolecular heteropolar and homopolar interactions in forming key reaction intermediates. It is deemed likely that the hydrogen release from nanoconfined ammonia borane is highly dependent on the precise surface conditions of the particular support material.

Compared to several other materials, the application of titania to the dehydrogenation of ammonia borane has received comparatively little research. Existing research has predominantly been toward the use of metal catalysts on titania supports, which have been shown to greatly accelerate hydrolytic dehydrogenation from ammonia borane. Contrastingly, the effect of titania toward thermolytic dehydrogenation is relatively unexplored, yet shows relatively good performance when compared to more established materials. This might be due to favourable surface properties exhibited by titania such as its surface acidity/basicity, which are better able to modify the reaction with ammonia borane. In conjunction, there have been numerous preparations of titania aerogels reported which allow the production of highly porous materials with properties advantageous for nanoconfinement of ammonia borane.

2.4.2 **Research Objectives**

The intersection of the above fields suggests considerable potential for acceleration of hydrogen release from ammonia borane by nanoconfinement within titania aerogels, forming the fundamental scope of this research. In light of this, the overarching objectives of this research were considered, as outlined below:

i) **Preparation and Characterisation of Titania Aerogels:** To prepare and characterise high performance titania aerogels, whilst gaining insight into the influence of several critical preparation parameters on the incipient material properties.

ii) **Nanoconfinement of AB within Titania Aerogels:** To demonstrate the novel application of titania aerogels as supports for the nanoconfinement of AB with comprehensive characterisation of the composite material. Subsequently, to compare the anticipated effects of nanoconfinement within titania on hydrogen release to that from bulk AB.

iii) **Understand the Hydrogen Release Mechanism from AB:** Contribute toward furthering current understanding of the evidently complicated hydrogen release mechanisms from bulk AB. Subsequently, to compare the release mechanisms of bulk and nanoconfined AB to clarify the precise promotional effects of nanoconfinement.

3.0 Experimental Methods

The following section details the experimental and analytical methods used throughout this research. The procedures described herein have been generalised to include all analyses for the given technique, with specific modifications detailed alongside the relevant results in the subsequent section, as seen in *4.0 Experimental Results*.

3.1 General Considerations

3.1.1 Chemicals & Gases

The chemicals used throughout this research have been compiled in Table 3.1 alongside their respective grade specifications. All chemicals were purchased from reputable suppliers and, unless expressly stated, were used without additional purification or modification.

Table 3.1: Grade specification of chemicals used throughout experimentation

Chemical	Formula	CAS	Acronym	Grade	Supplier
Gases					
Carbon dioxide	CO_2	124-38-9	CO_2	≥99 %	Carburos-Metalicos
Nitrogen	N_2	7727-37-9	N_2	≥99 %	BOC Gases Ltd.
Helium	He	7440-59-7	He	≥99 %	BOC Gases Ltd.
Compressed Air	O_2/N_2	-	O_2/N_2	N/A	Generated on-site
Reagents					
Ammonia borane	NH_3BH_3	13774-81-7	AB	97 %	Sigma-Aldrich Inc.
Titanium isopropoxide	$Ti(OCH(CH_3)_2)_4$	546-68-9	Ti-iPr	97 %	Sigma-Aldrich Inc.
Solvents					
Isopropanol	$CH_3CH(OH)CH_3$	67-63-0	iPr-OH	99.5 %	Sigma-Aldrich Inc.
Ethanol	CH_3CH_2OH	64-17-5	EtOH	99.8 %	Sigma-Aldrich Inc.
Tetrahydrofuran	$(CH_2)_4O$	109-99-9	THF	99.9 %	Sigma-Aldrich Inc.
Hexane	C_6H_{14}	110-54-3	-	95%	Sigma-Aldrich Inc.
Deionised water	H_2O	7732-18-5	H_2O	N/A	Generated on-site
Catalysts					
Nitric acid	HNO_3	7697-37-2	NA	70 %	Sigma-Aldrich Inc.

3.1.2 Sample Storage

Storage protocols were practised throughout experimentation to preserve the condition of the bulk AB and nanoconfined AB composites. Conditions recommended by literature for bulk AB include within a sealed container filled with inert gas stored in a cool and dry location (Rassat *et al.*, 2010)(Sigma-Aldrich, 2018b)(Storozhenko *et al.*, 2005). Thus, bulk and nanoconfined AB were stored in sealed sample vials within a desiccator filled with self-indicating silica gel desiccant (which was regenerated as needed upon observation of colour change). The desiccator itself was stored at ambient temperature and away from sources of

heat that could cause premature thermolytic dehydrogenation. Some authors describe the storage of AB at refrigerated temperatures (~10°C)(Moussa *et al.*, 2012), however this was not possible with the available equipment. Nevertheless, AB is reported to demonstrate excellent stability at ambient temperature (Sigma-Aldrich, 2018a). Similarly, recommended storage under inert atmosphere was practically difficult and instead the samples were stored under ambient air in sealed vials (Rassat *et al.*, 2010) (Sigma-Aldrich, 2018b). Additionally, the desiccator was covered to prevent exposure to light to eliminate possible photocatalytic dehydrogenation in the nanoconfined AB materials, as reported for a similar system by (Nirmala *et al.*, 2012). Overall, these protocols were found to result in satisfactory storage of bulk AB (as indicated by periodic testing over the course of experimentation), however they were insufficient for nanoconfined AB which was found to change over the course of storage.

3.2 Measurements & Error Analysis

In order to account for experimental errors, standard practise during this research involved conducting measurements as triplicates. Nevertheless, limitations on time and financial resources necessitated either duplicate or single measurements during some experiments. The number of repeats (n) for each experiment has been detailed the section for each respective analytical technique. Wherever applicable, the individual measurements (x_i) were used to calculate the mean average ($\bar{x}$) (Equation 3.1) and standard deviation (σ) (Equation 3.2), with the results then reported accordingly ($\bar{x} \pm \sigma$). The statistical significance between datasets ($\bar{x}_1$, $\bar{x}_2$) was determined using Student's t-test (Equation 3.3) with standard assumptions of zero null hypothesis (*i.e.* no difference between results), two-tailed distribution and unequal variance. These calculations resulted in the so-called t statistic (t), which was compared against a significance value (α_s) that corresponded to a 95% confidence interval ($\alpha_s = 0.05$). Thus, differences between calculated values can be determined to be insignificant ($p > 0.05$) or significant ($p \leq 0.05$) respectively.

$$\bar{x} = \frac{\sum_{i=1}^{n}(x_i)}{n} \quad \textbf{3.1}$$

$$\sigma = \sqrt{\frac{\sum(x_i - \bar{x})^2}{n}} \quad \textbf{3.2}$$

$$t = \frac{\bar{x}_1 - \bar{x}_2}{\sqrt{\frac{\sigma_1^2}{n_1} + \frac{\sigma_2^2}{n_1}}} \quad \textbf{3.3}$$

3.3 Preparation of Titania Materials

3.3.1 Preparation of Aerogels

The following section details the preparation of titania aerogels, an overview of which has been illustrated in Figure 3.1. Firstly, a titania alcogel was synthesised using a well-established acid catalysed sol-gel method (Dagan and Tomkiewicz, 1994), consistent with those in Table 2.5. A solution of acidified solvent was prepared by addition of HNO_3 to iPrOH in a beaker, into which the Ti-iPr precursor was subsequently added. This clear solution was then vigorously stirred by magnetic stirrer for a short duration (t ≈ 15 min), before dropwise addition of deionised H_2O. The molar ratio of Ti-iPr : iPrOH : H_2O : HNO_3 in this solution was 1 : 20 : 3.8 : 0.08, with all quantities measured by autopipette. The addition of deionised H_2O prompted the solution to rapidly develop a translucent white colour, which was attributed to hydrolysis of Ti-iPr to the corresponding hydroxide (Ti-OH) (Equation 3.4) (Debecker *et al.*, 2018). Soon thereafter (t ≈ 15 min), the solution formed a gel which was consistent with polymerisation of Ti-OH and/or Ti-iPr in respective oxolation (Equations 3.5 and 3.6) or olation (Equation 3.7) reactions (Debecker *et al.*, 2018).

$$\text{Ti-iPr} + H_2O \xrightarrow{[H^+]} \text{Ti-OH} + \text{iPrOH} \quad \textbf{3.4}$$

$$\text{Ti-OH} + \text{Ti-OH} \xrightarrow{[H^+]} \text{Ti-O-Ti} + H_2O \quad \textbf{3.5}$$

$$\text{Ti-OH} + \text{Ti-iPr} \xrightarrow{[H^+]} \text{Ti-O-Ti} + \text{iPrOH} \quad \textbf{3.6}$$

$$\text{Ti-OH} + \text{Ti-OH} \xrightarrow{[H^+]} \text{Ti-(OH)}_2\text{-Ti} \quad \textbf{3.7}$$

If this polymerisation occurred during vigorous stirring, the disruptive action of the stirrer produced a suspension of alcogel particles in solution. In contrast, if the solution was transferred to moulds without stirring, polymerisation proceeded the formation of a single alcogel monolith. The moulds used in these preparations were upturned syringes (V = 10 mL) with the upper portion of the barrel removed, allowing the monoliths to be extracted by operating the plunger. These procedures are herein referred to as 'Particles' (P) and 'Monolithic' (M) methods respectively. During both methods, it was imperative that the alcogels remain under the solvent to avoid damage by evaporative drying, which necessitated the addition of a small amount of iPrOH above the monolithic samples. The incipient alcogels remained in solution for a moderate duration (t ≈ 30 min), after which they were transferred

to storage vials with fresh iPrOH. Alcogels were aged for a minimum period (t = 3 days), during which the solution was decanted off and replaced with fresh THF every 24 h, effecting washing and solvent-exchange processes simultaneously. The selection of THF was due to the good stability and high solubility of AB relative to other solvents.

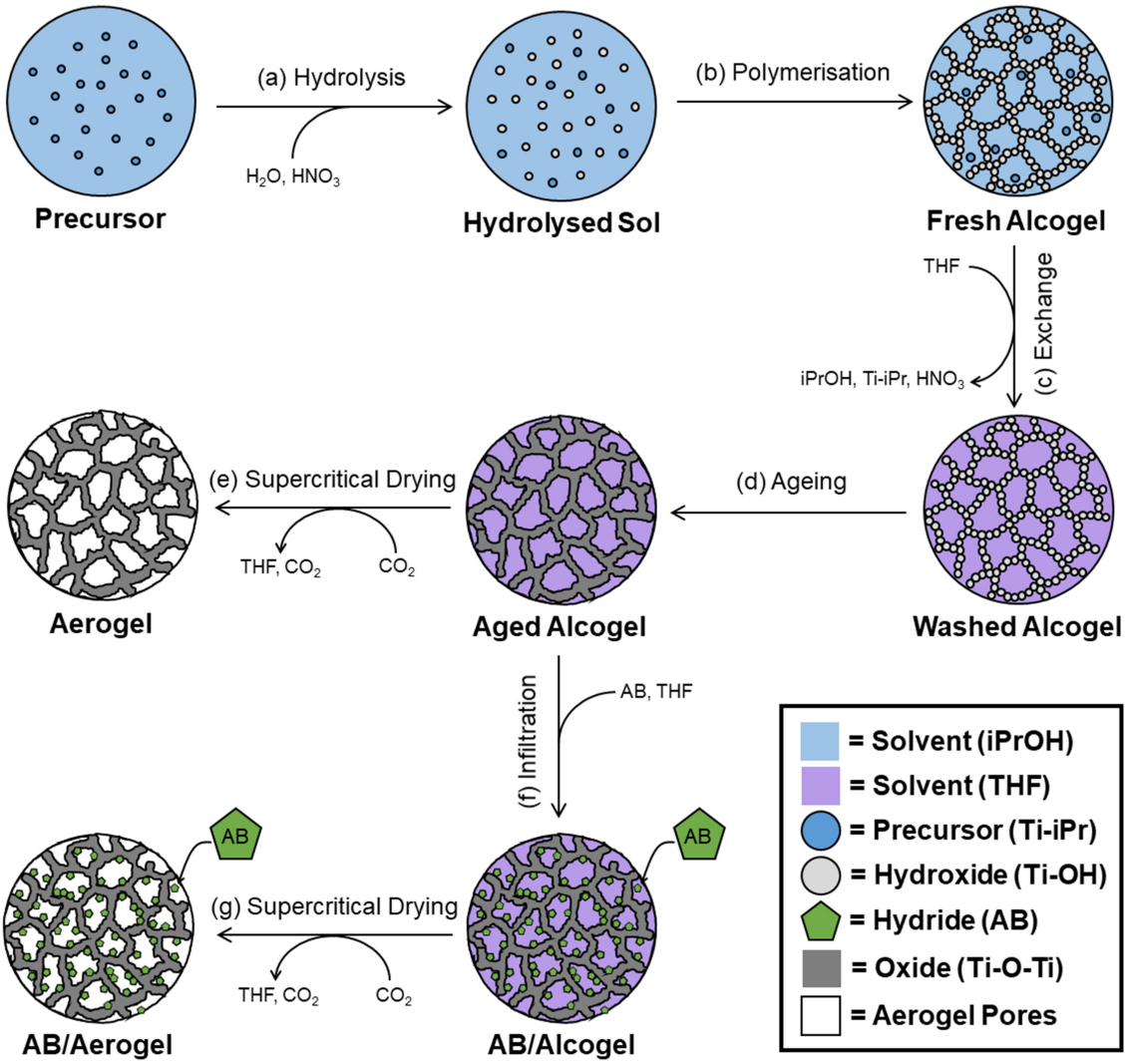

Figure 3.1: Illustration of the preparation of titania aerogels, including (a) hydrolysis and (b) polymerisation steps of the acid catalysed sol-gel method, followed by (c) solvent exchange, (d) ageing and (e,g) supercritical drying. Samples with nanoconfined AB also included (f) infiltration of dissolved AB.

Next, for nanoconfined samples, it was necessary to infiltrate the AB within the alcogel. A solution of alcogel was prepared with the addition of a measured quantity of alcogel (m ≈ 2 g) into a beaker containing THF (V = 2 mL). Simultaneously, a separate solution containing a corresponding amount of AB (m ≈ 0.1 g) was similarly prepared in THF (V = 1 mL), corresponding to an estimated AB loading of 30 wt% in the final aerogel material. These

quantities were based on previous experience by (Rueda *et al.*, 2017), who reported successful infiltration with up to 0.4 g of AB and 2 g of silica alcogel (corresponding to an AB loading of 60 wt%). As before, it was critical that the alcogels remain under solvent to prevent evaporative drying, and so the aforementioned beakers were covered to prevent solvent evaporation. Upon dissolution of the AB, the contents of the beaker were added to the alcogel with the mixture covered and gently stirred for a moderate duration (t = 30 min). During this time, the apparent concentration gradient between bulk solution and alcogel prompted diffusion of AB into the interstitial volume of the alcogel. Following this, the mixture was then immediately transferred to a stainless steel extraction vessel with a magnetic stir bar and sealed for subsequent processing. Infiltration of AB was exclusively conducted on particle samples since the time requirement for diffusion of AB into monolithic samples was predicted to be prohibitively long (due to their lower surface area to volume ratio presenting a higher diffusion resistance). Nevertheless, it must be noted that such preparation could be undertaken if enough time was allocated for the infiltration process.

The final step toward preparation of the aerogels was removal of the solvent from within the alcogel by supercritical solvent extraction (*i.e.* supercritical drying) (Pajonk, 1991). This was accomplished using equipment developed at Universidad de Valladolid, as shown in Figure 3.2 (Rueda *et al.*, 2017). Having loaded the alcogel into the extraction vessel, the system was slowly pressurised with CO_2 ($\Delta P \approx 5$ bar/min) to the desired pressure, after which heating raised the system to the desired temperature. The drying conditions studied were with the extractant in either the liquid phase (30 ^{o}C, 100 bar) and in the supercritical phase (40 ^{o}C, 120 bar), referred to herein as LCO_2 and SCO_2 respectively. Once these conditions were achieved, the recirculation pump was engaged which recirculated the extractant between the buffer vessel and the extraction vessel. During this process, THF within the interstitial volume of the alcogel dissolved into the bulk CO_2, effecting solvent removal from the incipient aerogel without capillary forces (and associated pore collapse), as described in *2.3.3 Preparation of Aerogels*. For nanoconfined samples, the difference in solubility of AB between THF and CO_2 causes the initially dissolved AB to undergo supercritical antisolvent (SAS) precipitation (Rueda, Sanz-moral and Martín, 2018). This causes the AB to form a highly dispersed layer of AB within the pores of the incipient aerogel, a fundamental requirement for achieving nanoconfinement of AB.

After a specified duration, the recirculation pump was stopped and the extraction vessel isolated to maintain the internal conditions. The buffer vessel was then rapidly depressurised, causing the THF to condense out of the gaseous CO_2 and collect at the bottom of the buffer vessel. Removal of this liquid was then simply a matter of opening the discharge valve and briefly flowing CO_2 through the system to displace the THF. The system was then

sealed and rapidly pressurised with fresh CO_2 to the precise pressure within the isolated extraction vessel. The extraction vessel was then opened and the recirculation pump reengaged to continue extraction of the THF from the alcogel. This effectively formed a semi-continuous drying process that was repeated until no THF was discharged from two consecutive cycles (typically within two cycles of 1 h, followed by two cycles of 2 h). After the final cycle, the system was slowly depressurised ($\Delta P \approx 5$ bar/min) and the extraction vessel opened to reveal a white powder that was collected and weighed. Note that a separate piece of equipment was used for the drying of monoliths, the operation of which was identical to the above. Monolithic alcogels proved to be extremely fragile and degraded to form powders during drying, however these samples are still referred to as monolithic due to their distinct preparation and to distinguish them from other materials. For all the synthesised aerogels, several samples (n_s = 1-3) were synthesised for use in subsequent analyses.

3.3.2 **Preparation of Precipitates**

For comparison to the above aerogels, separate materials were synthesised by precipitation and evaporative drying. The method of preparation involved the dropwise addition of a small amount of Ti-iPr (V = 4 mL) to a beaker containing H_2O (V = 40 mL) with vigorous stirring. This immediately formed a suspension of white precipitates, which was attributed to the excess of H_2O prompting immediate hydrolysis to form TiOH (as in Equation 3.4), with the absence iPrOH and HNO_3 preventing subsequent polymerisation. Similar to above, these precipitates were left in solution for a brief period (t = 30 min) to allow complete hydrolysis, before being dried overnight at 65 ^{o}C in an oven (t ≈ 16 h). In contrast to the aerogels above, these materials underwent evaporative drying and were expected to exhibit pore collapse consistent with capillary forces. The white powder that resulted from evaporation was collected and weighed, followed by optional calcination in a furnace (T = 100-600 ^{o}C). Some experiments used bulk AB doped with various titania precipitates. These mixtures were achieved by the addition of a known quantities of AB (m ≈ 50 mg) and titania precipitates (m ≈ 30-50 mg) to a glass vial corresponding to the desired AB loading (typically 20-60 wt%). This vial was then agitated by hand for a short duration (t ≈ 5 min) to homogenise the mixture, immediately followed by respective analyses. As above, several samples (n_s = 1-3) were produced for all precipitates studied during subsequent analyses.

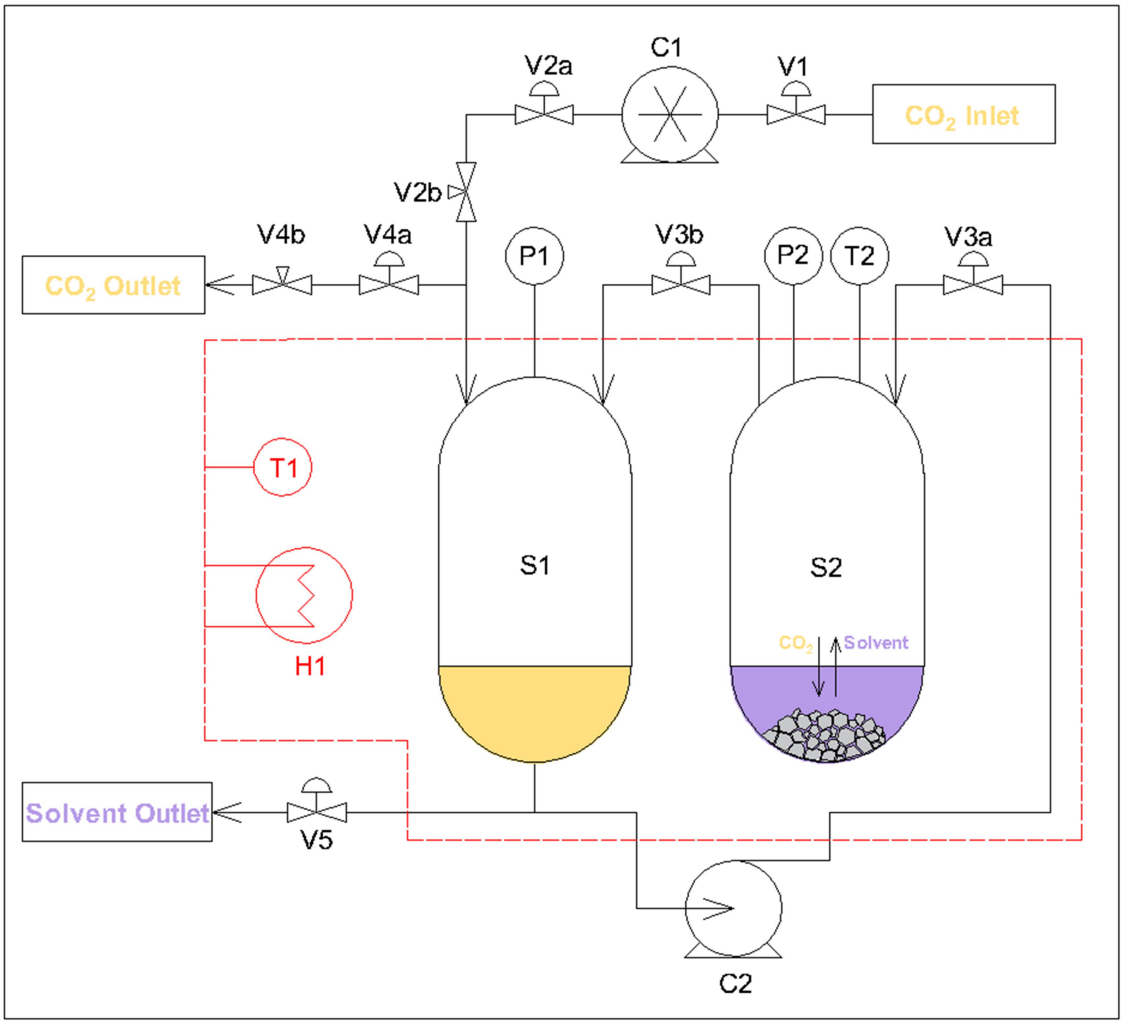

Item	Description	Item	Description
V1	Valve, shutoff	S1	Vessel, buffer
V2	Valves, pressurisation	S2	Vessel, extraction
V3	Valves, extraction isolation	P1	Pressure transducer, buffer vessel
V4	Valves, depressurisation	P2	Pressure transducer, extraction vessel
V5	Valve, solvent discharge	T1	Thermocouple, heater
C1	Compressor	T2	Thermocouple, extraction vessel
C2	Recirculation Pump	H1	Heater oven

Figure 3.2: Schematic of the equipment used for semi-continuous solvent extraction from titania alcogels and subsequent production of aerogels. Equipment developed by High Pressure Processes Group (Universidad de Valladolid, Spain).

3.4 Infrared Spectroscopy

3.4.1 Fundamental Theory

One technique used throughout this research was infrared (IR) spectroscopy which allowed the compositional analysis by identification and quantification of different intramolecular bonds (*e.g.* N-H, B-H, B-N, B=O, *etc.*) within a sample (Stuart, 2004). Typically, analyses of organic substances use the mid-infrared region (400-4000 cm^{-1}) due to the presence of characteristic absorption bands in this range (Stuart, 2004). The location of these absorption bands can be predicted by modelling the intramolecular bond as a simple harmonic oscillator (Zielinski *et al.*, 2005), as illustrated in Figure 3.3 and discussed below (Stuart, 2004).

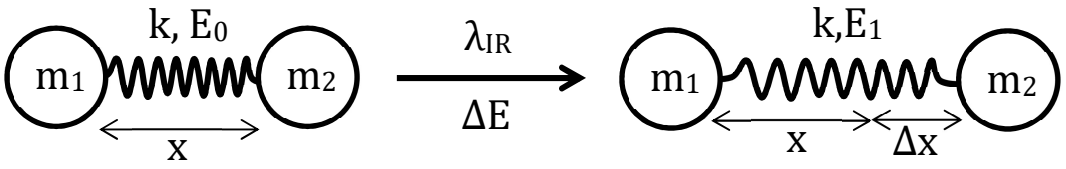

Figure 3.3: Modelling of intramolecular bonds using simple harmonic motion

As an illustrative example, consider the bond between two atoms (1 and 2) with respective masses (m_1 and m_2) displaced by a bond length (x). The system can be modelled by simple harmonic motion, whereby the bond exhibits a characteristic natural frequency (υ_n) and the spring constant (k) represents the bond strength. Exposure of this system to polychromatic IR radiation (λ_{IR}) will cause resonance whereby the bond absorbs wavelengths corresponding to its natural frequency. This is effectively the addition of energy (ΔE) to the system which transitions the molecule to a higher energy state ($E_0 \rightarrow E_1$) and causes stretching of the bond length (Δx). Comparison of the incident IR spectrum to the resultant transmitted/reflected spectrum will show reduced intensity for specific frequencies, which correlate to the natural frequencies being absorbed by the intramolecular bond. These are referred to as characteristic absorption bands and are conventionally reported as wavenumber (ω) values. The end product from modelling by simple harmonic oscillation is an expression, which is given in terms of the Planck constant (h), speed of light (c), the spring constant (k) and reduced mass (μ) terms, as in (Equation 3.8). For further information, the derivation of Equation 3.8 from first principles has been described elsewhere (Stuart, 2004)(Zielinski *et al.*, 2005). Importantly, the discussion above has only considered resonance in terms of the stretching of an intramolecular bond, however other vibrational modes have been identified (Stuart, 2004). These modes can be either symmetrical or asymmetrical and operate either

in-plane or out-of-plane (Stuart, 2004). The characteristic vibrations that result are conventionally known as stretching, wagging, twisting, scissoring and rocking (Stuart, 2004). For these modes to be detectable by IR, the vibration must fundamentally induce a change in dipole moment within the molecule, which is not always achieved (*e.g.* symmetric C-O stretching in CO_2 is undetectable by IR since it does not induce a net change in dipole moment due to the linearity of the molecule) (Williams and Fleming, 2007) (Stuart, 2004).

$$\omega = \frac{h}{2\pi c}\sqrt{\frac{k}{\mu}} \qquad \textbf{3.8}$$

A given molecule may exhibit a number of these vibrational modes depending on the specific stereochemistry present, with each mode presenting as a distinct band in either the functional group ($\omega \geq 1500$ cm^{-1}) or fingerprint ($\omega \leq 1500$ cm^{-1}) regions (Stuart, 2004). The functional group region typically contains fewer bands that are generally assigned to stretching modes, whereas the fingerprint region usually exhibits a complex set of bands assigned to the bending modes (Zielinski *et al.*, 2005)(Stuart, 2004).

3.4.2 **Equipment Configuration**

The spectrophotometer used during this research was a *Shimadzu IRAffinity-1S* and *Specac Quest ATR* unit equipped with a diamond crystal, which were operated by accompanying *LabSolutions IR* software. Analyses were exclusively performed using Fourier transformed infrared spectroscopy (FTIR), using an attenuated total reflectance (ATR) configuration. In this configuration, the incident IR beam is passed through a crystal in contact with the sample such that total internal reflection within the crystal is achieved (Stuart, 2004). Whilst ATR only allows analysis up to a few microns below the surface, the measurements are rapid and minimal sample preparation is required. This is in contrast to transmission configuration where the IR beam is transmitted through the sample allowing analysis of the subsurface, but where samples need to be prepared into potassium bromide (KBr) pellets (Stuart, 2004). For this research, analyses with FTIR-ATR were ideal since it reduced exposure of bulk and nanoconfined AB to atmospheric moisture, and thereby reduced potential for decomposition by hydrolytic dehydrogenation. Using this setup, the principal experimental parameters included the wavenumber range (ω), scan resolution (R_S) and number of scans (n_S), the maximum operable values of which were ω = 380-7800 cm^{-1} and R_S = 0.5 cm^{-1} respectively.

3.4.3 **Procedure for 1D-IR Spectra**

Analyses of samples by FTIR-ATR involved the following procedure. Note, the spectra produced by this method are referred to as '1D-IR' to clearly distinguish them from subsequent '2D-IR' spectra, as discussed in *3.3.5 Procedure for 2D-IR Spectra*. Firstly, immediately prior to measurement the crystal and clamp of the ATR unit were thoroughly cleaned with deionised H_2O and EtOH to remove trace contaminants. Subsequently, a background measurement was recorded, after which a small quantity of sample (~1-3 mg) was spread into an even layer across the entire area of the crystal. For powdered samples, the clamp was then engaged to ensure good contact with the crystal surface, whereas for liquid samples this was not necessary. The measurement parameters (namely ω, R_S and N_S) were then specified, all of which could be increased to improve the range and precision of the resulting 1D-IR spectra, but with the compromise of a longer scan completion time (t_s). An initial spectroscopic study on bulk AB found measurement parameters of ω = 400-4000 cm^{-1}, R_s = 1 cm^{-1} and n_s = 256 scans (with a corresponding t_s = 22 min) to provide relatively rapid collection of data with sufficient precision. Several samples were analysed (n_s = 1-3), and given good agreement a representative 1D-IR spectra was selected for subsequent analysis. These spectra were then processed in *OriginPro 2017* by baselining to account for variation between experiments (subtraction to ensure spectra were coincidental at 4000 cm^{-1}), and smoothing to reduce noise (typically weighted adjacent averaging with a 40 point window).

3.4.4 **Procedure for *Ex situ* Temperature Variation**

Due to equipment limitations, it was not possible to conduct *in-situ* temperature variation within the *IRAffinity-1S* spectrophotometer. Instead, samples were heated *ex situ* in a thermogravimetric analyser, as described in *3.4 Thermogravimetric Analysis*. This involved loading a small amount of sample (~1-3 mg) into the alumina sample pan, which was then rapidly heated (~40°C/min) to temperature under a flowrate of N_2 (20 mL/min). This temperature was then briefly maintained (t = 30 s) to compensate for thermal lag within the microfurnace, after which the sample was removed and immediately analysed by FTIR-ATR. This procedure for temperature variation relies on the fundamental assumption that upon removal from the microfurnace, all reactions are immediately quenched and the resulting thermolytic residues are metastable during subsequent analysis by FTIR-ATR (*i.e.* spectral features are retained at room temperature). This methodology was validated since a similar method was utilised by (Frueh *et al.*, 2011) where samples were likewise heated *ex situ* from subsequent spectroscopic analysis. These procedures are especially relevant to analyses using 2D-IR correlation spectroscopy since temperature was used as the external variable.

3.4.5 **Procedure for 2D-IR Spectra**

2D-IR correlation spectroscopy was used to monitor the influence of an external variable (*e.g.* temperature) on a set of 1D-IR spectra by application of the cross-correlation function (Noda and Ozaki, 2004). Such a procedure allows the determination of which absorption bands change in-phase (*i.e.* synchronously) and which change out-of-phase (*i.e.* asynchronously) with respect to each other and the external variable (Harrington, Urbas and Tandler, 2000) (Noda, 2015). The output of 2D-IR correlation analysis is two contour plots showing the synchronous and asynchronous correlations respectively. Each of these plots provides complementary information to the other and both are required for complete analytical understanding (Noda and Ozaki, 2004). For this research, a set of 1D-IR spectra were collected using the procedure detailed previously (Harrington, Urbas and Tandler, 2000),such that a number of spectra (m) were collected at a range of evenly-spaced temperatures. The spectra consisted of measurements at a number of wavenumbers (n) across the examined range. These spectra were arranged into a matrix (A) of corresponding ($m \times n$) dimension. The arithmetic mean average of this matrix produced a reference spectrum ($\bar{A}$), which was subtracted from A to produce the so-called dynamic spectrum ($\tilde{A}$). The synchronous correlation (Φ) was therefore evaluated as the product of $\tilde{A}$ and the transposed dynamic spectra ($\tilde{A}^T$), altogether scaled by $\frac{1}{m-1}$ (Equation 3.9). For the asynchronous correlation (Ψ), it was first necessary to evaluate the Hilbert-Noda transform matrix (N) which is specified with ($m \times m$) dimensions. The values of N are such that if the row and column number match ($i = j$) the value is zero, elsewise ($i \neq j$) the value is the reciprocal of the difference between column and row number (Equation 3.10). The product of these terms was then found and similarly scaled by $\frac{1}{m-1}$ to calculate Ψ (Equation 3.11).

$$\Phi = \frac{1}{m-1}\tilde{A}^T\tilde{A} \qquad \textbf{3.9}$$

$$N = \frac{1}{\pi}\begin{vmatrix} 0 & 1 & ½ & ⅓ & \dots \\ -1 & 0 & 1 & ½ & \dots \\ -½ & -1 & 0 & 1 & \dots \\ -⅓ & -½ & -1 & 0 & \dots \\ \dots & \dots & \dots & \dots & \dots \end{vmatrix} \quad \begin{matrix} i = j & N(i,j) = 0 \\ i \neq j & N(i,j) = \dfrac{1}{j-i} \end{matrix} \qquad \textbf{3.10}$$

$$\Psi = \frac{1}{m-1}\tilde{A}^T N\tilde{A} \qquad \textbf{3.11}$$

Synchronous (Φ) plots show autopeaks along the diagonal and crosspeaks symmetrically about either side (Noda, 2015). Autopeaks are a consequence of spectral features self-correlating, meaning they are purely synchronous and necessarily positive (Noda, 2015). In contrast, crosspeaks are the result of correlation between two different features and can be positive or negative (Noda, 2015). Positive values indicate both features are increasing or decreasing, whereas negative values indicate one is increasing whilst the other is decreasing (Noda, 2015). Strong synchronous correlation between two features evidences that these features are chemically related, or is due to coincidental change (Noda, 2015). Conversely, asynchronous (Ψ) plots show an absence of autopeaks along the diagonal, as well as crosspeaks which are anti-symmetrical about either side (Noda, 2015). The lack of autopeaks is due to the reason above, since autopeaks result self-correlation they are purely synchronous and have no asynchronous character (Noda, 2015). Temporal information can be derived from crosspeaks on both plots, essentially informing which features change before (*i.e.* 'lead') or occur after (*i.e.* 'lag') others. If the values for the synchronous and asynchronous peaks are both positive, the feature associated with the x-axis leads that of the y-axis. If the asynchronous peak is instead negative, the feature associated with the x-axis lags behind that of the y-axis (Noda, 2015). If the synchronous feature is negative, the relation above is reversed (Noda, 2015). The resulting 2D-IR spectra were processed into contour plots in *OriginPro 2017* software, where the contouring levels were adjusted to remove noise and show only the strongest correlations.

3.5 Thermogravimetric Analysis

3.5.1 Fundamental Theory

A core experimental technique used during this research was thermogravimetric analysis (TGA) and the related derivative thermogravimetric analysis (DTG). The fundamental basis of these analyses is the measurement of sample mass (m) as a function of temperature (T) and/or time (t), allowing subsequent calculation of the rate of mass change with respect to temperature ($\frac{dm}{dT}$) and time ($\frac{dm}{dt}$) respectively (Leng, 2013). As such, these techniques have been applied to the study of a range of solid-gas reactions (*e.g.* decomposition, adsorption, desorption, oxidation, *etc.*) where precise measurements allow evaluation of reaction kinetics (Armstrong and Kailas, 2017). Furthermore, correlation of apparent mass changes to specific reactions provides quantitative material characterisation including composition, chemical resistance and thermal stability (Leng, 2013). Precise measurements are typically achieved by a high-resolution microbalance attached to a sample pan, which itself is positioned within a microfurnace chamber connected to an adjustable gas supply (Armstrong and Kailas, 2017)

(Leng, 2013). Analyses can either be conducted with a fixed sample temperature over time (*i.e.* isothermal analysis), or with the sample temperature increased at either a fixed or variable heating rate (*i.e.* non-isothermal) (Leng, 2013). Often, TGA is integrating with other complementary analytical techniques such as differential scanning calorimetry (TGA-DSC), differential thermal analysis (TGA-DTA), or mass spectrometry (TGA-MS).

3.5.2 **Equipment Configuration**

Experiments were predominantly conducted with a *Perkin-Elmer TGA-7*, with a few analyses performed on a *Perkin-Elmer TGA-4000*, both of which were operated by accompanying *Pyris* software. These analysers were fundamentally identical, each comprised of a microbalance ($m \leq 100$ mg) attached to an alumina sample pan within a microfurnace ($T \leq 1000$ °C) that was connected to an adjustable gas supply. The predominant difference was that the *TGA-7* attached the microbalance to the sample pan by a nichrome hangdown wire, whereas for the *TGA-4000* this was by a ceramic support stem. Both analysers were connected to nitrogen (N_2), argon (Ar) and on-site compressed air (O_2/N_2), which were used to provide inert and oxidative atmospheres respectively. These were dried immediately prior to entering the equipment with inline moisture traps consisting of a front-end of molecular sieves (4 Å, Sigma Aldrich) and a back-end of self-indicating silica gel, which were regenerated as needed.

Throughout experimentation, accurate measurements were achieved by the high resolution of the equipment (±0.1 µg and ±1 °C respectively) coupled with proper calibration and maintenance procedures. Calibration of the microfurnace temperature was according to (ASTM, 2018c) using several reference materials across the entire range namely alumel, nickel, perkalloy and iron ($T = 153$, 358, 596 and 770 °C respectively). Similarly, calibration of the microbalance was according to (ASTM, 2018b) by precise measurement of a reference sample of known mass ($m \approx 100$ mg). In both cases, the reference and measured values were input to the *Pyris* software and the calibration automatically adjusted. This calibration was maintained by rigorous maintenance protocols. After each experiment, the alumina sample pan was cleaned by removing bulk residue followed by washing in deionised H_2O and EtOH, with the pan then dried in the microfurnace at a temperature exceeding that for subsequent experiment (typically 300 °C). More thorough cleaning involved calcination at 900 °C under O_2/N_2 until the mass signal had stabilised. Other areas of the analyser (*e.g.* microfurnace chamber) were periodically cleaned to remove residues that gradually accumulated over use.

3.5.3 **Procedure for Non-Isothermal Analyses**

The procedure described here is for the *Perkin-Elmer TGA-7*, since this was used for the majority of experiments, however the procedure for the other analyser was analogous. For non-isothermal analyses, the empty pan was placed onto the hangdown wire and the microfurnace raised to allow the flow of N_2 to purge the chamber of ambient air. Once the mass signal had stabilised (t ≈ 2 min), the microbalance was tared to record the empty mass of the pan. The pan was then removed and loaded with sample (m = 2 ± 0.3 mg), making sure to distribute the sample evenly across the pan. The loaded sample pan was then replaced onto the hangdown wire and the microfurnace raised to once again purge the chamber. Once the mass signal had stabilised (t ≈ 2 min) the sample mass was recorded and the microfurnace heated to temperature (T = 25-600 °C) at a fixed heating rate (β = 2-20 °C/min) under a flowrate of N_2 ($\dot{V}$ = 20 mL/min). Typically, analyses of AB are under a flowrate of Ar, however a preliminary study on bulk AB found no difference between samples heated under Ar and N_2. These conditions complied with those by (ASTM, 2018a) and allowed sufficiently precise measurements within reasonable completion times. Unless otherwise stated, all analyses were conducted a minimum of three times (n_s = 3), with the mean average and standard deviation reported. To account for variable sample mass, data was normalised by consideration of each measurement (m_i at $t = t_i$) with respect to the initial mass (m_0 at t = 0) (Equation 3.12). Data was also converted to fractional conversion (α_i at $t = t_i$) which was calculated with the initial and the final mass (m_f at $t = t_f$) (Equation 3.13), which removed deviations between datasets and represented change between fixed limits ($0 \leq \alpha \leq 1$).

$$m_i = \left(\frac{m_i}{m_0}\right) \times 100 \qquad \textbf{3.12}$$

$$\alpha_i = \frac{m_0 - m_i}{m_0 - m_f} \qquad \textbf{3.13}$$

3.5.4 **Procedure for Isothermal Analyses**

For isothermal analyses, the procedure was similar to that described above. However, after recording the sample mass of the loaded pan, the microfurnace was lowered and heated to the desired temperature with the microfurnace opening covered to stabilise the temperature. The pre-heated microfurnace was then raised to simulate near-instantaneous heating of the loaded pan to the desired temperature (T = 40-130 °C), after which it was held isothermally for an extended duration (t = 300 min) or until the mass signal had stabilised. This method allowed the sample to be heated near-instantaneously and facilitated measurements from the very onset. However, it did not allow time for ambient air to be purged from the chamber and for stabilisation of the mass signal prior to measurement, which undoubtedly introduced

slight error in the measurements. Nevertheless, such an error would present as a repeatable shift in the data, which would not affect the overall trend and potentially be accounted for when analysing the data in terms of fractional conversion (α) (Equation 3.13). The only alternative was to record the sample mass as described previously, followed by rapid heating to the desired temperature. Whilst this would have allowed stabilisation of the mass signal before measurements, even extreme heating rates would still be insufficient for observing initial mass loss (*e.g.* heating from 25 to 130 °C at 100 °C/min would take over 1 min, yet release from bulk AB at these temperatures is practically complete within 1-2 min). Hence, the method used was the best available despite the acknowledged shortcomings. Due to their long duration (t = 300 min), most samples were analysed once (n_s = 1), however the repeatability was checked by repeated analyses of for single isotherm (n_s = 3).

3.5.5 **Procedure for Determination of Activation Energy**

The above analyses were used during evaluation of the apparent activation energies (E_a) for the thermolytic dehydrogenation of AB. Several different procedures are reported for these calculations, including the Arrhenius, Kissinger, and Isoconversional Methods (Gangal and Sharma, 2013)(Mamleev *et al.*, 2004). These methods are founded on the premise that the rate of reaction (dα/dt) is the product of some function of conversion (f(α)) and a function for the rate constant (k(T)) (Equation 3.14). This expression can be integrated to an alternative form (Equation 3.15 to 3.16), with these known as the differential and integral forms respectively. The conversion function is fundamentally dependent on the chemical reaction and can be expressed by ideal rate laws (*e.g.* zero, first, second order) or more complicated laws (*e.g.* fractional orders, catalysed, *etc.*). The function for the rate constant is often expressed by the Arrhenius equation (Equation 3.17) (Gangal and Sharma, 2013)(Mamleev *et al.*, 2004), given in terms of the rate constant (k), pre-exponential factor (A), molar gas constant (R), and absolute temperature (T). Whilst this equation lacks the theoretical basis for application to heterogeneous reactions, it has nonetheless been widely used to approximate many solid-state reactions due to its convenience (Galwey and Brown, 2002).

$$\frac{d\alpha}{dt} = k(T)\, f(\alpha) \qquad \textbf{3.14}$$

$$\int_0^{\alpha} \frac{d\alpha}{f(\alpha)} = \int_0^{t} k(T)dt \qquad \textbf{3.15}$$

$$g(\alpha) = k(T)\, t \qquad \textbf{3.16}$$

$$k = Ae^{-\frac{E_a}{RT}} \qquad \textbf{3.17}$$

The first method, herein referred to as the Arrhenius Method, relies on conducting a set of isothermal TGA experiments such that the rate constant can be determined at various temperatures. The logarithm of the Arrhenius Equation then produces an expression where plotting the values of ln(k) against (1/T) allows the gradient ($-E_a/R$) and intercept (ln(A)) to be evaluated (Equation 3.18) (Gangal and Sharma, 2013). In this research, evaluation of the rate constant was accomplished by assuming a kinetic model for the studied reaction, with this model subsequently fitted to experimental data using the *Non-Linear Curve Fitting* functionality within *OriginPro 2017*. The Arrhenius Method has been used extensively in the study of AB (Gangal and Sharma, 2013) (Gutowska *et al.*, 2005) (Kang *et al.*, 2008).

$$\ln(k) = \ln(A) - \left(\frac{E_a}{R}\right)\frac{1}{T} \qquad \textbf{3.18}$$

Alternatively, the Kissinger Method has also been widely used (Demirci, 2017b). The technique is typically done by conducting several non-isothermal DSC experiments using a variety of constant heating rates (β), with the relative rates of reaction represented by the peak temperature (T_P) at which the maximum rate occurs (ASTM, 2015). Hence, by varying the rate of heat provided to the reaction and measuring the change in the peak temperature, the underlying reaction energetics can be determined (ASTM, 2015). Derivation of the Kissinger Method is outside the scope of this thesis, however the overall expression allows the plotting of values of $\ln(\beta/T_p^2)$ against (1/T), allowing the gradient ($-E_a/R$) and intercept ($\ln(AR/E_a)$) to be evaluated (Equation 3.19) (ASTM, 2015) (Gangal and Sharma, 2013). The Kissinger Method has been widely applied to the study of AB (He *et al.*, 2011)(Choi *et al.*, 2012)(Gangal and Sharma, 2013)(Si *et al.*, 2011), however its applicability is nonetheless questioned since its derivation assumes first order homogeneous reactions (ASTM, 2015). Rather than with DSC, this research conducted these analyses with sets of non-isothermal TGA experiments, specifically from their DTG profiles, which are analogous to DSC profiles.

$$ln\left(\frac{\beta}{T_p^2}\right) = \ln\left(\frac{AR}{E_a}\right) - \left(\frac{E_a}{R}\right)\frac{1}{T} \qquad \textbf{3.19}$$

A further technique for studying the activation energy of reactions includes the so-called Isoconversional Method (Budrugeac, Segal and Popescu, 2003). This method relies on the comparison of isothermal TGA profiles at different temperatures, with isoconversional points compared such that the reaction time becomes representative of the reaction rate (*e.g.* time taken for α = 0.1 will be different for isotherms at T = 80, 90, 100 ^{o}C, *etc.* correlating to the underlying reaction rate)(Budrugeac, Segal and Popescu, 2003)(Gangal and Sharma, 2013). The Isoconversional Method utilises the integrated rate equation (Equation 3.20) and Arrhenius equations (Equation 3.17). Logarithms of this yield a different expression

(Equation 3.21) which can be simplified by the reasonable assumption that the logarithm of the conversion function is negligible compared to the other terms (Equation 3.22) (Gangal and Sharma, 2013). Similar to the above methods, subsequent rearrangement results in a form whereby plotting of –ln(t) against (1/T) for specific values of conversion (α = 0.1, 0.2, 0.3, *etc.*) allows the values for the gradient ($-E_a/R$) and intercept (ln(A)) to be evaluated (Equation 3.23) (Budrugeac, Segal and Popescu, 2003) (Gangal and Sharma, 2013). Typically, this method is conducted for low values of conversion (α ≈ 0.1) since analyses in this range offer more accurate activation energy values. The Isoconversional Method has only sparingly been applied to the study of dehydrogenation of AB (Gangal and Sharma, 2013)

$$g(\alpha) = Ae^{-\frac{E_a}{RT}}\ t \tag{3.20}$$

$$ln\big(g(\alpha)\big) = ln(A) - \frac{E_a}{RT} + \ln(t) \tag{3.21}$$

$$ln\big(g(\alpha)\big) \cong 0 \tag{3.22}$$

$$-\ln(t) = ln(A) - \left(\frac{E_a}{R}\right)\frac{1}{T} \tag{3.23}$$

3.6 Differential Scanning Calorimetry

3.6.1 Fundamental Theory

Another analytical technique used was differential scanning calorimetry (DSC). The basis of this technique is the measurement of heat flow to two identical pans in order to maintain a set-point temperature (Leng, 2013). One pan is loaded with sample whilst the other is purposefully left unloaded, with these pans referred to as the sample and reference pans respectively (Armstrong and Kailas, 2017). Thermal events (*e.g.* phase changes, crystallisation, chemical reactions *etc.*) occurring within the sample can either be exothermic or endothermic resulting in the generation or consumption of heat respectively (Leng, 2013). Accordingly, these events affect the temperature of the sample pan and the heat flow required to maintain the set-point temperature (Leng, 2013). Since such thermal events do not occur in the reference pan, the difference in heat flow between the sample and reference pans can be entirely attributed to thermal events within the sample (Armstrong and Kailas, 2017). This allows evaluation of the nature of thermal events, as well as their onset temperature and the associated enthalpy change (Armstrong and Kailas, 2017). Unlike TGA, DSC is not reliant on the measurement of mass change meaning a wider range of reactions can be detected (which otherwise would not be detected by TGA) (Leng, 2013).

3.6.2 **Equipment Configuration**

The equipment used throughout experimentation was a *Perkin-Elmer Pyris 1*, which was operated by accompanying *Pyris* software. The sample and reference pans were heated by an internal microfurnace ($T \leq 300$ °C) and cooled by evaporative cooling from liquid nitrogen. During analyses, the pans were sealed in a compartment within the analyser to minimise the influence of external temperature variation. Additionally, this compartment was constantly purged by a flowrate of N_2 to remove gaseous contaminants evolved during analyses. Throughout experimentation, accurate measurements were ensured by the high temperature resolution (±1 °C) and proper calibration of the analyser. Temperature calibrations were by measurement of the melting point temperatures (T_m) of indium and zinc reference materials (T_m = 157 and 420 °C respectively) (ASTM, 2010). Heat flow calibrations were similarly by measurement of the standard latent heat of fusion ($\Delta_f H$) of the indium reference material ($\Delta_f H$ = 28.66 J/g) (ASTM, 2014). As was conducted with the TGA analyser, the measured and reference values for each of these calibrations were input into the Pyris software, with the equipment calibration automatically adjusted.

3.6.3 **Procedure for Analysis**

Analysis involved loading a known quantity of sample into an aluminium sample pan, taking care to spread the sample evenly throughout the pan. Analyses of bulk AB were typically conducted on smaller quantities ($m \approx 1$ mg) to prevent excessive contamination of the equipment, whereas analyses of all other nanoconfined and bulk materials used slightly larger quantities ($m \approx 6$ mg). The loaded pan was then hermetically sealed with an aluminium lid, into which a pinhole was bored to allow the release of evolved gases during heating. An identical pan was prepared without the addition of sample to serve as a reference pan. These pans were then placed into their respective positions within the analyser and the compartment sealed. The samples were subsequently heated to temperature (T = 25-300 °C) at a fixed heating rate (β = 10 °C/min), with a flowrate of N_2 ($\dot{V}$ = 30 mL/min) purging the compartment of evolved gases. At the onset of experimentation, an empty sample pan was analysed alongside an empty reference pan, with the expectation of a straight profile along the entire range (ΔH = 0 J/g). Nevertheless, this preliminary profile showed deviations which were believed due to equipment factors. These were accounted for by subtraction of this profile from subsequent analyses, thereby serving as an effective baseline. Throughout experimentation, analyses were typically repeated a number of times (n_s = 1-3), with the mean average and standard deviation reported wherever appropriate.

3.7 Scanning Electron Microscopy

3.7.1 Fundamental Theory

Another technique used to complement understanding from other analyses was scanning electron microscopy (SEM). Such analyses are able to generate an image of a specimen by interaction of the sample surface with a beam of electrons (Leng, 2013). In a vacuum, a beam of electrons are generated from an electron source and accelerated toward the specimen at a tuneable accelerating voltage (AV). This beam is passed through several electromagnetic lenses which, amongst other things, control the beam diameter incident upon the specimen surface, known as the spot size (SS) (Leng, 2013). Finally, the electron beam passes through a final objective lens aperture, which is displaced from the specimen surface by a working distance (WD), allowing the beam to be focussed at different magnifications (MAG) (Leng, 2013). The incident electron beam penetrate a few microns into the bulk of the specimen, with shallow penetration producing secondary electrons (SE), and deeper penetration producing backscattered electrons (BSE) and characteristic X-rays (K_α, K_β) (Leng, 2013). These emissions are measured by individual detectors, which analyse the collected measurements and generate an image of the specimen surface, known as a micrograph. General analyses use secondary electron imaging since their shallow penetration produces the highest image resolution, however backscattered electron imaging can be used to image deeper below the specimen surface albeit with lower image resolution (Leng, 2013). Alternatively, analyses of K_α/K_β emissions can be used to quantify the elemental composition of the specimen, since the wavelengths of these emissions are characteristic of chemical elements, with this technique called energy dispersive spectroscopy (EDS) (Leng, 2013).

3.7.2 Equipment Configuration

During this research, analyses were conducted with a *JEOL 6510(LA)* operated exclusively with secondary electron imaging. Prior to analyses, specimens were coated with an *Agar Manual Sputter Coater* connected to an adjustable flowrate of Ar and equipped with a gold foil target. The equipment allowed analyses across a range of operating parameters, including accelerating voltages (AV ≤ 30 kV), beam spot sizes (SS ≤ 70), beam working distances (WD ≤ 20 mm), and magnifications (MAG ≤ x300,000), which allowed the observation conditions to be adjusted for each sample. The instrumental precision is recognised to be highly dependent on the specific sample and observation conditions, however the manufacturers report nanoscale resolution (± 3-15 nm).

3.7.3 **Procedure for Textural Analysis**

Immediately prior to analyses, samples were prepared into mounted specimens to improve their electrical conductivity and reduce charge-up during observation (presenting as bright regions due to the accumulation of electrons on the specimen surface). In order to preserve their textural properties, the samples were not dispersed in solvent and were instead directly deposited onto the adhesive carbon discs mounted on aluminium sample stubs. Based on preliminary analyses with bulk AB, these specimens then underwent a gold-coating process to improve their conductivity. The coating procedure involved sealing the specimen within a chamber, which was placed under vacuum ($P \leq 0.05$ mbar) to remove ambient air, followed by the introduction of argon ($P \approx 0.04$ mbar) to establish the plasma connection between the specimen and the target. The coating process was then started whereby gold was deposited onto the specimen by plasma for a short duration ($t = 7$ s), with these conditions calibrated to effect a coating of thickness between 10-20 nm.

The specimens were then immediately transferred to the *JEOL 6510(LA)*, where they were loaded into the equipment and placed under high vacuum. The analysis parameters (WD, AV, SS and MAG) were then adjusted to achieve sufficient resolution and image quality. The WD parameter was set based on the measured specimen height (WD ≈ 11 mm), taken from the base of the aluminium stub to the top surface of the carbon disc. Selection of the AV parameter involved initial analysis at relatively low values (AV ≈ 3 kV), after which this value was incrementally increased. Higher AV values improved image resolution, but also resulted in the loss of fine detail and greater charge-up on the sample, with the selected value (AV ≈ 5-15 kV) a compromise between these two considerations. Throughout experimentation, the SS value was not significantly adjusted from the standard value (SS = 50). For each specimen, both low and high magnifications (MAG = x50-x10,000) were studied to inform about the particle morphology and surface texture respectively. Finally, before image acquisition at each magnification, the quality was refined by adjusting the imaging parameters (*i.e.* focus, brightness, contrast and astigmatism).

3.7.4 **Procedure for Particle Size Analysis**

During this research, particle size analysis was accomplished with separate analyses and subsequent image processing in *Image J* software. The specimen preparation method described above was modified in order to produce highly dispersed particles suitable for size analyses. The sample was initially added to a small volume of hexane, with the suspension of insoluble particles then pipetted onto the surface of the carbon disc. The hexane then rapidly

evaporated to deposit the particles as a highly dispersed layer conducive for particle counting and size evaluation, after which these specimens were coated as above. In subsequent analyses, several micrographs were acquired from separate regions of each specimen in order to achieve a representative dataset consisting of a large number of particles. These micrographs were then individually processed by first adjusting their contrast and brightness, followed by background removal by thresholding the images. The subsequent binary images then underwent noise removal wherein isolated single-pixel features were eliminated. A direct consequence of this was the loss of particles below this critical diameter, meaning this method was unsuitable for analyses in the sub-micron region (D_P < 0.5 μm, at MAG = x50). Nevertheless, observation of all micrographs indicated the majority of particles were present in the micron region, validating the use of this technique. The above processing produced an image consisting of black particles on a white background, which allowed identification of discrete particles across the entire area of the specimen. After setting the scale of the image by measurement of the scale-bar, the particles were analysed by *Image J*, which effectively calculated the apparent area occupied by each particle. These area measurements were then converted to corresponding particle diameters (often by making necessary assumptions about the particle morphology). Subsequently, for each sample, the results from several micrographs were compiled into a single dataset and the particle size distribution plotted as a histogram. For samples unable to be dispersed in hexane, specimens were prepared by direct deposition as described previously. However, the poorer dispersion typically produced clusters of particles, which challenged analysis by the above method since *Image J* was unable to accurately size superimposed particles. This necessitated manually outlining the particles, followed by particle area and diameter calculation as above.

3.8 Nitrogen Porosimetry

3.8.1 Fundamental Theory

The basis of porosimetry is founded on the physical adsorption/desorption of a probe molecule (*e.g.* N_2, Ar, CO_2) onto/from the surface of a sample material, which after several assumptions allow surface properties to be calculated (BSI, 2016). These experiments are typically conducted by precise adjustment of the equilibrium pressure (P) of the probe gas whilst maintaining isothermal conditions, leading to the resulting profiles being referred to as isotherms (BSI, 2016). These isotherms describe the quantity of adsorbed probe gas (Q_{ads}) on the sample surface in response to changes in relative pressure (P/P_0), with their characteristics allowing them to be categorised as Type I-VI (with Types IV and V subcategorised as Type H1-H4) (Thommes *et al.*, 2015). An example isotherm for a porous

material has been included in Figure 3.4 to help schematically illustrate the following discussion. Initially, the material surface is completely free from adsorbed species (Point A), such that the fractional coverage is defined as zero (θ_0) (Thommes *et al.*, 2015). However, increasing the pressure of the probe molecule causes selective adsorption onto low energy sites at the material surface (Thommes *et al.*, 2015). This continues until such sites are saturated (Point B), effectively forming a single layer of adsorbed molecules (θ_1) referred to as a monolayer (Thommes *et al.*, 2015). Further pressurisation progressively fills higher energy sites such that multilayers ($\theta_2, \theta_3, \theta_4$, *etc*.) of adsorbed molecules are formed (Point C) (Thommes *et al.*, 2015). At a specific point, a phenomenon known as capillary condensation occurs (Point D) which causes unrestricted multilayer formation (θ_i) of condensed molecules within the material. This point is defined as the saturation pressure (P_0), which allows all isotherms to be expressed in the same range of relative pressures (P/P_0 = 0-1) (Thommes *et al.*, 2015). Finally, subsequent reductions in pressure cause desorption of these condensed molecules, however their greater physical stability requires lower pressure to effect desorption effectively forming a hysteresis loop (Point E) (Thommes *et al.*, 2015). Alternatively, hysteresis might originate from complex pore structures that limit the rate of desorption (*e.g.* ink-bottle pore shapes) (BSI, 2016). From these complete isotherms, surface properties can be then calculated using one from a number of different methods, each with respective underlying models and assumptions (BSI, 2016).

Currently, the predominant method for evaluation of surface area (S) is by the Brunauer-Emmett-Teller (BET) method (Thommes *et al.*, 2015)(Rouquerol, Llewellyn and Rouquerol, 2007). The method is relies on several key assumptions, which allow derivation of the BET equation (Equation 3.24), expressed in terms of the equilibrium pressure (P), saturation pressure (P_i), quantity adsorbed at equilibrium (Q), quantity adsorbed at monolayer (Q_1) and the so-called BET constant (C). Plotting experimental measurements according to this equation produces a linear trend with meaningful gradient and intercept that allow calculation of the values of Q_1 and C respectively (Thommes *et al.*, 2015). The BET surface area (S_{BET}) can then be calculated by multiplication of Q_1 with the cross-sectional area of the probe molecule (s) and Avogadro's constant (N) with division by the molar volume of the probe gas (V_n) and the mass of the sample material (m) (Equation 3.25) (Thommes *et al.*, 2015). Likewise, the predominant method of evaluating pore size distribution and pore volume (V_P) is by statistical thickness methods that assume the Kelvin model of pore filling, such as the Barrett-Joyner-Halenda (BJH) method (Thommes *et al.*, 2015). These methods are principally applied to the desorption isotherm due to the critical assumption of meniscus formation within the pore, which is only apparent after capillary condensation has taken place (*i.e.* upon θ_i at Point D, on Figure 3.4) (Thommes *et al.*, 2015). Calculations are based on the so-called t-plot (Equation 3.27), which is the linear plot of Q against the layer thickness (t)

adsorbed on the material surface alongside, with the value of t often estimated using the empirical equation developed by Harkins-Jura (HJ) (Equation 3.28) (Thommes *et al.*, 2015). This enables calculation of the pore size distribution, which are classified by their diameter (D_P) as being either microporous (D_P < 2 nm), mesoporous (D_P = 2-50 nm) or macroporous (D_P > 50 nm) (Thommes *et al.*, 2015). The cumulative sum of these Q values across the entire range of D_P therefore represents the total pore volume of the material. Finally, the intercept and gradient of the t-plot allow the contributions of microporous (S_{MIC}) and external (S_{EXT}) areas toward S_{BET} to be evaluated respectively (where 'external' is the sum of mesoporous and macroporous areas) (Thommes *et al.*, 2015).

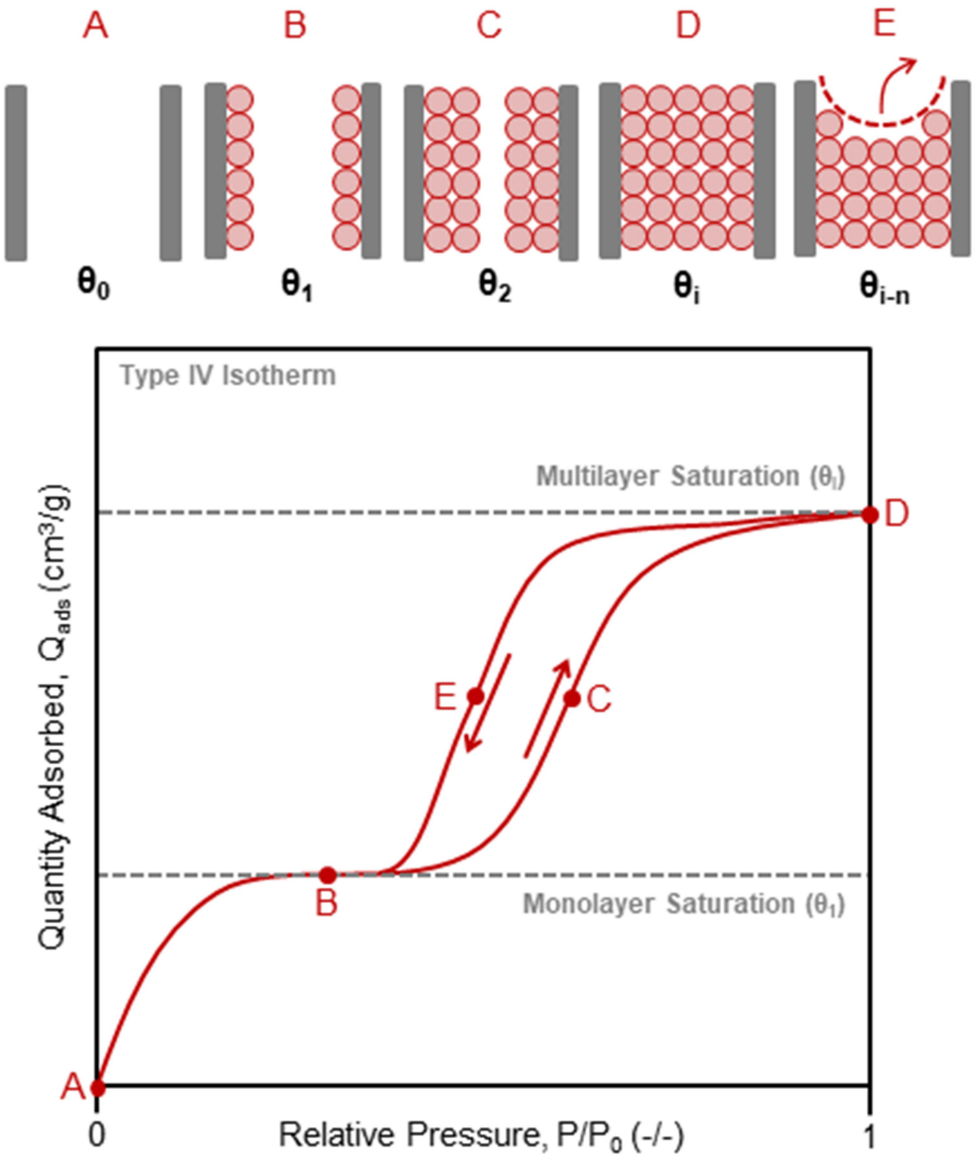

Figure 3.4: Schematic of typical adsorption-desorption isotherm illustrating the fundamental principle of nitrogen porosimetry and related BET and BJH calcuations

$$\frac{1}{Q[\left(\frac{P_0}{P}\right)-1]} = \frac{C-1}{Q_1 C}\left(\frac{P}{P_i}\right) + \frac{1}{Q_1 C} \quad \textbf{3.24}$$

$$S_{BET} = \frac{Q_1 N s}{V_n m} \quad \textbf{3.25}$$

$$C = e^{\frac{\Delta E_1 - \Delta E_L}{RT}} \quad \textbf{3.26}$$

$$Q = Q_{MIC} + k\, S_{EXT}\, t \left(\frac{P}{P_0}\right) \quad \textbf{3.27}$$

$$t = 0.1\left[\frac{13.99}{0.034 - \log(\frac{P}{P_0})}\right]^{0.5} \quad \textbf{3.28}$$

3.8.2 **Equipment Configuration**

Before analyses, sample mass was recorded using a high-precision mass balance (m ± 0.1 mg) and the sample degassed using a *Micromeritics VacPrep 061*. Subsequent nitrogen porosimetry experiments were conducted with a *Micromeritics 3Flex Physisorption* operated with accompanying *3Flex* software. In general, the apparatus conformed to relevant standards for porosimetric analyses (BSI, 2016). Namely, the equipment enabled measurements across a wide range of pressures (P ≈ 7-1300 mbar) with high precision transducers (± 13 mbar) that allowed measurements above a threshold surface area (S_{BET} ≈ 0.01 m^2/g). Cylinders of helium and nitrogen were connected to the analyser for use in free-space measurement and as the probe gas respectively. The equipment was also equipped with a dewar containing liquid nitrogen to ensure isothermal (T ≈ -196 ^oC) conditions during analyses. It must be noted that persistent issues with free-space calibration produced erroneous desorption isotherms as seen in subsequent results sections (*i.e.* where the desorption isotherm crosses below the adsorption isotherm). Such observations were consistent throughout experimentation and could not be explained by improper degassing of the samples. Nevertheless, the consistency of this error suggested comparisons between samples would still be valid in spite of any doubt as to the precise values calculated.

3.8.3 Procedure for Analysis

A typical procedure involved the addition of a known quantity of sample to a glass adsorption tube. Prior to analyses, samples were degassed to remove adsorbed atmospheric gases. This was achieved by heating them to temperature (T ≈ 150 °C) under high vacuum for an extended duration (t ≈ 16 h). The samples were then immediately transferred to the porosimetry equipment for analyses, where they were placed under high vacuum (P = 0.013 mbar) for a short period (t = 10 min) to remove atmospheric gases that may have adsorbed during transfer. Measurement conditions were across the entire operational pressure range (P/P_0 = 1 x 10^{-6} to 0.99), with a variable pressure increment of (P/P_0 = 0.001, 0.01 then 0.05) and equilibration time (t = 10-30 s). These conditions were found to produce sufficiently high resolution within acceptable completion time. Subsequent calculations were conducted on the *3Flex* software. Calculation of S_{BET} was conducted with the aforementioned BET method in the appropriate region (P/P_0 = 0.05-0.2) of the isotherm, alongside other standard recommendations (Rouquerol, Llewellyn and Rouquerol, 2007). Additionally, a standard value for the molecular cross-sectional area of the nitrogen probe molecules (s_{N2} = 0.162 nm^2) was assumed (Thommes *et al.*, 2015). The validity of the BET method using these conditions was evidenced by measurements for the value of C (Equation 3.26) being both positive and within the acceptable range (C > 2), as detailed by (Thommes *et al.*, 2015) and (Rouquerol, Llewellyn and Rouquerol, 2007). Similarly, evaluation of S_{MIC}, S_{EXT}, V_P and D_P were by the aforementioned BJH and HJ methods, however the range used in calculations (t = 5-8 Å) was outside those widely recommended (t = 3.5-5 Å) (Thommes *et al.*, 2015). However, this was necessary to ensure a positive value for C and maintain the physical significance of the calculations, despite deviation from standard practises. Throughout experimentation, a number of analyses were conducted for each sample (n_a = 2-3), with the mean average and standard deviation values reported alongside representative isotherms.

3.9 Mass Spectrometry

3.9.1 Fundamental Theory

Another technique that was used was mass spectrometry (MS), which allowed the identification and quantification of the species within the evolved gases. An informative overview of the technique has been reported in literature (de Hoffman and Stroobant, 2007). Fundamentally, this technique relies on the ionisation of inlet gases by thermionic emission from a heated filament, which causes the components to breakdown into mass fragments with corresponding mass-to-charge ratios (m/z) (de Hoffman and Stroobant, 2007). Within a vacuum, these fragments are then accelerated and passed through a variable electromagnetic

quadrupole that stabilises the trajectories of certain mass fragments based on their precise m/z values (de Hoffman and Stroobant, 2007). This effectively filters the entire distribution of mass fragments by only allowing certain m/z values to pass through successfully to a detector. By altering this electromagnetic quadrupole during analysis, a range of charged fragments pass through to detection, producing a mass spectrum of the intensity detected for each m/z value (de Hoffman and Stroobant, 2007). For a given molecule, a mass spectrum typically consists of a molecular ion peak corresponding to the entire charge molecule, alongside a range of molecular fragments, the most prominent of which is referred to as the base peak (de Hoffman and Stroobant, 2007). As an analytical technique, MS has been abundantly applied to temperature- and time-resolved analyses of a diverse range of reactions (Urban, Chen and Wang, 2016).

3.9.2 **Equipment Configuration**

Analyses were conducted within a tubular reactor with outlet gases analysed by a *Hiden HPR-20 QIC* spectrometer, as illustrated in Figure 3.5. The tubular reactor was constructed from stainless steel compression fittings with appropriate internal diameter (D_i = 7.1 mm) and length (L = 50 mm) (Yakub, 2018). The reactor was supplied with an adjustable flow of helium (He) from a cylinder controlled by a pressure regulator and mass flow controller, which carried the volatilised gases through tubing (L ≈ 3 m) to the spectrometer for analysis (Yakub, 2018). Heating of the reactor was achieved by a tubular furnace (T ≤ 600 ^{o}C) with the temperature increased at a fixed rate (β = 0.1-5 ^{o}C/min), with a thermocouple measuring temperature at the top of a quartz wool bed in close proximity to the loaded sample (Yakub, 2018). A portion of the outlet gases from the reactor were then continuously analysed by the spectrometer, with the remainder discharged to prevent saturation of the detector and help limit the analysis pressure (Yakub, 2018). The spectrometer was operated at standard conditions of voltage (V_e = 875 V), electron energy (E_e = 70 eV) and electron emission (I_e = 20 μA), which were found to be sufficient for general analyses (Yakub, 2018). Detection of mass fragments was by a secondary electron multiplier (SEM) detector, which operated between 1 x 10^{-14} and 1 x 10^{-7} torr and had been calibrated using a range of gases in the region of interest (m/z = 2-44) (Yakub, 2018). For transient analyses, the detection mode used was ‘discrete’, which allowed rapid measurement of the partial pressures (P_i) of precise m/z values throughout analysis, generally consistent with equipment configurations reported elsewhere in literature (Urban, Chen and Wang, 2016).

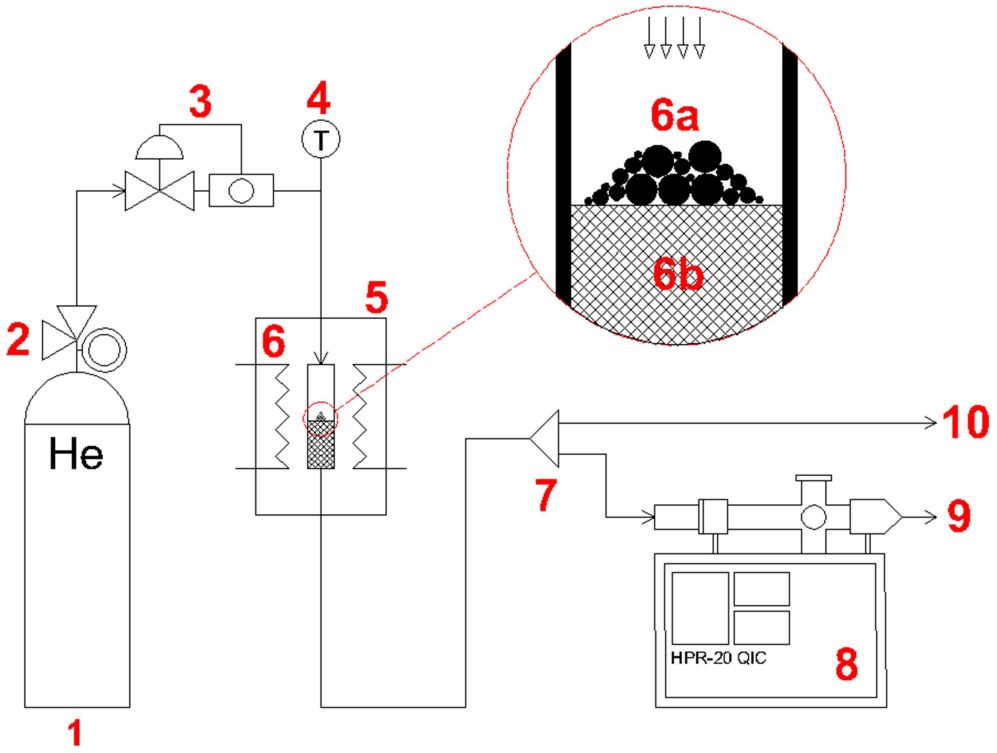

Item	Description	Item	Description
1	Gas Cylinder (He)	6	Reactor, (a) Sample (b) Quartz Wool
2	Gas Regulator	7	Flow Splitter
3	Mass Flow Controller	8	Mass Spectrometer
4	Thermocouple (Reactor Bed)	9	Sampled Gas, Outlet
5	Furnace	10	Unsampled Gas, Outlet

Figure 3.5: Equipment configuration during mass spectrometry experiments

3.9.3 **Procedure for Analysis**

Initially, the reactor was loaded with a known quantity of sample (m ≈ 5 mg), which was distributed across the top surface of the quartz wool catalyst bed. The reactor was then sealed and purged of ambient gases with a flowrate of He ($\dot{V}$ = 150 mL/min) for an extended duration (t ≈ 16 h). Subsequently, measurements were started a short duration (t ≈ 10 min) before heating to observe the baseline, after which the reactor was heated at a fixed rate (β = 0.5–5 ^{o}C/min) to the desired temperature (T = 300 ^{o}C). This effected dehydrogenation and volatilisation of gaseous species, which were carried to the spectrometer and continuously detected over the entire duration of the experiment. The total pressure was noted at the onset of experimentation (P ≈ 4 x 10^{-7} torr), and periodically recorded. Following analyses, partial pressure (P_i) measurements were then deconvoluted by consideration of the relative fragment intensities (RFI) of the anticipated species (as seen in Figure 2.7), which were either experimentally verified or reported in literature (Babenko *et al.*, 2017).

Deconvoluted values of P_i were then adjusted by the relative sensitivity (RS) factor (Equation 3.29), which yielded the actual partial pressure of each species (P_i') present in the gas stream (correcting for differences in ionisation, transmission, detection, *etc.*). RS values for common species were derived experimentally using the aforementioned calibration gases, whereas those for uncommon species were assumed based on literature (Hiden Analytical, 2018).

$$P_i' = \frac{P_i}{RS} \qquad \textbf{3.29}$$

Table 3.2: Relevant RFI and RS values used during mass spectrometry analyses

Species	Mass, M_W (g/mol)	Relative Fragment Intensity[a], RFI m/z(%)	Relative Sensitivity, RS (-)
Carrier/Atmospheric			
He	4.00	**1**(4.93), **2**(0.02), **3**(100)	1.00 [b]
H_2O	18.02	**16**(2.13), **17**(26.0), **18**(100), **19**(5.08)	8.48 [b]
N_2	28.01	**14**(9.28), **28**(100), **29**(0.7)	1.70 [b]
O_2	32.00	**16**(11.97), **32**(100), **33**(0.08), **34**(0.39)	0.95 [b]
CO_2	44.01	**12**(7.98), **13**(0.04), **16**(17.55), **22**(1.60), **28**(10.78), **29**(0.08), **44**(100), **45**(1.11), **46**(0.37)	1.54 [b]
Volatilised Species			
H_2	2.02	**1**(29), **2**(100)	3.19 [b]
BH_3	13.83	**10**(23.23), **11**(100), **12**(30.71), **13**(28.28), **14**(19.80)	0.70 [c]
NH_3	17.03	**14**(0.90), **15**(3.10), **16**(78.1), **17**(100), **18**(6.30)	1.30 [b]
DB	27.66	**10**(6.25), **11**(28.37), **12**(18.27), **13**(24.52), **14**(0.48), **21**(1.92), **22**(11.06), **23**(45.67), **24**(89.42), **25**(56.73), **26**(100), **27**(97.60), **28**(0.48)	0.90 [c]
MAB	28.85	**10**(1.20), **11**(6.01), **12**(1.00), **13**(1.20), **25**(2.00), **26**(12.83), **27**(50.50), **28**(100), **29**(25.85)	0.80 [c]
B_2NH_x	36.63	**37**(6.86), **38**(17.32), **39**(18.30), **40**(41.50), **41**(27.12), **42**(70.59), **43**(100), **44**(45.10)	1.50 [c]
iPrOH	60.01	**14-16**(<2.86), **17**(0.625), **18**(0.670), **19-26**(<1.67), **27**(5.63), **28**(0.66), **29**(7.50), **30**(0.83), **31**(24.76), **32-38**(2.38), **39**(11.43), **40**(21.14), **41**(28.69), **42**(5.36), **43**(21.96), **44-56**(<3.2), **57**(18.81), **58**(0.74) **59**(100), **60**(6.38), **61**(0.76)	**4.20**[c]
THF	72.11	**15**(4.00), **26**(3.00), **27**(17.00), **28**(5.00), **29**(9.00), **31**(3.00), **39**(10.00), **40**(8.00), **41**(40.00), **42**(100), **43**(19.00), **44**(4.00), **71**(30.00), **72**(32.00)	4.80 [c]
BZ	80.50	**51**(15.45), **52**(44.09), **53**(56.82), **54-60**(~2), **61**(8.18), **62**(20.91), **63**(24.09), **64-75**(~2), **76**(11.36), **77**(14.55), **78**(24.09), **79**(62.27), **80**(100), **81**(39.55)	1.50 [c]

[a] Relative Fragmentation Intensity (RFI): Reported in (Babenko *et al.*, 2017), (Dampc *et al.*, 2011)
[b] Relative Sensitivity (RS): Evaluated experimentally by (Yakub, 2018)
[c] Relative Sensitivity (RS): Estimated based on (Hiden Analytical, 2018)

The relative and absolute quantities of detected species were estimated by integration of the peaks against their respective baselines. The total partial pressure (P_i(Total)) for a given species (i) was found by the cumulative sum of the integrated areas for all peaks (n = 1, 2, 3, *etc.*) (Equation 3.30), which was used to indicate the absolute quantity of that species. The total analysed partial pressure (P(Total)) was then calculated by the sum of these pressures for all detected species (i = H_2, NH_3, H_2O, *etc.*) (Equation 3.31), which allowed the relative

quantity (Q_i) of these species to be evaluated (Equation 3.32). Due to the limited time available with instrument, the number of samples analysed by MS during this research was rather small. Nevertheless, in order to perform a rudimentary check of the analyses, each sample was analysed twice (n_s = 2), once at a lower (β = 1.5 ^{o}C/min) and higher (β = 5 ^{o}C/min) heating rate each. Typically, the results for the lower heating rate have been reported alongside their corresponding release profiles.

$$P_i(\text{Total}) = \sum_{n=0}^{n=n} P_i(n) \quad \textbf{3.30}$$

$$P(\text{Total}) = \sum_{i=i}^{i=k} P_i(\text{Total}) \quad \textbf{3.31}$$

$$Q_i = \frac{P_i(\text{Total})}{P(\text{Total})} \times 100 \quad \textbf{3.32}$$

3.10 X-Ray Diffraction

3.10.1 Fundamental Theory

Powder X-ray diffraction (XRD) is a technique where an X-ray beam diffracts from the crystallographic planes present within a powder sample, allowing identification and quantification of the constituent crystalline phases (Leng, 2013). This is possible due to the long-range order exhibited by crystalline materials, which reflect X-rays at specific diffraction angles corresponding to the crystallographic planes within the material (Leng, 2013). Conversely, amorphous materials lack such character and cannot be identified by XRD. This has been schematically illustrated in Figure 3.6 below, to illustrate the following discussion.

Consider an incident beam of X-rays (I_0) with monochromatic wavelength (λ) that is directed at a given angle (θ) toward two crystallographic planes separated by a distance (d). Upon reaching the first plane, a fraction of the X-rays will be reflected from the plane (I_1) with the corresponding reflection angle, shown by the path (A→C'). However, some of these incident X-rays will be transmitted to the second plane, wherein they are similarly reflected (I_2), shown by path (A→B→C). In order for reflected beams I_1 and I_2 to remain in-phase and exhibit constructive interference, the additional distance travelled by I_2 (namely A→B→C minus A→C') must correspond to an integer number (n) of wavelengths. Subsequent application of trigonometric identities allows this to be expressed in terms of the distance between the crystallographic planes (d) (Equation 3.33). Practically, sweeping the beam through a range of incident angles will produce peaks at certain angles due to the constructive interference between I_1 and I_2 for each plane, whereas other angles will not

produce such peaks since I_1/I_2 are out-of-phase and do not satisfy the conditions for constructive interference. This allows crystalline materials to be identified by their set of characteristic peaks, with their magnitude proportional to the quantity of that plane in the sample. These peaks are routinely reported as corresponding 'two theta' (2θ) values as opposed to the aforementioned diffraction angle (Leng, 2013). The size of the crystallites (τ) can be estimated (Equation 3.34) in terms of a shape factor (K), the monochromatic wavelength (λ), the peak broadening (β), and the aforementioned incident angle (θ). The value for the shape factor estimated based on the crystal shape (typically $K \approx 0.9$), and the peak broadening is evaluated as the full width at maximum height (FWHM) (Leng, 2013).

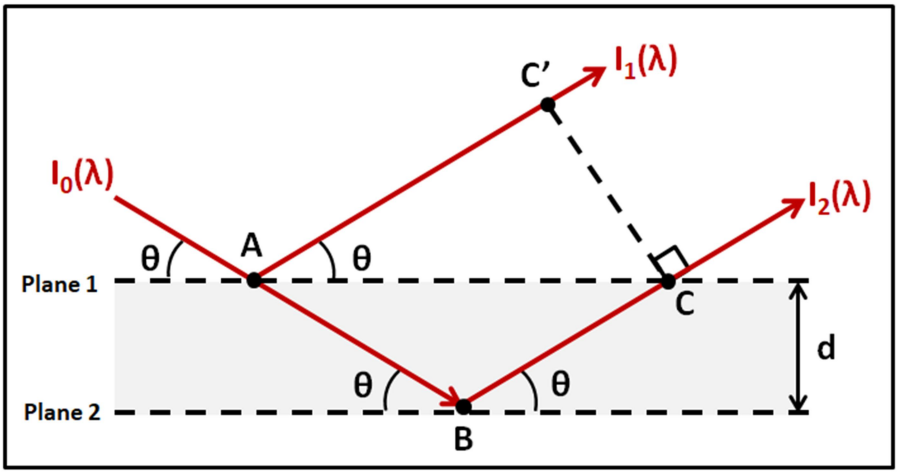

Figure 3.6: Schematic of diffraction of X-rays from crystallographic planes (Leng, 2013)

$$n\lambda = 2d\sin(\theta) \qquad \textbf{3.33}$$

$$\tau = \frac{K\lambda}{\beta\cos(\theta)} \qquad \textbf{3.34}$$

3.10.2 Equipment Configuration

Measurements were made with two analysers, namely a *STOE STADI P (Mo PSD)* and a *Bruker D2 Phaser*. Measurements of titania materials were conducted with the *STOE STADI P* operated by accompanying *WinXPOW* software, which produced a monochromatic beam (Mo-$K\alpha_1$, λ = 0.7090 Å) under standard working conditions (namely V = 40 kV, I = 45 mA). The equipment was arranged in the Bragg-Brentano (2θ:θ) configuration with asynchronous specimen rotation (Leng, 2013). This equipment configuration allowed a wide working range (2θ = 0.2–80°) and highly precise angle increments (Δ2θ = 0.02°). Analysis of heated samples was achieved by *ex situ* calcination in a furnace (T = 100-600 °C) immediately followed by

analysis with XRD. Conversely, measurements of bulk and nanoconfined AB were conducted using the *Bruker D2 Phaser*, which produced a different of monochromatic beam (Cu-Kα_1, λ = 1.5406 Å) and was arranged in the Bragg-Brentano (θ:θ) configuration without sample rotation (Leng, 2013). This equipment configuration allowed a similar working range (2θ = 5–160°) and angle increments ($\Delta 2\theta$ = 0.02°). Both pieces of equipment were calibrated using standard silicon reference materials (NIST 640d).

3.10.3 Procedure for Analysis

Sample preparation procedures were slightly different for the *STOE STADI* and *D2 Phaser*. For the *STOE STADI*, a small quantity of sample (m ≈ 5 mg) was transferred to an agate mortar and ground for a moderate duration (t ≈ 5 min) until a fine powder was produced. This powder was then fixed to an acrylic disc using a small amount of polyvinyl acetate adhesive, with samples then dried using a heat gun (T ≤ 80 °C). These specimens were then secured within stainless steel sample mounts and transferred to the equipment for analysis. Typically, samples were analysed between 2θ = 5–40° with increments of $\Delta 2\theta$ = 0.02°. Conversely, for the *D2 Phaser*, a similar quantity of sample was also ground but was then distributed across a polymethyl methacrylate sample holder without adhesive. The sample was then scraped with a glass slide to achieve a flat surface for analysis and to minimise effects from preferred orientation of the powder. For all samples, identification was achieved by comparison of the measured diffraction pattern to the database available in *PDF-4+* software. In order to conveniently present diffraction patterns on the same figure, data collected from the *STOE STADI* was then converted to a simulated Cu-Kα_1 pattern (Equation 3.35). All samples were only analysed once (n_a = 1) for each samples.

$$\theta_{Cu} = \sin^{-1}\left(\frac{\lambda_{Cu}}{\lambda_{Mo}}\sin(\theta_{Mo})\right) \qquad \textbf{3.35}$$

4.0 Results & Discussion

The following section outlines the results of this research. The data recorded during these experiments are presented alongside subsequent analysis to produce the fundamental results of this research. Discussion of these results with respect to the aforementioned literature and hypotheses has been conducted at the end of each section respectively.

4.1 Characterisation of Synthesised Titania Materials

Importantly, thorough characterisation of the synthesised titania materials was fundamental for understanding subsequent application toward thermolytic dehydrogenation of AB. As such, initial experiments were directed toward investigating the respective properties of these materials. For clarity, the naming convention used to refer to titania materials in subsequent sections has been summarised in Table 4.1 below.

Table 4.1: Naming convention for titania materials synthesised during this research

Sample[a]	Substance	Material	Drying	Form
TP(65)	Titania	Precipitate	Evaporative (65 ^{o}C, 16 h)	Particles
TP(500)	Titania	Precipitate	Evaporative (500 ^{o}C, 5 h)	Particles
TA(L)	Titania	Aerogel	Extraction (LCO_2)	Particles
TA(S)	Titania	Aerogel	Extraction (SCO_2)	Particles
TA(S,M)	Titania	Aerogel	Extraction (SCO_2)	Monolithic[a]

[a] Naming Example: Titania Precipitate dried at 65^{o}C denoted as “TP(65)”

4.1.1 Surface Properties

The surface properties of the synthesised materials were of inherent interest to this research since subsequent interaction with nanoconfined AB was predicted to fundamentally occur within the pores of the titania aerogel. Characterisation of these surface properties was therefore deemed critical for establishing understanding of nanoconfinement effects and any modification of hydrogen release from AB. Hence, analyses with nitrogen porosimetry (as described in *3.7 Nitrogen Porosimetry*) were conducted to evaluate the surface properties of the synthesised titania materials. These experiments were repeated three times per sample (n_a =3), however equipment issues meant some samples were only analysed based on two repeats (n_a = 2). The averaged isotherms for each material have been displayed in Figure 4.1

overleaf, highlighting the distinct profiles exhibited by each material. All samples appeared to exhibit characteristic Type IV isotherms (Thommes *et al.*, 2015), comprised of multilayer adsorption with capillary condensation and subsequent desorption showing a hysteresis loop characteristic of ink-bottle shaped pores. Nevertheless, the isotherm shape and quantity adsorbed (Q_{ads}) exhibited by these materials varied greatly, evidencing differences in their respective surface properties. These were subsequently calculated with average values for BET surface area (S_{BET}), pore volume (V_P) and pore size (D_P) distribution presented in Figure 4.2(a)-(c) respectively. Note that Figure 4.2(a) has been divided between constituent microporous (S_{MIC}) and external (S_{EXT}) areas, the latter of which is attributed to the sum of mesoporous and macroporous areas. These results were then statistically analysed using t-tests with the assumption of a zero null hypothesis (*i.e.* no difference between materials) with two-tailed distribution and unequal variance. The significance value (α_s) was selected to correspond with a 95% confidence interval ($\alpha_s = 0.05$). Thus, differences between calculated values can be determined to be insignificant ($p > 0.05$) or significant ($p \leq 0.05$) respectively.

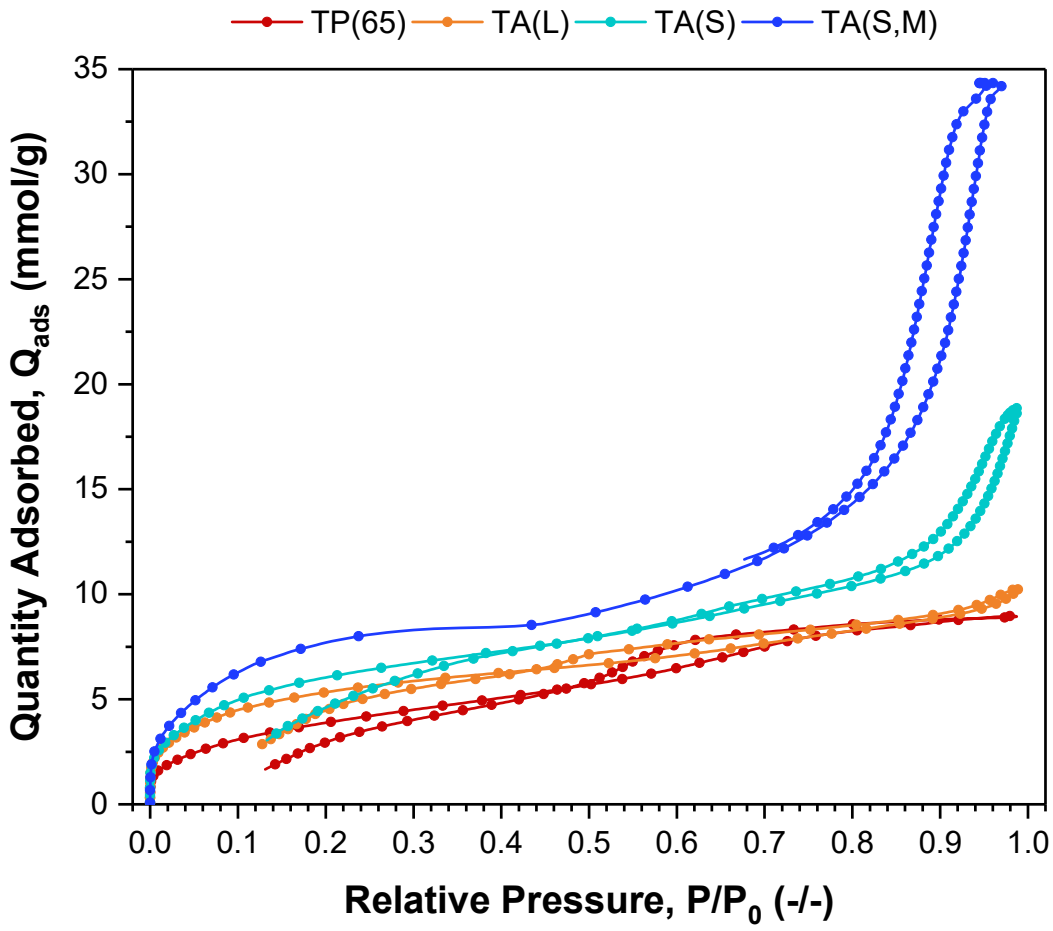

Figure 4.1: Nitrogen adsorption-desorption isotherms for the synthesised titania materials used to calculate their respective surface properties

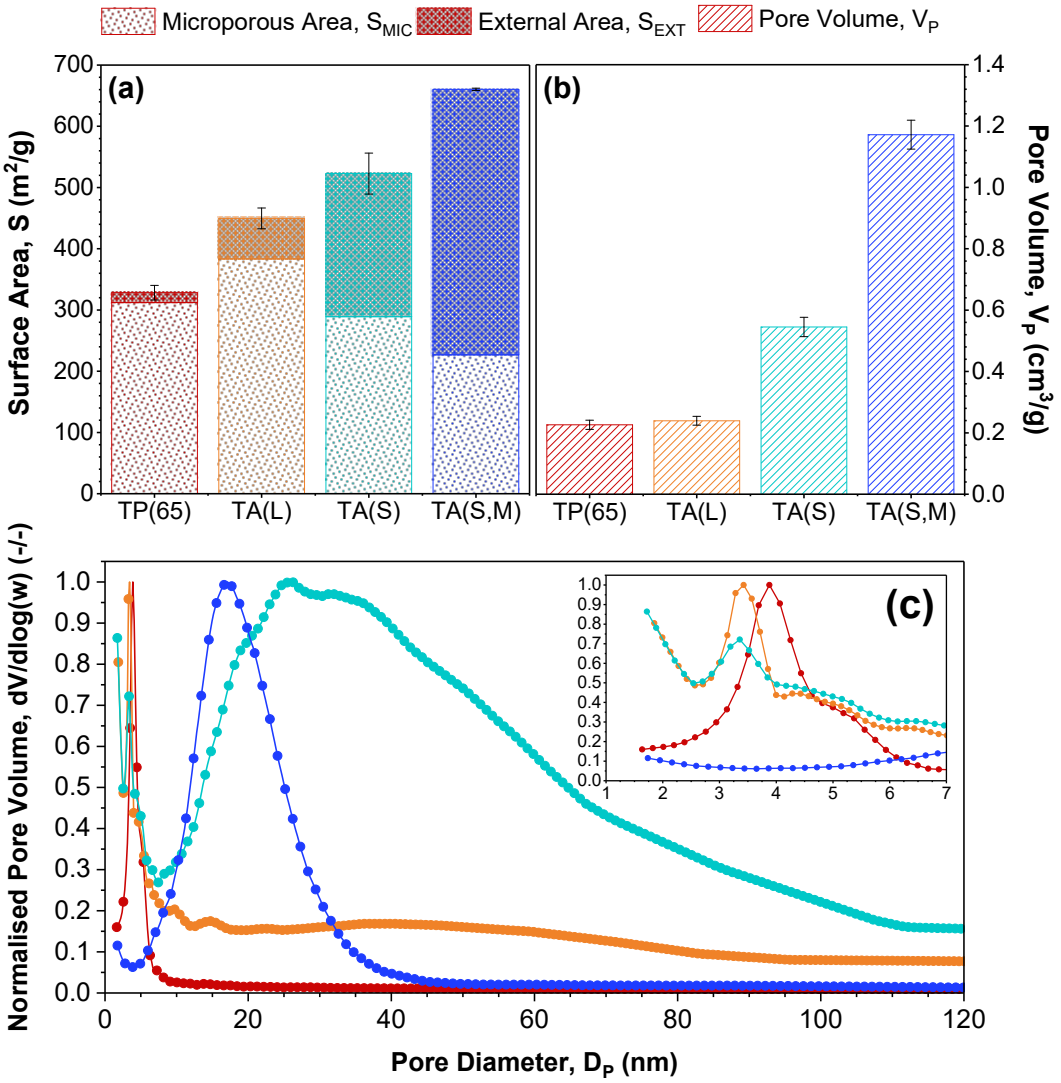

Figure 4.2: Calculated average surface properties for the synthesised titania materials, namely (a) surface areas, (b) pore volumes, and (c) pore size distribution

Examination of Figure 4.2(a)-(c) highlighted considerable differences between the synthesised titania materials. For instance, TP(65) demonstrated poor surface properties mainly characterised by a relatively low surface area comprised of micropores with correspondingly small pore volume. This in contrast to TA(L), TA(S) and TA(S,M) which generally appeared to demonstrate improved surface properties in these areas. In comparison with TP(65), TA(L) showed a significant ($p = 0.044$) increase in surface area and a larger fraction of external area, however this was not the case for pore volume which showed insignificant difference ($p = 0.535$). In contrast, comparison of TA(L) against TA(S) showed insignificant difference ($p = 0.087$) in total surface area although this was achieved with an even greater contribution from external area. Furthermore, and unlike previously, the difference between these materials with regard to pore volume was statistically significant ($p = 0.001$). Finally, comparison of TA(S) and TA(S,M) showed significant differences for both surface area ($p = 0.027$) and pore volume ($p = 0.0196$), with the majority

of the surface area now being attributed to external area. These findings were complimented by examination of Figure 4.2(c), which generally supported the above trend. The pore size distribution exhibted by TP(65) exclusively showed a narrow distribution of small mesopores, highlighting the presence of pores in close proximity to the microporous range. TA(L) and TA(S) showed comparably sized pores, however these materials also had broad distributions that extended across the mesoporous and macroporous ranges. Finally, TA(S,M) exclusively exhibited a range of larger mesopores, well within the mesoporous region, and the comparative absence of pores adjacent to the microporous region. For completeness, the calculated values discussed above have been summarised in Table 4.2.

Table 4.2: Calculated values for surface properties of synthesised titania materials

Material	Surface Area, S (m^2/g)			Pore Volume, V_P (cm^3/g)	Pore Diameter, D_P (nm)
	S_{BET}	S_{MIC}	S_{EXT}		
TP(65)	328 ± 12	312 ± 12	16 ± 1	0.23 ± 0.01	3.9
TA(L)	450 ± 17	383 ± 22	66 ± 5	0.24 ± 0.01	3.4, 38.6
TA(S)	523 ± 33	289 ± 30	234 ± 6	0.55 ± 0.03	3.4, 29.5
TA(S,M)	660 ± 2	227 ± 79	433 ± 81	1.17 ± 0.04	17.1

[a] Analysis: Average ± Standard Deviation, from a number of analyses (n_a) where [TP(65); $n_a = 3$], [TA(L); $n_a = 2$], [TA(S); $n_a = 3$], [TA(S,M); $n_a = 2$]

4.1.2 **Textural Properties**

It was also hypothesised that the textural properties of the material surface might similarly affect interactions of nanoconfined AB with titania aerogel. Conceivably, the different methods of preparation might have produced titania materials with different surface textures. Hence, to complement above analyses with nitrogen porosimetry the synthesised titania materials were qualitatively studied with scanning electron microscopy (SEM) to observe their respective textual properties (according to procedures in *3.6.3 Procedures for Textural Analysis*). Following respective sample preparation and coating, these specimens underwent analysis at several magnifications (MAG = x200, x2,000 and x10,000) with the resulting micrographs presented in Figure 4.3(a)-(c). These figures showed the synthesised titania materials were comprised of irregular micron-sized particles, however these exhibited considerably greater amorphous characteristic. Furthermore, these materials demonstrated quite varied surface textures, with an apparent trend across the TP(65), TA(L) and TA(S) series, as seen across Figure 4.3(a)-(c). The surfaces of TP(65) lacked roughness and obvious macroporous characteristic, indirectly supporting the previous findings from nitrogen

porosimetry that TP(65) was predominantly microporous. TA(L) showed a similar lack of macroporous characteristic, although the surface roughness was noticeably increased compared to TP(65). Finally, TA(S) showed even greater surface roughness and the appearance of macroporous characteristic, as suggested by the pitted surface observed on Figure 4.3(d) at higher magnifications (MAG = x10,000).

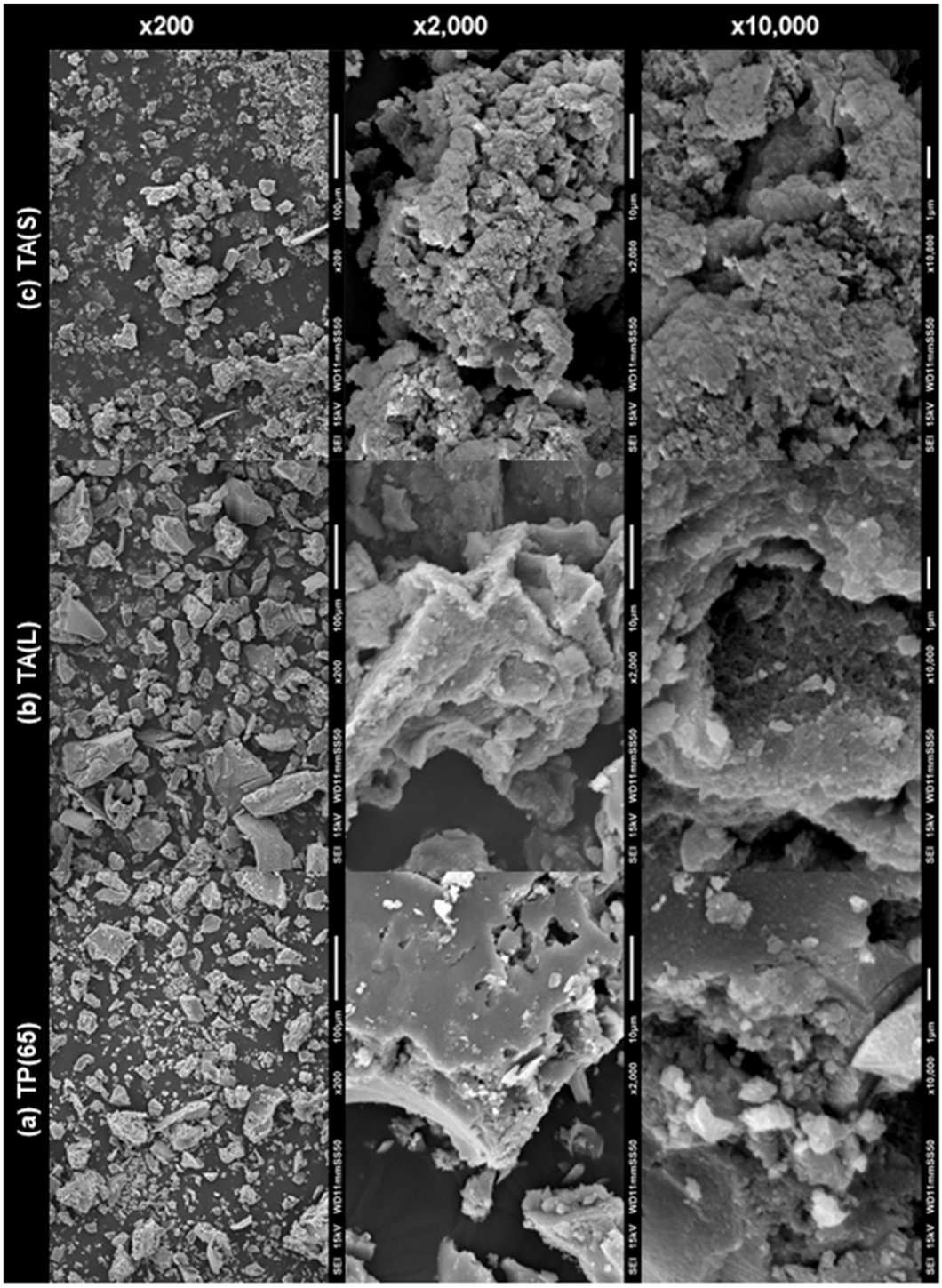

Figure 4.3: SEM micrographs of (a) TP(65), (b) TA(L) and (c) TA(S). Specimens coated with gold to a target thickness of 10-20 nm. Analyses conducted at AV = 10-15 kV, SS = 50, WD = 11 mm, MAG = x200-x10,000.

4.1.3 **Particle Size Distribution**

The particle size distributions of the synthesised titania materials were quantitatively evaluated using SEM and subsequent image processing in *Image J* software (as detailed in *3.6.4 Particle Size Analysis*). For each micrograph, the software detected discrete particles within the image and subsequently calculated the area occupied by each particle (A_P). This value was then converted to an equivalent particle diameter (D_P) with the assumption of perfect spherical morphology with a circular cross-sectional area (Equation 4.1). Whilst this assumption neglected the true morphology of the particles, it was nevertheless necessary since their irregularity prevented more accurate calculation.

$$A_P = \frac{\pi {D_P}^2}{4} \quad \textbf{4.1}$$

$$C = C_0 + \left(\frac{A}{\sqrt{2\pi} w D_P}\right) e^{\left(\frac{-\left(\ln(D_P/D_{P,C})\right)^2}{2w^2}\right)} \quad \textbf{4.2}$$

The particle diameters for each material were subsequently plotted as a histogram as seen in Figure 4.4(a)-(d). These figures have been presented in the lower micron range (D_P = 1-20 μm) since the vast majority of particles were observed in this region, with considerably fewer particles observed above this (D_P = 20-100 μm). Particles above this cumulative range were practically absent from the measurements. It should be reiterated that due to the analytical procedures used, sub-micron particles could not be detected during analyses (D_P < 0.5 μm). Examination of the profiles in Figure 4.4(a)-(d) appeared to show lognormal distributions, which have been extensively reported in literature and reportedly result from competing particle growth and break-up processes during preparation (Penner and Chang, 1978). Hence, lognormal distribution curves (Equation 4.2) were fitted to the data, in terms of the particle count (C), particle diameter (D_P), particle diameter at peak centre ($D_{P,C}$), peak area (A) and log standard deviation (w). During this research, the offset term was neglected (C_0 = 0). Fitting parameters for these lognormal curves have been summarised in Table 4.3. These curves were then normalised and analysed for statistical differences using t-tests, as described previously. The distribution for TP(65) was statistically significant (p = 0.027) compared to TA(L), confirming the smaller average particle diameter produced by the precipitation method. Conversely, comparison of TA(L) with TA(S) and separately TA(S) with TA(S,M) showed insignificant difference (p = 0.809 and p = 0.239), evidencing the respective preparations do not have an appreciable affect on the average particle diameter of the synthesised titania material.

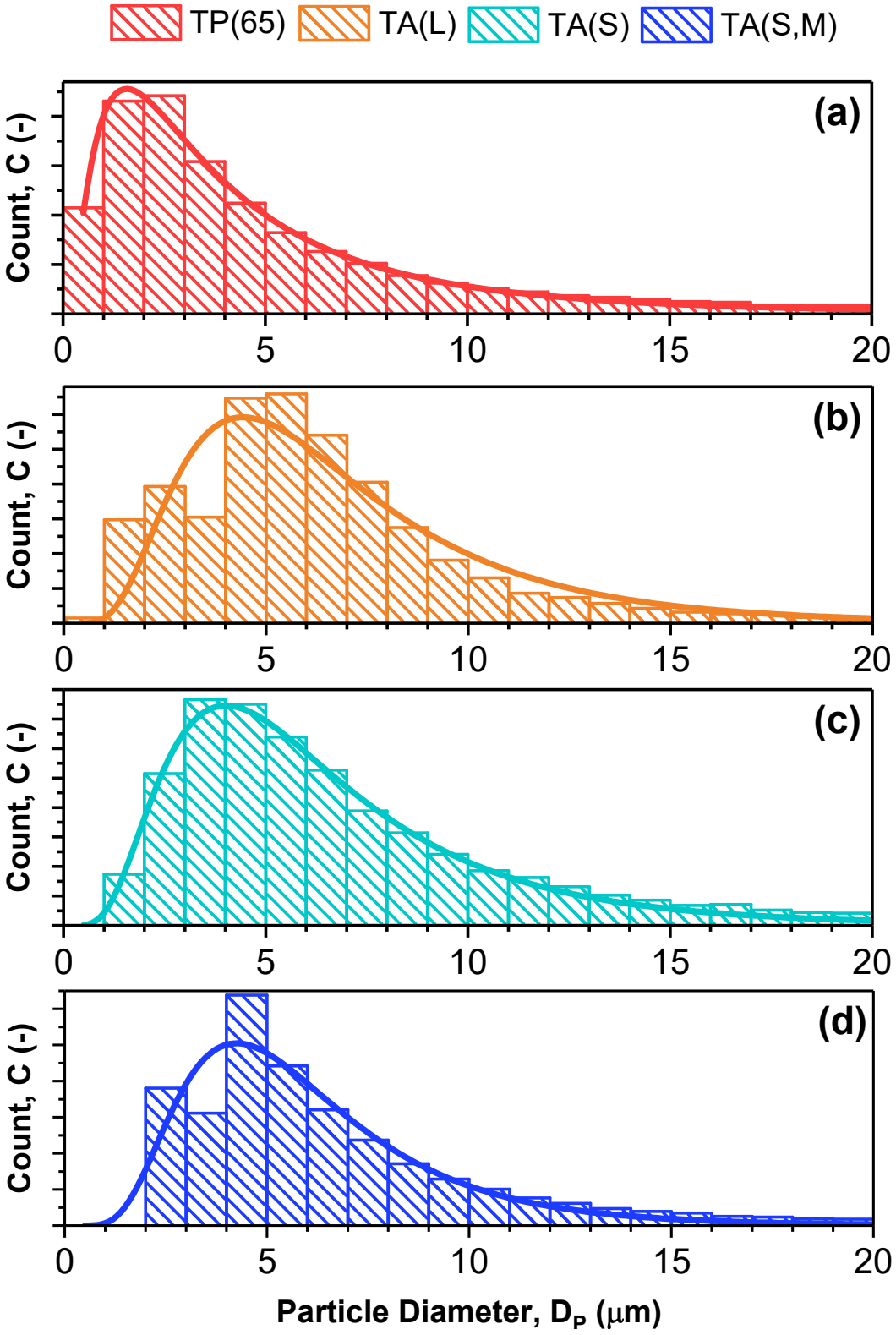

Figure 4.4: Particle size distribution of synthesised titania materials, namely (a) TP(65), (b) TA(L), (c) TA(S) and (d) TA(S,M). Calculated diameters shown as histogram and lognormal fitting overlaid as curve.

Table 4.3: Fitting parameters of lognormal distribution curves applied to particle size distributions of synthesised titania materials

Material[a]	Particle Diameter, $D_{P,C}$		Log Std Dev, w (-)	Area, A (-)	Std Dev, σ (-)	Fitting, R^2 (-)
	Centre	Mean				
TP(65)	3.55 ± 0.05	5.34 ± 0.11	0.903	24,353	5.996	0.993
TA(L)	6.00 ± 0.16	6.99 ± 0.25	0.551	4,216	4.162	0.909
TA(S)	5.61 ± 0.04	6.65 ± 0.06	0.580	25,737	4.210	0.995
TA(S,M)	5.34 ± 0.11	6.09 ± 0.15	0.490	29,702	3.175	0.936

[a] Analysis: Analysis conducted across a number of micrographs (n_M) with a total number of particles (n_P) where [AB; n_M = 3, n_P = 365], [TP(65); n_M = 5, n_P = 27,371], [TA(L); n_M = 5, n_P = 4,889], [TA(S); n_M = 5, n_P = 28,322], [TA(S,M); n_M = 5, n_P = 32,875]

4.1.4 Crystalline Properties

The crystallinity of the synthesised titania materials were also of interest since the properties of the material are intrinsically affected by the precise phase composition (Oi *et al.*, 2016). This is of particular interest since it has been identified that the choice of extractant during high pressure solvent extraction can affect the crystallinity of the final aerogel (as reviewed in Table 2.5). Previously, the use of carbon dioxide extractants has almost exclusively produced amorphous titania aerogels, which can subsequently be crystallised by heating to above the specific crystallisation temperature. In order to confirm the phase composition of the titania aerogels synthesised in this research, analyses were conducted with X-ray diffraction (XRD) according to procedures in *3.9 X-Ray Diffraction* to confirm. Analyses were solely conducted on TA(L) since the effect of carbon dioxide extractants on the phase of titania aerogels has already been established, meaning these studies were only required to provide confirmation. The results from these analyses have been presented overleaf in Figure 4.5. The absence of diffraction peaks for TA(L) indicated the synthesised aerogel was indeed amorphous, in agreement with previously reviewed literature. Upon heating (T = 100-600 °C) for a moderate duration (t ≈ 4 h), this amorphous phase was observed to persist up to 300 °C. Thereafter, diffraction peaks were observed at 2θ = 25.2, 37.8, 47.9, 54.0, 55.0, 62.6°, which have been extensively assigned to the (101), (004), (200), (105), (211) and (204) planes of an anatase phase (ICDD = 00-021-1272). Thus, crystallisation was must have occurred between 300-400 °C. The size of the crystallites was estimated by consideration of the (101) peak with Equation 3.34, which showed sizes of 7.6, 9.6 and 9.9 nm produced at produced at 400, 500 and 600 °C respectively (which also evidenced crystallite growth upon heating). Hence, when used throughout further experimentation with nanoconfined AB, the TA(L) support material was evidenced to remain amorphous when heated between 25-300 °C.

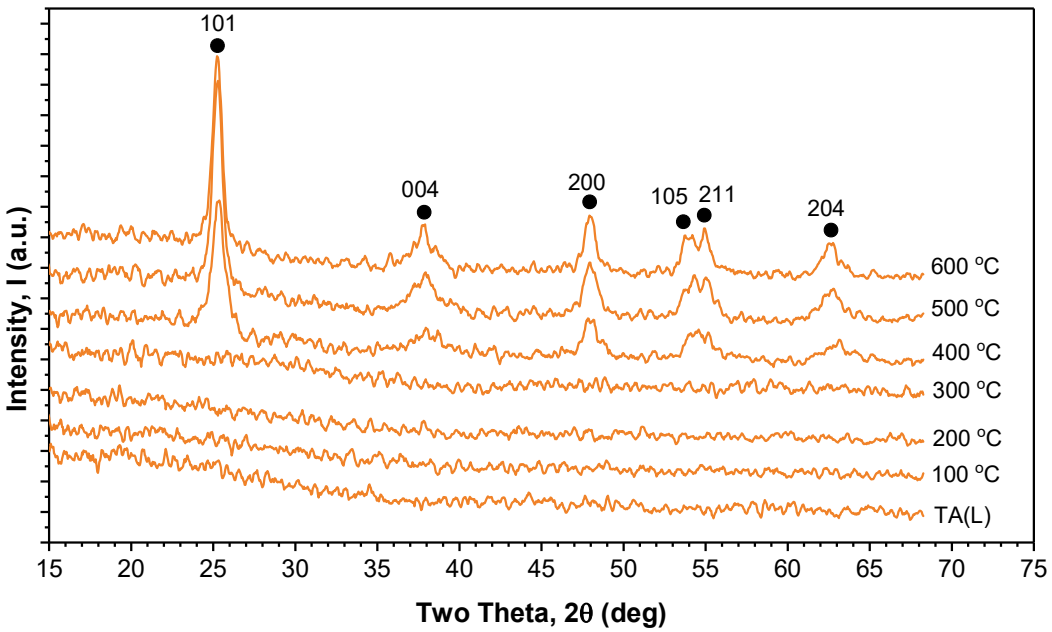

Figure 4.5: XRD patterns of synthesised titania aerogel TA(L), followed by subsequent heating between 100-600 °C for 4 h, showing peaks assigned to the anatase phase (●)

4.1.5 Chemical Composition

The chemical composition of the synthesised titania materials were also of fundamental interest to this research. Analysis of the composition of these materials was to understand their material properties as well as evaluate the relative effects of their respective preparation methods. These investigations were conducted according to procedures outlined in *3.3.3 Procedures for 1D-IR Spectra*, the results from which have been presented in Figure 4.6 and summarised in Table 4.4. Examination of Figure 4.6(a)-(b) highlighted extensive similarities between TA(S) and TA(L). The spectra for both materials were practically identical with only minor differences appearing in several highly convoluted bands between 1700-1200 cm^{-1}. These complex features were deconvoluted into five overlapping bands for TA(L), as indicated on Figure 4.6 from (i) to (v), which allowed subsequent assignment. Both TA(S) and TA(L) exhibited a strong, broad band between 3600-2600 cm^{-1} that was indicative of O-H stretching in a carboxyl functionality (Nolan, et al., 2009), complemented by corresponding O-H bending at 1635 cm^{-1} (Nolan, et al., 2009). The presence of carboxyl groups was further evidenced by bands at 1563 and 1431 cm^{-1} which were suggestive of asymmetric and symmetric COO^- stretching in carboxylates (Vasconcelos et al., 2011) (Qu et al., 2010). The distance between these modes (Δw) has been used to identify the coordination mode in carboxylates, being assigned to either monodentate (Δw ≈ 425 cm^{-1}), bidentate chelating (Δw ≈ 80 cm^{-1}) or bidentate bridging (Δw ≈ 160 cm^{-1}). The distance between these bands (Δw ≈ 132 cm^{-1}) was somewhat suggestive of carboxylate groups in the bidentate bridging mode on the surface of TA(L) (Vasconcelos et al., 2011). This

assertion was supported by the presence of a band at 1021 cm^{-1} and the absence of a band at 1720 cm^{-1}, which announced the existence of C-O stretching and lack of free C=O stretching respectively (Moran et al., 1998). Otherwise, relatively sharp bands at approximately 2971, 2933 and 2881 cm^{-1} were typical of asymmetric and symmetric C-H stretching in alkyl groups, further supported by bands at 1375, 1159 and 1123 cm^{-1} assignable to the associated C-H bending and rocking modes respectively (Qu et al., 2010) (Moran et al., 1998). Also observed were bands at 947 cm^{-1} and broad features below 947 cm^{-1} which were believed due to Ti-O-C and Ti-O-Ti stretching respectively (Vasconcelos et al., 2011) (Moran et al., 1998). In contrast, the spectra for TP(65) exhibited considerably fewer bands with generally reduced intensity. As above, the material exhibited a strong, broad band between 3600-2400 cm^{-1} which was indicative of O-H stretching (Nolan, et al., 2009). However, the centre of this band relative to TA(S)/TA(L) was significantly shifted (3050 cm^{-1} compared to 3208 cm^{-1}), highlighting the absence of the carboxyl functionality. As previously, this band was complemented by the corresponding O-H bending mode at 1627 cm^{-1} (Nolan, et al., 2009). A further difference included the relatively elevated presence of Ti-O-Ti stretching for TP(65) between 900-400 cm^{-1} (Moran et al., 1998).

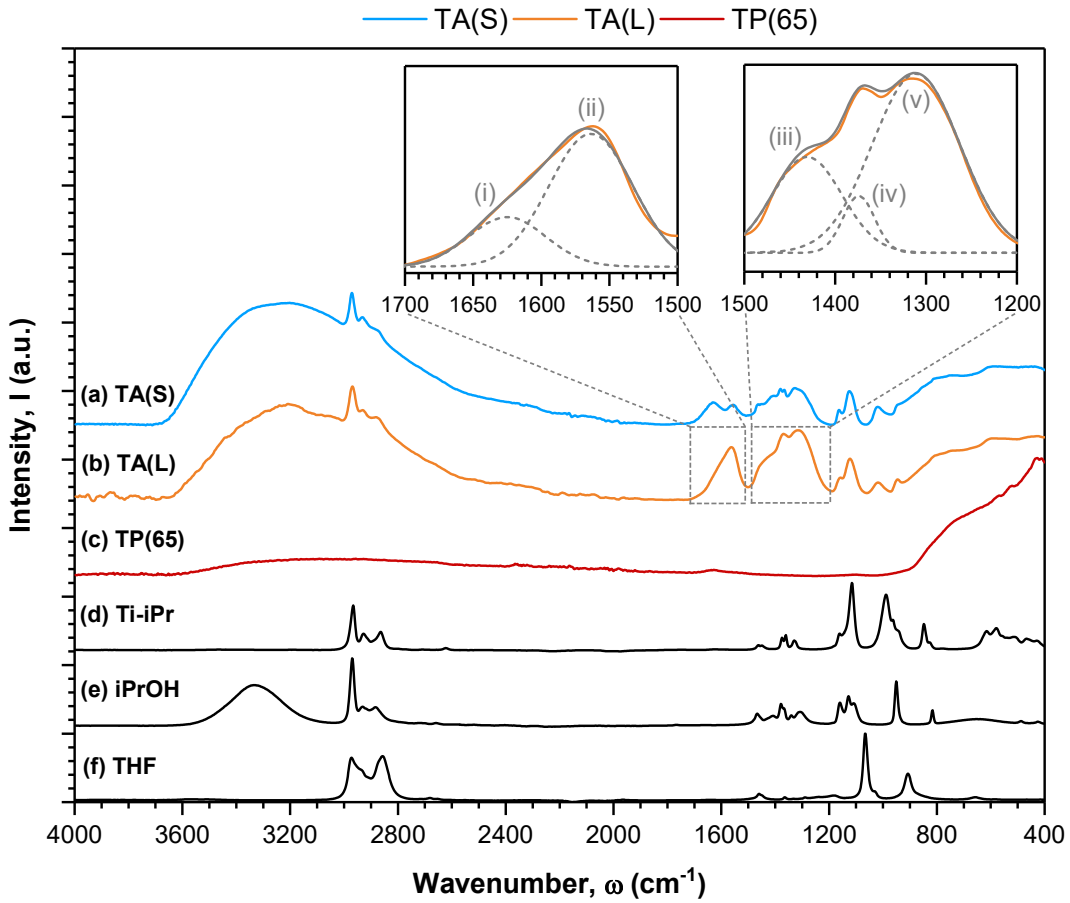

Figure 4.6: 1D-IR spectra of synthesised titania materials namely (a) TA(S), (b) TA(L) and (c) TP(65), compared to a selection of reagents used during preparation namely (d) Ti-iPr, (e) iPrOH, and (f) THF. Analysed at ω = 400-4000 cm^{-1}, R_S = 1 cm^{-1}, n_S = 256.

Table 4.4: FTIR spectra assignments for synthesised titania materials

Wavenumber, ω (cm^{-1}) TA(S)	TA(L)	TP(65)	Characteristic	Assignment	[Reference], ω (cm^{-1})
3208	3208	-	s, br	v(O-H)	[1] 3500-2800
-	-	3050	s, br	v(O-H)	[1] 3500-2800
2971	2969	-	w, sh	$v_{as}(CH_3)$	[3] 2960, [4] 2968
2933	2929	-	w, sh	$v_{as}(CH_3)$	[3] 2920, [4] 2930
2875	2877	-	w, sh	$v_s(CH_3)$	[3] 2850, [4] 2866
1632	1625	1627	m	δ(O-H)	[1] 1610
1557	1563	-	m	$v_{as}(COO^-)$	[1] 1550, [3] 1510
1461	1431	-	m	$v_s(COO^-)$	[1] 1350, [2] 1445, [3] 1414
1380	1374	-	w	$\delta_s(CH_3)$	[2] 1380, [4] 1376
1326	1311	-	m	δ(C-H)	[4] 1307
1164	1159	-	w	$\delta_r(CH_3)$	[4] 1160
1126	1123	-	m	$\rho_r(CH_3)$	[4] 1115
1021	1021	-	w	v_s(C-O)	[4] 1180
949	947	-	w	v_x(Ti-O-C)	[2] 1080, [4] 940
<949	<947	<1000	w	v_{as}(Ti-O-Ti)	[1] 450, [2] 800-400 [4] 583

[a] **Character**: *s* = strong, *m* = medium, *w* = weak, *sh* = sharp, *br* = broad
[b] **Assignment**: v = stretching, δ = bending, ρ = rocking, s = symmetrical, as = asymmetrical
[c] **References:** [1] (Nolan, et al., 2009) [2] (Vasconcelos *et al.*, 2011) [3] (Qu *et al.*, 2010) [4] (Moran *et al.*, 1998)

4.1.6 **Thermal Properties**

The thermal properties of the titania materials were necessarily of fundamental interest since mass loss upon heating would indicate the evolution of residual volatiles (*e.g.* solvent, precursor, catalysts). The extent and temperatures of these mass losses evidence the identity of the evolved gases and give an indication to the composition of the analysed materials. Investigations were conducted by complementary non-isothermal thermogravimetric (TGA), derivative thermogravimetric (DTG) and differential scanning calorimetry (DSC) analyses, described in *3.4 Thermogravimetric Analyses* and *3.5 Differential Scanning Calorimetry* respectively. The results from these analyses have been presented in Figure 4.7(a)-(b) and Figure 4.8 respectively, as well as being summarised in Table 4.5.

For TP(65), Figure 4.7(a)-(b) showed the mass loss to occur immediately across three poorly-defined steps between 25-230, 230-340 and 340-470 °C, with corresponding peak temperatures of 44, 272 and 406 °C respectively. These temperatures appeared to correlate well with previous research on similar materials (Calzada *et al.*, 2002). The initial mass loss accounted for 14.9 wt% with the temperature correlating to the removal of weakly adsorbed H_2O (Madarász, Brăileanu and Pokol, 2008), whereas the second mass loss accounted for only 2.4 wt% and correlated with previous reports for the release of chemisorbed H_2O and the decomposition of residual Ti-iPr into organics (*e.g.* into CO_2, $(CH_3)_2CO$, CH_3COOH, *etc.*) (Calzada et al., 2002). The third mass loss similarly resulted in a change of 2.5 wt%, and was also previously the aforementioned species, presumably due to the their elimination during crystallisation to the anatase phase (*e.g.* surface hydroxyls to release H_2O) (Calzada et al.,

2002). This was supported by the presumption that TP(65) exhibited a similar phase change characteristics to that observed for TA(L) in Figure 4.5, wherein crystallisation from amorphous to anatase phases was observed to occur between 300-400 °C. Cumulatively these steps accounted for a total sample mass loss of 19.8 wt%, which corresponded to a relatively high final sample mass of 80.2 wt%. Comparison of the mass loss profiles of TP(65) with TA(L) and TA(S) showed evident differences which did not require validation with a t-test, overall evidencing significant differences between these materials.

In contrast, TA(L) and TA(S) appeared to exhibit considerable similarity, which was confirmed by the absence of statistically significant difference ($p = 0.888$) between the respective mass loss profiles in Figure 4.6(a). Examination of the profiles in Figure 4.7(b) suggested mass loss in TA(L)/TA(S) progressed through broad and overlapping steps, which were deconvoluted by consideration of subsequent calorimetric analyses of TA(L), as presented in Figure 4.8. This appeared to show three overlapping exothermic peaks, alongside an unresolved peak between 280-300 °C (which was not considered during deconvolution). Hence, mass loss was believed to progress through three unresolved steps between around 25-140, 140-190, and 190-340 °C. The peak temperatures calculated by thermogravimetric and calorimetric methods were generally in agreement with the respective values for TA(L) calculated as 34, 161 and 221 °C compared to 117, 182 and 236 °C. Regardless of the precise temperature, the first mass loss accounted for around 8.5 wt% which was explained by the removal of residual volatiles (*e.g.* H_2O, THF, iPrOH) weakly adsorbed within the material (Calzada *et al.*, 2002). The second mass loss represented approximately 4.1 wt% and was presumed due more tightly bound volatiles confined within the pores of the aerogels and/or the elimination of surface groups (*e.g.* surface carboxyls to release CO_2) (Madarász, Brăileanu and Pokol, 2008). Finally, the temperature of the last mass loss was again consistent with the decomposition of residual Ti-iPr and accounted for roughly 11.4 wt% (Calzada *et al.*, 2002). Cumulatively, these steps effected a total mass loss of 24.0 wt% from TA(L)/TA(S), and a corresponding final sample mass of 76 wt%.

Table 4.5: Thermal properties of synthesised titania materials

Material	Temperature, T (°C)			Mass, m (wt%)		
	Onset, T_o	Peak, T_p	Range, T	Loss, dm	Total Loss, dm_t	Final Mass, m_f
TP(65)	25	44	25 - 230	14.9		
	230	272	230 - 340	2.4		
	340	406	340 - 470	2.5	19.8	80.2
TA(L)	25	66	25 – 115	8.4		
	115	161	115 - 190	4.0		
	190	220	190 – 340	11.7	24.1	75.9
TA(S)	25	37	25 - 132	8.7		
	132	196	132-226	4.2		
	226	241	140 - 340	11.1	24.0	76.0

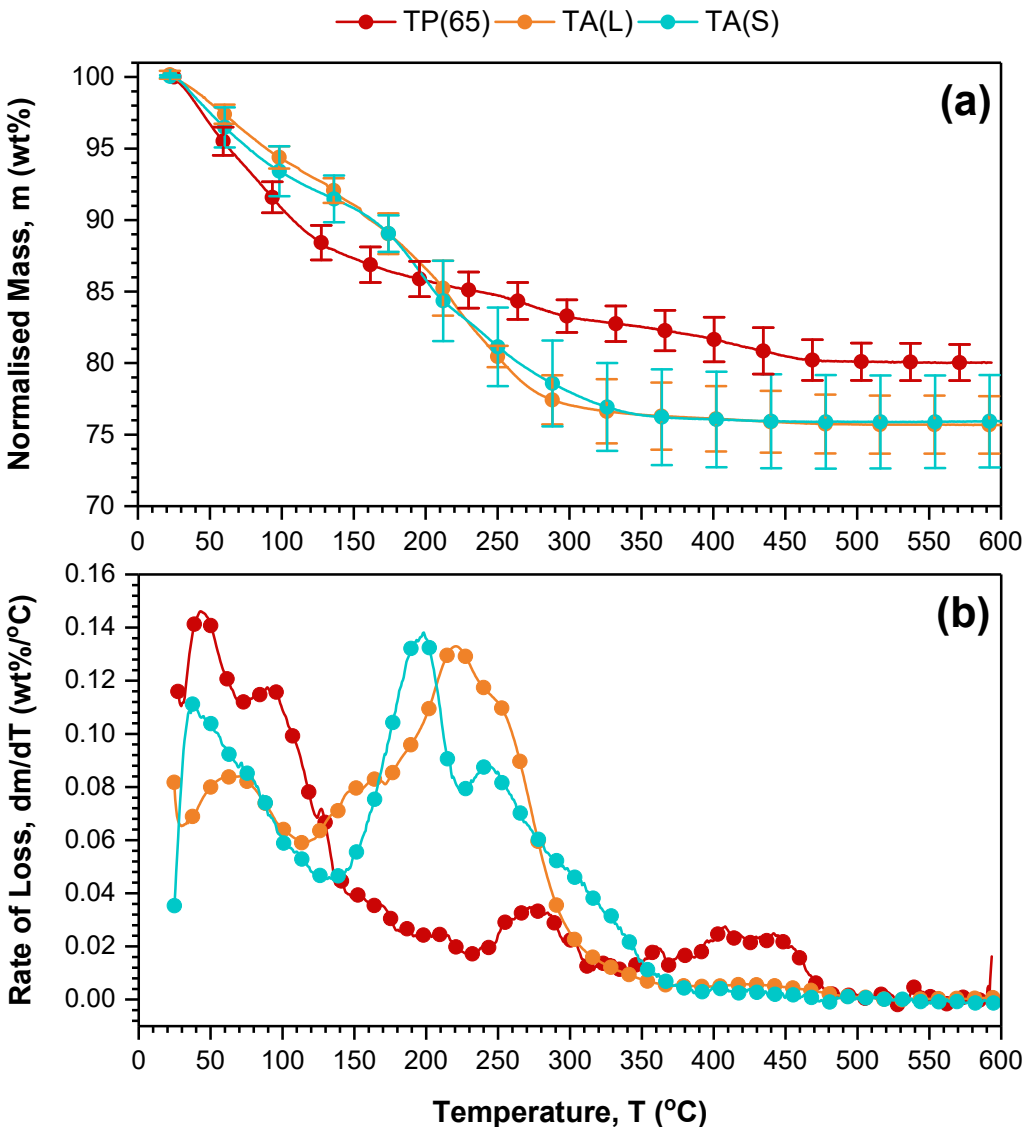

Figure 4.7: Non-isothermal (a) TGA and (b) DTG of synthesised titania materials. Analysis conducted with m = 2 mg, T = 25-600 °C, β = 5 °C/min, V̇ = 20 mL/min of N_2.

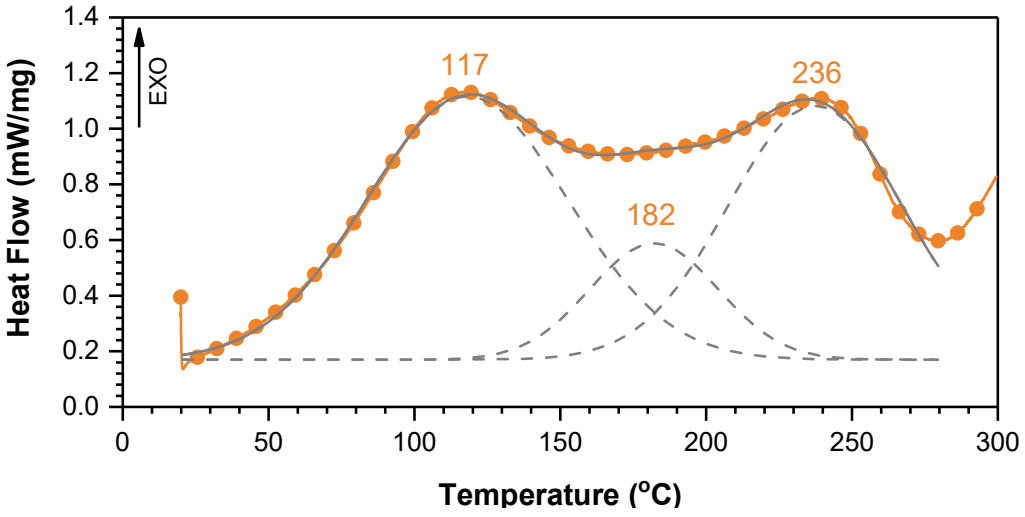

Figure 4.8: Non-isothermal DSC of TA(L), showing experimental data (●) and fitted curves (–). Analysed at m = 1-6 mg, T = 25-300 °C, β = 10 °C/min, V̇ = 20 mL/min of N_2

4.1.7 Discussion of Results

In summary, the experimental results gathered during this research generally point toward the successful preparation of titania materials with many advantageous properties. A comparison of TP(65), TA(L), TA(S) and TA(S,M) against similar titania materials reported in literature has been presented in Table 4.6 (the full account of which is in Table 2.5). As an indication of relative performance, the materials have been arranged in order of BET surface area (S_{BET}), however other properties have also been discussed.

Table 4.6: Selection of properties for titania materials synthesised during this research compared to similar materials in literature, as reviewed in Table 2.5.

Reference	Properties				
	Form[a] (P/M)	Phase[b] (-/A/B/R)	S_{BET} (m^2/g)	V_P (cm^3/g)	d_P (nm)
(Stengl, Bakardjieva and Szatmary, 2006)	P	-	1085	3.4	20-80
(Ayen *et al.*, 1988)	M	-	600-750	1.9-3.6	15-18
(Choi *et al.*, 2018)	P	-	590-685	1.7-2.4	11-16
TA(S,M) (This research)	**M**	**-**	**660**	**1.2**	**17**
(Campbell, Na and Ko, 1992)	P	-	650	2.1	2-10
(Sadrieyeh and Malekfar, 2017)	M	-	639	2.3	14
(Cerhová *et al.*, 2018)	M	-	634	-	-
TA(S) (This research)	**P**	**-**	**523**	**0.6**	**3.4, 30**
(Kong, Shen and Cui, 2013)	M	A	519	2.9	-
(Rafael *et al.*, 2015)	P	-	510	-	18
(Lermontov *et al.*, 2018)	M	-	>500	-	-
TA(L) (This research)	**P**	**-**	**450**	**0.2**	**3.4, 39**
(Zu *et al.*, 2015)	M	A	361	1.5	11
TP(65) (This research)	**P**	**-**	**328**	**0.2**	**3.9**
(Dagan and Tomkiewicz, 1994)	P	-	316	1.1	5.8
(Lv, Qin and Wei, 2013)	P	A	39-242	0.1-0.4	7-11
(Shimoyama *et al.*, 2010)	P	-	190	-	-
(Brown, Anderson and Carroll, 2012)	M	-	127-188	0.5-0.7	10-15
(Lermontov *et al.*, 2018)	M	-	150	-	-
(Desario *et al.*, 2019)	P	-	130-150	0.6	4-30
(Kong, Shen and Cui, 2014)	M	-	110	1.5	-
(Moussaoui, Elghniji and Elaloui, 2017)	P	A	89	-	-
(Wang and Lin, 2008)	P	A	76	-	-
(Raj and Viswanathan, 2009)	P	A,R	56	0.25	17.5

[a] Form: P = Particulate, M = Monolithic
[b] Phase: - = Amorphous, A = Anatase, B = Brookite, R = Rutile
[c] Properties: S_{BET} = BET Surface Area, V_P = Pore Volume, d_P = Average Pore Diameter

Examination of Table 4.6 showed the titania materials prepared during this research offered competitive performance to those previously reported, with the performance generally decreasing from TA(S,M) > TA(S) > TA(L) > TP(65). Overall, TA(S,M) was found to be comprised of irregular micron-sized particles (D_P = 6.1 μm) that exhibited excellent surface

properties. In particular, the calculated BET surface area (S_{BET} = 660 m^2/g) for this material was among the highest values reported, such as those by (Stengl, Bakardjieva and Szatmary, 2006), (Ayen *et al.*, 1988) and (Choi *et al.*, 2018). Furthermore, this material was predominantly mesoporous (65%) and exhibited a narrow distribution of mesopores (d_P = 17 nm) in good agreement with previously reported values (Ayen *et al.*, 1988)(Choi *et al.*, 2018). Given these notable properties, the pore volume calculated for this material (V = 1.2 cm^3/g) was relatively low, but nevertheless within the range previously reported. Thus, a minor contribution of this research is the procedure for the facile preparation of a mesoporous titania aerogel with highly competitive surface properties.

Alternatively, TA(S) and TA(L) were comprised of comparable particles (D_P = 6.7 and 7.0 μm), that offered reduced performance relative to TA(S,M). Nevertheless, the BET surface areas (S_{BET} = 523 and 450 m^2/g) exhibited by these materials were competitive compared to many of the reviewed materials. Regarding porosity, TA(S) and TA(L) predominantly exhibited micropores (55-85%), alongside a considerable fraction of mesopores (15-45%). These pores exhibited a bimodal distribution with smaller (d_P = 3.4 nm) and larger (d_P = 30 and 39 nm) diameters that were at the lower and upper limits of those previously reported (Campbell, Na and Ko, 1992)(Desario *et al.*, 2019). As before, the pore volumes for these materials (V_P = 0.6 and 0.2 cm^3/g) were unexpectedly lower than many of the aerogels reviewed in Table 4.6. In terms of composition, the presence of C-H vibrational modes assignable to $–CH_3$ groups coupled with mass loss between 25-115 ^oC evidenced residual amounts of iPrOH, accounting for mass loss of 8.5 wt% in TA(S) and TA(L). Similarly, additional Ti-O-C vibrational modes suggested these materials to contain unreacted Ti-iPr, which was accounted for mass loss of 11.4 wt% between 190-340 ^oC. Contrastingly, the absence of modes corresponding to C-O-C and $–CH_2$- supported the absence of THF within these materials. These findings were generally consistent with similar studies in literature (Vasconcelos et al., 2011) (Nolan, Seery and Pillai, 2009) (Qu *et al.*, 2010) (Calzada *et al.*, 2002).

The detection of O-H vibrations confirmed expectations of surface Ti-OH groups, however there was also evidence for COO^- vibrations that suggested the unexpected presence of surface carboxylates ($RCOO^-$). The reaction of M-OR and CO_2 to produce such species has been reported (Sakakura, Choi and Yasuda, 2007) (Palmer, 1983), meaning such vibrations could be explained by the presence of formate (R = H), acetate ($R = CH_3$) or bicarbonate (R = OH) groups deriving from Ti-iPr or Ti-OH (all of which exhibit highly similar COO^- vibrations). Based on reports by (Mino, Spoto and Ferrari, 2014), these bands were tentatively assigned to surface bicarbonates ($Ti\text{-}CO_3H$) in the bidentate bridging mode, which are proposed to form during solvent extraction by the mechanism in Figure 4.9 (Mino, Spoto and Ferrari, 2014). Similar formation of surface bicarbonates has been reported by exposure of TiO_2 to

H_2O and CO_2 (Henderson, 1998). On this basis, the surface Ti-OH and Ti-CO_3H groups were believed to account for mass loss of 4.1 wt% between 115-226 °C, with these temperatures in agreement with values of ~150 °C for similar species (Shafeeyan *et al.*, 2010). The formation of such species is reported for other titania materials where their preparation typically requires the inclusion of carboxylic acids (Nolan, Seery and Pillai, 2009) (Qu *et al.*, 2010) (Vasconcelos *et al.*, 2011), however is completely unreported for titania aerogels (as well as other aerogels composed of other metal oxides). Hence, this research is believed to report the first preparation of titania materials with carboxylate surface functionality by treatment of titania alcogels with liquid (LCO_2) and supercritical (SCO_2) carbon dioxide, without the explicit need for carboxylic additives. The convenient preparation of highly porous materials with highly functionalised surfaces will surely be of interest to a wide variety of applications.

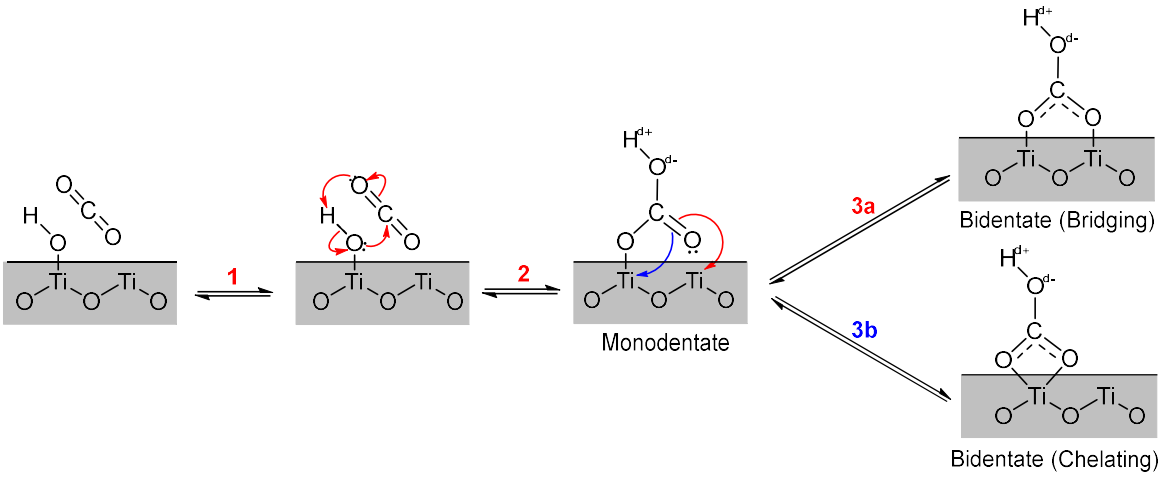

Figure 4.9: Proposed mechanism for the formation of carboxyl groups on the surface of titania aerogels during solvent extraction, namely (1) contacting of Ti-OH with LCO_2/SCO_2, (2) nucleophilic attack and rearrangement to form monodentate carboxylic, followed by (3) nucleophilic attack to form bidentate (a) bridging or (b) chelating bicarbonates. Proposed based on (Mino, Spoto and Ferrari, 2014)**.**

In contrast, these investigations found that TP(65) was made up of slightly smaller particles (D_P = 5.3 µm) that demonstrated somewhat reduced surface properties, most evident from the relatively low BET surface area (S_{BET} = 328 m^2/g) relative to the aforementioned aerogels. Nonetheless, this value was unexpectedly high and exceeded the values of several aerogels in Table 4.6 as well as other precipitated materials (*i.e. Degussa P25 Evonik*) (Raj and Viswanathan, 2009). The materials was overwhelmingly composed of micropores (95%) with only a small fraction of mesopores (d_P = 3.9 nm) and a low overall pore volume (V_P = 0.2 cm^3/g). Unlike the above, TP(65) only exhibited strong vibrational modes for O-H

vibrations associated with surface Ti-OH groups, with the absence of vibrations for C-H, COO^-, Ti-O-C, *etc.* Indeed the mass loss assignable to Ti-iPr was limited to 2.4 wt% between 230-340 °C, whereas the loss of surface Ti-OH accounted for 14.9 wt% between 25-230 °C and a further 2.5 wt% due to presumed crystallisation between 340-470 °C (Kurajica *et al.*, 2017). In general, the preparation of precipitated titania served as an adequate baseline material and was in agreement with the vast majority of similar materials reported in literature (Calzada *et al.*, 2002)(Moran et al., 1998) (Schneider and Baiker, 1997) (Montoya *et al.*, 1992).

Table 4.7: Statistical significance of results for the characterisation of titania materials

Comparison		Property	Effect	p value[a]	Difference
Effect of Preparation Method					
TP(65)	TA(L)	S_{BET}	Increase	0.044	Significant
TP(65)	TA(L)	V_P	None	0.535	Insignificant
TP(65)	TA(L)	d_P	Increase	-	Significant
TP(65)	TA(L)	D_P	Increase	0.027	Significant
TP(65)	TA(L)	dm	Increase	-	Significant
TP(65)	TA(L)	v(COO^-)	Increase	-	Significant
Effect of Extractant Conditions					
TA(L)	TA(S)	S_{BET}	None	0.087	Insignificant
TA(L)	TA(S)	V_P	Increase	0.001	Significant
TA(L)	TA(S)	d_P	Increase	-	Significant
TA(L)	TA(S)	D_P	None	0.809	Insignificant
TA(L)	TA(S)	dm	None	0.888	Insignificant
TA(L)	TA(S)	v(COO^-)	None	-	Insignificant
Effect of Monolith Preparation					
TA(S)	TA(S,M)	S_{BET}	Increase	0.027	Significant
TA(S)	TA(S,M)	V_P	Increase	0.020	Significant
TA(S)	TA(S,M)	d_P	Increase	-	Significant
TA(S)	TA(S,M)	D_P	None	0.239	Insignificant

[a] Absence of p value indicates t-test was not required or not applicable

Furthermore, in addition to establishing the materials synthesised during this research offered competitive performance, the experimental results were analysed to understand the effect of various preparation conditions toward achieving these properties. A summary of the statistical significance of these results has been presented in Table 4.7. Firstly, the effect of the aerogel and precipitate methods were evaluated by comparison of TP(65) and TA(L). Statistically significant increases were observed for surface area, pore diameter, particle diameter, as well as amounts of Ti-iPr and Ti-CO_3H, whereas insignificant changes were observed for pore volume. These results were directly attributed to the manner in which TA(L) was prepared. Firstly, the sub-stoichiometric quantity of H_2O during alcogel preparation (Ti-iPr:H_2O = 1:3.8 as opposed to 1:4) limited the rate and extent of hydrolysis of

Ti-iPr to Ti-OH (Dagan and Tomkiewicz, 1994). This allowed greater time for HNO_3 to catalyse condensation between Ti-OH and/or Ti-iPr, resulting in particle growth with a three-dimensional network of oxygen-bridged species (Ti-O-Ti) which was mostly preserved by solvent extraction with LCO_2 (Pajonk, 1991). Correspondingly, the properties of TP(65) were explained by the rapid hydrolysis of Ti-iPr in the vast excess of H_2O, which inhibited the formation of such a network and was further damaged by pore collapse during evaporative drying. This understanding was consistent with established literature (Aguado-Serrano and Rojas-Cervantes, 2006), and explained the significantly larger presence of unhydrolysed Ti-iPr in TA(L), as well as its relative absence in TP(65). Finally, the appearance of Ti-CO_3H groups in TA(L) by the mechanism proposed in Figure 4.9 was consistent with elevated reactivity of H_2O in LCO_2/SCO_2 (Mcgrail *et al.*, 2009), which also explained the absence of these groups in TP(65).

Unlike the above, a statistically insignificant difference was observed between the pore volumes of TP(65) and TA(L), which was supported by subsequent comparison of TA(L) and TA(S). Crucially, these materials showed insignificant difference in most of their properties, which suggested that LCO_2 and SCO_2 performed similarly during solvent extraction from TA(L) and TA(S) respectively. Nevertheless, TA(L) demonstrated significantly reduced pore volume and pore diameter compared to TA(S), mirroring observations in literature (Schneider and Baiker, 1997), which was attributed to the occurrence of capillary forces within LCO_2 causing partial pore collapse. One approximation is that the magnitude of capillary forces are linearly proportional to the surface tension (γ) (Berthier, 2013). Given that LCO_2 exhibits a considerably smaller surface tension ($\gamma \approx 0.57$ mN/m) (Jianxin and Yigang, 2009) compared to iPrOH/THF ($\gamma \approx 27$ mN/m) (Wohlfarth, 2016), this would estimate the magnitude of capillary forces as almost fifty times smaller. It is proposed that the magnitude of the forces when drying with LCO_2 were sufficient to cause partial collapse of the mesopores within TA(L), effecting less mesoporosity and reducing the total pore volume. However, their magnitude was insufficient to cause complete collapse and so TA(L) retained a relatively higher surface area compared to TP(65). This understanding also accounted for the significant increase in pore volume and mesoporosity of TA(S) since such capillary forces are entirely absent in the supercritical phase. As above, these results supported conventional knowledge in aerogel literature (Schneider and Baiker, 1997)(Pajonk, 1991) and reiterated the effect of extractant conditions on the incipient surface properties of the material.

Finally, the relative effects of the particulate and monolithic preparation methods were understood by comparison of TA(S) and TA(S,M), which showed statistically significant increases in surface area, pore volume and pore diameter for TA(S,M). Many authors report the preparation of particulate (Desario et al., 2019) (Choi et al., 2018) (Moussaoui, Elghniji

and Elaloui, 2017) and monolithic (Lermontov et al., 2018) (Cerhová et al., 2018) (Sadrieyeh and Malekfar, 2017) aerogels respectively . However, this research appears to be the first direct comparison of particulate and monolithic aerogels prepared under otherwise identical conditions. Hence, these results must have derived from the absence of stirring within the moulds of the monolithic samples during the condensation of Ti-OH and/or Ti-iPr species. It was conceived that condensation in the static solution occurred homogeneously throughout solution and proceeded growth of a network in all directions until linking with an adjacent network. This coupled with the understanding that alkoxides often proceed condensation with selective stereochemistry (Ng and Mccormick, 1996), meant the fundamental structure of TA(S,M) was uniformly determined relatively rapidly. This would explain the increased mesoporosity, narrow pore size distribution, large pore volume and high surface area of TA(S,M). This is in contrast to materials prepared by the particulate procedure, where convection of the suspended particles meant non-uniform condensation might have occurred over a longer duration and by random-branching kinetics (Ng and Mccormick, 1996). Furthermore, the disruptive action of the stirrer bar could have mechanically disrupted the formation of larger pores. Conceptually, these would explain the reduced mesoporosity and broader pore size distributions of TA(S) when compared to TA(S,M). These results require further examination, however the implication at this point is that better and more uniform surface properties can be realised within aerogel materials by monolithic preparation.

4.2 Characterisation of Bulk and Nanoconfined AB

Having characterised the synthesised titania materials, subsequent research examined their application toward nanoconfinement of AB within TA(L), according to the methods described in *3.2 Preparation of Titania Aerogels* and illustrated in Figure 3.1. Of the synthesised materials, TA(L) was selected since the conditions required for solvent extraction with LCO_2 have been found to reduce premature thermolysis of AB relative to SCO_2 (Rueda *et al.*, 2017). The following section presents the characterisation of bulk AB and nanoconfined AB/TA(L), with their subsequent comparison used to understand the effects of nanoconfinement.

4.2.1 Textural Properties

Initially, bulk AB and nanoconfined AB/TA(L) were studied by SEM in order to characterise the effect of the nanoconfinement on the surface texture of the particles. It was conceived that the infiltration of AB from THF within the pores of TA(L) might negatively affect textural properties due to mechanical stresses (*e.g.* growth of AB crystallites within the pores causing cracking). To investigate this, several micrographs were collected for bulk AB and AB/TA(L) at several magnifications (MAG = x200, x2,000 and x10,000) as presented in Figure 4.1(a)-(c) overleaf where they are compared to unloaded TA(L). During initial experiments it was discovered that uncoated AB was unstable under the observation conditions, which was resolved by ensuring samples were gold-coated.

Observation of Figure 4.10(a) at low magnification showed bulk AB to consist of micron-sized agglomerates composed of irregular particles with angular morphology, which suggested the AB was present in a crystalline phase. This was supported by examination at higher magnifications which showed the surface of bulk AB to be smooth and lacking macroporosity, consistent with a crystalline substance. Conversely, at low magnifications Figure 4.10(c) showed the particle morphology of nanoconfined AB/TA(L) was differed slightly from both bulk AB and TA(L). The micrographs appeared to show particles that exhibited rounded morphology compared to bulk AB and TA(L), which suggested the preparation used to prepare AB/TA(L) had indeed influenced the textural properties of the final particles. This can be further seen at higher magnifications, wherein the surface of AB/TA(L) appeared to exhibit characteristics between bulk AB and TA(L). The surface seemed to be comprised of a rough underlying texture on top of which a smoother layer was deposited, with these being attributed to TA(L) and precipitated AB respectively. This was explained by the intuitive precipitation of AB from solution not only within the pores of the incipient TA(L), but also across the entire external surface area of the particles during preparation.

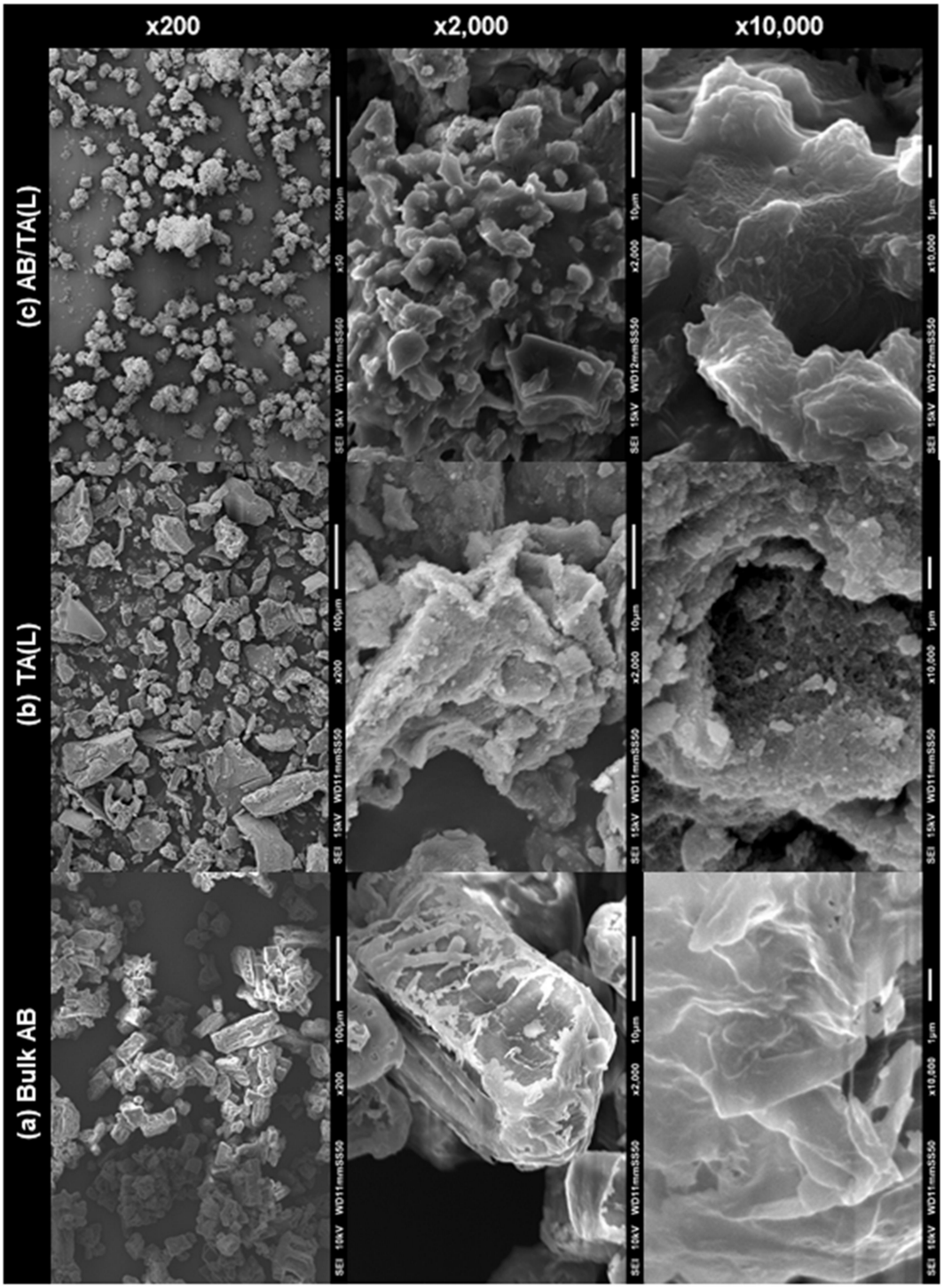

Figure 4.10: SEM micrographs of (a) bulk AB, (b) TA(L) and (c) AB/TA(L). Specimens gold-coated with a target thickness of 10-20 nm. Analyses at AV = 10-15 kV, SS = 50, WD = 11 mm, MAG = x200-x10,000.

4.2.2 **Particle Size Distribution**

Furthermore, similarly to discussion for textural analyses, the nanoconfinement of AB within TA(L) might have caused particle breakage and affected the particle size distribution of the incipient AB/TA(L). Hence analyses were conducted to determine the size distributions of bulk AB and nanoconfined AB/TA(L) for subsequent comparison to unloaded TA(L), as seen by the histograms in Figure 4.11(a)-(c). The distribution for bulk AB in Figure 4.11(a) exhibited a normal distribution in the higher micron range (D_P = 40-140 μm) in agreement

with previous studies (Lai *et al.*, 2012), whereas Figure 4.11(b)-(c) highlighted the similar profiles of AB/TA(L) and TA(L) within the same range (D_P =1-20 μm). As previously, these distributions were normalised and lognormal curves (Equation 4.2) fitted to these data, with the resulting fitting parameters summarised in Table 4.1 alongside corresponding values for TA(L). Statistical assessment was not required for the comparison of bulk AB due to its evident differences, however a t-test was required to establish the significance between AB/TA(L) and TA(L). Despite the apparent similarity of these materials, this comparison found AB/TA(L) exhibited a significantly ($p = 9.995 \times 10^{-6}$) smaller average diameter than TA(L), suggesting that nanoconfinement somehow affects particle size during preparation.

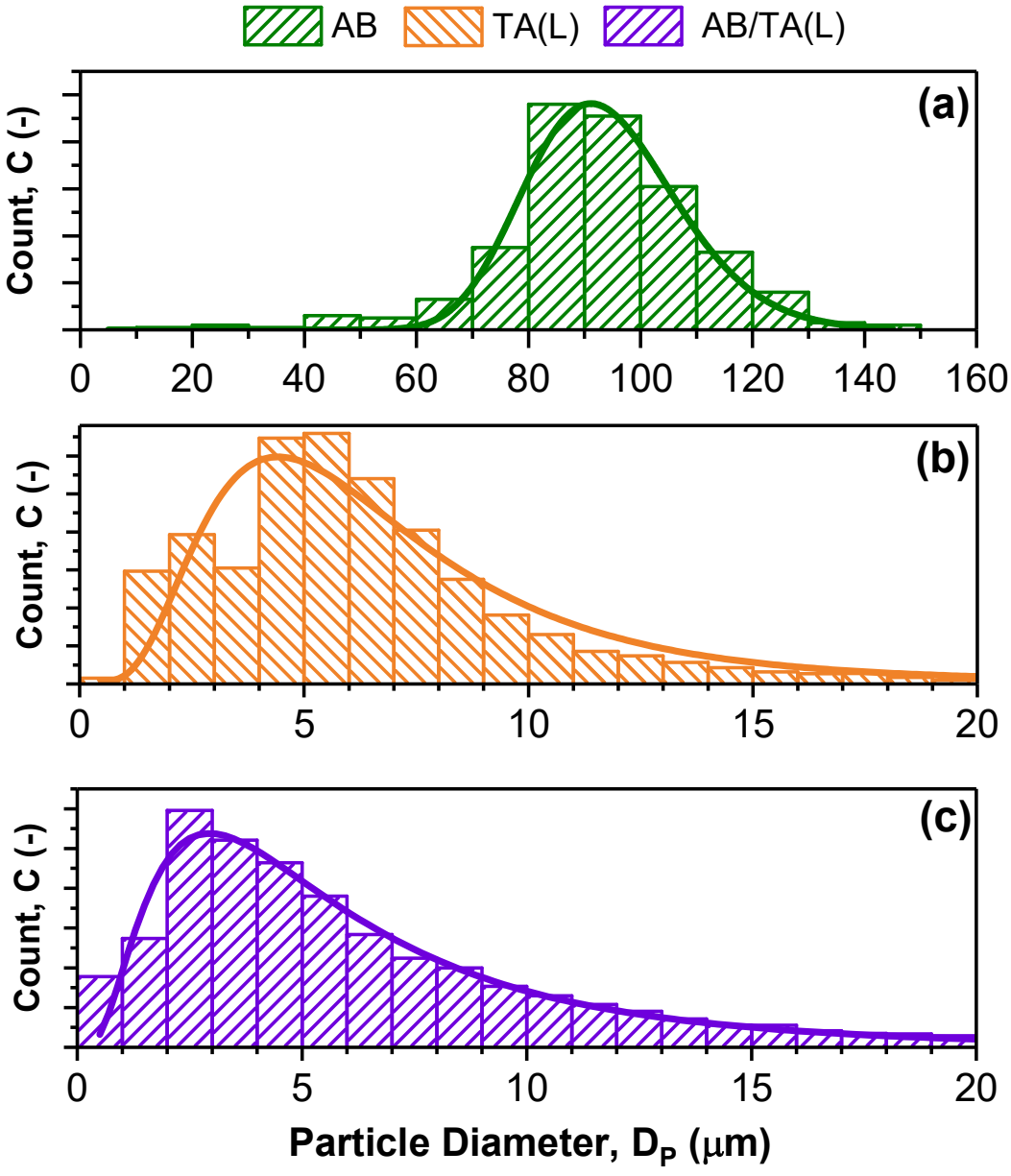

Figure 4.11: Particle size distribution of (a) bulk AB, (b) TA(L) and (c) AB/TA(L). Calculated diameters shown as histogram and lognormal fitting overlaid as curve.

Table 4.8: Fitting parameters for lognormal distribution curve applied to the particle size distributions of bulk AB, TA(L) and AB/TA(L), as illustrated in Figure 4.11(a)-(c).

Material[a]	Particle Diameter, D_P		Log Std Dev, w (-)	Area, A (-)	Std Dev, σ (-)	Fitting, R^2 (-)
	Centre	Mean				
AB	93.1 ± 0.7	94.1 ± 0.8	0.146	3,240	13.78	0.973
TA(L)	6.00 ± 0.16	6.99 ± 0.25	0.551	4,216	4.162	0.909
AB/TA(L)	5.15 ± 0.08	6.82 ± 0.16	0.748	7,857	5.906	0.971

[a] Analysis: Analysis conducted across a number of micrographs (n_M) with a total number of particles (n_P) where [AB; n_M = 3, n_P = 365], [TA(L); n_M = 5, n_P = 4,889], [AB/TA(L); n_M = 5, n_P = 8660]

4.2.3 Crystalline Properties

Analysis of the crystallinity has been used to study the nanoconfinement of AB, with fundamental changes being assigned to interaction with the support surface. In particular, several studies have reported diffraction peaks associated with the key intermediate diammoniate of diborane (DADB), leading to the suggesting that nanoconfinement of AB causes isomerisation to DADB (and thereby accelerates hydrogen release) (Rueda *et al.*, 2017) (Roy, Manna, *et al.*, 2018). Some of these also report diffraction peaks associated with polyaminoborane (PAB), which is suggested to be due to hydrogen release by formation of DADB and/or interaction with surface hydroxyls (Rueda *et al.*, 2017) (Moussa *et al.*, 2012). To explore this, the phase composition of bulk AB and nanoconfined AB/TA(L) were investigated using XRD, as detailed previously, with the results shown in Figure 4.12(a)-(b).

For bulk AB, the observation of strong diffraction peaks in Figure 4.12(a) evidenced a crystalline phase, with the pattern observed in excellent agreement with those widely reported in literature (*e.g.* ICDD = 00-013-0292), corresponding to a tetragonal, body-centred lattice with I4mm space group. The peaks measured at 2θ = 24.2, 24.5, 34.3, 35.6, 42.6, 43.4, 49.2, 50.2, 55.4 and 57.6° corresponded to the (110), (101), (200), (002), (121), (112), (220), (022), (130) and (013) planes (Demirci, 2017a). Additional peaks at 2θ = 66.9 and 68.7° were consistent with the reference pattern but have not been formally identified. This result confirmed the crystalline morphology observed in micrographs of bulk AB, as in Figure 4.10(a), with an estimated crystallite size of 20.3 nm by consideration of the (110) plane.

In contrast, the results for AB/TA(L) in Figure 4.12(b) showed extensive differences, evidencing change to AB during nanoconfinement within TA(L). Firstly, the sample showed comparatively weak diffraction peaks suggesting the phase composition was predominantly amorphous, which was further evidenced by the detection of several broad peaks at around 2θ = 28.3, 44.2 and 61.6°. These broad peaks were comparable to patterns reported for cyclic polyborazylene (PBZ), which has been reported to present broad peaks at approximately

2θ ≈ 22-26, 40-45, and 77-79° (Maleki *et al.*, 2016)(Zou *et al.*, 2014), (Moury *et al.*, 2012). On this basis, these peaks were assigned to the (002), (01) and (11) planes of amorphous PBZ. In addition to these, measurements also detected an assortment of sharp diffraction peaks at 2θ = 19.1, 23.8, 25.3, 25.4, 27.9, 29.1, 30.7, 33.5, 35.0, 37.6, 42.7 and 44.5° which indicated the presence of defined crystalline phases. The peaks at 2θ = 25.3 and 42.7° were in reasonable agreement with those exhibited by turbostratic boron nitride (tBN), which presents predominant peaks at 2θ = 25.5 and 42.4° (Zou *et al.*, 2014). Based on this presumption, these were assigned to the (200) and (100) planes of tBN respectively, with the crystallite size estimated as 11.4 nm based on the (200) plane. In terms of structure, tBN is characterised by sheets of cyclic boron nitride that exhibit two-dimensional order, but which are randomly cross-linked and thereby disordered in the third dimension (Salles and Bernard, 2016). This is in contrast to hexagonal boron nitride (hBN) which displays regular crosslinking between adjacent sheets, for which no evidence was found on Figure 4.12(b).

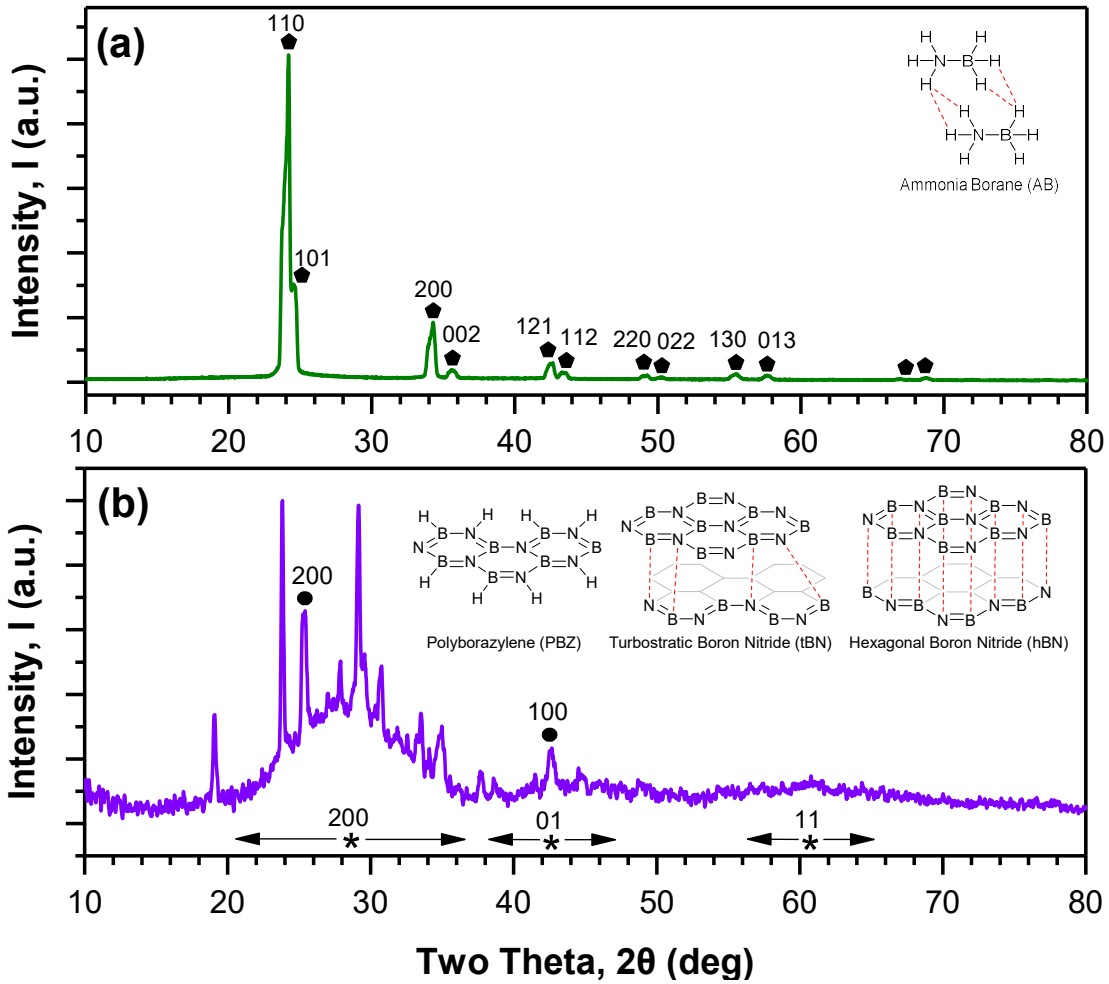

Figure 4.12: XRD patterns of (a) Bulk AB, and (b) AB/TA(L). Highlighted peaks are those assigned to the AB (⬟), PBZ (✱) and tBN (●) phases respectively.

The remainder of the diffraction peaks could not be assigned despite extensive comparison to reference databases against anticipated materials (*i.e.* those containing N, B, H, Ti, O and C). The unassigned peaks were not attributable to phase changes in TA(L) (*e.g.* TiO_2, Ti_2O_3, Ti_3O_5), previously reported changes to nanoconfined AB (*e.g.* PAB, DADB), or interactions between these components (*e.g.* TiB_x, TiN_x). It was speculated that these peaks might result from the formation of specific aminoborane polymers since even slight changes in structure have a pronounced effect on the diffraction pattern as is evidenced by comparison of AB, PAB and DADB (ICDD = 00-013-0292, 00-019-0419, and 00-017-0269 respectively).

4.2.4 **Chemical Composition**

As previously, the chemical composition of bulk AB and AB/TA(L) were evidently of interest to this research. Nanoconfinement has been found to alter AB and form a variety of products that result from dehydrogenation and/or interactions with the surface of the support even prior to thermolysis (Rueda *et al.*, 2017)(Moussa *et al.*, 2012)(Zhao *et al.*, 2010). Thus, measurements of the compositions of these materials can evaluate the types of chemical bonding present and so understand the effects of nanoconfinement. As such, analyses were conducted on these materials using FTIR spectroscopy by to previously detailed procedures, with the results presented in Figure 4.13(a)-(c) and summarised in Table 4.9.

The spectrum for bulk AB, as seen in Figure 4.13(a), exhibited bands between 3305-3244 cm^{-1} consistent with asymmetric and symmetric N-H stretching which were complemented by corresponding N-H bending modes at 1598 and 1374 cm^{-1}, together giving a strong indication for the $–NH_3$ moiety (Huang et al., 2014). Likewise, the opposing $–BH_3$ moiety was evidenced by bands appearing between 2372-2278 cm^{-1} that have been assigned to asymmetric and symmetric B-H stretching, as well as related bending modes at 1198 and 1157 cm^{-1} (Hess et al., 2008). Bonding between these moieties was suggested by bands at 1055 and 726 cm^{-1} indicative of N-B-H rocking modes, and bands at 799 cm^{-1} and 783 cm^{-1} for stretching in ^{10}B-N and ^{11}B-N respectively (Dillen and Verhoeven, 2003). Cumulatively, these bands provided confirmation for the composition of bulk AB closely resembled previous spectra reported in literature (Demirci, 2017a)(Frueh *et al.*, 2011). However, additional bands suggested a degree degradation and contamination. The bands and shoulder at 1556 and 1125 cm^{-1} have been previously assigned to N-H and B-H stretching in tetrahedrally bonded $–NH_2$ and $–BH_2$ (Frueh *et al.*, 2011), suggesting a portion of the AB had undergone premature thermolysis to PAB. Similarly, bands appearing at 1240 cm^{-1} and 878 cm^{-1} might correspond to asymmetric and symmetric C-O-C stretching that could indicate the presence of trace THF solvent (Jash, Meaux and Trenary, 2012). Nevertheless, the amount of these species proved to be inconsequential, as evidenced by subsequent TGA and MS analyses respectively.

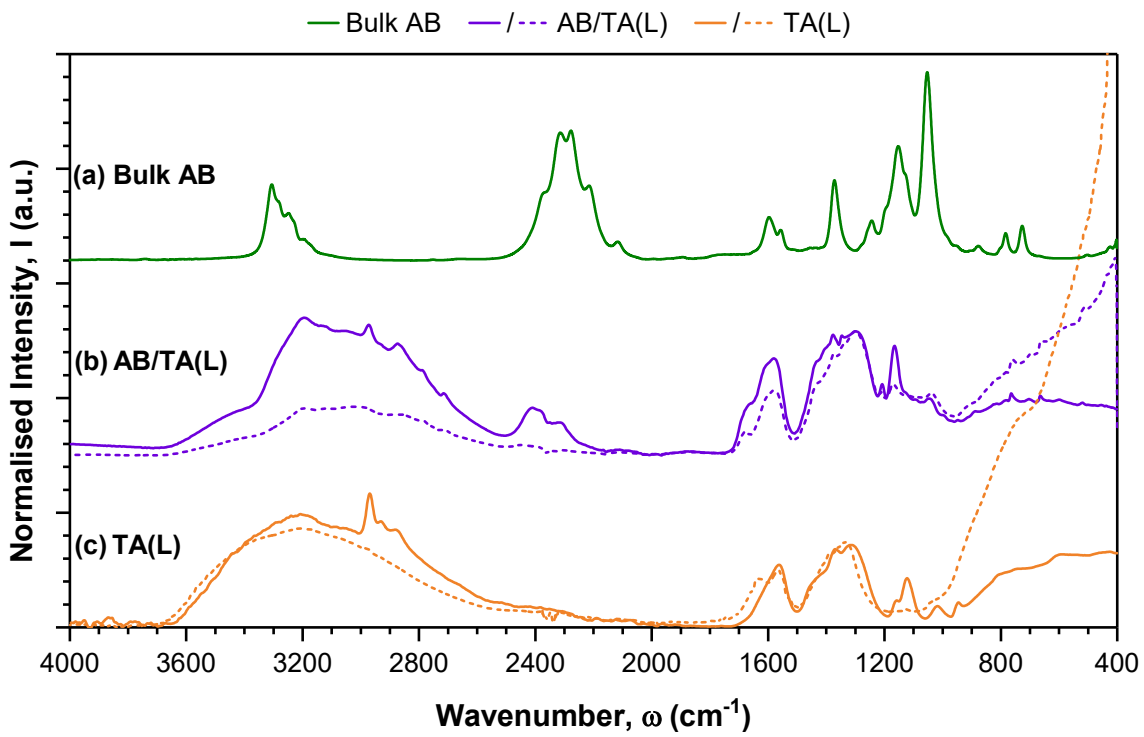

Figure 4.13: 1D-IR spectra of (a) Bulk AB, (b) AB/TA(L) and (c) TA(L) measured immediately after preparation (–) and after arbitrary storage duration (- -) (t ≈ 2 mo). Analysed at ω = 400-4000 cm^{-1}, R_S = 1 cm^{-1}, n_S = 256.

The spectrum for AB/TA(L) in Figure 4.13(b) appeared to exhibit a mixture of characteristics from the spectra of both bulk AB and TA(L). The majority of the bands arising from nanoconfined AB could not be confidently assigned due to substantial convolution with the underlying spectra of TA(L), particularly in the region between 1800-900 cm^{-1}. This was further complicated by the observation that the spectra for both TA(L) and AB/TA(L) changed over the course of storage. This has been illustrated on Figure 4.13(b)-(c) by comparison of the respective spectra immediately after preparation (solid line), compared to the spectra after an arbitrary storage duration (dashed line).

In the case of TA(L), Figure 4.13(c) showed bands assigned to C-H vibrational modes to disappear (namely 3000-2800 and 1400-1100 cm^{-1}) (Moran *et al.*, 1998) which suggested the continued hydrolysis of Ti-iPr and/or evaporation of iPrOH. This was accompanied by substantial growth in the region associated with Ti-O-Ti stretching (namely <1000 cm^{-1}) (Moran *et al.*, 1998), which suggested strengthening of the Ti-O-Ti network during storage. In contrast, the bands proposed to derive from surface carboxylates on TA(L) (namely 1563 and 1431 cm^{-1}) (Nolan, et al., 2009) exhibited insignificant change, which suggested these surface species were stable throughout storage. Regarding AB/TA(L), identical changes were observed for C-H and Ti-O-Ti vibrational modes, which could be attributed to the constituent TA(L). However, in addition to these AB/TA(L) exhibited substantial reductions for modes assignable to N-H and B-H stretching, which suggested the gradual release of hydrogen

during storage. Simultaneously, reductions were observed in the region (namely 1700-1300 cm^{-1}) (Nolan, et al., 2009) containing bands the aforementioned surface carboxylates. On one hand, this might be a convoluted N-H bending band from nanoconfined AB (Frueh *et al.*, 2011), but on the other, it could suggest the involvement of the surface carboxylates in the ambient temperature release of hydrogen.

To aid understanding and assignment of these bands, the normalised spectra for TA(L) was subtracted from that for AB/TA(L) in order to infer the isolated spectral features derived from nanoconfined AB, as seen in Figure 4.14. Subsequent deconvolution suggested possible bands centred at 3199, 2999 and 2797 cm^{-1}, as indicated by (i)-(iii). These could all be assigned to various modes of N-H stretching, with the downward shift in wavenumber relative to bulk AB explained in literature as weakening in the constituent N-H bonding (Rueda *et al.*, 2017). Deconvolution also identified potential bands centred at 2407 and 2305 cm^{-1}, as indicated by (iv)-(v), which might have been from B-H stretching, but contrastingly these modes were shifted upward relative to bulk AB, which suggested strengthening of the hypothesised constituent B-H bonds. Furthermore, if these bands were due to N-H and B-H stretching, an unexplained difference would be with regard to their relative amounts, where nanoconfined AB exhibited significantly less B-H stretching compared to bulk AB. This might be accounted for by considering interactions between nanoconfined AB and TA(L). The previously discussed band indicated by (i) at 3199 cm^{-1} could instead be assigned to B-OH stretching (Moon *et al.*, 2004), which would explain the relative absence of B-H stretching and suggest interactions of the nanoconfined AB with the TA(L) support before thermolysis (Rueda *et al.*, 2017).

Additionally, the deconvoluted bands centred at 1676 and 1595 cm^{-1} indicated by (vi) and (vii) might be upward shifted N-H bending and stretching in $-NH_3$ and $-NH_2$ respectively (Frueh *et al.*, 2011). The former is in partial agreement with the sharp band at 1167 cm^{-1} which is situated between the asymmetric and symmetric B-H bending modes of $-BH_3$, whereas the corresponding $-BH_2$ bands are notably absent at 1125 cm^{-1} (Frueh *et al.*, 2011). However, as introduced above, these bands might instead derive from B-O vibrational modes which have been reported to present between 1190-1460 cm^{-1} (Moon *et al.*, 2004). An interesting interpretation was based around the similarity of the bands at (vi) and (vii) to the C=O stretching and C-N-H bending modes of species with amide functionality (Barth, 2007), which might derive from the reaction between the $-NH_3$ moiety of AB and the surface carboxylates previously identified for TA(L). Such reactions have a strong basis in organic chemistry seen by the well-established dehydration reaction between NH_3 and carboxylic groups (RCOOH) to form the corresponding amide groups ($R\text{-}CONH_2$) (Shafeeyan *et al.*, 2010). Such a surface reaction might also explain the complex bands appearing between

1700-1300 cm^{-1} (Nolan, Seery and Pillai, 2009) which could result from changes to the carboxylate mode from bidentate bridging, to either bidentate chelating or monodentate modes (Nolan, Seery and Pillai, 2009). For easy comparison of bulk AB and nanoconfined AB/TA(L), all the above assignments and wavenumbers have been summarised in Table 4.9.

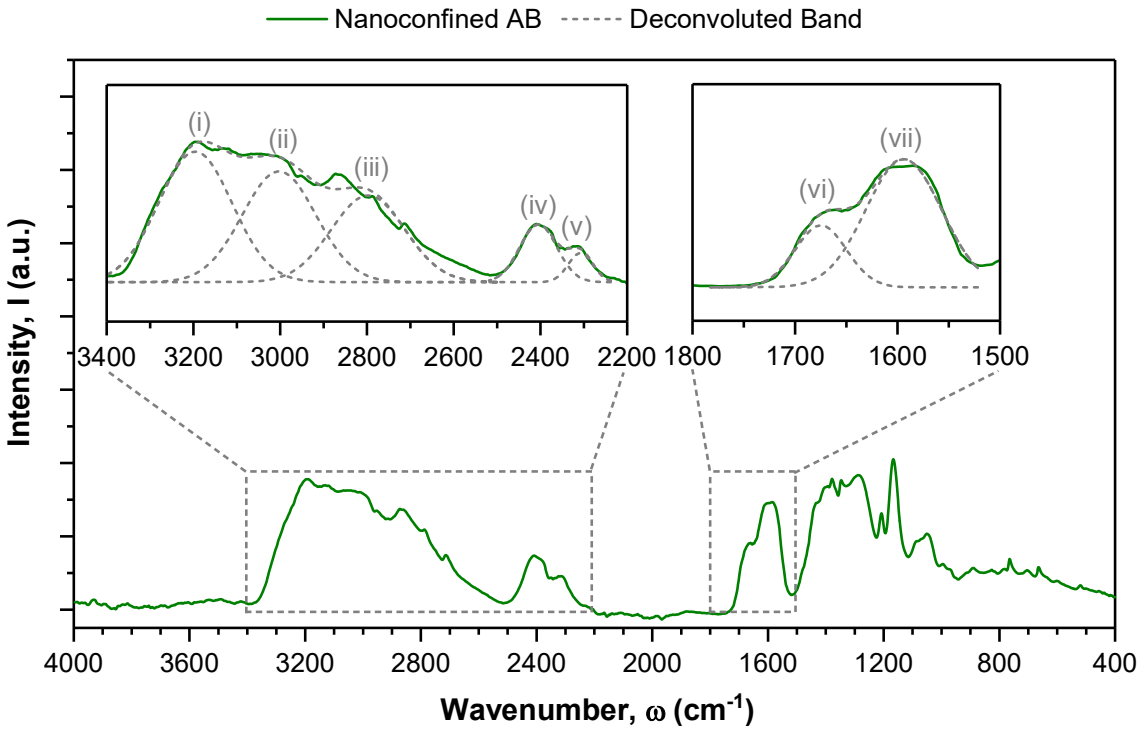

Figure 4.14: Inferred 1D-IR spectra of nanoconfined AB within TA(L). Spectrum inferred from subtraction of respective spectra from AB/TA(L) and TA(L) in Figure 4.13.

Table 4.9: 1D-IR spectra assignments for bulk AB and nanoconfined AB within TA(L)

Bulk AB				Nanoconfined AB			
Band / Character / Assignment ω (cm^{-1})			[Ref], ω (cm^{-1})	Band / Character / Assignment ω (cm^{-1})			[Ref], ω (cm^{-1})
3305	m	ν_{as}(N-H)	[1]-[4] 3406-3310	3199	s, br	ν(N-H)/ν(B-OH)	[1]-[4]/[5] 3220
3244	m	ν_{s}(N-H)	[2]-[4] 3248-3255	2999	s, br	ν(N-H)	[2]-[4]
2372	m	ν_{as}(B-H)	[2]-[4] 2373-2375	2797	s, br	ν(N-H)	[1]-[4]
2278	m	ν_{s}(B-H)	[1]-[4] 2272-2280	2407	m	ν(B-H)	[1]-[4]
1598	w	δ_{as}(N-H)	[2]-[4] 1596-1597	2305	m	ν(B-H)	[2]-[4]
1374	m, sh	δ_{s}(N-H)	[2]-[4] 1375-1377	1676	m	δ(N-H)/ν(C=O)	[6]1601 / [7]1650
1198	w	δ_{as}(B-H)	[1]-[4] 1167-1221	1595	m	ν(N-H)/δ(C-N-H)	[6]1556 / [7]1550
1157	m	δ_{s}(B-H)	[1]-[4] 1151-1161	1500-1287	-	Convoluted	-
1055	s, sh	ρ_{as}(N-B-H)	[2]-[4] 1058-1069	1208	w, sh	δ(B-H)	[2]-[4]
799	w	ν(^{10}B-N)	[2]-[4] 798-802	1167	m, sh	δ(B-H)	[2]-[4]
783	w, sh	ν(^{11}B-N)	[2]-[4] 782-787	1090-1050	-	Convoluted	-
726	w, sh	ρ_{as}(N-B-H)	[2]-[4] 726-728	-	-	-	-

[a] **Band Characteristic**: *s* = strong, *m* = medium, *w* = weak, *sh* = sharp, *br* = broad
[b] **Vibrational Mode**: ν_x = stretching, δ_x = bending, ρ_x = rocking, s = symmetrical, as = asymmetrical
[c] **Reference:** [1] (Dillen and Verhoeven, 2003) [2] (Custelcean and Dreger, 2003) [3] (Hess *et al.*, 2008)
[4] (Huang *et al.*, 2014) [5] (Moon *et al.*, 2004) [6] (Frueh *et al.*, 2011) [7] (Barth, 2007)

4.2.5 **Thermal Properties**

Necessarily, the thermal properties of bulk AB and AB/TA(L) are of critical importance for investigation of their thermolytic dehydrogenation. Specifically, mass losses and thermal events during heating would indicate the release of hydrogen and volatilised contaminants, with the extent and temperature of these releases providing insight into the reaction(s). As such, investigations were conducted using TGA/DTG and DSC, as seen in Figures 4.15(a)-(b) and Figure 4.16 respectively, with results summarised in Table 4.10.

In Figure 4.15(a)-(b), mass loss in bulk AB was observed to progress through two defined steps, ranging between 101-127 ^{o}C and 127-210 ^{o}C respectively. The onset and peak temperatures for the first step were 101 and 109 ^{o}C respectively, whereas for the second step these values were 144 and 162 ^{o}C. These steps resulted in respective mass losses of 17.1 and 28.3 wt%, corresponding to a total mass loss of 45.4 wt% and final sample mass of 54.7 wt%. Both mass losses were correlated with the previous reports for the evolution of hydrogen and gaseous contaminants from bulk AB (as reviewed previously in Table 2.3). Complementary DSC analysis in Figure 4.16 was in general agreement, with the profile dominated by two large exothermic events centred at 124 and 173 ^{o}C, attributed to the aforementioned mass losses (Kondrat'Ev *et al.*, 2015). The shift in temperatures was explained by the faster heating rate employed during these experiments. Additionally, bulk AB also exhibited two repeatable small exothermic events at approximately 99 and 113 ^{o}C that preceded the release of hydrogen and were not associated with mass loss, indicated as (i) and (ii) on Figure 4.16. A plausible interpretation is that the left-hand edge of the peak at (ii) is actually the onset of mass loss, meaning (ii) could be assigned to the endothermic melting of AB centred at 114 ^{o}C, in general agreement with literature (see Table 2.1) (Frueh *et al.*, 2011). This interpretation was validated by its duplicated repeatability (n_a = 2) and similar observations in literature, where the onset of release preceded melting (Baitalow *et al.*, 2006). Conversely, despite its own repeatability (n_a = 2), no definitive explanation could be offered for the event at (i), however its magnitude suggested a trace contaminant (Petit, Miele and Demirci, 2016).

The results for AB/TA(L) showed mass loss progressing through several broad and overlapping steps, comparable to the majority of profiles for nanoconfined AB materials reported in literature (Rueda *et al.*, 2017)(Moussa *et al.*, 2012)(Salameh *et al.*, 2018). Furthermore, the mass loss profile of AB/TA(L) in Figure 4.15(b) and Figure 4.16 appeared to consist of constituent peaks previously identified for TA(L) alongside additional peaks presumed to derive from nanoconfined AB. To avoid repeating previous discussion regarding mass loss in TA(L), the profiles for TA(L) were subtracted from the respective profiles for AB/TA(L) in order to isolate the inferred profiles for nanoconfined AB. These profiles have been presented in Figure 4.17(a)-(b) and Figure 4.18 accordingly.

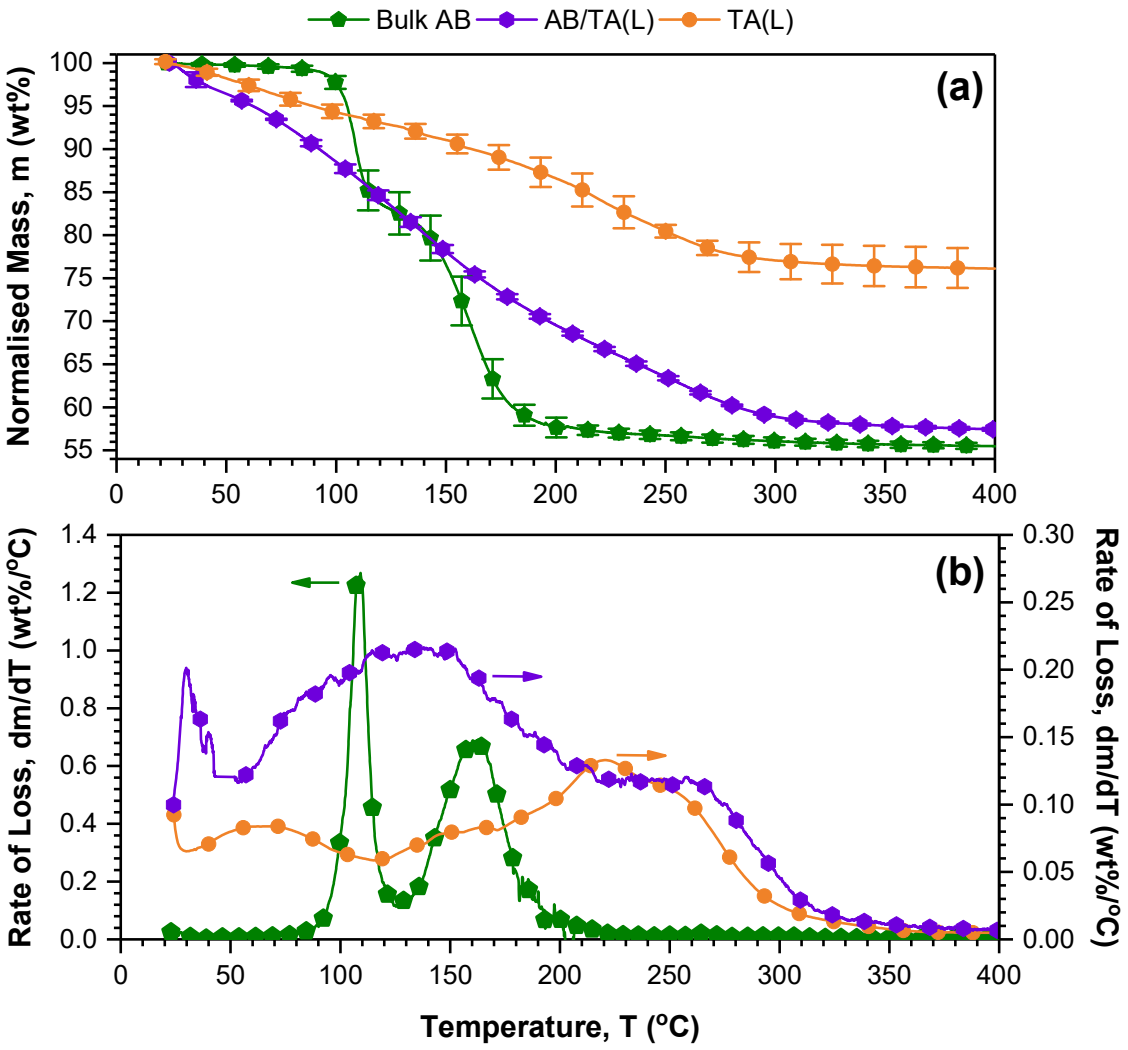

Figure 4.15: Non-isothermal (a) TGA and (b) DTG of bulk AB and AB/TA(L). Analysis conducted with m = 2 mg, T = 25-600 °C, β = 5 °C/min, $\dot{V}$ = 20 mL/min of N_2.

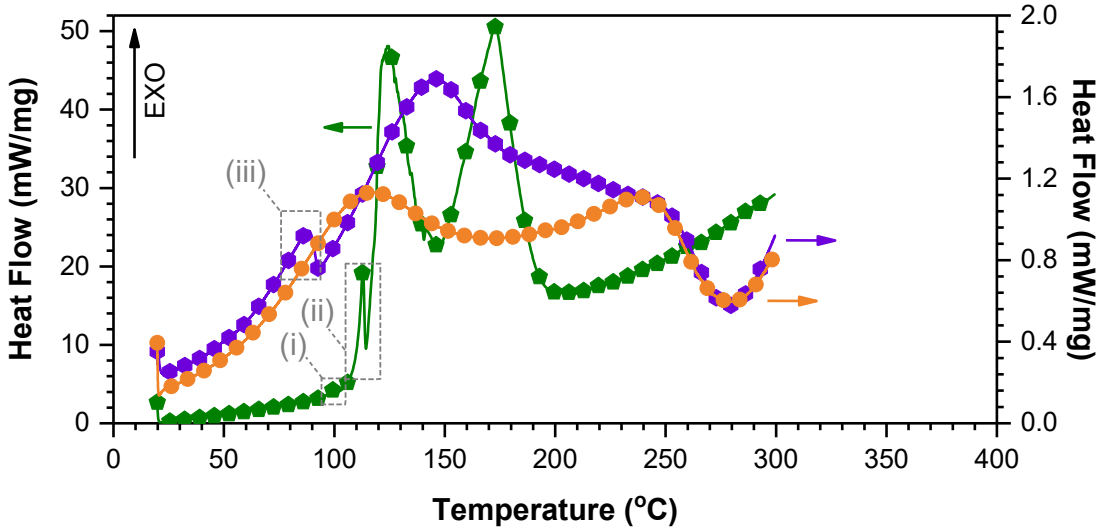

Figure 4.16: Non-isothermal DSC of bulk AB and AB/TA(L). Analysis conducted with m = 1-6 mg, T = 25-300 °C, β = 10 °C/min, $\dot{V}$ = 20 mL/min of N_2

Hence, Figure 4.17(b) appeared to show three mass losses associated with nanoconfined AB. These mass losses progressed between 25-53, 53-223 and 253-319 °C with respective peak temperatures of 29, 120 and 280 °C, in reasonable agreement with similar nanoconfined AB materials (Moussa *et al.*, 2012)(Lai *et al.*, 2012) (Gadipelli *et al.*, 2012). The corresponding mass loss for by each of these steps was 2.0, 15.1 and 1.4 wt%, which accounted for a total mass loss of 18.5 wt% and a final sample mass of 81.5 wt%. Having removed the contributions from TA(L), these mass losses were evidenced to be the release of hydrogen alongside other volatilised contaminants. In order for these inferred values to be meaningful they were compared to the corresponding values for AB/TA(L) at the same temperature ranges, which were evaluated as 3.9, 28.7 and 9.6 wt% respectively, with total loss and final mass of 42.2 and 57.8 wt%. Comparison of these values suggested the mass loss contributions from nanoconfined AB at these temperatures were approximately 51, 53 and 15% of the total mass loss in AB/TA(L). This evidenced that a considerable proportion of the mass loss in AB/TA(L) was derived from nanoconfined AB, particularly within the low temperature region (< 250 °C), however there also existed large amounts of other species.

These findings were generally supported by Figure 4.17(a) and Figure 4.18, which appeared to show three exothermic events that correlated with the aforementioned mass losses, occurring between 27-86, 96-241 and 241-278 °C with peak temperatures of 86, 146 and 259 °C. Interestingly, a pronounced endothermic peak was observed to onset and peak at 86 and 97 °C that was not associated with mass loss, indicated by (iii) on Figure 4.16 and Figure 4.18. As discussed for bulk AB, an endothermic event in this region could be explained by the melting of AB. If this is the case, the significant reduction in temperature relative to bulk AB suggests considerable disruption of the intermolecular dihydrogen bonds ($N\text{-}H^{\delta+}\cdots H^{\delta-}\text{-}B$) that usually stabilise AB (Kulkarni, 1999), thereby leading to a lower melting temperature.

Table 4.10: Thermal properties of bulk AB, TA(L), AB/TA(L) and nanoconfined AB

Material	Temperature, T (°C)			Mass, m (wt%)		
	Onset, T_o	Peak, T_p	Range, T	Loss, dm	Total Loss, dm_t	Final Mass, m_f
Bulk AB	101	109	101 - 127	17.1		
	144	162	127 - 210	28.3	45.4	54.6
TA(L)	25	66	25 – 115	8.4		
	115	161	115 - 190	4.0		
	190	220	190 – 340	11.7	24.1	75.9
AB/TA(L)	25	30	25 – 57	3.9		
	57	133	57 – 217	28.7		
	217	234	217 – 353	9.6	42.2	57.8
Nanoconfined AB[a]	25	29	25 - 53	2.0		
	53	120	53 - 213	15.1		
	253	280	252 - 329	1.4	18.5	81.5

[a] Nanoconfined AB: Inferred profile from subtraction of TA(L) from AB/TA(L)

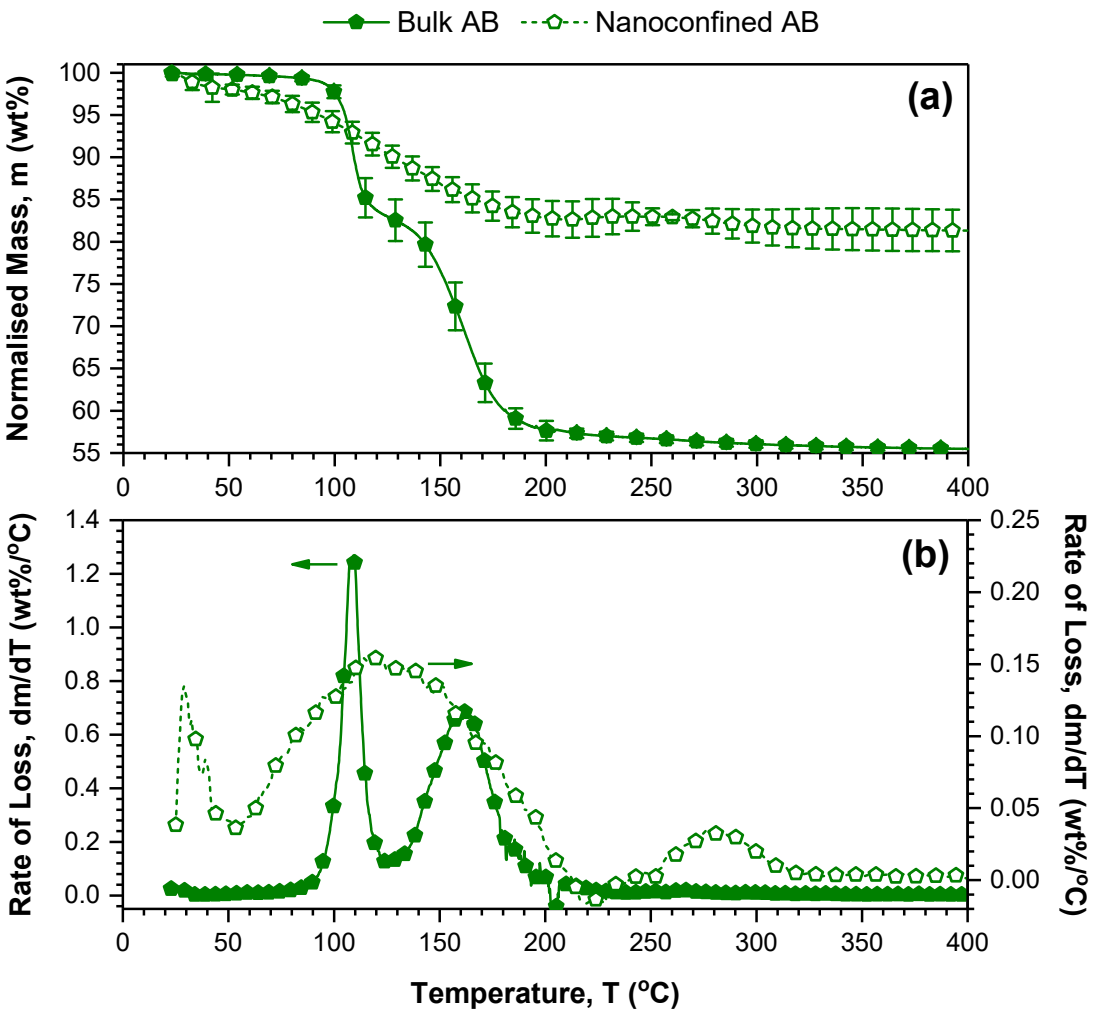

Figure 4.17: Inferred non-isothermal (a) TGA and (b) DTG of bulk and nanoconfined AB. Profile achieved by subtraction of AB/TA(L) and TA(L) profiles in Figure 4.15(a)-(b).

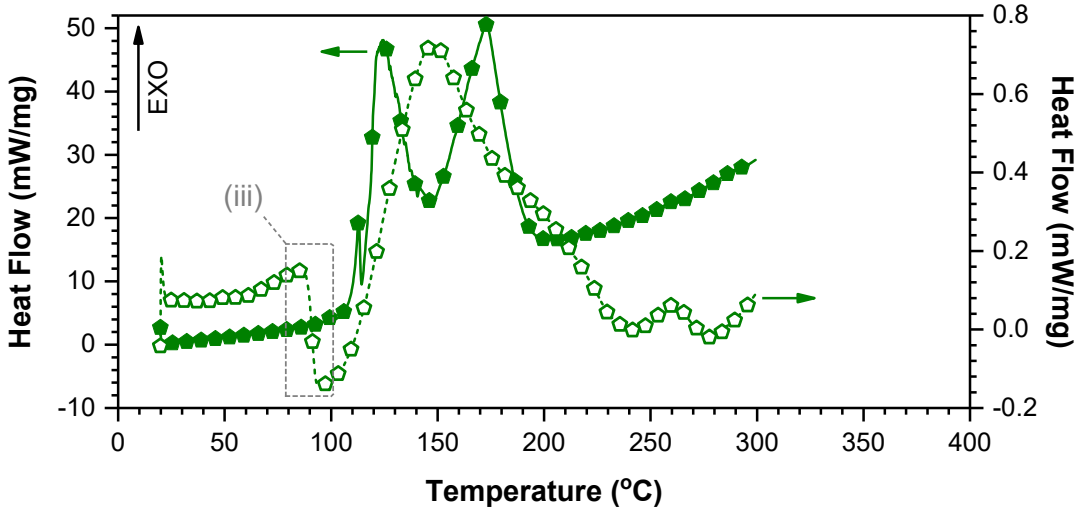

Figure 4.18: Inferred non-isothermal DSC of bulk and nanoconfined AB. Profile achieved by subtraction of AB/TA(L) and TA(L) profiles in Figure 4.16.

It was conceived that the preparation of AB/TA(L) had not achieved nanoconfinement and instead the above results were caused by precipitation of the AB from solution onto the external surface of TA(L), effectively resulting in modification of AB by solid-state doping. In order to confirm the previous observation, similar experiments were conducted with solid-state doping of bulk AB with TP(65) and TP(500). These mixtures were created with loadings of 20 and 60 wt% AB, which were thoroughly mixed with TP(65) and TP(500) immediately prior to analysis so as to avoid premature decomposition of AB. Mixtures with 60 wt% AB showed statistically insignificant difference ($p = 0.06$) to each other, which was believed due to insufficient contact between particles of AB and TP(65)/TP(500), meaning the samples behaved analogously to bulk AB. As such, these samples have not been discussed and have instead have been omitted for clarity. The results shown in Figure 4.19(a)-(b) compare the mass losses from bulk AB, nanoconfined AB/TA(L) and doped mixtures of AB-TP(65) and AB-TP(500) with a loading of 20 wt% AB.

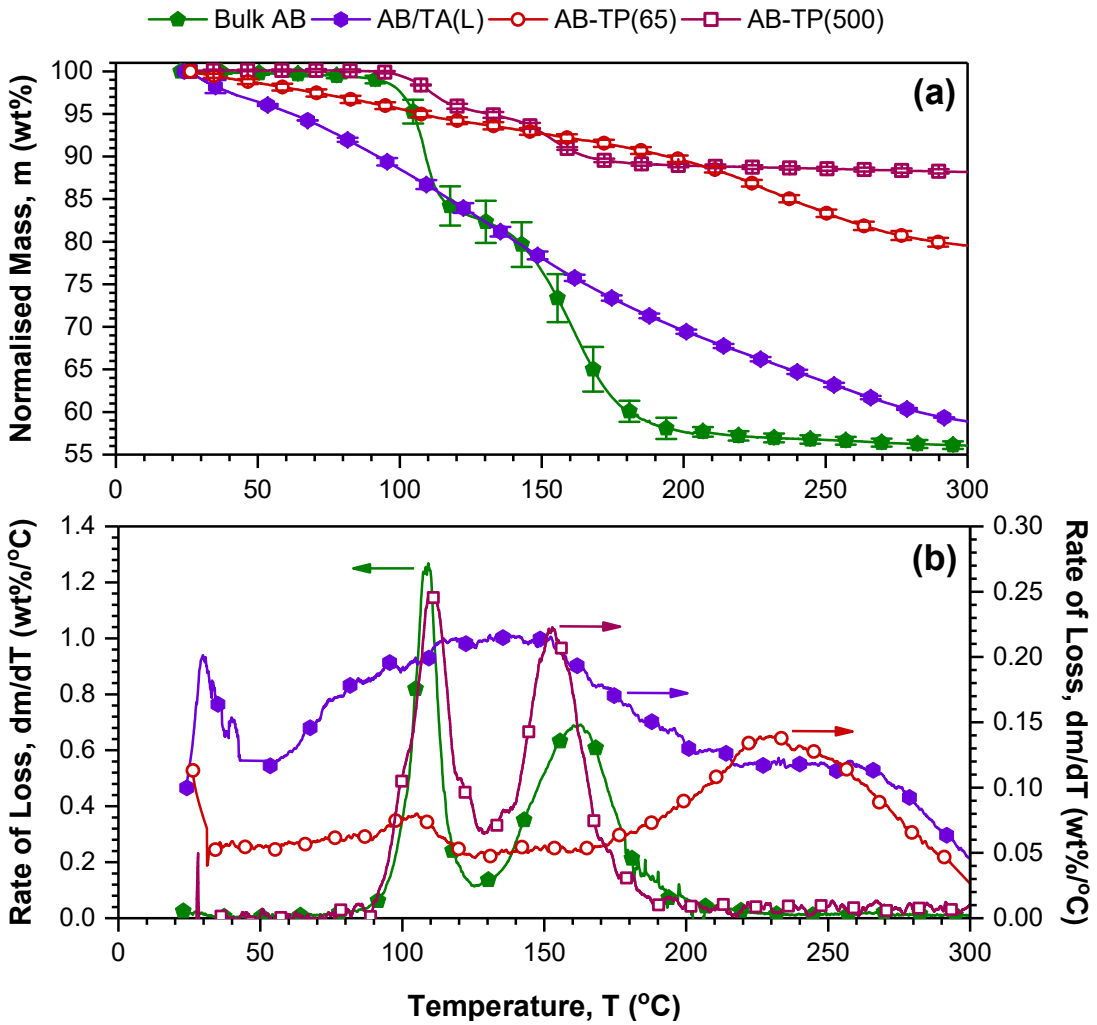

Figure 4.19: Non-isothermal (a) TGA and (b) DTG of AB-TP(65) and AB-TP(500) with 20 wt% AB loading compared to bulk AB and AB/TA(L). Analyses conducted with m = 2 mg, T = 25-300 °C, β = 5 °C/min, $\dot{V}$ = 20 mL/min of N_2.

The results showed extensive differences between the profiles for bulk, nanoconfined and doped AB. Not including the expected differences in magnitude, the mass loss from AB-TP(500) appeared to progress through two defined steps identically to bulk AB. In contrast, the profile for AB-TP(65) showed more gradual mass loss that was nonetheless evidently different from bulk AB, AB/TA(L) and AB-TP(500). No comparable results exist in literature for AB-TP(65), however the results for AB-TP(500) showed in good agreement with previously reported values (Komova *et al.*, 2011, 2013). On this basis, the nanoconfinement of AB within TA(L) evidenced to have occurred, and the previous results characterising AB/TA(L) were accepted as a consequence of nanoconfinement instead of solid-state doping.

4.2.6 **Volatilised Contaminants**

The thermolytic dehydrogenation of bulk AB and AB/TA(L) were then studied using mass spectrometry (MS), as described in *3.8 Mass Spectrometry*, which allowed evaluation of the relative quantities of hydrogen and contaminant species. For these analyses, several mass-to-charge (m/z) values were monitored (m/z = 2, 4, 17, 18, 27, 31 and 80) which corresponded to measurement of H_2^+, He^+, NH_3^+, H_2O^+, $B_2H_6^+$, OCH_3^+ and $B_3N_3H_6^+$ fragments respectively (Babenko *et al.*, 2017)(Wood *et al.*, 2017)(NIST, 2019). These were attributed to the molecular ion peaks of H_2, He, NH_3, H_2O, DB and BZ, with the OCH_3^+ fragment highly indicative of iPrOH, THF and/or Ti-iPr. The absence of THF was evidenced by the FTIR analyses (Figure 4.6) and so was not considered during these analyses. The selected fragments are widely examined in literature, *e.g.* (Li, Zhu, et al., 2010) (Roy, Manna, et al., 2018). Furthermore, distinction between iPrOH and Ti-iPr was not possible (since the hydrolysis of Ti-iPr yields iPrOH), and so the detection of $OCH_3^+$was entirely attributed to iPrOH (NIST, 2019). Deconvolution of the fragment intensities (I_n, where n = m/z) to calculate the partial pressure (P_i) for each species was by consideration of the relative fragmentation intensity (RFI) and relative sensitivity (RS) values reported in Table 3.2 (Equations 4.3-4.9).

$$P_{He} = I_4 \quad \textbf{4.3}$$

$$P_{H_2} = I_2 - \left(\frac{0.02}{100} I_4\right) \quad \textbf{4.4}$$

$$P_{NH_3} = I_{17} - \left(\frac{26}{100} P_{H_2O}\right) - \left(\frac{0.625}{100} P_{iPrOH}\right) \quad \textbf{4.5}$$

$$P_{H_2O} = I_{18} - \left(\frac{6.3}{100} P_{NH_3}\right) - \left(\frac{0.670}{100} P_{iPrOH}\right) \quad \textbf{4.6}$$

$$P_{DB} = \left(\frac{100}{97.60}\right)\left(I_{27} - \frac{5.63}{100} P_{iPrOH}\right) \quad \textbf{4.7}$$

$$P_{iPrOH} = \left(\frac{100}{24.76}\right) I_{31} \quad \textbf{4.8}$$

$$P_{BZ} = I_{80} \quad \textbf{4.9}$$

Results from these analyses have been presented for bulk AB and nanoconfined AB/TA(L) in Figure 4.11(a)-(f), with each dataset normalised and presented individually to clearly show their respective profiles. The numbers on the figure indicate the peak temperature for each release, with this information summarised in Table 4.11. In the absence of heating, Figure 4.20 showed that bulk AB was stable under the analysis conditions as indicated by the absence of signals prior to heating ($t \leq 0$). Nevertheless, thermolytic dehydrogenation was induced upon heating, as seen by the appearance of multiple release profiles. Figure 4.20(a) showed the onset for evolution of H_2 was at approximately 101 ^{o}C, with the release profile then progressing through two distinct steps peaking at 107 and 152 ^{o}C, which corresponded to 64.3 and 35.7% of the released H_2 respectively. Figure 4.20(d) showed a similar trend for DB which exhibited onset and peak temperatures at approximately 89, 97 and 158 ^{o}C, with the amount of DB released being 55.8 and 44.2% at the respective peaks. Contrastingly, Figure 4.20(b) and (f) showed the release profiles of NH_3 and BZ exhibited dissimilar profiles to H_2, with release at relatively higher temperatures. In the case of NH_3, Figure 4.20(b) showed the onset of release to be 140 ^{o}C, with subsequent release peaking at 167 ^{o}C. The profile appeared to show the onset of a second release at approximately 238 ^{o}C, which could not be resolved before the completion of the analysis at 321 ^{o}C. The amount of NH_3 evolved during these two steps was 52.9 and 47.1% respectively. For BZ, Figure 4.20(f) showed the onset of release to be 123 ^{o}C with the entire release occurring with a single peak at 161 ^{o}C. Unexpectedly, Figure 4.20(c) appeared to show the unintuitive release of H_2O correlating with the dehydrogenation of AB, characterised by the onset of release at 100 ^{o}C with 32.4 and 67.6% of the released H_2O occurring at 107 and 161 ^{o}C respectively. Finally, the expected absence of change in Figure 4.20(e) suggested residual iPrOH was not present within bulk AB, which confirmed that any signal in subsequent measurements for nanoconfined AB/TA(L) must derive from TA(L).

As such, AB/TA(L) then was studied by identical procedures which highlighted considerable differences compared to bulk AB, also presented in Figure 4.20(a)-(f) respectively. Importantly, the release profiles of AB/TA(L) indicated instability under the flow of carrier gas at ambient temperature. This was evident from the observed volatilisation of many species prior to heating ($t \leq 0$), namely H_2, NH_3, H_2O DB, and iPrOH. Nevertheless, release at ambient temperature did not account for the entirety of release, and further volatilisation was induced upon heating. Figure 4.20(a) showed the detected profile for H_2 exhibited two onsets for release at 18 and 85 ^{o}C with the second release peaking at 186 ^{o}C, accounting for 58.6 and 41.4% of release respectively. Similarly unstable were NH_3 and DB, as seen in Figure 4.20(b) and (d), which also exhibited onset of release at 18 ^{o}C, however the release profiles of these species were distinct from that demonstrated by H_2. The release of NH_3 increased steadily until peaking at approximately 80 ^{o}C, after which the signal was apparently

sustained for the duration of experimentation until 301 °C. For DB this release showed a comparable trend, which was nevertheless subdued at lower temperatures and peaked at 180 °C before subsequently decreasing. Examination of Figures 4.20(c) and (e) showed the profiles for H_2O and iPrOH to show considerable similarity, with the onset of release for both species at 18 °C and release characterised by a single release across a broad temperature range (peaking at 49 and 32 °C respectively). Finally, Figure 4.20(f) showed the absence of a release profile for BZ with the measurements below detectable limits across the entire temperature range, which suggested a lack of volatilisation of this species.

Table 4.11: Non-isothermal MS analyses of a selection of species volatilised during thermolytic dehydrogenation of bulk AB and nanoconfined AB/TA(L)

Species	Temperature[a], T (°C)			Release, R[a]	Quantity, Q[b]
	Onset, T_o	Peak, T_P	Range, T	(%)	(vol%)
Bulk AB					
H_2	101	107	101-130	64.3	96.4
	130	152	130-201	35.7	
NH_3	140	167	140-238	52.9	2.5
	238	321	238-321	47.1	
H_2O	100	107	100-129	32.4	1.0
	129	161	129-239	67.6	
DB	89	97	89-110	58.6	0.01
	126	158	126-185	41.4	
iPrOH	n.d	n.d	n.d	n.d	n.d
BZ	123	161	123-211	100	0.04
Nanoconfined AB/TA(L)					
H_2	18	18	18	58.6	17.2
	85	186	85 - 301	41.4	
NH_3	18	78	18 - 301	100	55.2
H_2O	18	51	18 - 301	100	15.3
DB	18	177	18 - 301	100	10.9
iPrOH	18	32	18 - 301	100	1.4
BZ	n.d.	n.d.	n.d.	n.d.	n.d

[a] Temperature: n.d. = not detected
[b] Release: Percentage of total release associated with each peak
[c] Quantity: Volume percentage of species relative to all measured species

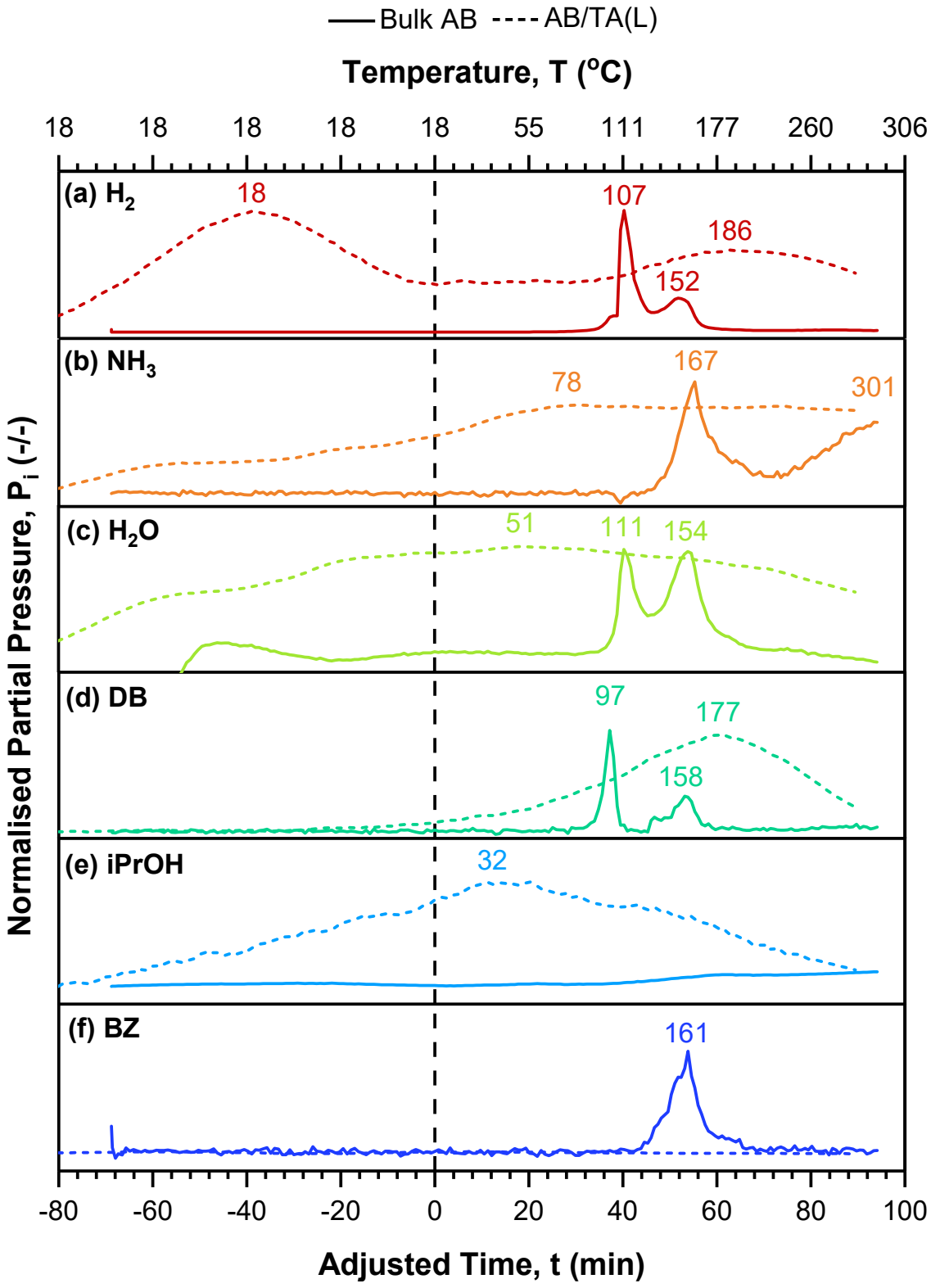

Figure 4.20: MS analyses showing several volatilised species during non-isothermal thermolytic dehydrogenation of bulk AB (–) and nanoconfined AB/TA(L) (- -), namely (a) H_2, (b) NH_3, (c) H_2O, (d) DB, (e) THF and (f) BZ. Adjusted time indicates onset of heating (t = 0).

The relative and absolute quantities of these species were estimated by integration of the peaks in Figure 4.20(a)-(f) against their respective baselines, with the relative quantities summarised in Table 4.11 and the absolute quantities presented in Figure 4.21. These results showed the thermolytic dehydrogenation of bulk AB to predominantly release H_2 (96.4 vol%) with relatively small amounts of NH_3 (2.5 vol%) and H_2O (1.0 vol%), as well as trace amounts of DB (0.01 vol%) and BZ (0.04 vol%). In comparison, identical calculations for AB/TA(L) suggested the sample released a significantly reduced fraction of H_2 (17.2 vol%) contaminated by remarkable quantities of NH_3 (55.2 vol%), and significant amounts of H_2O (15.5 vol%), DB (10.9 vol%), and iPrOH (1.4 vol%). These changes were also reflected in the absolute quantities of these volatilised species, as illustrated in Figure 4.21. This was principally observed for H_2, where the quantity released by AB/TA(L) was approximately two order of my magnitude less than that by bulk AB. In contrast, AB/TA(L) volatilised roughly equivalent amounts of NH_3 and H_2O, as well as an order of magnitude more DB. These trends were magnified when the release from AB/TA(L) was normalised to the amount of nanoconfined AB within TA(L) (*i.e.* torr/mg_{AB} instead of torr/$mg_{AB/TA(L)}$), thereby accounting for the additional mass of TA(L). On this basis, nanoconfined AB volatilised remarkably more NH_3, DB and to a lesser degree H_2O.

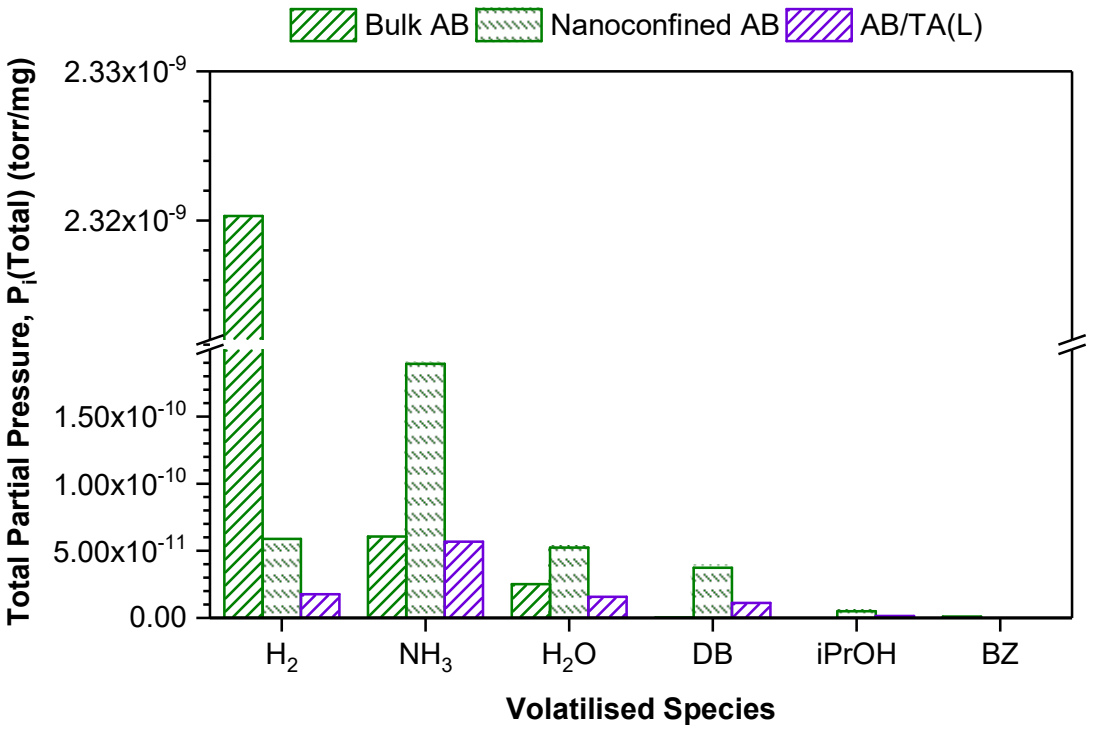

Figure 4.21: Total quantity of volatilised species for bulk AB, AB/TA(L) and inferred amount for nanoconfined AB. Calculated from integration of the respective release profiles across the entire temperature range.

4.2.7 **Isothermal & Non-Isothermal Release Kinetics**

To investigate the release kinetics of bulk AB and nanoconfined AB/TA(L), a series of isothermal and non-isothermal TGA experiments were conducted the procedures for which are detailed in *3.5.3 Non-Isothermal Analyses* and *3.5.4 Isothermal Analyses* respectively . Due to their long duration, these experiments were not repeated (n_a = 1), however isotherms at 80 °C were repeated (n_a = 3) to observe repeatability. The experimental data were adapted to show the fractional conversion (α) such that the data was represented from $0 \leq \alpha \leq 1$. The data can be seen as the scatter points in Figure 4.22(a)-(d). Figure 4.22 showed sigmoidal release profile from bulk AB with the rate accelerated at elevated temperatures. The data was well represented by nucleation and growth models, with particularly good likeness shown by the Avrami-Erofeev model (Equation 4.10). Application of this model to release from bulk AB has been extensively reported in literature (Bowden and Autrey, 2011)(Gangal and Sharma, 2013), where the critical nucleation event is believed to be the initial formation of DADB from which further polymerisation of PAB/PIB occurs, as detailed in Figure 2.4 and/or Figure 2.5.

$$\alpha = 1 - e^{-(kt)^n} \qquad \textbf{4.10}$$

$$n = \Psi + \Gamma \qquad \textbf{4.11}$$

The Avrami-Erofeev model relies on several assumptions including that; (i) nucleation occurs randomly and homogeneously, (ii) the growth rate is not a function of conversion, and (iii) growth occurs in all directions. With these, the model (Equation 4.10) describes the reaction in terms of fractional conversion (α), rate constant (k) and characteristic Avrami exponent (n). The Avrami exponent can be further expressed as contributions from the dimensionality of growth (Ψ) and the nucleation process (Γ) (Equation 4.11). The dimensionality of growth takes an integer value ($\Psi = 1$, 2 or 3) corresponding to the number of growth dimensions. The nucleation process may take any value ($0 \leq \Gamma \leq 1$) corresponding to the speed of nucleation, ranging from instantaneous nucleation from pre-formed nuclei ($\Gamma = 0$) to rate-limiting nucleation ($\Gamma = 1$). Thus, the Avrami-Erofeev model can be used to describe one- ($1 < n < 2$), two- ($2 < n < 3$), and three-dimensional ($3 < n < 4$) growth respectively. This model was subsequently fitted to the experimental data using the *Non-Linear Curve Fitting* functionality within *OriginPro 2017* with four different fitting scenarios explored. Three scenarios examined idealised rate-limiting nucleation in one-, two- and three-dimensions ($\Gamma = 1$, $\Psi = 1, 2, 3$) resulting in fixed values of Avrami exponent ($n = 2, 3, 4$), with the rate constant as the sole fitting variable. For the fourth scenario, the assumption of rate-limiting nucleation was neglected, leaving both the rate constant and the Avrami exponent as fitting variables. The profiles for these scenarios can be seen as the fitted curves in Figure 4.22(a)-(d) respectively, with a summary of the converged fitting variables given in Table 4.12.

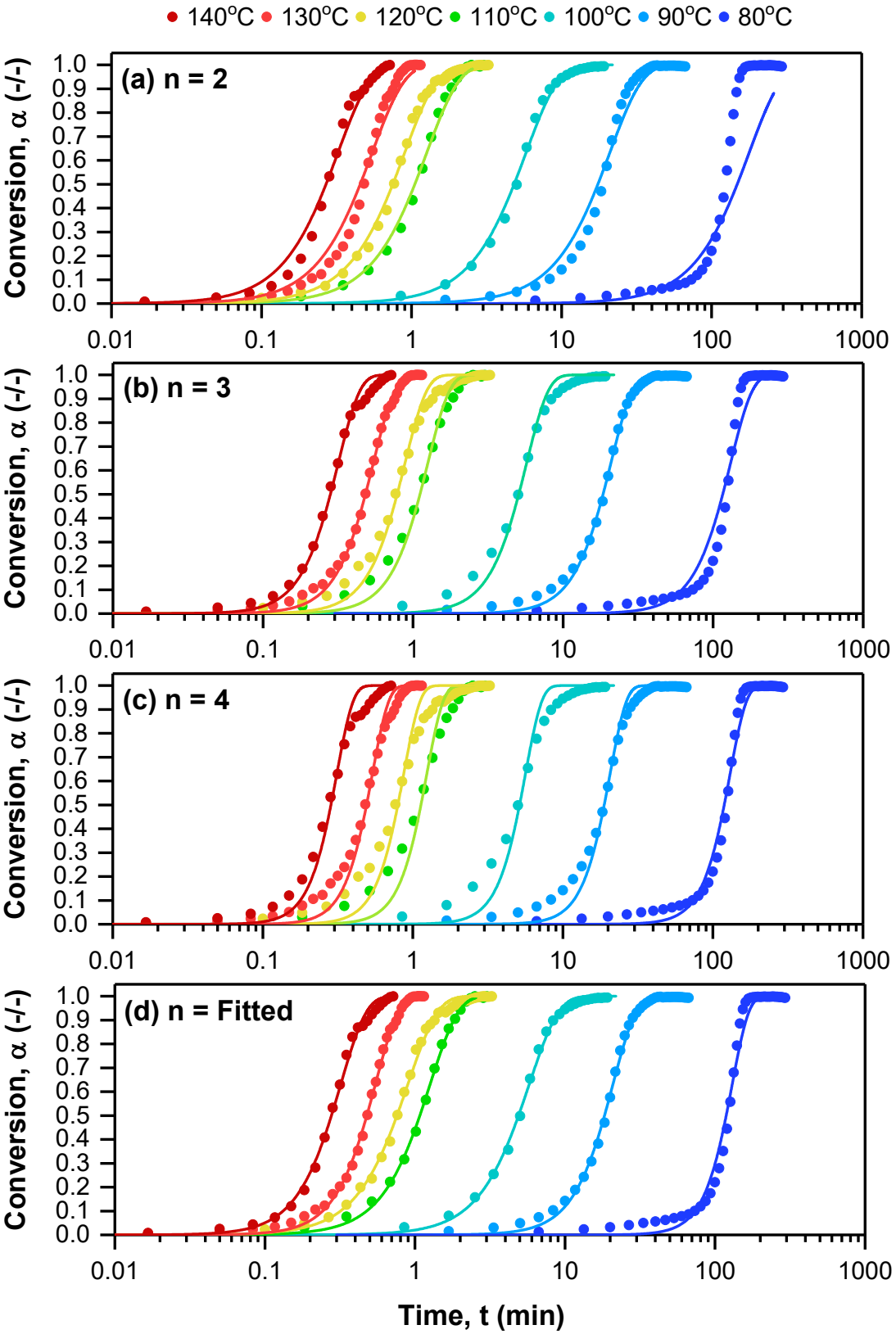

Figure 4.22: Isothermal TGA analyses showing the thermolytic dehydrogenation for bulk AB between 80-140 °C, with experimental data (•) and fitted Avrami-Erofeev models (–) including (a) n = 2, (b) n = 3, (c) n = 4, and (d) n = Fitted.

Table 4.12: Fitting parameters for Avrami-Erofeev model applied to isothermal thermolytic dehydrogenation of bulk AB between 80-140 °C, seen in Figure 4.22(a)-(d).

Parameter	Temperature (°C)						
	80	90	100	110	120	130	140
(a) n = 2							
k	0.008	0.048	0.173	0.792	1.109	1.830	3.095
R^2	0.924	0.980	0.997	0.995	0.996	0.980	0.988
(b) n = 3							
k	0.008	0.048	0.175	0.796	1.129	1.838	3.148
R^2	0.974	0.997	0.989	0.987	0.986	0.997	0.993
(c) n = 4							
k	0.008	0.048	0.177	0.806	1.149	1.857	3.209
R^2	0.991	0.983	0.969	0.956	0.964	0.982	0.976
(d) n = Fitted							
n	3.94	2.80	2.21	2.31	2.17	2.77	2.54
Ψ	3.00	2.00	2.00	2.00	2.00	2.00	2.00
Γ	0.94	0.80	0.21	0.31	0.17	0.77	0.54
k	0.008	0.048	0.173	0.792	1.112	1.837	3.114
R^2	0.990	0.997	0.998	0.999	0.997	0.998	0.996

[a] Convergence: Convergence achieved for all fittings, within a chi squared tolerance of $1x10^{-9}$

Calculation of the apparent activation energy (E_a) by the Arrhenius Method using the rate constant fitted during three scenarios (n = 2, 3, 4) can be seen in Figure 4.23(a). An analysis of the fourth scenario (n = Fitted) was not pursued since the inclusion of the exponent as a fitting variable necessarily affected the fitted rate constant, with this effect varied throughout experiments at different temperatures (making any subsequent analysis meaningless). The data in Figure 4.23(a) clearly showed a strong linear trend ($R^2 \geq 0.979$), with all fitting scenarios appearing to show the reaction of bulk AB to exhibit two distinct regions occupying the temperature ranges between 80-110 °C and 110-140 °C, indicated by (i) and (ii) respectively. In the first region between 80-110 °C, the calculated values of E_a were 171 ± 7, 171 ± 7, and 128 ± 5 kJ/mol for scenarios of n = 2, 3 and 4 respectively, whereas in the second region between 110-140 °C these values were 60 ± 5, 61 ± 5 and 45 ± 4 kJ/mol. These values are summarised at the end of this section in Table 4.14 with all other calculated values of E_a for bulk AB and nanoconfined AB/TA(L). These findings were compared with similar calculations by the Isoconversional Method, which instead utilised the fitted dataset (n = Fitted) as they most closely represented the experimental data. Since the Isoconversional Method is a so-called "model free" method (Gangal and Sharma, 2013), the technique is insensitive to model-specific issues and instead simply benefits from the best fitted data. The results from this analysis between α = 0.1-0.9 has been shown in Figure 4.23(b) (only shown for α = 0.1 and 0.9 for clarity), where the strong linearity of the data was apparent ($R^2 \geq 0.97$). Again, the dehydrogenation of bulk AB was exhibited distinct values of E_a in the aforementioned ranges. In the lower temperature region, the average value was calculated as 176 ± 11 kJ/mol whereas in the higher region the average value was 59 ± 5 kJ/mol.

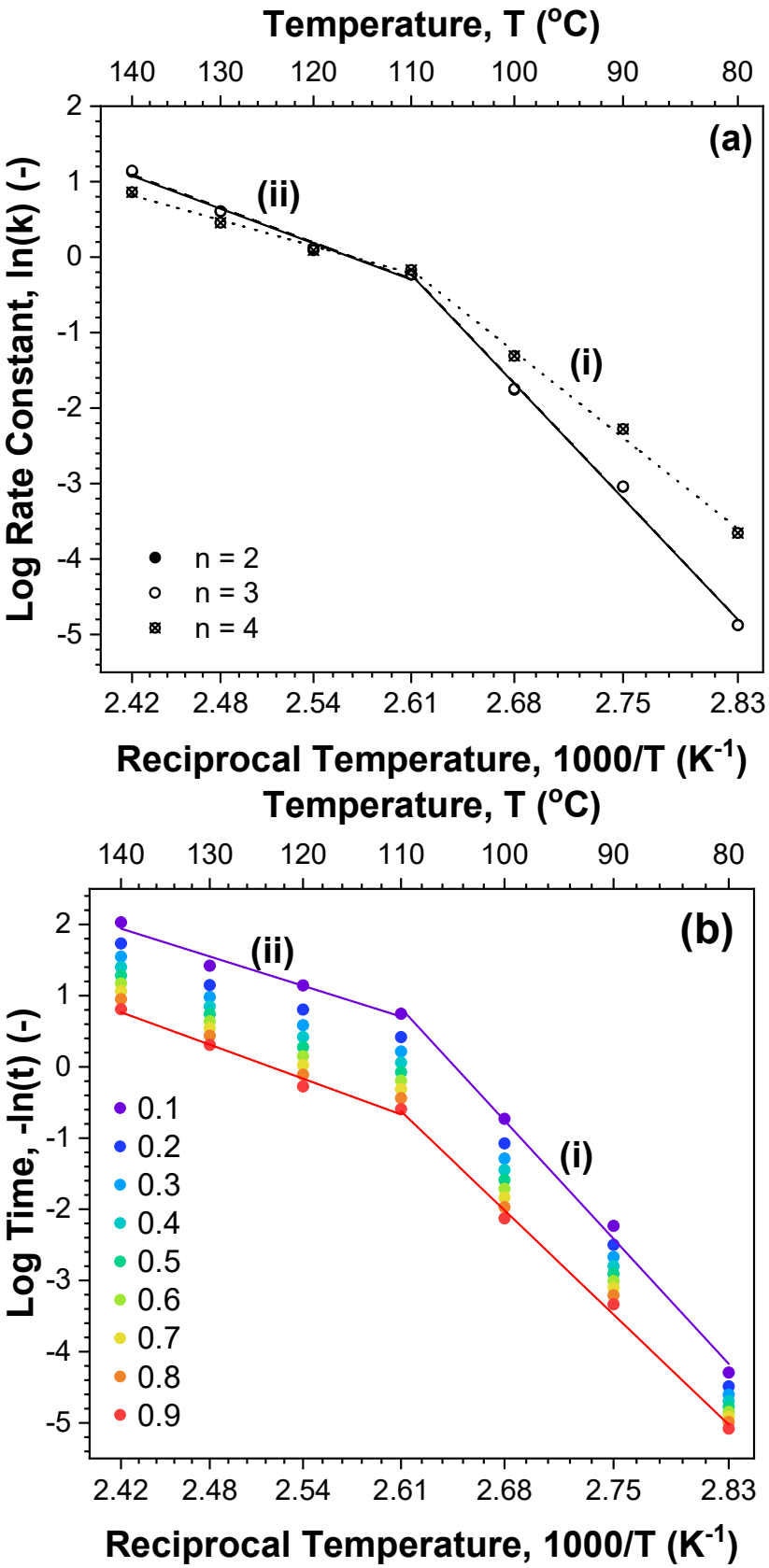

Figure 4.23: Calculation of activation energy for dehydrogenation of bulk AB with a fitted Avrami-Erofeev model by (a) Arrhenius plot with fitted value of rate constant for three Avrami exponents (n = 2, 3, 4), and (b) Isoconversional plot for a fitted Avrami exponent (n = Fitted) between α = 0.1 to 0.9. Note: For (a) the data and linear plots for n = 2 and n = 3 are practically coincidental.

To complement these isothermal analyses, a series of non-isothermal TGA experiments were conducted for the thermolytic dehydrogenation of bulk AB with a variety of fixed heating rates (β = 2-20 °C/min), as detailed in *3.5.3 Non-Isothermal Analyses*. The results from these analyses have been presented in Figure 4.15(a)-(b), showing the TGA and DTG profiles respectively. Note that analyses were repeated three times (n_a = 3) at each heating rate with the mean average profile shown, although error bars have been omitted for visual clarity. The identification of peak temperatures (T_P) from the respective DTG profiles in Figure 4.15(b) facilitated the Kissinger Method and subsequent plotting of Figure 4.24(a)-(b).

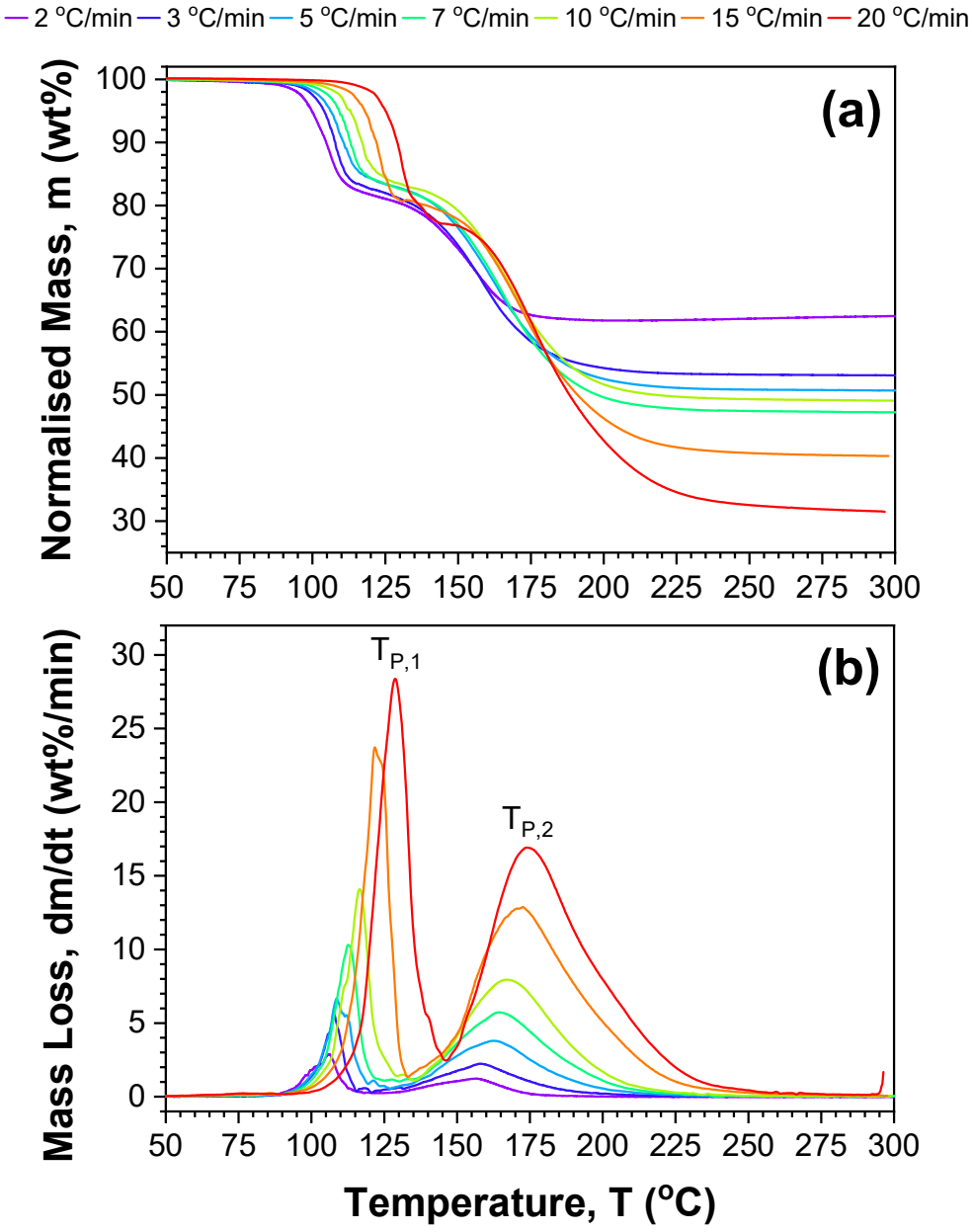

Figure 4.15: Non-isothermal (a) TGA and (b) DTG of the thermolytic dehydrogenation of bulk AB with fixed heating rates of 2-20 °C/min between 25-300 °C

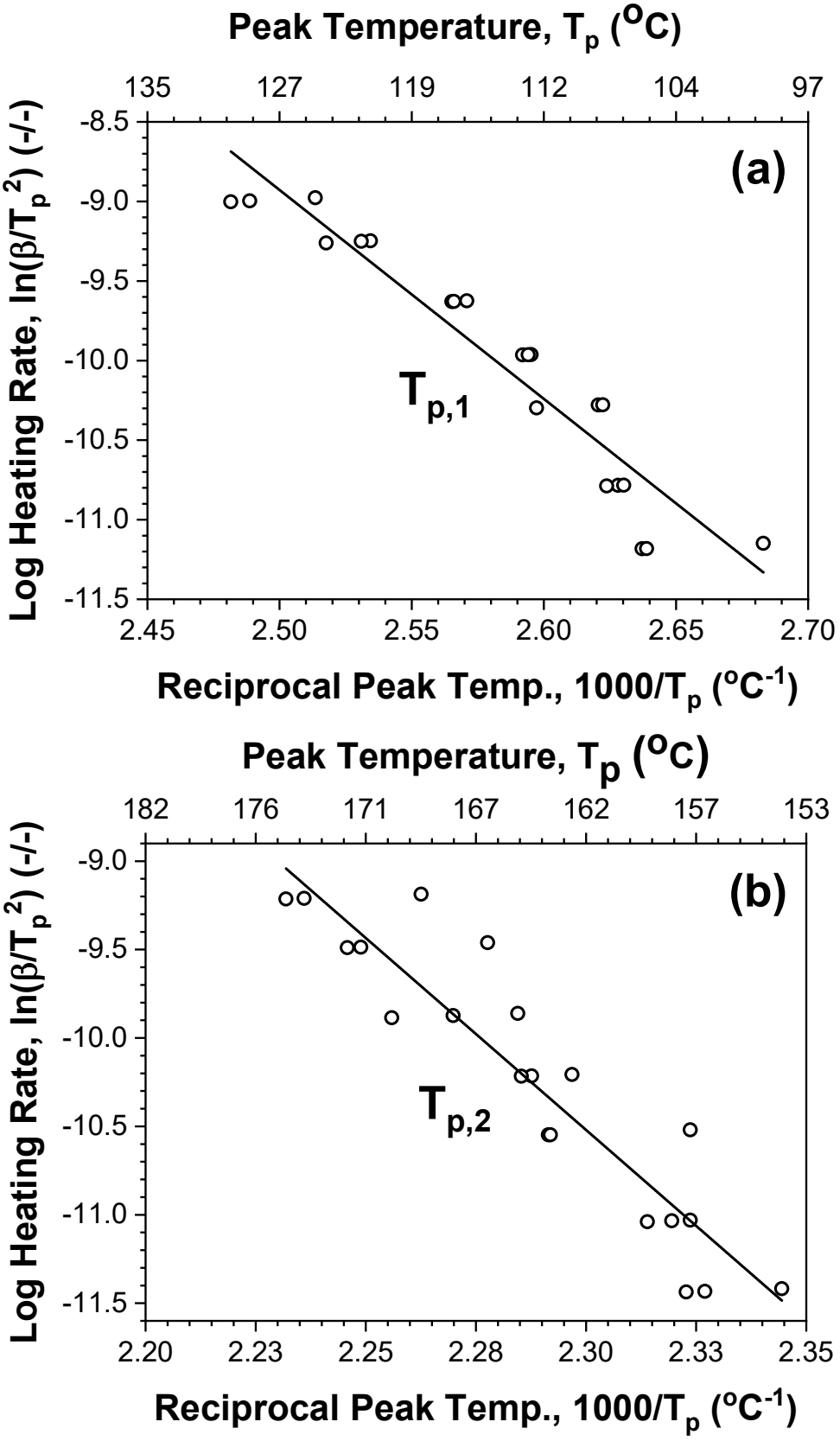

Figure 4.24: Calculation of activation energy for dehydrogenation steps of bulk AB by the Kissinger Method using non-isothermal DTG data for (a) first, and (b) second peak temperatures, between 100-130 °C and 150-180 °C respectively.

The Kissinger plots in Figure 4.24(a)-(b) for the first ($T_{P,1}$) and second ($T_{P,2}$) dehydrogenation steps each showed moderately good linearity ($R^2 \geq 0.899$ and $R^2 \geq 0.854$ respectively), with the corresponding E_a values calculated as 109 ± 8 and 180 ± 17 kJ/mol. Unlike the results from the Arrhenius and Isoconversional Methods, this analysis showed the relative absence of two well-defined regions between 80-110 and 110-140 °C, previously denoted (i) and (ii). Discussion of the individual methodologies and comparison of the calculated E_a values for bulk AB has been reserved for the subsequent section *4.2.8 Discussion of Results*.

An identical exercise was undertaken for nanoconfined AB/TA(L), with the isothermal TGA experiments presented in Figure 4.25(a)-(c). The profiles observed for AB/TA(L) were fundamentally different to those seen for bulk AB, with complete elimination of the induction period and rapid release from the very onset. Fitting of the Avrami-Erofeev (n = Fitted) model to these data yielded invalid values for the Avrami exponent (n < 1), suggesting the release mechanism no longer occurred by nucleation and growth. Instead, the release profiles exhibited by AB/TA(L) showed considerable resemblance to desorption, such as that described by the Langmuir model. Thus, an equation with the same general form of the Langmuir model was fitted to the experimental data (Equation 4.12), which evaluated conversion in terms of a scaling coefficient (A), rate constant (k) and exponent (n) term. Ideally, the scaling coefficient would be neglected ($A = 1$) since analysis of the data in terms of conversion necessarily defines maximum desorption at complete conversion ($\alpha = 1$). However, the upward trend of the data at the end of the experimental duration required the inclusion of this coefficient for adequate fitting. In the true Langmuir model, the inclusion of the equilibrium constant (K) describes whether adsorption ($K > 1$) or desorption ($K < 1$) predominate. The dynamic conditions within the TGA experiments (*i.e.* removal of evolved gas by the flow of N_2) invalidate the assumption of equilibrium. Hence, the equilibrium constant was replaced with a simple rate constant (k) which was fitted to model the rate of the reaction (and should not be understood as a true adsorption-desorption equilibrium).

$$\alpha = A\frac{(kt)^n}{1 + (kt)^n} \qquad \textbf{4.12}$$

Finally, the exponent term (n) describes the fundamental surface reaction with defined integer values for associative ($n = 1$) or dissociative ($n = 0.5$) adsorption mechanisms, which involve one and two active sites on the material surface respectively. During fitting, three different scenarios investigated. Two scenarios examined idealised desorption from one site (n = 1) and desorption preceded by a surface reaction between two sites (n = 0.5), analogous

to the reverse of associative and dissociative adsorption discussed above. During analysis of these scenarios, the value of the exponent was fixed leaving the scaling coefficient and rate constant parameters as fitting variables, whereas the final scenario was conducted with all parameters as fitting variables. The fitted profiles for these scenarios can be seen in Figure 4.25(a)-(c) respectively, with the fitting variables summarised in Table 4.13.

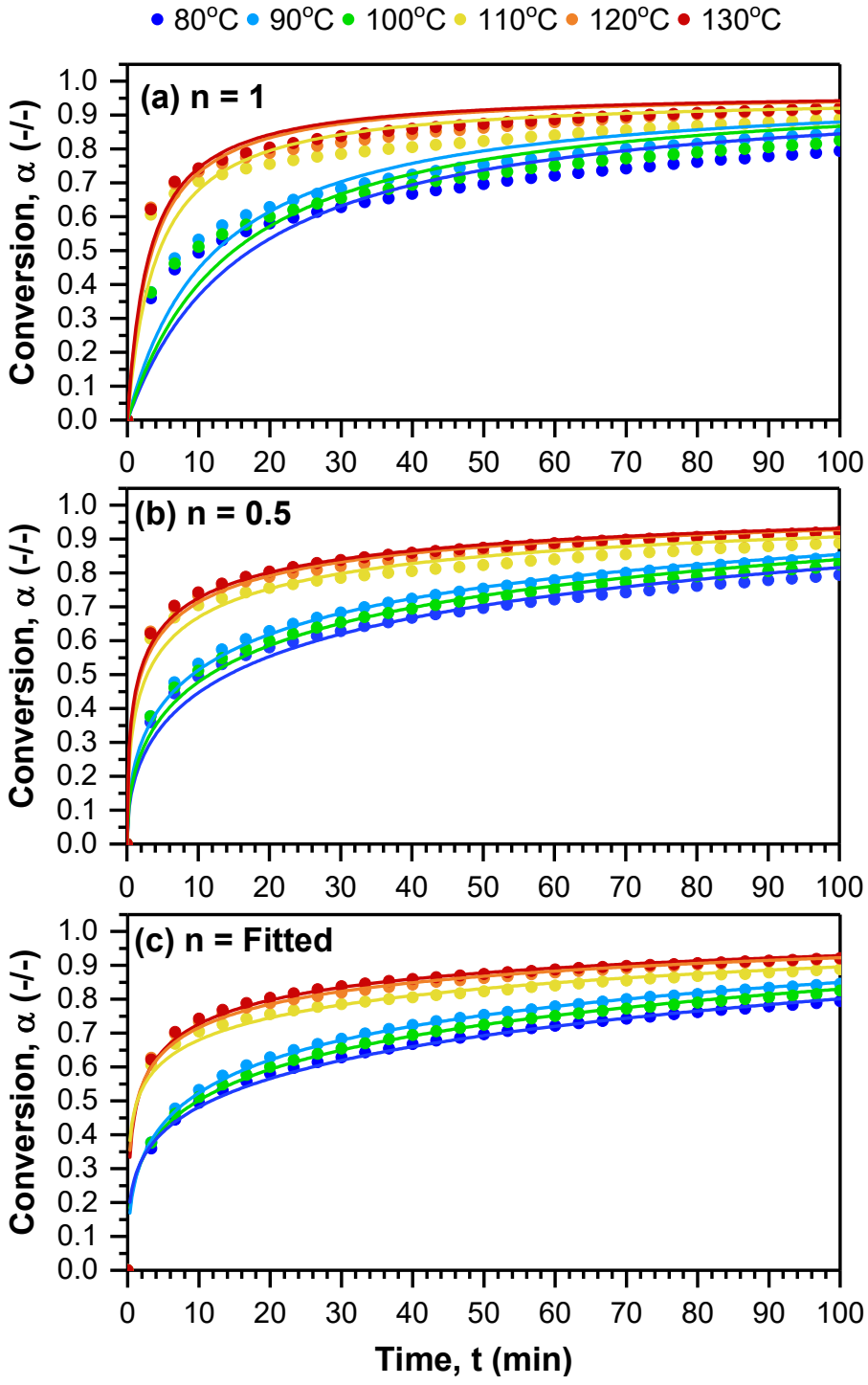

Figure 4.25: Isothermal TGA analyses showing the thermolytic dehydrogenation for nanoconfined AB/TA(L) between 80-130 °C, with experimental data (●) and fitted Langmuir models (–) where (a) n = 1, (b) n = 0.5, and (c) n = Fitted

Table 4.13: Langmuir-type kinetics fitted to Experimental Data

Parameter[a]	Release Temperature (°C)					
	80	90	100	110	120	130
(a) n = 1.0						
A	0.987	0.986	0.995	0.958	0.970	0.971
k	0.059	0.083	0.068	0.244	0.304	0.328
R^2	0.883	0.920	0.902	0.767	0.823	0.854
(b) n = 0.5						
A	1.325	1.236	1.293	1.087	1.078	1.073
k	0.026	0.050	0.034	0.256	0.381	0.436
R^2	0.984	0.996	0.992	0.956	0.981	0.986
(c) n = Fitted						
A	2.987	1.369	1.762	1.507	1.180	1.120
k	2.78×10^{-4}	0.032	0.007	0.046	0.328	0.431
n	0.280	0.422	0.350	0.251	0.366	0.420
R^2	0.997	0.998	0.998	0.986	0.991	0.989

[a] Fitting: Convergence achieved for all scenarios with a minimum residual tolerance of 1×10^{-9},

Two fitting scenarios (n = 0.5 and 1.0) were analysed by the Arrhenius Method to calculate the corresponding values of E_a. During these analyses, the experimental data gathered at 100 °C were neglected since they appeared anomalous to the prevalent trend between 80-130 °C. Furthermore, analysis of the third scenario (n = Fitted) was not pursued since the inclusion of the exponent as a fitting variable would necessarily affect the fitted values of the rate constant, identically to that discussed for bulk AB. The resulting Arrhenius plot for nanoconfined AB/TA(L) can be seen in Figure 4.26(a). As was observed for bulk AB with the same technique, the dehydrogenation of AB/TA(L) appeared to show two regions occupying between 80-110 and 110-140 °C, indicated by (i) and (ii) on Figure 4.26(a). For both fitting scenarios, the former region exhibited stronger linearity ($R^2 \geq 0.971$) than that shown by the latter ($R^2 \geq 0.865$). In the lower temperature region, the values of E_a were calculated as 54 ± 7 and 87 ± 6 kJ/mol for n = 1.0 and n = 0.5 respectively, whereas in the higher region these were substantially lower at 19 ± 5 and 34 ± 9 kJ/mol respectively. For comparison, a single fitting scenario (n = 0.5) was analysed by the Isoconversional Method, with this scenario selected since it represented the experimental data well and retained a fixed exponent value (allowing greater consistency than with the (n = Fitted) scenario with a variable exponent value). The resulting Isoconversional plot has been presented in Figure 4.26(b) for the range of studied conversions between α = 0.1-0.9. These data initially (α = 0.1) showed the two aforementioned regions, however they became practically indistinguishable at high conversion (α = 0.9). This was evidenced by the superior fit of a single trend line across the entire temperature range ($R^2 = 0.98$), compared to two separate trends over the respective ranges ($R^2 = 0.94$). This observation suggested an initial difference in reaction mechanism in the respective temperature ranges, which converged as the reaction neared completion.

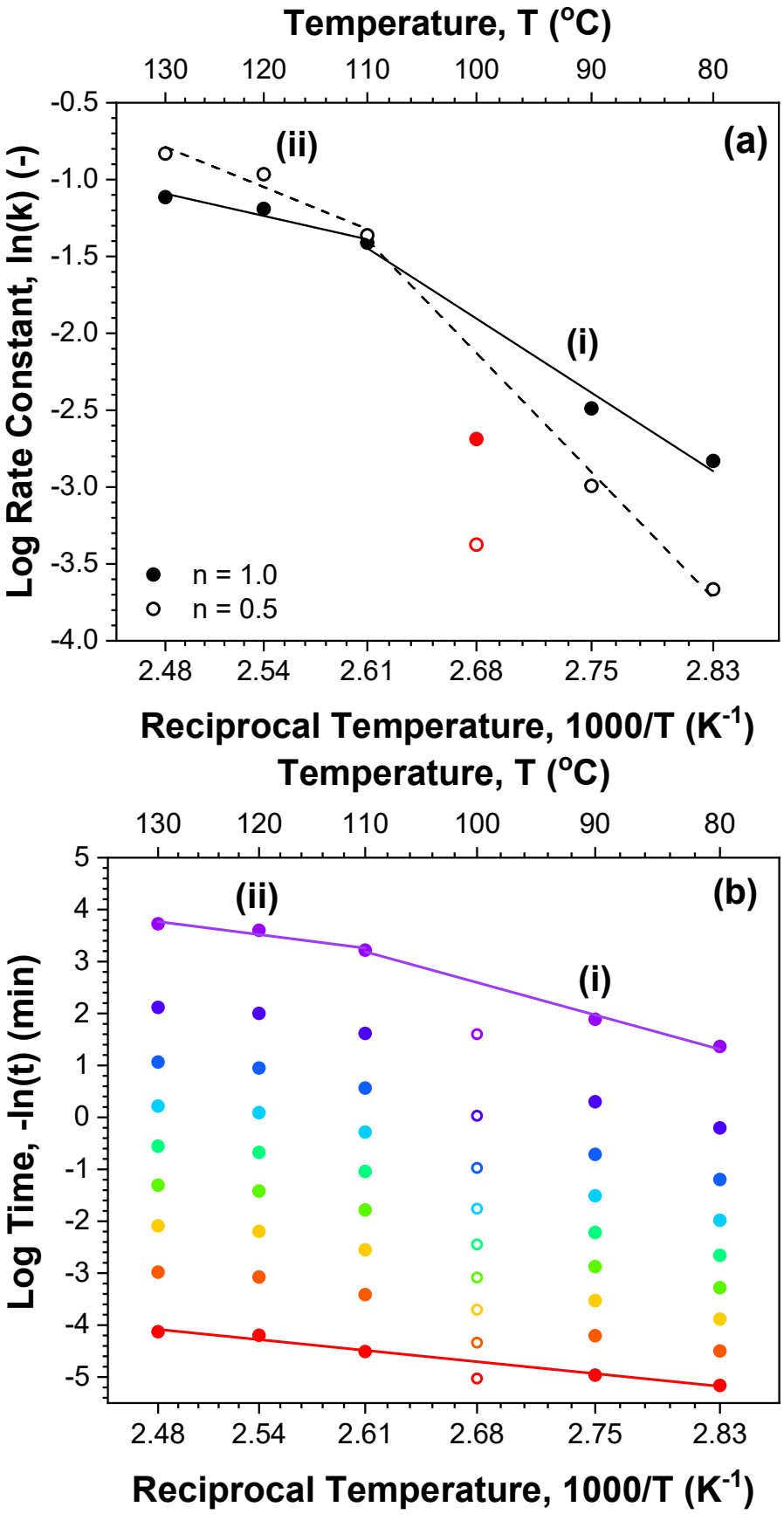

Figure 4.26: Calculation of activation energy for dehydrogenation of nanoconfined AB/TA(L) with a fitted desorption model by (a) Arrhenius plot with fitted exponent values (n = 0.5, 1.0), and (b) Isoconversional plot for a fitted exponent (n = Fitted) between α = 0.1 to 0.9.

Such an observation cannot be satisfactorily explained by a single reaction, and the large variations in E_a suggested simultaneous and convoluted reactions that nonetheless predominated at onset and end of the reaction respectively. This appeared consistent with the profiles in Figure 4.25(a)-(c), which showed initially rapid dehydrogenation at the onset ($\alpha \approx 0.1$-0.5) followed by much slower reaction thereafter ($\alpha \approx 0.6$-1.0). Initially ($\alpha = 0.1$), the calculated E_a values in the lower and higher temperatures regions were found to be 70 ± 5 and 33 ± 9 kJ/mol respectively, however near completion ($\alpha = 0.9$) these values both converged at approximately 26 ± 2 kJ/mol. As mentioned above, these results appeared to suggest the reaction mechanisms in the aforementioned temperature regions were initially different, but became identical as the reaction progressed.

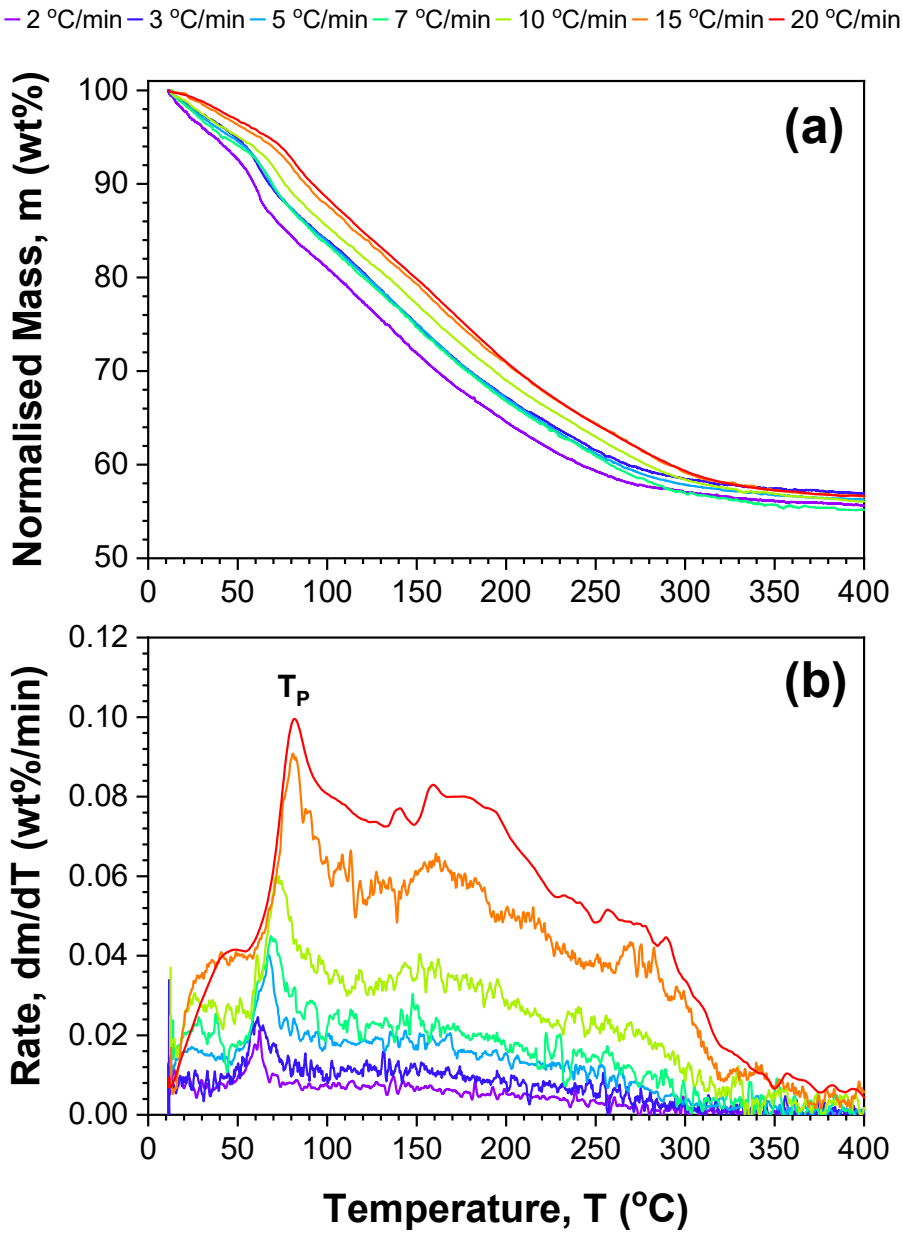

Figure 4.27: Non-isothermal (a) TGA and (b) DTG of the thermolytic dehydrogenation of nanoconfined AB/TA(L) with fixed heating rates of 2-20 °C/min between 25-300 °C

As an accompaniment to the above, a set of non-isothermal TGA experiments were conducted for the thermolytic dehydrogenation of nanoconfined AB/TA(L) with a series of fixed heating rates (β = 2-20 °C/min), as outlined in *3.5.3 Non-Isothermal Analyses*. The TGA and DTG profiles from these experiments have been presented overleaf in Figure 4.27(a)-(b) respectively. These experiments were repeated (n_a = 3) at each heating rate with the mean average profiles shown, however error bars have been omitted on the figure for visual clarity. From the profiles in Figure 4.27(b) the respective peak temperatures (T_P) were identified, allowing subsequent analysis by the Kissinger Method as presented in Figure 4.28. Although several convoluted reaction steps can be inferred from Figure 4.27(b), only a single peak temperature could be reliably evaluated from the data within the lower temperature region between 90-110 °C (as indicated on the corresponding figure). Hence, the application of the Kissinger Method subsequently found the values of E_a to be 85 ± 8 kJ/mol for the initial dehydrogenation of nanoconfined AB/TA(L). All the above activation energy values calculated for both bulk AB and nanoconfined AB/TA(L) have been summarised in Table 4.14.

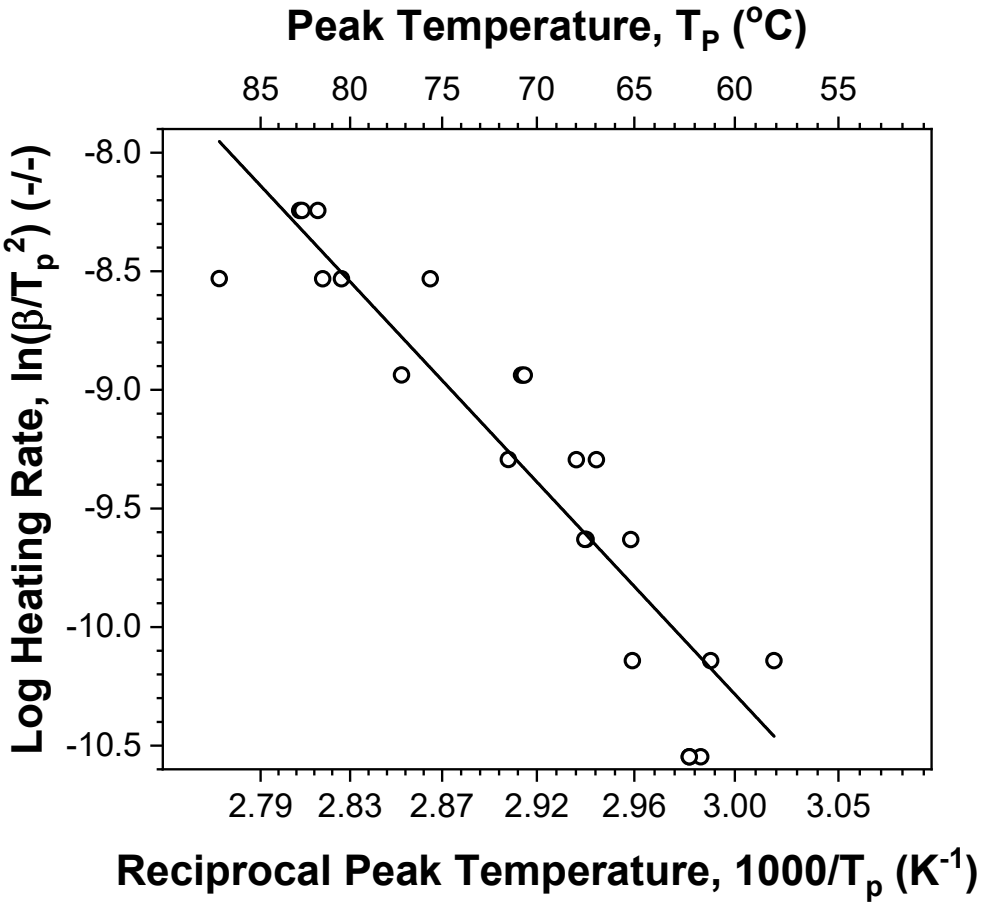

Figure 4.28: Calculation of activation energy for the initial dehydrogenation of nanoconfined AB/TA(L) by the Kissinger Method using non-isothermal DTG data for peak temperatures between 40-100 °C.

Table 4.14: Calculated activation energy values for thermolysis of bulk AB and nanoconfined AB/TA(L) by Arrhenius, Isoconversional and Kissinger Methods

Scenario	Dataset	Method	Activation Energy			
			(i) 80-110 °C		(ii) 110-130 °C	
			E_a (kJ/mol)	R^2	E_a (kJ/mol)	R^2
Bulk AB						
n = 2	Isothermal TGA	Arrhenius	171 ± 7	0.995	60 ± 5	0.979
n = 3	Isothermal TGA	Arrhenius	171 ± 7	0.995	61 ± 5	0.980
n = 4	Isothermal TGA	Arrhenius	128 ± 5	0.995	45 ± 4	0.980
n = Fitted	Isothermal TGA	Isoconversional	176 ± 11	0.997	59 ± 5	0.980
-	Non-Isothermal DTG	Kissinger	109 ± 8	0.899	180 ± 17	0.854
Nanoconfined AB/TA(L)						
n = 1.0	Isothermal TGA	Arrhenius	54 ± 7	0.971	19 ± 5	0.869
n = 0.5	Isothermal TGA	Arrhenius	87 ± 9	0.991	34 ± 9	0.865
n = Fitted	Isothermal TGA	Isoconversional	70 ± 5	0.988	33 ± 9	0.855
-	Non-Isothermal DTG	Kissinger	85 ± 8	0.848	-	-

4.2.8 **Discussion of Results**

Overall, from these results it was abundantly clear that the preparation of AB/TA(L) had caused extensive and fundamental changes in the nanoconfined AB, which lead to substantially different material properties compared to bulk AB. The differences between these materials were plainly evident during analyses, meaning t-tests were generally not required to establish significance during comparison of bulk AB and nanoconfined AB/TA(L). The discussion herein compares these results for bulk AB against those reported in literature, followed by subsequent comparison of nanoconfined AB/TA(L) to both bulk AB and other nanoconfined AB materials reported in literature.

Firstly, with regard to bulk AB, the majority of experimental results generally supported findings in literature, however a few notable discrepancies were also observed. A comparison of the results from this research and those reported in literature can be seen in Table 4.15. This research observed bulk AB by SEM to consist of micron-sized (D_P = 94 μm) agglomerates composed smaller constituents with crystalline morphology. Similar sizes have been reported for as-purchased AB ($45 \leq D_P \leq 150$ μm) (Baier, Ramachandran and Son, 2019), and previous SEM micrographs closely resemble the observed particle morphology (Rueda *et al.*, 2017). The crystallinity of bulk AB was confirmed by XRD analyses, which detected nanosized crystallites (d_c = 20.3 nm) in a crystalline phase (I4mm) extensively reported in literature (Petit and Demirci, 2018). Also in concordance were FTIR analyses, which showed strong

evidence for the expected $-NH_3$, $-BH_3$ and B–N vibrational modes in bulk AB throughout the entire wavenumber range (Huang *et al.*, 2014) (Hess et al., 2008) (Dillen and Verhoeven, 2003) (Custelcean and Dreger, 2003). Nevertheless, small spectral bands believed to originate from $-NH_2$, $-BH_2$, and C-O-C groups evidenced trace contaminants of PAB and THF within the bulk AB (Frueh *et al.*, 2011)(Jash, Meaux and Trenary, 2012), which were nonetheless inconsequential throughout research.

Table 4.15: Comparison of a selection of results for bulk AB with relevant literature

Reference	Properties[a]		Peak Volatilisation Temperature, T_p (°C)			
	T_m (°C)	dm (wt%)	H_2	NH_3	DB	BZ
Bulk AB (This Research)	**114**	**17, 28**	**107, 152**	**167, 312**	**97, 158**	**161**
(Roy, Hajari, Manna, *et al.*, 2018)	-	~15, ~30	129, 170	130, 185	173	167
(Frueh *et al.*, 2011)	110	~15, ~35	110, 130	-	-	110, 130
(Li, Guo, *et al.*, 2010)	110	-	110, 154	-	-	-
(Li, Zhu, *et al.*, 2010)	110	-	114, 150	118,155	155	155
(Zhao *et al.*, 2010)	-	-	106, 154	n.d	170	175
(He *et al.*, 2009)	100	-	100, 160	-	-	-
(Li *et al.*, 2009)	100	~10, ~10	105, 140	105	-	n.d
(Kang *et al.*, 2008)	107	~5, ~5	114, 153	-	153	153
(Sepehri, Garcia and Cao, 2008)	-	-	115, 150	-	-	-
(Gutowska *et al.*, 2005)	114	-	110, 155	-	-	160
(Lai *et al.*, 2012)	111	~17, ~28	122, 170	110, 190	104	117, 173

[a] Properties: T_m = Melting Temperature, dm = Mass Loss, E_A = Activation Energy, T_P = Peak Temperature

Upon heating of bulk AB, non-isothermal TGA analyses found mass loss to progress through two defined steps between approximately 101-127 and 127-210 °C, which were associated with the loss of 17.1 and 28.3 wt% respectively. The peak temperatures of 107 and 152 °C determined for each step were in good agreement with previously reported values, which tended to range between 100-129 and 130-170 °C (as reviewed in Table 4.15) (Frueh et al., 2011)(Gutowska *et al.*, 2005)(Lai *et al.*, 2012). This observation supported empirical understanding that thermolytic dehydrogenation of bulk AB proceeded by initial formation of PAB, followed by subsequent production of PIB (as shown in Figure 2.3) (Demirci, 2017a). Nevertheless, the total observed mass loss (Δm_t = 45.4 wt%) significantly exceeded the stoichiometric hydrogen capacity of bulk AB (19.6 wt%) (Wietelmann, Felderhoff and Rittmeyer, 2016), strongly evidencing the volatilisation of other contaminant species (as discussed subsequently). This was evidenced as due to the heating rate employed during these experiments (β = 5 °C/min), since additional experiments with different heating rates (β = 2 - 20 °C/min) resulted in varied observed mass losses (Δm_t = 37.6 - 68.5 wt%). Slower heating rates were observed to result in lower mass losses, with these gradually approaching the aforementioned hydrogen capacity of AB. This effect was consistent with previous

literature (Baitalow *et al.*, 2002)(Baitalow *et al.*, 2006), where heating at extremely low rates (β = 0.15 °C/min) effected mass loss corresponding to two mole equivalents of hydrogen ($\Delta m_t \approx 13$ wt%), indirectly evidencing the absence of volatilised contaminants. This result corroborates existing literature and reinforces the vital importance of minimising heating rate during thermolysis of bulk AB to suppress volatilisation of contaminants.

Complementary studies by non-isothermal DSC were used to study the thermal events during the thermolytic dehydrogenation of bulk AB. These studies observed an endothermic event not associated mass loss that peaked at around 114 °C. This appeared consistent with the reported melting point temperatures of AB in literature, which typically ranged between 107-114 °C, as presented in Table 4.15 (Frueh et al., 2011)(Kang et al., 2008) (Gutowska *et al.*, 2005). In addition to this, two large exothermic events were observed to peak at 124 and 173 °C, which correlated to the aforementioned mass losses observed during TGA. These exothermic events were hence consistent with the previously discussed dehydrogenation reactions, in general agreement with wider literature (Kondrat'Ev et al., 2015) (Kang et al., 2008) (Wolf et al., 2000). A much smaller exothermic event was repeatedly observed at 99 °C, which reliably preceded both melting and the onset of subsequent hydrogen release. A similar observation can be made in some other profiles in literature (Rueda *et al.*, 2017), however this unnoticed event was undiscussed. A similar exothermic event had been reported for pure DADB in literature, albeit at slightly higher temperatures ($T \approx 110$ °C) (Fang *et al.*, 2011). A suggestion of this research is that this small exothermic event is infact due to the partial formation of DADB within a fraction of the bulk AB. With the current understanding, this DADB then serves as the critical nucleation event that prompts subsequent release of hydrogen, due to the greater reactivity of DADB and nucleation allowing subsequent growth of PAB (Shaw et al., 2010)(Bowden and Autrey, 2011). To be clear, although the importance of DADB to dehydrogenation of AB has long been accepted, its absence as a detectable thermal event during analyses of AB has not been widely addressed. This result serves to direct further research, but remains speculative until more experiments can unequivocally prove the identity of this exothermic event to be formation of DADB.

Further supporting studies by non-isothermal MS analyses (β = 3 °C/min) showed that, of the detected species, mass loss from bulk AB overwhelmingly consisted of H_2 (96.4 vol%) with smaller amounts detected for NH_3 (2.5 vol%), H_2O (1.0 vol%), DB (0.01 vol%) and BZ (0.04 vol%). Approximately similar compositions have been reported in literature for H_2 (~87 vol%) (Babenko *et al.*, 2017), although with seemingly differing amounts of DB (~1.6 vol%) and BZ (~2.6 vol%) (Wood *et al.*, 2017), as well as a considerable amounts of MAB (~8.3 vol%) (Babenko *et al.*, 2017)(Baitalow *et al.*, 2006). These results must certainly have been affected by the purities of their respective bulk AB feedstocks (between 90 - 97 %).

Nevertheless, given the previous discussion on the effect of heating rate on evolution of contaminants and the varied heating rates of these studies (between β = 0.5 – 10 ^{o}C/min), these results were deemed in moderately good agreement with literature (Babenko *et al.*, 2017) (Baitalow *et al.*, 2006).

The release of H_2 peaked at temperatures of 107 and 152 ^{o}C, and was consistent with both the aforementioned mass losses and temperatures reported in literature, ranging between 100-129 and 130-170 ^{o}C as seen in Table 4.15 (Frueh et al., 2011) (Kang *et al.*, 2008) (Lai *et al.*, 2012). However, the volatilisation temperatures of many contaminants differed compared to literature. The observations for NH_3 included an onset of evolution at 140 ^{o}C, which peaked at 167 ^{o}C and was followed by an unresolved release at 321 ^{o}C. This was predominantly after the release of H_2, and considerably later than the range reported for the two releases in literature between 105-130 and 155-190 ^{o}C (Li, Zhu, et al., 2010) (Li et al., 2009), as reviewed in Table 4.15. Nevertheless, some authors report the onset for a release of NH_3 as high as 185-190 ^{o}C (Lai *et al.*, 2012) (Roy, Hajari, Manna, *et al.*, 2018). Also seen in Table 4.15, the volatilisation of BZ was exclusively during the second mass loss and peaked at 161 ^{o}C, generally in good agreement with a wide number of reports in literature(Roy, Hajari, Manna, et al., 2018) (Zhao et al., 2010) (Gutowska et al., 2005). An unexpected observation included that the volatilisation of H_2O correlated with release of H_2. Although this could not be satisfactorily explained, the quantity of H_2O (1 vol%) was small and could have been due to an unaccounted experimental variable (*e.g.* degassing of the quartz wool).

A significant observation was with regard to the volatilisation of DB, which substantially preceded the bulk release of H_2 and was not accompanied by simultaneous evolution of NH_3 (expected from the stoichiometry of AB). The onset temperatures for DB, H_2 and NH_3 were 89, 101 and 140 ^{o}C respectively. This observation was believed to evidence the occurrence of homopolar (B-$H^{\delta-}\cdots H^{\delta-}$-B) interactions within AB, where BH_3 acted as a Lewis acid during the formation of DADB, as previously discussed in Figure 2.5 (Chen *et al.*, 2011). Similar results have been reported through both simulation- (M. T. Nguyen *et al.*, 2007) and experimentally-based research (Al-kukhun, Hwang and Varma, 2012), generally corroborating the catalytic effect of BH_3 and/or DB. Moreover, the reaction of DB with two mole equivalents of NH_3 has been reported to form DADB (Nguyen *et al.*, 2008), potentially also explaining the absence of detected NH_3. This was further supported by the close proximity of the onset temperature for DB and the previously discussed exothermic event attributed to formation of DADB (at 89 and 99 ^{o}C respectively) when the error in the onset temperatures was considered (*i.e.* ΔT_{on} = 7 ^{o}C for H_2). Thus, a novel contribution of this research was to tentatively identify a thermal event corresponding to homopolar (B-$H^{\delta-}\cdots H^{\delta-}$-B) interactions in AB.

Further insight into the role of DADB was gained during subsequent isothermal analyses, during which the dehydrogenation of bulk AB was observed to exhibit a sigmoidal release profile. This was consistent with similar experiments in literature (Bowden and Autrey, 2011)(Bowden *et al.*, 2006)(Komova et al., 2013), agreeing with the consensus that this sigmoidal profile is due to the role of DADB as the critical nucleation event that onsets bulk hydrogen release (observed experimentally as a suddenly accelerated release after an extended duration without change) (Al-kukhun, Hwang and Varma, 2012) (Bowden and Autrey, 2011). The applicability of nucleation and growth kinetics was further supported by subsequent fitting of the Avrami-Erofeev model, which generally achieved excellent fittings. Specifically, the best fittings were found for the scenario (n = 3) that corresponded to rate-limiting nucleation ($\Gamma = 1$) with two-dimensional growth ($\Psi = 2$) (where $0.973 \leq R^2 \leq 0.997$). In line with current understanding, this result appeared to confirm that the formation of DADB was rate-limiting, whilst the suggestion of two-dimensional growth was consistent with the formation of planar sheets of PBZ. This result was in contrast to similar studies which found greater evidence for three-dimensional growth ($\Psi = 3$) (Simagina *et al.*, 2017) (Roy, Hajari, Kumar, *et al.*, 2018). Ultimately, the difference in these results despite similarity in experimental conditions highlights the complexity of the reaction pathways and their sensitivity to the precise reactions conditions.

This was also reflected in the calculated values of apparent activation energy (E_a), which utilised both isothermal and non-isothermal TGA experiments to calculate the value of E_a by three different methods; the Arrhenius, Isoconversional and Kissinger Methods. These methods have all been used before in literature (Gutowska *et al.*, 2005) (Kang *et al.*, 2009) (Gangal and Sharma, 2013). These studies suggested bulk AB to exhibit distinct activation energies between temperatures of 80-110 and 110-140 ^{o}C which, based on the detected melting point (T_m = 114 ^{o}C), were attributed to solid and liquid AB respectively. Despite a large number of experiments being conducted on this topic such a distinction has not yet been accounted for in the reported values of E_a, but nonetheless seems intuitive. The calculated values of E_a were in generally good agreement with literature, as reviewed in Table 4.16, with the all the methods giving approximately equivalent results. The large discrepancy between the values of E_a between 80-110 and 110-140 ^{o}C suggested a fundamental change in the mechanism upon melting of AB. On one hand, this might simply be due to the melting of AB causing relaxation of the intermolecular dihydrogen (N-$H^{\delta+}\cdots H^{\delta-}$-B) bonding network and forming a 'mobile phase' of AB (Kulkarni, 1999), as discussed in Figure 2.4 (Demirci, 2017a). On the other, this might evidence a different reaction pathway involving favourable homopolar (B-$H^{\delta-}\cdots H^{\delta-}$-B or N-$H^{\delta+}\cdots H^{\delta+}$-N) interactions which have (conflictingly) both been observed to predominate above the melting point of AB (Petit and Demirci, 2018) (Wolstenholme *et al.*, 2012) (Al-kukhun, Hwang and Varma, 2012).

Table 4.16: Comparison of activation energy values for bulk AB reported in literature

Reference (Scenario)	Experimental Range		Activation Energy	
	β (°C/min)	T (°C)	E_a (kJ/mol)	R^2 (-)
Arrhenius Method				
(Gutowska *et al.*, 2005)	-	70 - 85	184	-
(Kang *et al.*, 2008)		100 - 150	183	-
(Patel, Kale and Miotello, 2012)	-	95 - 110	179	-
This Research (n = 3)	**-**	**80 - 110**	**171 ± 7**	**0.995**
(Li, Guo, *et al.*, 2010)	-	70 - 85	138	-
(Bowden *et al.*, 2006)	-	80 - 100	136	-
(Li *et al.*, 2015)	-	75 - 105	135	-
(Tang *et al.*, 2012)	-	80 - 100	135	-
This Research (n = 3)	**-**	**110 - 130**	**61 ± 5**	**0.980**
(Gangal *et al.*, 2012)	-	90 - 150	47	-
Isoconversional Method				
This Research (n = Fitted)	**-**	**80 - 110**	**176 ± 11**	**0.997**
(Gangal and Sharma, 2013)	-	90 - 180	102	-
This Research (n = Fitted)	**-**	**110 – 130**	**59 ± 5**	**0.980**
Kissinger Method				
(Si *et al.*, 2011)	1, 2, 3	100 - 120	182	-
This Research (None)	**2, 3, 5, 7, 10, 15, 20**	**130 - 300**	**180 ± 17**	**0.854**
(Sepehri and Cao, 2009)	2, 5, 10	55 - 155	160	-
(Gangal and Sharma, 2013)	2, 3, 5, 10	50 - 200	148	-
(Choi *et al.*, 2012)	1, 5, 10	30 - 180	144	-
(Yang *et al.*, 2017)	2, 5, 10, 15	110 - 135	131	-
(Roy, Manna, *et al.*, 2018)	2, 5, 10	110 - 130	130	-
(He *et al.*, 2009)	0.5, 1, 2, 3	30 - 180	129	-
(He *et al.*, 2011)	0.5, 1, 2, 3	30 - 180	125	-
This research (None)	**2, 3, 5, 7, 10, 15, 20**	**25 - 130**	**109 ± 8**	**0.899**

In contrast, the results for nanoconfined AB/TA(L) revealed a highly complicated composition with properties distinct from bulk AB, and an assortment of similarities to other nanoconfined systems in literature, as reviewed in Table 4.17. Superficially, the preparation of AB/TA(L) was found to effect micron-sized (D_P = 6.8 μm) particles that exhibited slightly smaller average diameter than constituent TA(L) (D_P = 7.0 μm) which was nonetheless statistically significant ($p = 9.995 \times 10^{-6}$). Silica aerogel materials produced with the same equipment exhibited slightly larger, but nonetheless micron-sized ($12 \leq D_P \leq 30$ μm) particles (Rueda *et al.*, 2014). This evidenced a slight increase in particle breakage, which was presumed due to the fragility of the support coupled with rapid recrystallization of AB within the pores of TA(L). Additionally, SEM analyses suggested the surface of these particles exhibited characteristics from both bulk AB and TA(L), which was presumed due to the intuitive precipitation of AB onto the external surface of the incipient aerogel.

Furthermore, fundamental alterations were observed by XRD analyses which showed AB/TA(L) to demonstrate a notable lack of peaks associated with the aforementioned phase of bulk AB (I4mm). Similar observations have been made in the study of some other nanoconfined systems, with these tentatively attributed to PAB and/or DADB (Rueda *et al.*,

2017). Instead, diffraction peaks were measured that were suggestive of amorphous PBZ and crystalline tBN (Maleki *et al.*, 2016)(Zou *et al.*, 2014)(Moury *et al.*, 2012), as well as additional peaks for unidentified crystalline phases. The presence of these species prior to heating suggested a degree of premature dehydrogenation during storage at ambient temperature, which was ultimately confirmed by subsequent FTIR analyses (as discussed subsequently). Release at such low temperatures has only ever been reported for a single nanoconfined AB/Carbon material (Moussa *et al.*, 2012), where the destabilisation of AB was attributed to the Brønsted acidity of surface carboxylic groups (COOH) (Moussa *et al.*, 2012). In contrast, nanoconfined AB/PMA (Zhao *et al.*, 2010) with similar surface groups ($COOCH_3$) did not observe ambient temperature release, and instead was proposed to occur by the Lewis basicity of the carbonyl (C=O) groups (Zhao *et al.*, 2010).

Table 4.17: Comparison of a selection of results for AB/TA(L) with relevant literature

Reference	Material	Properties[a]			Peak Volatilisation Temperature, T_p (°C)			
		T_m (°C)	dm (wt%)	E_A (kJ/mol)	H_2	NH_3	DB	BZ
AB/TA(L)	**AB/TA(L)**	**97**	**18**	**+56, +30**	**18, 186**	**18-301**	**18-301**	**n.d.**
(Rueda *et al.*, 2017)	AB/ Silica	62-68	33	-	69, 109	-	-	-
(Lai *et al.*, 2012)	AB/MCM-41	n.d.	15	-	113, 146	100	120	153
(Lai *et al.*, 2012)	AB/SBA-15	n.d.	19	-	116, 151	102	150	151
(Paolone *et al.*, 2009)	AB/MCM-41	-	-	-	-	-	-	-
(Wang *et al.*, 2009)	AB/MCM-41	-	-	-	-	-	-	-
(Gutowska *et al.*, 2005)	AB/SBA-15	n.d.	-	+67	95	-	-	140
(Autrey *et al.*, 2004)	AB/SBA-15	-	-	-	-	-	-	-
(Li *et al.*, 2015)	AB/MOF-5	n.d.	-	+68	84	84	n.d	n.d
(Gadipelli *et al.*, 2012)	AB/MOF-74	n.d.	14	-	102	102	103	102, 140
(Zhong *et al.*, 2012)	AB/ZIF-8	n.d.	-	-	82, 133	-	-	-
(Li, Zhu, *et al.*, 2010)	AB/JUC-32	n.d.	10	-	84	n.d	n.d	n.d
(Yang *et al.*, 2017)	AB/CEMC	n.d	13	+75	86	n.d	-	-
(Moussa *et al.*, 2012)	AB/Carbon	110	3	+64	110	150	-	120
(Sepehri and Cao, 2009)	AB/BN-Carbon	n.d.	9	+115	103	-	-	-
(Li *et al.*, 2009)	AB/CMK-3(Li)	n.d.	7	+98	95	95	-	n.d
(Sepehri *et al.,* 2008)	AB/Carbon	-	-	+150	101	-	-	-
(Sepehri *et al.*, 2007)	AB/Carbon	n.d.	9	+150	-	-	-	-
(Feaver *et al.*, 2007)	AB/Carbon	n.d.	9	-	90	-	-	n.d
(Tang *et al.*, 2012)	AB/GO	103	12	+30	99, 125	n.d	n.d	n.d
(Li, Guo, *et al.*, 2010)	AB/CNT(Pt)	n.d.	11	+106	108, 150	-	-	n.d
(Alipour *et al.,* 2015)	AB/PMA-CNT	80-106	11	-	80	-	-	-
(Zhao *et al.*, 2010)	AB/PMA	-	-	-	95	120	n.d	n.d
(Salameh *et al.*, 2018)	AB/BN	n.d.	8	-	118	-	-	-
(Roy *et al.*, 2018a)	AB/$AlPO_4$	90-95	25	-	109	111	n.d.	170
(Roy *et al.,* 2018b)	AB/Clay	n.d.	8	+121	120, 150	-	n.d.	n.d.

[a] Properties: T_m = melting temperature, E_A = activation energy (kJ/mol), T_p = peak temperature, dm_t = total mass loss
[b] Volatilisation: H_2 = hydrogen, NH_3 = ammonia, BH_3 = borane, DB = diborane, BZ = borazine, n.d. = not detected

The similarity of AB/TA(L) to the former appeared to confirm the presence strongly acidic surface groups, although this conflicted with the previous assignment of TA(L) surface species as bidentate bridging bicarbonate groups. Specifically since bicarbonates only exhibit amphoteric characteristic and are typically limited to weak acidity (Shi *et al.,* 2014). One

potential conclusion was that the amphoteric nature of these bicarbonates meant they were able to engage in acid-base reaction with both $-NH_3$ and $-BH_3$ moieties of AB, leading to these species mediating proton transfer during dehydrogenation. In fact, this might explain the trend observed in literature whereby solid-state doping of AB with more amphoteric oxides (*i.e.* TiO_2, Al_2O_3) (Virga *et al.*, 2018) resulted in more rapid dehydrogenation than the most acidic (*i.e* SiO_2) and basic (*i.e.* MgO) (Simagina *et al.*, 2017)(Carre, Roger and Varinot, 1992). Whereas most research has concentrated on destabilisation of AB with materials of ever greater Brønsted acidity (and to a lesser extent Lewis basicity) (Lai *et al.*, 2012) (Simagina *et al.*, 2017), this novel understanding instead implies efforts should instead be focussed on materials with amphoteric surface characteristic.

Further evidence supporting the substantial differences between bulk AB and nanoconfined AB/TA(L) were observed during FTIR analyses, which revealed highly convoluted bands that suggested a complicated composition for AB/TA(L). Immediately after preparation, there was evidence for significantly shifted N-H and B-H vibrational modes, with the opposing shifts suggesting lengthening and shortening of the N-H and B-H bonds respectively. Similar shifts have been calculated during simulations (V. S. Nguyen *et al.*, 2007) (M. T. Nguyen *et al.*, 2007), as well as observed experimentally for other nanoconfined systems (Rueda *et al.*, 2017), both of which point toward destabilisation of AB. The detected intensity for N-H and B-H bands gradually reduced during storage ($t \approx 2$ months) strongly evidencing dehydrogenation at ambient temperature. The involvement of surface bicarbonates in this accelerated release was reinforced by relative increases in the region previously assigned to COO^- vibrational modes within TA(L) ($\omega \approx 1550\text{-}1430\ cm^{-1}$) (Nolan, et al., 2009) (Vasconcelos et al., 2011) (Qu et al., 2010), followed by reduction in these bands during storage (despite this region exhibiting stability during storage in TA(L)).

The changes to nanoconfined AB/TA(L) were also observed by the dramatic acceleration of release during non-isothermal TGA. After removing the contributions from TA(L), the mass loss for nanoconfined AB was evidenced to occur across three broad steps between 25-53, 53-213 and 252-329 ^oC, which contributed mass losses of 2.0, 15.1 and 1.4 wt% respectively. The loss between 25-53 ^oC exhibited a remarkably low onset that was unparalleled except by the aforementioned AB/Carbon system (Moussa *et al.*, 2012). This validated the spectral changes observed during storage and reinforced previous evidence of strong destabilisation within AB/TA(L). Cumulatively, these mass losses accounted for a total mass loss of 18.5 wt% from nanoconfined AB out of a total loss of 42.2 wt% for AB/TA(L). Whilst comparison to Table 4.17 is complicated by different loadings of AB and mass losses associated with each support material, the value demonstrated by AB/TA(L) was nevertheless somewhat higher than many sources (Lai et al., 2012) (Gadipelli et al., 2012) (Alipour et al., 2015).

These mass losses were contextualised by MS analyses, which showed extensive volatilisation of gaseous contaminants. The composition of detected contaminants included a significantly reduced quantity of H_2 (17.2 vol%) alongside contaminants such as NH_3 (55.2 vol%), DB (10.9 vol%), H_2O (15.3 vol%) and iPrOH (1.4 vol%), whereas volatilisation of BZ appeared to have been eliminated. Comparison to literature was challenged by the relative absence of quantitative results reported by authors in Table 4.17. Nevertheless, of the detected species, nanoconfined AB/SBA-15 and AB/MCM-15 were suggested to release H_2 (~77 mol%), NH_3 (~17 mol%), DB (~0.5 mol%) and BZ (~5 mol%) (Lai *et al.*, 2012). This comparison showed AB/TA(L) to release hydrogen that was substantially contaminated (particularly with NH_3, DB and H_2O) both in comparison to bulk AB and to nanoconfined materials in literature (Lai *et al.*, 2012). Moreover, the profiles for these contaminants extended across broad temperature ranges, pointing toward ambiguous release reactions that could not be clearly correlated with the aforementioned mass losses. Similarly broadened release profiles are reported for a large number of nanoconfined systems (Li, Zhu, *et al.*, 2010) (Gadipelli *et al.*, 2012) (Si *et al.*, 2011) (Lai *et al.*, 2012). A specific difference compared to bulk AB was with regard to the proposed role of DB and DADB toward initiating hydrogen release. In AB/TA(L) the release of hydrogen at ambient temperature occurred without preceding detection of DB, which was in stark contrast to observations for bulk AB and suggested DADB was not a requirement in the release mechanism. Instead, the simultaneous volatilisations of large quantities of DB and NH_3 suggested the surface bicarbonates of TA(L) caused excessive cleavage of the B-N bonds within AB, with these gases then evolving before further reaction could properly effect release of H_2. This is an extension of previous conclusions in literature where AB/SBA-15 and AB/MCM-15 were believed to only cause 'weakening' of the B-N bonds (Lai *et al.*, 2012), highlighting the excessive destabilising effect of TA(L) on nanoconfined AB.

The above conclusions were also reflected in the calculated values for E_a for AB/TA(L), using both isothermal and non-isothermal TGA experiments with the Arrhenius, Isoconversional and Kissinger Methods (as summarised in Table 4.18). During isothermal release, AB/TA(L) exhibited a profile that resembled desorption models, with similar release profiles widely reported in literature across many types of nanoconfined systems (Li *et al.*, 2015) (Zhong *et al.*, 2012) (Gadipelli *et al.*, 2012). This evidenced that dehydrogenation of AB/TA(L) followed a fundamentally different reaction mechanism than the nucleation and growth exhibited by bulk AB. In the absence of deeper mechanistic analyses, the apparent complexity of release prevented further understanding of any apparent release mechanism(s). Nevertheless, as was observed for bulk AB, distinct characteristics were apparent in the temperature regions between 80-110 and 110-140 ^oC, again suggesting the melting of AB (T_m = 114 ^oC) profoundly altered the reaction. The values of E_a calculated by the different methods were approximately equivalent, and substantially lower than the corresponding values for bulk AB (reflecting the

significant acceleration of release). Comparable E_a values are reported in literature for other nanoconfined systems (Yang et al., 2017) (Li et al., 2009) (Tang et al., 2012), however depending on the method and temperature range the values for AB/TA(L) tended to be somewhat lower. Overall, the calculated values of E_a reflected the observed destabilisation of AB when nanoconfined within TA(L), and were consistent with drastically accelerated low temperature release.

Table 4.18: Comparison of activation energy values for nanoconfined AB in literature

Reference (Scenario)	Material	Experimental Range		Activation Energy	
		β (°C/min)	T (°C)	E_a (kJ/mol)	R^2 (-)
Arrhenius Method					
(Li, Guo, *et al.*, 2010)	AB / CNT(Pt)	-	70 - 95	106	-
(Li *et al.*, 2009)	AB / CMK-3(Li)	-	60 – 90	98	-
This Research (n = 0.5)	**AB / TA(L)**	**-**	**80 - 110**	**87 ± 9**	**0.991**
(Yang *et al.*, 2017)	AB / CEMC	-	90 - 150	75	-
(Li *et al.*, 2015)	AB / MOF-5	-	75 - 105	68	-
(Gutowska *et al.*, 2005)	AB / SBA-15	-	45 - 65	67	-
(Moussa *et al.*, 2012)	AB / Carbon	-	85 - 120	64	-
This Research (n = 0.5)	**AB / TA(L)**	**-**	**110 – 130**	**34 ± 9**	**0.865**
(Tang *et al.*, 2012)	AB / GO	-	70 - 100	30	-
Isoconversional Method					
This Research (n = Fitted)	**AB / TA(L)**	**-**	**80 - 110**	**70 ± 5**	**0.988**
This Research (n = Fitted)	**AB / TA(L)**	**-**	**110 - 130**	**33 ± 9**	**0.855**
Kissinger Method					
(Sepehri *et al.,* 2008)	AB / Carbon	**2, 5, 10**	90 - 120	150	**-**
(Sepehri *et al.*, 2007)	AB / Carbon	**2, 5, 10**	90 - 120	150	**-**
(Roy, Manna, *et al.*, 2018)	AB / Clay	2, 5, 10	110 - 130	121	-
(Sepehri and Cao, 2009)	AB / BN-Carbon	2, 5, 10	55 - 155	115	-
This research (None)	**AB / TA(L)**	**2, 3, 5, 7, 10, 15, 20**	**25 - 110**	**85 ± 8**	**0.848**

4.3 Release Mechanisms of Bulk and Nanoconfined AB

Despite thorough characterisation with a broad range of analytical techniques, uncertainty persisted regarding the underlying reactions during thermolytic dehydrogenation of bulk AB and nanoconfined AB/TA(L). Hence, it was decided to interrogate these reactions using a combination of TGA and *ex situ* FTIR, with these results then analysed by subsequent 2D-IR spectroscopy (according to procedures detailed in *3.3.5 Procedure for 2D-IR Spectra*). The outcomes from this study could then be correlated against results from the preceding section to provide insight into the release mechanisms of bulk AB and AB/TA(L).

4.3.1 Release Mechanism of Bulk AB

Initially the release mechanism from bulk AB was investigated, as seen by the correlated non-isothermal TGA and *ex situ* FTIR analyses presented in Figure 4.29(a)-(b). For reference, a tabulated summary of the TGA data has been presented in Table 4.19 to help correlate the extent of mass loss to temperature in subsequent discussion. Initially (T = 25 °C), the 1D-IR spectrum of bulk AB in Figure 4.29(b) exhibited the previously discussed vibrational modes associated with anticipated $-NH_3$, $-BH_3$, and B–N moieties respectively. Upon heating, the intensity and characteristic of the bands in these spectra were maintained without appreciable change below the onset of mass loss (T ≤ 80 °C), as seen on Figure 4.29(a). Upon further heating, appreciable mass loss was observed from bulk AB, which progressed along two steps as previously discussed. This mass loss coincided with observable and disproportionate changes in the corresponding 1D-IR spectra, indicating the occurrence of reactions comprising thermolytic dehydrogenation, with these changes discussed herein.

Table 4.19: Summary of TGA/DTG analyses of bulk AB

Temperature, T (°C)	Mass, m (wt%)	Mass Loss, dm (wt%)	Rate of Loss, dm/dT (wt%/°C)
25	100.0	0.0	0.02
80	99.4	0.6	0.02
100	97.7	2.3	0.35
110	89.0	11.0	1.24
120	83.7	16.3	0.19
130	82.4	17.6	0.14
140	80.6	19.4	0.27
150	76.6	23.4	0.52
160	70.5	29.5	0.69
170	63.9	36.1	0.54
180	60.1	39.9	0.23
190	58.5	41.5	0.15
200	57.7	42.3	0.07
210	57.5	42.5	0.04

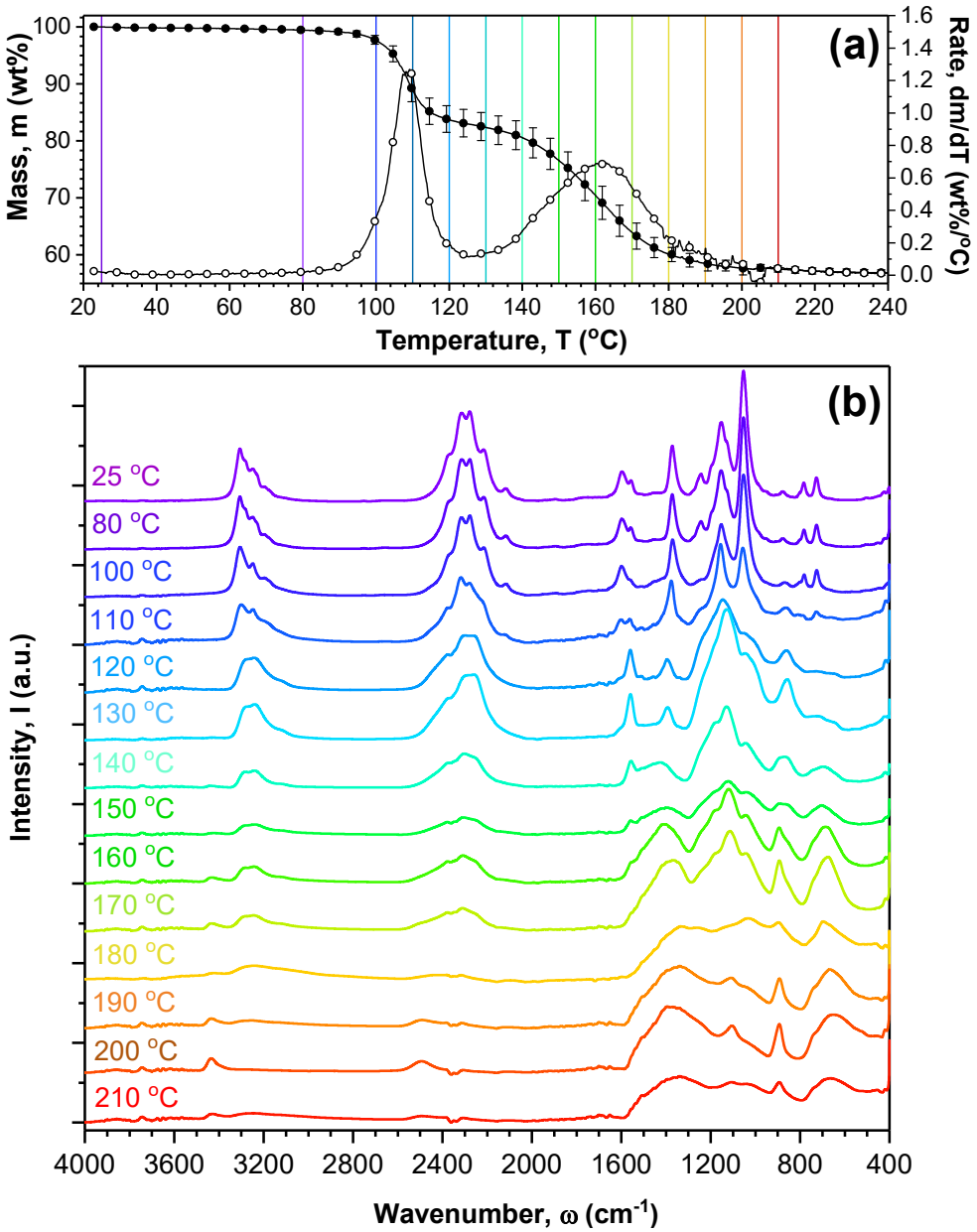

Figure 4.29: Comparison of (a) mass loss from TGA and (b) stacked 1D-IR spectra for bulk AB with *ex situ* heating from 25-210 °C. Unstacked spectra omitted for visual clarity. The temperature of the spectra are indicated by the coloured vertical lines.

Figure 4.30(a) showed the N–H stretching modes were initially centred at 3306 cm^{-1} and exhibited strong intensity, which was maintained until 80 °C after which they rapidly declined until slowing at 120 °C. This loss of intensity was accompanied by broadening and downward shift of these bands to around 3258 cm^{-1}, which suggested lengthening of the constituent N–H bonds. Continued heating after 120 °C showed an overall reduction in N–H intensity until 210 °C. These reductions were reflected in Figure 4.30(c)-(d) for the intensities of N-H bending modes in $–NH_3$ at 1598 and 1376 cm^{-1} (Frueh *et al.*, 2011). Upon heating to 120 °C, Figure 4.30(d) highlighted upward shift in the band at 1376 cm^{-1} to 1394 cm^{-1}, which had previously been assigned to umbrella modes of free NH_3 (Frueh *et al.*, 2011), however this was soon obscured by the growth an emergent band at 1400 cm^{-1}. Simultaneous to these

changes was the transient growth in the band at 1557 cm^{-1} assignable to N-H stretching in tetrahedrally bonded $–NH_2$ until 130 °C (Frueh *et al.*, 2011), as seen in Figure 4.30(c), after which it was quickly reduced and obscured. Similarly, a band at 3435 cm^{-1} indicative of B=N–H stretching (Frueh *et al.*, 2011) was initially absent on Figure 4.30(a) but appeared upon heating to 120 °C, with considerable increase in intensity between 150 to 210 °C.

Analogous changes were observed for the B–H vibrational modes. Figure 4.30(b) showed the losses in intensity for B–H stretching bands centred at 2302 cm^{-1} occurred after 80 °C, with similarly rapid loss followed by slowing at 120 °C and then continued losses until 210 °C. In contrast to N–H stretching modes, the broadening of these bands appeared to show slight upward shift of the band that suggested shortening of the constituent B–H bonds. This was also supported by Figure 4.30(e) in which stretching of N-B-H at 1053 cm^{-1} was observed to quickly reduce upon heating to 100 °C and, despite fluctuating between 100-180 °C, saw overall reductions when heated to 210 °C. Furthermore, Figure 4.30(e) showed the intensities of bands at 1152 and 1125 cm^{-1} assigned to $–BH_3$ and tetrahedrally bonded $–BH_2$ (Frueh *et al.*, 2011). However, these bands were somewhat convoluted, so for clarity the profile for $–BH_3$ was omitted from Figure 4.30(e). Nonetheless, significant growth in $–BH_2$ modes were observed exclusively after 100 °C and despite fluctuations they eventually decreased upon heating to 210 °C. As with discussion for N–H modes, analogous N=B–H stretching and bending bands at 2495 and 668 cm^{-1} (Frueh *et al.*, 2011) were observed to appear on Figure 4.30(b) and (f) upon heating to 120 °C, with considerable increases between 150-210 °C.

Evidence for B–N bonding included the above discussion for the N-B-H vibrational modes, in addition to B–N, B=N and B–N=B modes in Figure 4.30(d) and (f) (Frueh *et al.*, 2011)(J. Li *et al.*, 2010). In Figure 4.30(f), the band associated with B–N stretching at 783 cm^{-1} was observed to disappear at 110 °C, however the intensity profile has been omitted for visual clarity. The band for B=N stretching at 1398 cm^{-1} in Figure 4.30(f) was initially obscured by the shifted N–H bending band at 1410 cm^{-1}, however was unambiguously present after around 150 °C. Similarly, an unidentified band at 879 cm^{-1} was observed to grow substantially whilst shifting downwards to 857 cm^{-1} by 130 °C, with this emergent band previously assigned to B-N stretching bonding in a tetrahedral environment (Frueh *et al.*, 2011). Further heating until 170 °C realised consistent growth of a band at 893 cm^{-1} consistent with B–N=B bending (J. Li *et al.*, 2010), which subsequently decreased until 210 °C. Cumulatively, these results provided convincing evidence for thermolytic dehydrogenation of bulk AB proceeding along the empirically proposed route in Figure 2.3 (Demirci, 2017a). Namely, stability of bulk AB below 80 °C with the onset of release at 100 °C coinciding with the transient formation of tetrahedrally bonded PAB until 120/130 °C, then followed by further hydrogen release and the apparent formation of a species resembling PIB.

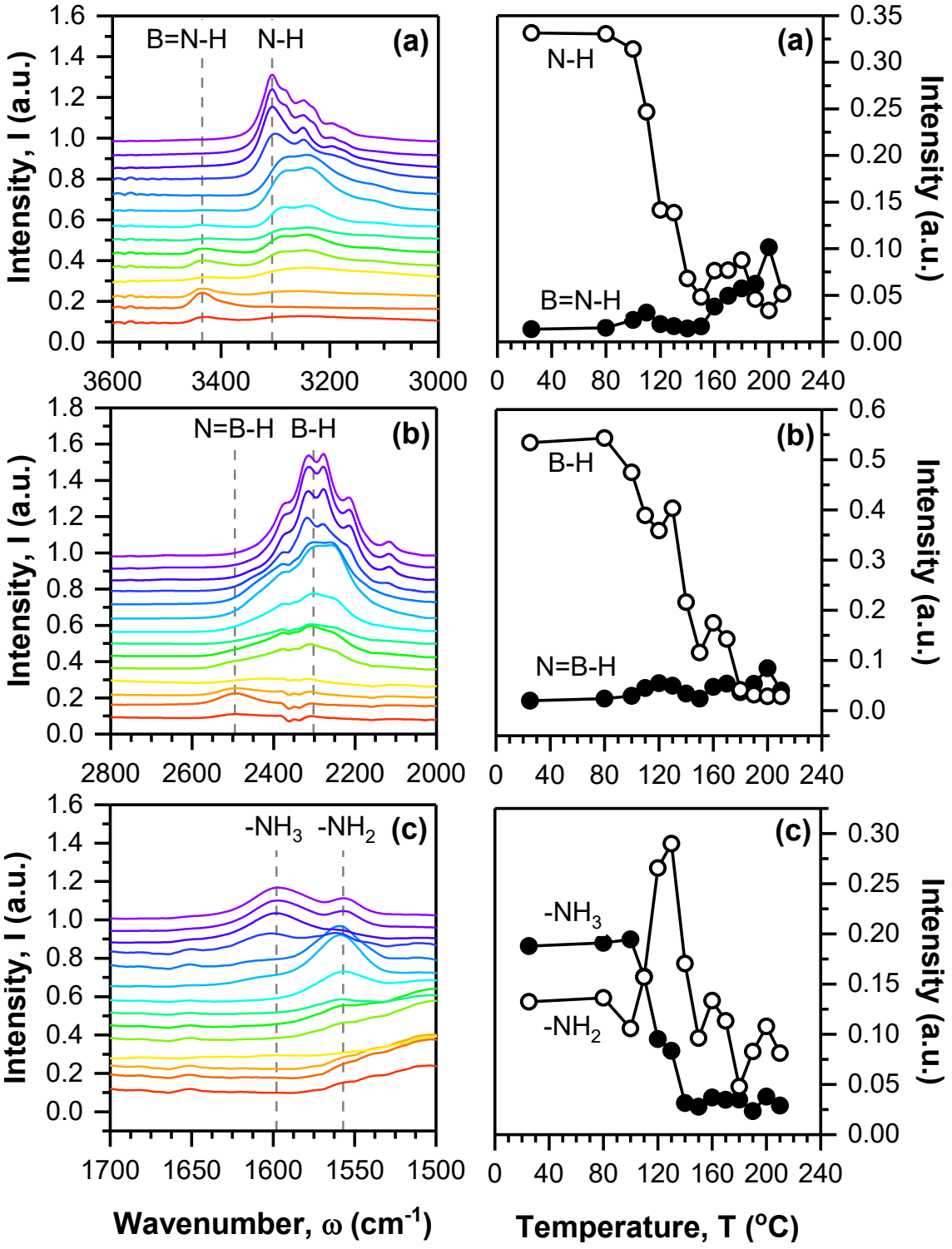

Figure 4.30: TGA-FTIR analysis of thermolytic dehydrogenation of bulk AB between 25-210 °C, showing 1D-IR spectra and absorption intensity in wavenumber regions (a) through (f) between 4000-400 cm^{-1}. Note: spectra have been stacked for visual clarity, however actual values are reported on the corresponding intensity plots.

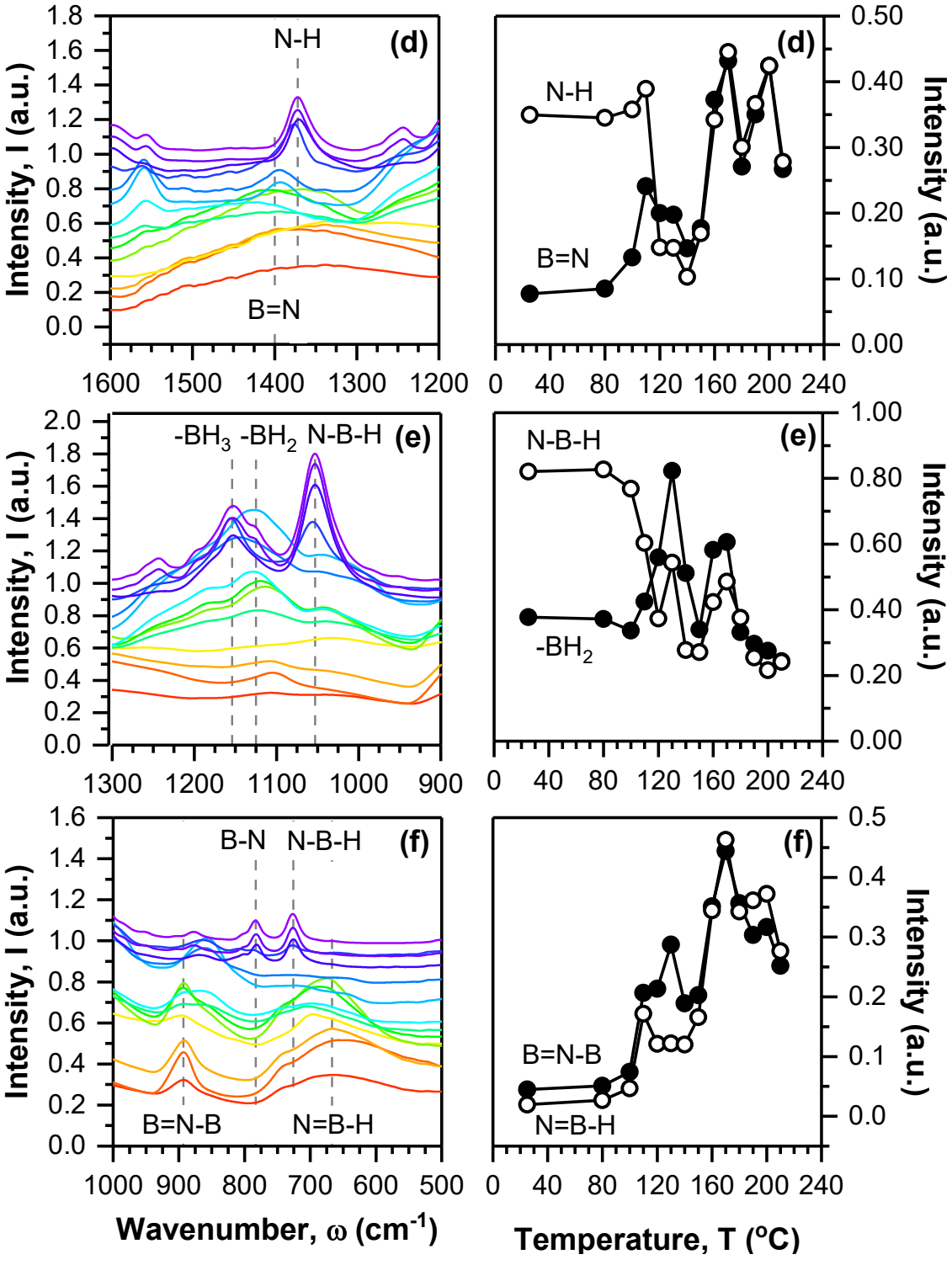

Figure 4.30 (Continued): TGA-FTIR analysis of thermolytic dehydrogenation of bulk AB between 25-210 °C, showing 1D-IR spectra and absorption intensity in wavenumber regions (a) through (f) between 4000-400 cm^{-1}. Note: spectra have been stacked for visual clarity, however actual values are reported on the corresponding intensity plots.

In an attempt to understand the initial stages of dehydrogenation, the spectra for bulk AB between 25-130 ^{o}C were subsequently analysed using 2D-IR correlation spectroscopy. For visual clarity, the resulting 2D-IR spectra have been presented between two separate regions to magnify their features, namely those between 4000-2000 cm^{-1} and 1700-600 cm^{-1} in Figure 4.31(a)-(b) and (c)-(d) respectively. The magnitude of these synchronous and asynchronous correlations have been quantified in Table 4.20 alongside their proposed assignments to aid subsequent discussion. Notably, comparison of the 1D-IR spectra from 25-130 ^{o}C in Figure 4.30(b) and the 2D-IR spectra in Figure 4.31(a)-(d) showed a degree of shifting between the bands of the former and the crosspeaks of the latter. This was conceivably due to the *ex situ* measurements taken during these analyses, which likely introduced slight variation between the spectra at each temperature and so disrupted the subsequent correlations. Despite this, assignment of shifted crosspeaks to corresponding bands was mostly intuitive when examining the respective wavenumbers. These have been discussed below with reference to their Indices in Table 4.20.

Generally, the results from these analyses further evidenced the conventional understanding that thermolytic dehydrogenation of bulk AB initially progressed through PAB, as described in Figure 2.3 (Demirci, 2017a). This was extensively evidenced by the observation that the appearance of tetragonal $–NH_2$ and $–BH_2$ lagged behind the preceding disappearance of corresponding $–NH_3$ and $–BH_3$ modes, with several strong correlations observed (Index 6, 7, 10 and 11). These changes were reflected by the fact that changes in N-B-H modes generally occurred before the above modes, presumably due to cleavage of the coordinate B-N bond, with especially strong correlations observed for the effect on $–BH_2$, $–BH_3$ and tetragonal B-N modes (Index 16, 21 and 23). Contrastingly, substantially weaker correlations were observed for $–NH_2$ and $–NH_3$ modes, despite intuition suggesting changes to the coordinate B-N bond would equally affect the $–NH_3$ and $–BH_3$ moieties of AB.

Nevertheless, several other significant correlations suggested additional complexities. For instance, strong correlations were observed that indicated the formation of tetragonal B-N modes occurred simultaneously to reductions in $–BH_3$ (Index 29) but lead subsequently delayed increases in $–BH_2$ modes (Index 27). However, correlations for the $–NH_3$ and $–NH_2$ counterparts were much weaker and both suggested concerted change to the tetragonal B-N. Also noteworthy were the distinct changes observed for free NH_3. Whilst the appearance of free NH_3 occurred entirely synchronously to the reduction in N-B-H (Index 19), again explained by cleavage of the coordinate B-N bond, its increased was entirely asynchronous compared to changes in both $–BH_3$ and $–BH_2$ (Index 3 and 13). According to literature, such occurrences are rather rare and suggest the sequential order of the changes is indeterminable (Noda and Ozaki, 2004)

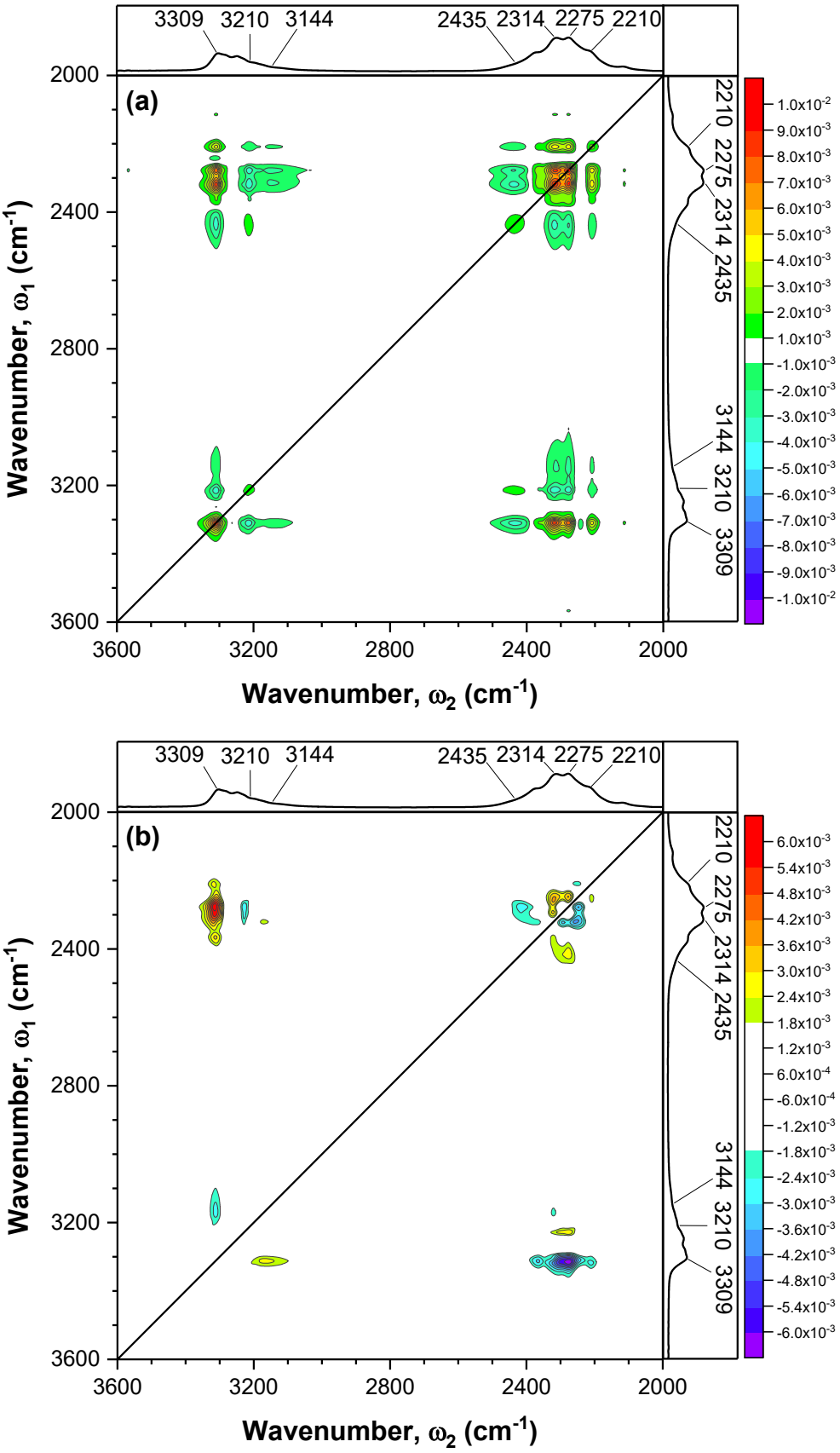

Figure 4.31: 2D-IR analyses for thermolytic dehydrogenation of bulk AB between 25-130 °C, showing synchronous and asynchronous plots for (a)-(b) 3600-2000 cm^{-1} and (c)-(d) 1700-600 cm^{-1} respectively.

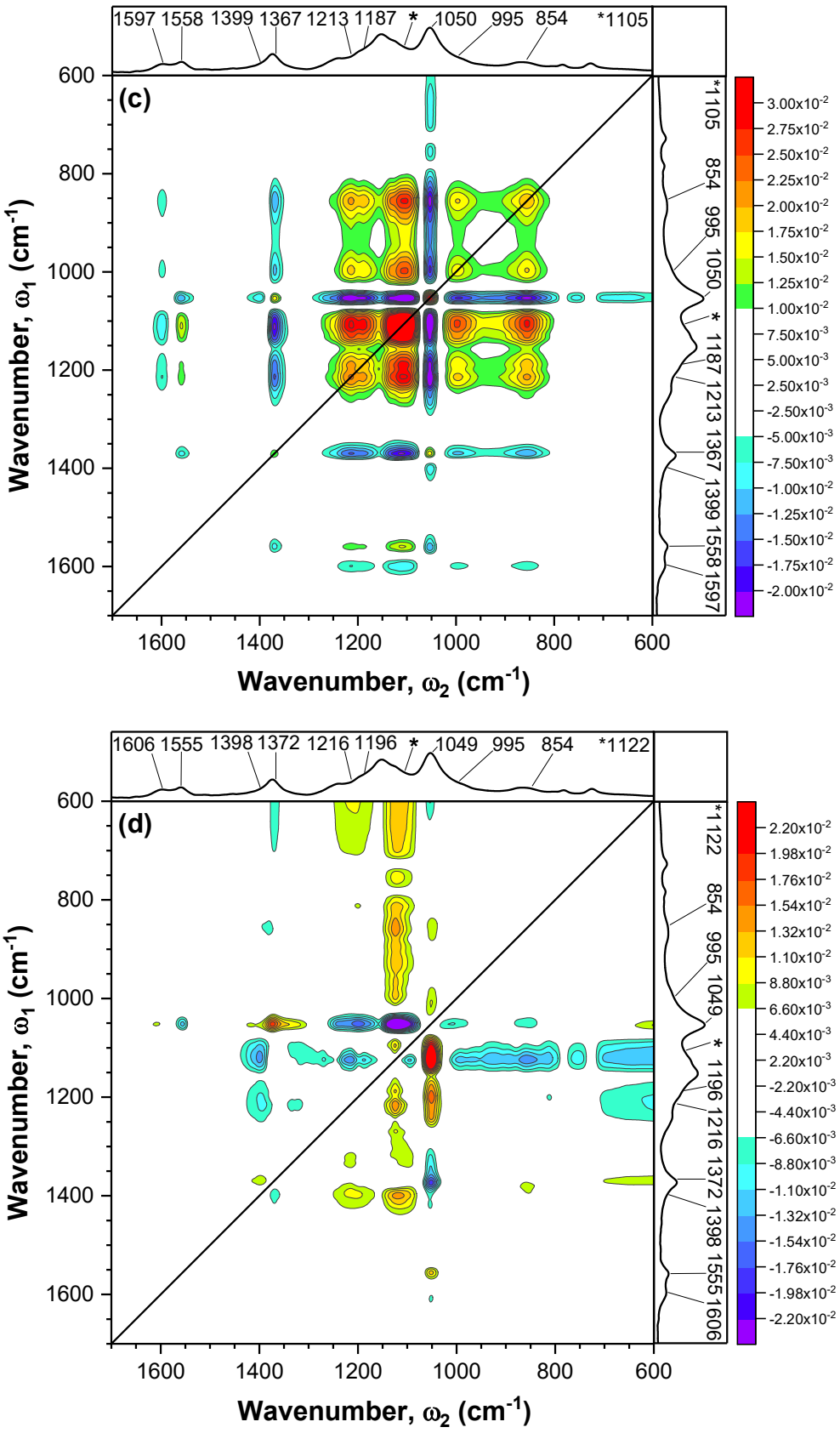

Figure 4.31 (Continued): 2D-IR analyses for thermolytic dehydrogenation of bulk AB between 25-130 °C, showing synchronous and asynchronous plots for (a)-(b) 3600-2000 cm^{-1} and (c)-(d) 1700-600 cm^{-1} respectively.

Table 4.20: 2D-IR synchronous and asynchronous correlations for thermolytic dehydrogenation of bulk AB between 25-130 °C, as seen in Figure 4.31.

	Synchronous			Asynchronous			Species 1	Effect[a]	Species 2
	Value	ω_1 (cm^{-1})	ω_2 (cm^{-1})	Value	ω_1 (cm^{-1})	ω_2 (cm^{-1})			
1	+0.008	2314	3309	+0.006	2297	3309	$-BH_3$	leads	$-NH_3$
2	+0.007	2275	3309	+0.006	2276	3309	$-BH_3$	leads	$-NH_3$
3	-	-	-	-0.010	1190	1397	$-BH_3$	async with	Free NH_3
4	-0.010	1369	1558	-	-	-	$-NH_2$	sync with	$-NH_3$
5	-0.010	1560	2276	+0.007	1560	2276	$-NH_2$	lags	$-BH_3$
6	**-0.020**	**1112**	**1369**	**+0.006**	**1125**	**1365**	**$-BH_2$**	**lags**	**$-NH_3$**
7	**+0.029**	**1107**	**1191**	**-0.010**	**1125**	**1189**	**$-BH_2$**	**lags**	**$-BH_3$**
8	+0.015	1109	1558	-0.010	1122	1562	$-BH_2$	lags	$-NH_2$
9	-0.010	1107	1599	-	-	-	$-BH_2$	sync with	$-NH_3$
10	**-0.020**	**1106**	**3309**	**+0.011**	**1127**	**3309**	**$-BH_2$**	**lags**	**$-NH_3$**
11	**-0.020**	**1103**	**2317**	**+0.017**	**1122**	**2312**	**$-BH_2$**	**lags**	**$-BH_3$**
12	-0.010	1103	2276	+0.020	1111	2276	$-BH_2$	lags	$-BH_3$
13	-	-	-	-0.010	1125	1397	$-BH_2$	async with	Free NH_3
14	+0.016	1055	2317	-	-	-	N-B-H	sync with	$-BH_3$
15	+0.015	1055	2276	-0.010	1055	2276	N-B-H	lags	$-BH_3$
16	**-0.030**	**1055**	**1106**	**-0.030**	**1054**	**1124**	**N-B-H**	**leads**	**$-BH_2$**
17	+0.016	1054	3309	+0.007	1052	3309	N-B-H	leads	$-NH_3$
18	-0.010	1054	1558	-0.010	1054	1557	N-B-H	leads	$-NH_2$
19	-0.010	1054	1397	-	-	-	N-B-H	sync with	Free NH_3
20	+0.016	1054	1369	+0.018	1052	1368	N-B-H	leads	$-NH_3$
21	**-0.020**	**1054**	**1191**	**-0.020**	**1055**	**1190**	**N-B-H**	**leads**	**$-BH_3$**
22	+0.008	1053	1599	+0.006	1053	1599	N-B-H	leads	$-NH_3$
23	**-0.020**	**858**	**1053**	**+0.008**	**856**	**1053**	**Tetr B-N**	**lags**	**N-B-H**
24	-0.010	857	2317	+0.005	862	2315	Tetr B-N	lags	$-BH_3$
25	-0.010	857	2276	+0.007	856	2276	Tetr B-N	lags	$-BH_3$
26	-0.010	857	1369	-0.010	857	1369	Tetr B-N	lags	$-NH_3$
27	**+0.028**	**857**	**1106**	**+0.015**	**857**	**1124**	**Tetr B-N**	**leads**	**$-BH_2$**
28	-0.010	856	3309	-	-	-	Tetr B-N	sync with	$-NH_3$
29	+0.019	856	1191	-	-	-	Tetr B-N	sync with	$-BH_3$
30	+0.010	855	1558	-	-	-	Tetr B-N	sync with	$-NH_2$

[a] Effects: Lags = Change in (1) occurs after change in (2) , **Leads** = Change in (1) occurs before change in (2), **Sync with** = Change in (1) occurs simultaneously to change in (2), **Async with** = Change in (1) occurs unrelated to (2) (unusual event for which sequential order indeterminable).

4.3.2 **Release Mechanism from Nanoconfined AB/TA(L)**

An identical exercise was conducted for nanoconfined AB/TA(L) involving analogous non-isothermal TGA and *ex situ* FTIR analyses. At the onset additional analyses were conducted for unloaded TA(L) in order to compensate for the underlying spectra of TA(L) within AB/TA(L), as seen in Figure 4.32(a)-(c) overleaf. Nevertheless, the relative intensities of the spectral bands for TA(L) remained in proportion throughout the entire examined temperature range, suggesting they would offer negligible conflation in subsequent study of AB/TA(L). Hence, the TGA and 1D-IR data for TA(L) was deemed of little scientific interest and not so a detailed analysis was not conducted. The corresponding analyses for AB/TA(L) have been presented in Figure 4.33(a)-(c) with the mass loss data compiled in Table 4.21

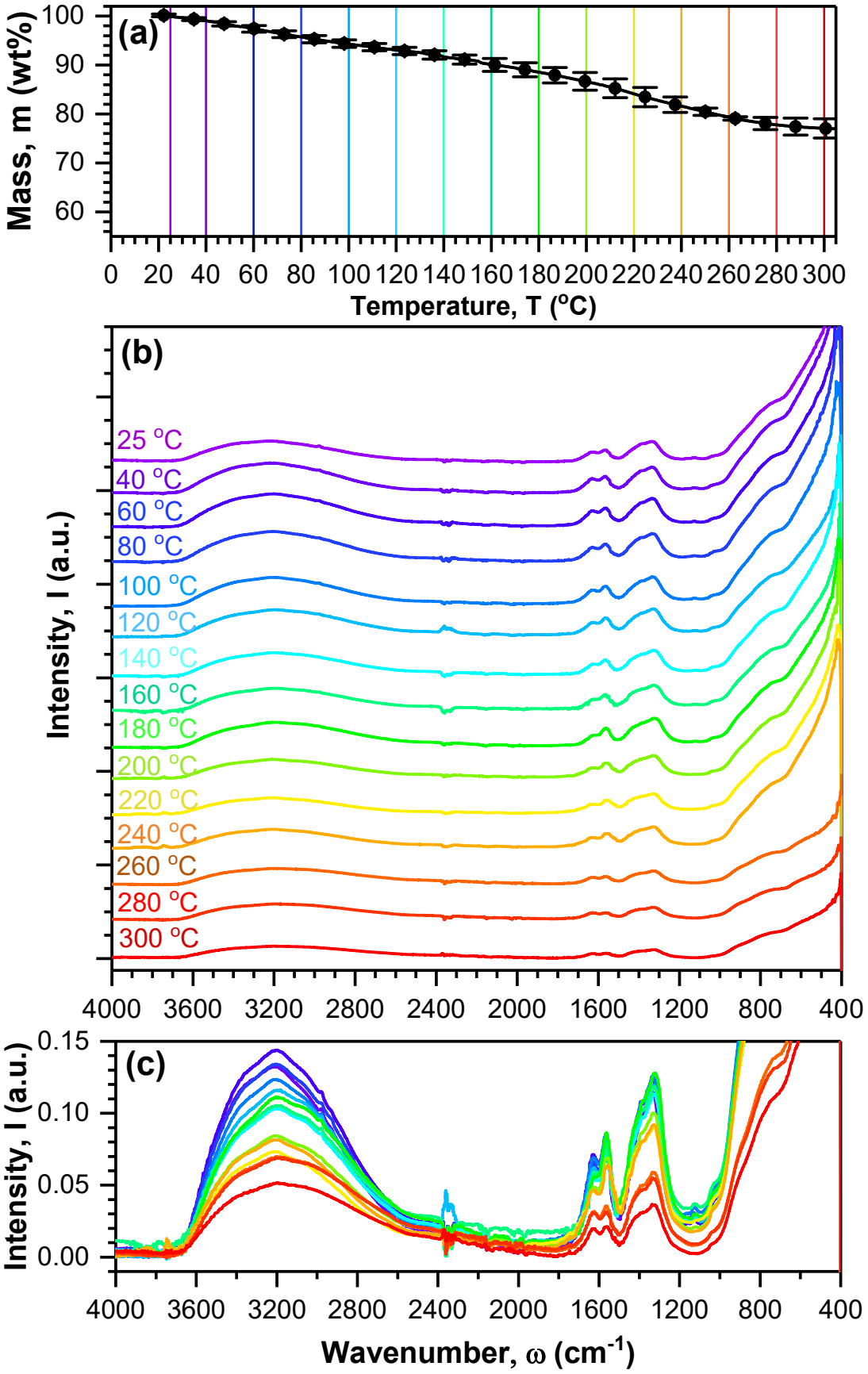

Figure 4.32: Comparison of (a) mass loss from TGA, compared to (b) stacked and (c) unstacked 1D-IR spectra for unloaded TA(L) with *ex situ* heating from 25-300 °C. The temperature of the spectra are indicated by the coloured vertical lines.

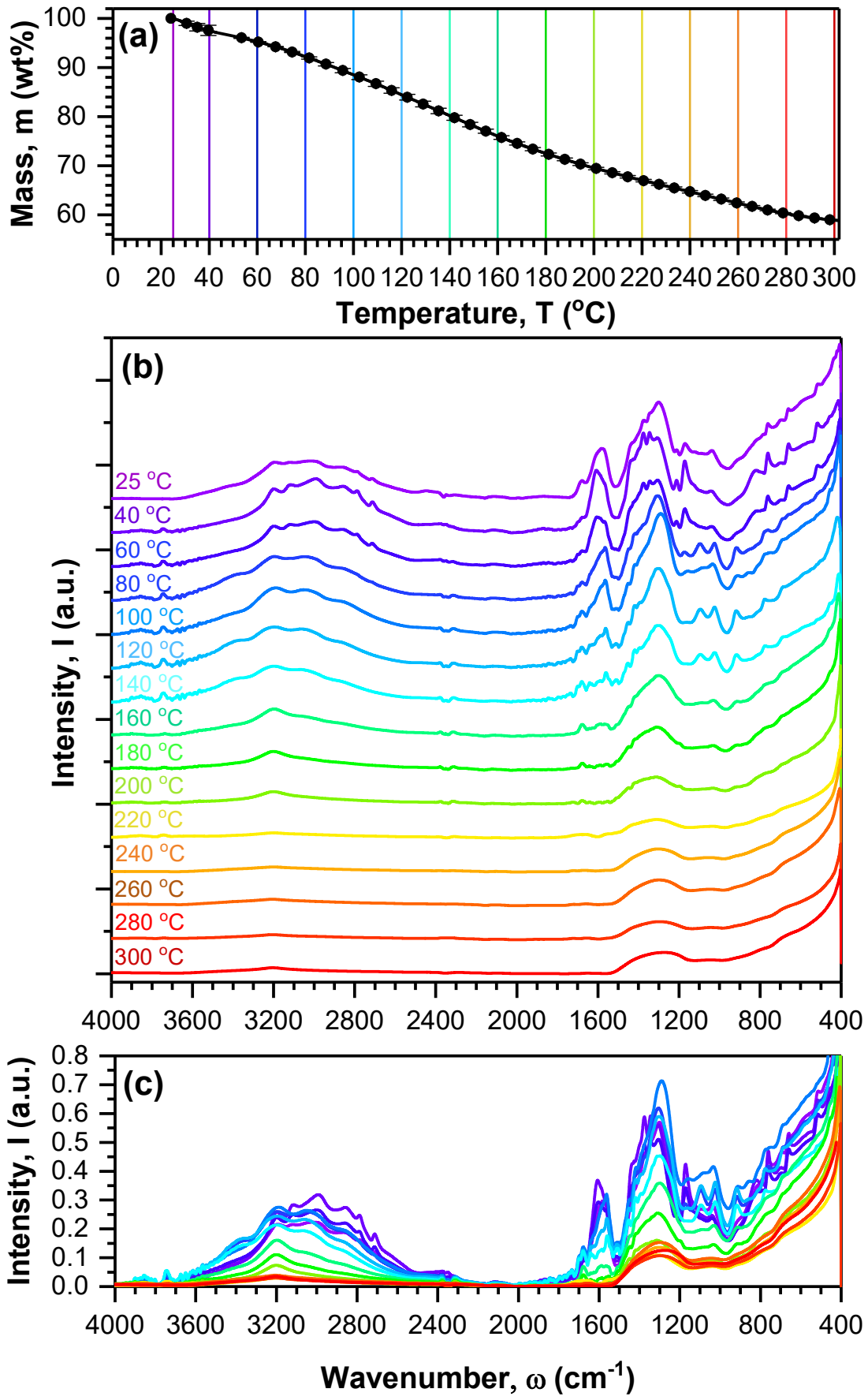

Figure 4.33: Comparison of (a) mass loss from TGA, compared to (b) stacked and (c) unstacked 1D-IR spectra for nanoconfined AB/TA(L) with *ex situ* heating from 25-300 °C. The temperature of the spectra are indicated by the coloured vertical lines.

Table 4.21: Summary of TGA/DTG analyses of nanoconfined AB/TA(L)

Temperature, T (°C)	Mass, m (wt%)	Mass Loss, dm (wt%)	Rate of Loss, dm/dT (wt%/°C)
25	99.9	0.1	0.12
40	97.5	2.5	0.15
60	95.3	4.7	0.13
80	92.2	7.8	0.17
100	88.5	11.5	0.19
120	84.5	15.5	0.21
140	80.2	19.8	0.22
160	76.1	23.9	0.19
180	72.5	27.5	0.16
200	69.6	30.4	0.13
220	67.1	32.9	0.12
240	64.7	35.3	0.12
260	62.4	37.6	0.12
280	60.2	39.8	0.09
300	58.9	41.1	0.05

Examination of Figure 4.33 showed the 1D-IR spectra could be grouped into three ranges that each appeared to exhibit distinct spectral characteristics, namely 25-60, 80-200, and 220-300 °C. These temperature range correlated well with those previously identified for each of the mass losses occurring in nanoconfined AB/TA(L), namely 25-53, 53-213 and 252-329 °C as presented in Table 4.10. This suggested distinct release reactions occurring during each of these temperature ranges. Initially (T = 25-60 °C), the spectra exhibited evidenced for the previously discussed vibrational modes for N–H, B–OH, C=O and C–N–H bands (as well as the highly convoluted set of bands which could not be assigned). The severe extent of degradation during storage prior to these experiments can be seen by the practical absence of B–H modes between 2600-2200 cm^{-1}, which were barely visible on Figure 4.33(b)-(c). Upon heating, these bands exhibited subtle changes that became significantly more pronounced upon reaching 80 °C, with several bands transiently increasing before they steadily decreased throughout further heating (T = 80-200 °C). Following this range, further elevation in temperature (T = 200-300 °C) seemingly had inconsistent effects, which was attributed to experimental error since the heating method for *ex situ* FTIR analyses used a rapid temperature ramp ($\beta \approx 40$ °C/min) whereas that indicated on Figure 4.33(a) proceeded at a slower rate ($\beta \approx 5$ °C/min).

Irrespective, the disproportionate changes in the 1D-IR spectra of Figures 4.33(b)-(c) pointed toward the occurrence of novel dehydrogenation reactions, reflected in the changing composition of bonds within the sample. Since the bands within TA(L) were seen to remain approximately in proportion throughout heating in Figure 4.32, these changes must have derived from the (now degraded) nanoconfined AB. In particular, the substantial shift in N-H stretching modes between 60-80 °C evidenced a distinct change in the nanoconfined AB that

was consistent with the peak temperatures of mass loss previously identified in Figure 4.27(b). Thus, in spite of severe degradation during storage, a considerable quantity of chemical species were available for reaction AB/TA(L). Despite degradation complicating further analyses, for a superficial comparison to bulk AB the onset of dehydrogenation in AB/TA(L) was also analysed by 2D-IR correlational spectroscopy. This has been presented between 3800-2400 cm^{-1} and 1800-400 cm^{-1} in Figure 4.34(a)-(b) and (c)-(d) respectively. These results showed several correlations generally concentrated in the stretching region between 3400-2600 cm^{-1} and in the highly convoluted region existing between 1700-1100 cm^{-1}. In the former region, relatively strong purely synchronous correlations were observed between bands at 3110, 2984, and 2853 cm^{-1}, but interestingly not for the bands at 3196, 2784 and 2707cm^{-1}. The purely synchronous correlations between bands at 3110, 2984, and 2853 cm^{-1} were thus attributed to N-H stretching, whereas the lack of correlation for the band at 3196 cm^{-1} suggested this as unrelated and therefore evidenced to be B-OH. In contrast, within the latter region between 1700-1100 cm^{-1}, other correlations were observed however their position within the highly convoluted region meant their identities could not be assigned. Without confident assignments of the spectral bands, any further examination of AB/TA(L) would be highly speculative and any assertions ultimately questionable.

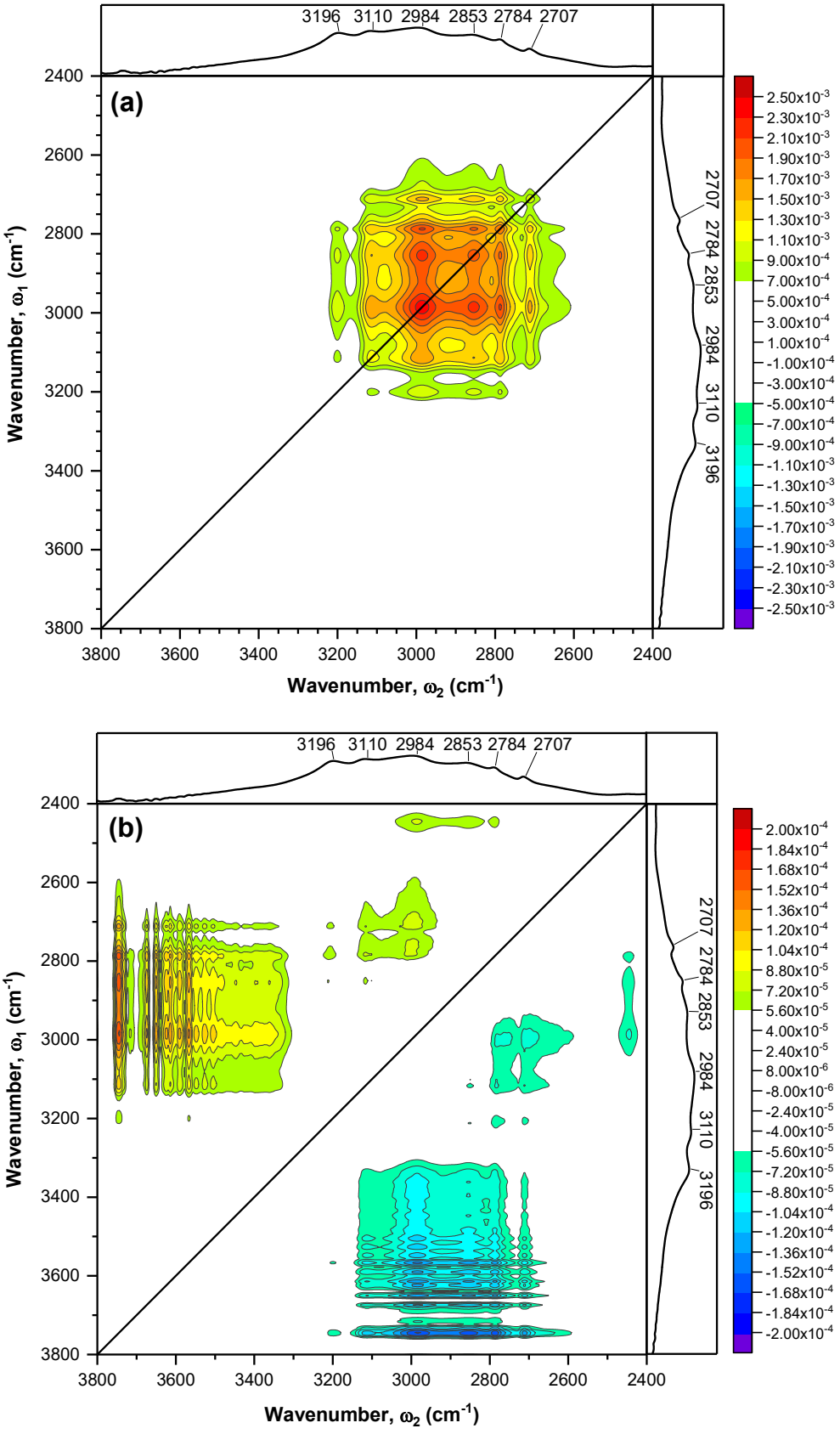

Figure 4.34: 2D-IR analyses for thermolytic dehydrogenation of nanoconfined AB/TA(L) between 25-60 °C, showing synchronous and asynchronous plots for (a)-(b) 3800-2400 cm^{-1} and (c)-(d) 1800-400 cm^{-1} respectively.

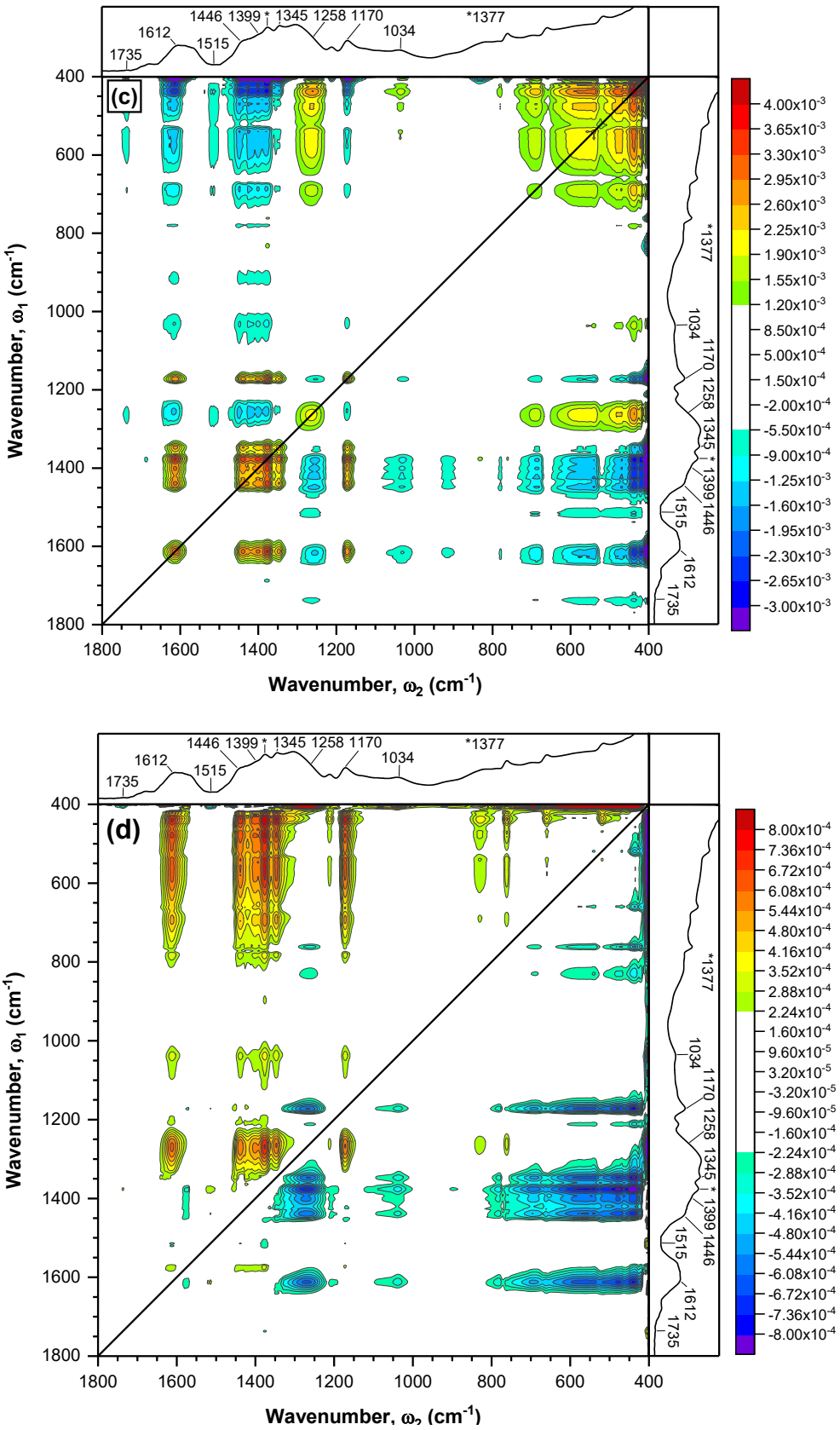

Figure 4.34 (Continued): 2D-IR analyses for thermolytic dehydrogenation of nanoconfined AB/TA(L) between 25-60 °C, showing synchronous and asynchronous plots for (a)-(b) 3800-2400 cm^{-1} and (c)-(d) 1800-400 cm^{-1} respectively.

4.3.3 **Discussion of Results**

In summary, these analyses interrogated the thermolytic dehydrogenation of bulk AB using a combination of TGA and FTIR analyses in order to fundamentally relate temperature, mass loss and changes in chemical bonding within the material. Particular focus was placed on the initial stages of mass loss (T = 25-130 ^{o}C) with the intention of understanding the chemical reactions that constitute the onset of hydrogen release. To achieve this, the 1D-IR spectra gathered using FTIR were analysed using 2D-IR correlational spectroscopy such that the relation between spectral bands could be observed. Although a range of 1D-IR studies of dehydrogenation from bulk AB have been reported in literature (Babenko *et al.*, 2017)(Frueh *et al.*, 2011)(Zhang *et al.*, 2011), the application of 2D-IR correlation spectroscopy has not thus been explored. This research demonstrated its use with varying levels of success. Whereas the study of bulk AB was rather successful, the same process applied to AB/TA(L) was ultimately hindered by degradation of the sample prior to analyses and highlighted several technical shortcomings in the 2D-IR technique.

With regard to bulk AB, the majority of experimental results and analyses reflected conventional understanding that thermolytic dehydrogenation of bulk AB progressed through PAB and PIB (Bowden and Autrey, 2011). This can be seen by the resemblance of the TGA and 1D-IR spectra to previously reported data in literature (Frueh *et al.*, 2011)(Zhang *et al.*, 2011)(Li *et al.*, 2015). Between 25-80 ^{o}C, the lack of release was evidenced by negligible mass loss from bulk AB (Δm = 0.6 wt%) and undetectable change in the respective 1D-IR spectra at these temperatures. Nevertheless, upon heating to 100 ^{o}C, the onset of significant mass loss was observed (Δm = 2.3 wt%) which was accompanied by subtle shifting and broadening in the 1D-IR spectra. Broadening was particular evident in the N–H and B–H stretching modes, which was consistent with disruption of the intermolecular (N-$H^{\delta+}\cdots H^{\delta-}$-B) bonding network that normally stabilise bulk AB (Rueda *et al.*, 2017) (Bowden and Autrey, 2011). The rapid loss of mass that then occurred between 100-130 ^{o}C was complemented by analogous reductions in the modes associated with N–H, B–H, N–B–H, and B–N vibrations (Frueh *et al.*, 2011). Alongside this reduction was the contrasting increase in modes indicative of tetragonal $–NH_2$, $–BH_2$, and B–N (Frueh *et al.*, 2011), which was consistent with the dehydrogenation of AB to produce the anticipated structure of PAB. However, the increases in these modes were seen to be transient and subsequently reduced upon heating thereafter (between 130-210 ^{o}C). Coincidental to this change was the growth in bands that resembled PIB, including N=B–H, B=N–H and B=N–B modes (Frueh *et al.*, 2011). The onset for these modes was between 100-130 ^{o}C, indicating nominal production of PIB alongside PAB. Such bonding at this temperature has been previously evidenced by the observation of volatilised BZ between 100-130 ^{o}C (Frueh *et al.*, 2011)(Lai *et al.*, 2012).

Further insight to the dehydrogenation from bulk AB was gained from the complementary 2D-IR spectra, which examined the onset of hydrogen release in an attempt to understand the initial reaction mechanism. These analyses generally supported the current empirical understanding of dehydrogenation from AB (Petit and Demirci, 2018), but also found additional complexities. Specifically, conventional understanding in literature predicts that intermolecular heteropolar (N-$H^{\delta+}\cdots H^{\delta-}$-B) interactions predominate throughout the reaction (as depicted in Figure 2.4)(Wolstenholme *et al.*, 2012)(Al-kukhun, Hwang and Varma, 2012), which would conceivably manifest as strong synchronous (Φ) and weak asynchronous (Ψ) correlations between the opposing $-NH_3$ and $-BH_3$ moieties (since interaction of one with the other will effect dehydrogenation to effect $-NH_2$ and $-BH_2$ respectively). No such correlations were observed, and instead only weak correlations (Φ = +0.007, Ψ = +0.006) were seen that implied reductions in $-BH_3$ lead subsequent reductions in $-NH_3$. Although these correlations were weak, their detection in spite of the above hypothesis suggested changes on the $-BH_3$ side of AB were critical for driving subsequent dehydrogenation. This was generally supported by the observation that correlations for groups deriving from the $-BH_3$ side of AB showed stronger correlations than those from the opposing $-NH_3$ side. Overall, this was believed to strongly evidence the occurrence of homopolar (B-$H^{\delta-}\cdots H^{\delta-}$-B) interactions (Wolstenholme *et al.*, 2012) (Al-kukhun, Hwang and Varma, 2012) (Petit and Demirci, 2018), as discussed further herein.

Among the strongest correlations, it was seen that reductions in N-B-H modes principally occurred before decreases in $-BH_3$ (Φ = -0.020, Ψ = -0.020), as well as before increases in both $-BH_2$ (Φ = -0.030, Ψ = -0.030) and tetragonal B-N (Φ = -0.020, Ψ = +0.008). However, similarly strong correlations found tetragonal B-N to form entirely synchronously with reductions in $-BH_3$ (Φ = +0.019, Ψ = n.d.), but before the progressive formation of $-BH_2$ (Φ = +0.028, Ψ = +0.015). This was reinforced by strong correlations that found the formation of $-BH_2$ lagged behind decreases in both $-BH_3$ (Φ = +0.029, Ψ = -0.010) and $-NH_3$ (Φ = -0.020, Ψ = +0.011). Apart from those explicitly mentioned above, the corresponding correlations for the $-NH_3$ groups were either not detected or substantially weaker. Again, this general observation was inconsistent with heteropolar interactions and instead evidenced the important role of the $-BH_3$ side during dehydrogenation, thereby evidencing the occurrence of homopolar (B-$H^{\delta-}\cdots H^{\delta-}$-B) interactions.

Based on the order of precedence outlined above, the reductions in N-B-H were thought to be the first detected change in chemical bonding and were believed due to the cleavage of the dative B-N bond forming free NH_3 and BH_3, supported by the (albeit weak) entirely synchronous correlation between N-B-H and free NH_3 (Φ = -0.010, Ψ = n.d.). This correlation identified the simultaneous release of free NH_3 upon cleavage of the B-N bond. Unfortunately,

a band corresponding to free BH_3 could not be identified for counterpart correlations between N-B-H and free BH_3. In any case, the role of free NH_3 in the onset of hydrogen release was discredited by the finding of purely asynchronous correlation with both $-BH_3$ and $-BH_2$, which therefore suggested no relation and an indeterminable sequential order (Noda and Ozaki, 2004). Indeed, free NH_3 did not correlate with any vibrational modes, leading to the suggestion it was unrelated to dehydrogenation of AB. This might be explained by the umbrella mode of free NH_3 being highly detectable even at low concentrations (Frueh *et al.*, 2011), meaning even small amounts of NH_3 were detectable. Importantly however, the formation of tetragonal B-N occurred entirely synchronously with reductions in $-BH_3$ ($\Phi = +0.019$, Ψ = n.d.), but before subsequent formation of $-BH_2$. This was believed to fundamentally evidence homopolar ($B\text{-}H^{\delta-}\cdots H^{\delta-}\text{-}B$) interactions, since the formation of tetragonal B-N is indicative of the key intermediate DADB (Chen *et al.*, 2012), and this result directly implicates the $-BH_3$ side of AB during this process. Yet again, the formation of tetragonal B-N was substantially less correlated with $-NH_3$ and $-NH_2$, further highlighting the significance of the opposing $-BH_3$ species. Although previous research has supposedly detected the occurrence of homopolar ($B\text{-}H^{\delta-}\cdots H^{\delta-}\text{-}B$) interactions based thermolysis of deuterium labelled AB (ND_3BH_3 or NH_3BD_3) (Wolstenholme *et al.*, 2012) (Al-kukhun, Hwang and Varma, 2012), their results were underpinned on the complete absence of hydrogen-exchange in the molecules of AB prior to (or indeed during) thermolysis (Petit and Demirci, 2018). This result appears to provide the first spectroscopic evidence that confirms these homopolar interactions without the possibility of hydrogen-exchange.

Conversely, regarding the analysis of nanoconfined AB/TA(L), the validity of the experiments was generally compromised by the degradation observed in the sample. Although relatively high amounts of N-H stretching were observed, the corresponding bands for B-H stretching were significantly reduced, indicating degradation during storage ($t \approx 2$ months). Somewhat interestingly, this result appeared to show degradation selectively occurred on the $-BH_3$ side of nanoconfined AB, with a larger proportion of the $-NH_3$ counterpart retained within TA(L). Similar observations have been made during the heating of bulk AB (Al-kukhun, Hwang and Varma, 2012), suggesting the degradation followed the same fundamental process but greatly accelerated. Furthermore, this was in agreement with reports in literature for the reaction of nanoconfined AB and the TA(L) to form the corresponding B-O functionality, resulting in a larger proportion of $-BH_3$ degradation compared to $-NH_3$. This was later supported by the detection of the band at around 3200 cm^{-1} which on 2D-IR plots did not appear to correlate with surrounding N-H stretching modes, giving rise to the suggestion that it was due to stretching modes of B-OH (Moon *et al.*, 2004).

Nonetheless, despite identifying the presence of distinct dehydrogenation reactions (as opposed to simply desorption), the analysis of AB/TA(L) by 2D-IR was ultimately unsuccessful and highlighted some of the relative weaknesses of the analytical technique. The complicated composition of AB/TA(L) was reflected in the convoluted region between 1700-1100 cm^{-1}, which could not be deconvoluted to allow confident assignment of the underlying bands. Hence, despite subsequent 2D-IR plots showing some strong correlations, these could not be meaningfully interpreted since the assignments of the correlations could only be speculated. This appeared to highlight an intrinsic shortcoming of the study of this material with FTIR, which evidently was unable to sufficiently resolve the bands belonging to the nanoconfined AB and/or TA(L). Nevertheless, an interesting proposition from this research would be to repeat these analyses with solid-state NMR, which depending on the probe could selectively analyse the nanoconfined AB. Previous studies have used various forms of NMR with good effect (Penner, Chang and Hutzal, 1999) (Al-kukhun, Hwang and Varma, 2012) (Petit and Demirci, 2018) (Kobayashi *et al.*, 2014). Subsequent application of analogous 2D-NMR correlational spectroscopy might then be applied and realise more meaningful results.

5.0 Conclusions

5.1 Summary of Research

In summary, the continued combustion of fossil hydrocarbons to meet the global energy demand is widely considered unsustainable and there is substantial motivation to transition toward renewable energy sources. Nevertheless, these renewable energy sources are challenged by their unreliability and intermittency, which necessitate the installation of robust energy storage systems. Hydrogen is an attractive option for energy storage and alternative fuel, but widespread adoption is confronted by a number of challenges including the insufficient performance exhibited by current storage technologies. One storage candidate that exhibits considerable promise is the chemical hydride ammonia borane (AB). Whilst AB demonstrates several exceptional properties, there are nonetheless challenges that require resolution in order to satisfy internationally recognised storage targets. These principally include (i) accelerating release of hydrogen at lower temperatures, (ii) reducing volatilisation of gaseous contaminants, and (iii) formation of specific polymeric residues that enable facile regeneration. Significant progress towards these objectives has been made by nanoconfinement of AB within a porous support, with previous research examining a range of materials including carbon, metal oxides, aerogels, metal-organic frameworks, polymers, and others. Current opinion is the surface properties of the support are central in determining the dehydrogenation of nanoconfined AB, however there persists considerable uncertainty about their precise role in affecting dehydrogenation, with various mechanisms being proposed.

Research in this field has predominantly examined nanoconfinement of AB within silica materials, for which excellent results have been widely reported. In comparison, the application of titania has been largely unexplored, and mostly limited to as a support for an active metal catalyst during hydrolytic dehydrogenation. Sparingly little research has studied the effect of titania on the thermolytic dehydrogenation of AB, yet under controlled experiments solid-state doping of AB with titania show improved performance relative to bulk AB as well mixtures with silica dopant. Specifically, doping of AB with titania was proposed to disrupt the stabilising intermolecular dihydrogen bonding between molecules of AB and accelerate the formation of key reaction intermediates which proceeded the rapid release of hydrogen. Separately, numerous publications detail the preparation of highly porous titania aerogels that exhibit remarkable surface properties which could be advantageously applied to nanoconfinement of AB. The intersection of these fields suggested considerable potential for the nanoconfinement of AB within titania aerogels to greatly accelerate hydrogen release, forming the fundamental basis for this research.

5.1.1 Characterisation of Synthesised Titania Materials

As such, one aim of this programme of research was the preparation of titania aerogels that could be subsequently applied to nanoconfinement of AB. After their preparation, the material properties of these aerogels were thoroughly characterised and compared against conventionally precipitated titania. Different methods of preparation were examined which included the production of particulate aerogels that underwent solvent extraction with either liquid (LCO_2) or supercritical (SCO_2) carbon dioxide, effecting materials referred to as TA(L) and TA(S) respectively. A further method prepared monolithic aerogels using SCO_2, with the resulting material accordingly referred to as TA(S,M). These aerogels were compared to precipitated materials that underwent solvent removal by evaporative drying at 65 ^oC, indicated as TP(65). Characterisation of these materials included their surface, textural, particle, crystalline and thermal properties, as well as their chemical composition.

Hence, a minor novelty of this research is a new method of preparation for amorphous titania aerogels with excellent surface properties. Overall, these experiments found TA(S,M) to highly competitive surface properties including remarkable surface area (S_{BET} = 660 m^2/g), pore volume (V_P = 1.17cm^3/g) and controlled mesoporosity (d_P = 17 nm). These were amongst the highest values reported in literature for such materials, demonstrating the effectiveness of the preparation method. Whereas, TA(S) and TA(L) offered comparatively reduced surface properties that were nonetheless competitive with those reported in literature, offering high surface area (S_{BET} = 450-523 m^2/g), moderate pore volumes (V_P = 0.2-0.6 cm^3/g) and limited mesoporosity (d_P = 30-39 nm). In comparison to TP(65), these materials demonstrated statistically significant improvements across most surface properties, evidencing the distinct advantages of materials synthesised by the aerogel preparation method as opposed to precipitation and evaporative drying.

Comparisons between the synthesised aerogel materials provided further insight to the effect of several preparation conditions. Comparison of TA(L) and TA(S) showed extraction with LCO_2/SCO_2 effected highly similar materials that only differed with regard to their respective pore diameters. This confirmed existing understanding of partial pore collapse due to capillary forces in LCO_2, leading to reduced pore volumes and less mesoporous characteristic. Similarly, comparison of TA(S) and TA(S,M) showed the comprehensively improved surface properties achieved by the preparation of particular and monolithic aerogels. This appears to be the first direct comparison of such aerogels synthesised at otherwise identical conditions, with the differences exclusively due to the monolithic versus particulate forms. These results suggested better and more uniform surface properties can realised within aerogel materials by preparation of monoliths as opposed to particulates.

A somewhat more significant finding from this research was the presence of carboxylate functionality on the surfaces of TA(L) and TA(S), evidenced to be surface bicarbonate species. Although the formation of such surface species on titania materials has been generally reported before, their preparation typically requires the inclusion of precursors such as carboxylic acids. Whereas, this research found their formation resulted during the solvent removal process when surface hydroxyls (TiOH) on the incipient aerogel reacted with the surrounding LCO_2/SCO_2. Such a result is unreported in the reviewed aerogel literature, at this time suggesting this is the first report for the preparation of such functionalised surfaces by contacting with LCO_2/SCO_2. The distinct characteristic of this preparation compared to those previously reported is lack of requirement for carboxylic additives during synthesis. This material was subsequently applied to the nanoconfinement of AB, but will no doubt have implications for a variety of applications that require highly porous materials with greatly functionalised surfaces.

5.1.2 **Characterisation of Bulk and Nanoconfined AB**

Subsequently, the material TA(L) was applied to the nanoconfinement of AB where the resulting material, referred to as AB/TA(L), was thoroughly characterised and compared against bulk AB. These results showed comprehensive changes to have occurred upon nanoconfinement of AB within TA(L), which fundamentally altered the thermolytic dehydrogenation and bulk release characteristics relative to bulk AB. Although many of these characteristics inhibit the application of AB/TA(L) as a viable hydrogen storage candidate, the findings here identify material characteristics that can be used to develop further materials for nanoconfinement of AB.

Firstly, with regards to bulk AB, the majority of results were in excellent agreement with those reported in literature. Upon non-isothermal heating, the onset temperature for mass loss from bulk AB was relatively high (T = 101 ^{o}C) and then proceeded across two steps which appeared consistent with the progressive formation of polyaminoborane (PAB) followed by polyiminoborane (PIB). The gases evolved upon heating of bulk AB were found to predominantly consist of H_2 (96.4 vol%), with smaller amounts of volatilised contaminants including ammonia (NH_3) (2.5 vol%) water (H_2O) (1.0 vol%), diborane (DB) (0.01 vol%) and borazine (BZ) (0.04 vol%). The majority of these contaminants predominated during the second step, with the notable exception of DB for which the onset (T = 89 ^{o}C) preceded hydrogen release. This was suggested to signify the occurrence of homopolar ($B\text{-}H^{\delta-}\cdots H^{\delta-}\text{-}B$) interactions during the formation of diammoniate of diborane (DADB), a critical nucleation event for the onset of hydrogen release, and a small exothermic event (T = 99 ^{o}C) not associated with mass loss was tentatively assigned. This event has appeared in other results

in literature (without being discussed), however this research is the first to tentatively attribute it to the formation of DADB. Furthermore, isothermal heating showed a sigmoidal release profile from bulk AB that was well represented by the Avrami-Erofeev model of nucleation and growth kinetics, both of which were generally consistent with literature. This supported existing understanding in literature that DADB is the critical nucleation event that prompts subsequent hydrogen release, with dehydrogenation of AB resulting in progressive growth of PAB then PIB. Whereas literature generally finds this reaction best represented by three-dimensional growth, this research instead found superior likeness from two-dimensional growth which was consistent with the formation of products such as planar sheets of polyborazylene (PBZ). The apparent activation energies for both isothermal and non-isothermal dehydrogenation were then calculated by the Arrhenius, Isoconversional and Kissinger Methods. Generally, these methods showed distinct values in temperature regions either side of the melting temperature of AB (80-110 and 110-140 ^{o}C), a distinction which is often neglected in literature. Overall, the three methods showed reasonable agreement in their values, with the activation energy of the respective ranges taken as around 171 ± 7 and 61 ± 5 kJ/mol. The large difference between these values indicated a fundamental change in the release energetics and/or mechanism upon melting.

In comparison, AB/TA(L) demonstrated notably different release characteristics which fundamentally derived from interactions between the nanoconfined AB and the aforementioned surface bicarbonates of TA(L). Nanoconfined AB/TA(L) demonstrated the onset of hydrogen release at low temperatures (T = 25 ^{o}C), with further heating progressing with a broad release profile toward the formation of polyborazylene (PBZ) and turbostratic boron nitride (tBN). Indeed, these species were observed to gradually form over the duration of storage which evidenced ambient temperature release, something that has only been reported for a single system in literature. In that case, the effect was attributed to strongly acidic surface groups however this was opposed to the assignment of bicarbonate surface functionality within TA(L). A major proposition of this research is that the amphoterism of these bicarbonate surface groups mean they are able to react with both –NH_3 and –BH_3 groups of AB, leading to these species mediating proton transfer and greatly accelerating dehydrogenation. This conclusion represents a distinct difference to current opinion in literature, but nonetheless explains some of the trends reported whereby more amphoteric metal oxides outperform those with greater surface acidity and basicity.

The strong destabilisation of nanoconfined AB was further evidenced by analysing the composition of the evolved gases, which were observed to contain a significantly reduced quantity of H_2 (17.2 vol%) in addition to substantially more NH_3 (55.2 vol%), DB (10.9 vol%), H_2O (15.3 vol%) and iPrOH (1.4 vol%), whilst BZ appeared to have been eliminated. The large

quantities of DB and NH_3 evidenced the excessive cleavage of the coordinate B-N bond of nanoconfined AB without dehydrogenation. Furthermore, the ambient temperature release of H_2 was observed to occur without the preceding release of DB, evidencing that the release mechanism was distinct from AB and did not involve the formation of DADB as a critical nucleation event. This was reflected in the isothermal and non-isothermal release profiles for AB/TA(L), which no longer resembled nucleation and growth and instead appeared similar to desorption kinetics. This accelerated release was reflected in the reduced activation energy values exhibited by AB/TA(L), which also showed distinct values based on the melting temperature of AB, with values of around 85 ± 8 and 33 ± 9 kJ/mol respectively.

Overall, despite seemingly improved performance in some regards, AB/TA(L) generally demonstrated insufficient performance for immediate use in hydrogen storage applications. In this case, the excessive destabilisation of nanoconfined AB by the bicarbonate functionality of TA(L) introduced several challenges. Firstly, although the energy required to effect release at ambient temperature is small, the low temperature would necessitate cooling to ensure premature release does not occur during storage. Secondly, the thorough cleavage of the B-N bond of nanoconfined AB caused significantly reduced the quantity of evolved H_2, and increased volatilisation of DB and NH_3. This would reduce the overall efficiency of storage and necessitate removal of contaminants prior to downstream processes. Thirdly, the volatilisation of these components alongside partial formation of tBN would mean a significant fraction of the original AB is unavailable for regeneration, again serving to reduce the overall storage efficiency. Nevertheless, although AB/TA(L) showed insufficient performance in these areas, the novel identification of surface bicarbonates as strongly destabilising has promising implications for the future design of other nanoconfined AB materials.

5.1.3 **Release Mechanism of Bulk and Nanoconfined AB**

Finally, the release mechanisms for thermolytic dehydrogenation of bulk AB and nanoconfined AB/TA(L) were interrogated by a combination of TGA and FTIR analyses. Particular focus was placed on the initial stages of mass loss in an attempt to understand the reaction(s) involved with the onset of hydrogen release since, although literature has evidenced the role of DADB as a critical nucleation event, there remains much uncertainty about the mechanism of dehydrogenation. On one hand, intuitive heteropolar ($N\text{-}H^{\delta+}\cdots H^{\delta-}\text{-}B$) interactions have been conventionally implicated in formation of DADB, whereas more recent research has found evidence for unexpected homopolar ($B\text{-}H^{\delta-}\cdots H^{\delta-}\text{-}B$) interactions. This was investigated by analysis of 1D-IR spectra, as well as by the novel application of 2D-IR correlational spectroscopy to observe the relation between the spectral features of bulk and

nanoconfined AB. This research demonstrated the application of 2D-IR with varying levels of success. Whereas the study of bulk AB was rather successful, the same process applied to AB/TA(L) was ultimately hindered by degradation of the sample prior to analyses and highlighted several technical shortcomings in the 2D-IR technique.

For bulk AB, extensive evidence was found that supported the empirically understood dehydrogenation of AB widely reported in literature. Upon heating, bulk AB was initially observed to be thermally and spectroscopically stable (T < 80 ^{o}C), after which the spectra were observed to gradually broaden, indicating changes in the intermolecular dihydrogen bonding (N-H$^{\delta+}$···H$^{\delta-}$-B). Subsequent elevations in temperature (T = 100-130 ^{o}C), realised coincidental mass loss and reduction of intensity for bands associated with N–H and B–H that signified the onset for release of hydrogen. Simultaneous to this release, the preponderance of evidence for tetragonal –NH_2, –NH_2, and B–N was consistent with the formation of PAB. Above this temperature range (T = 130-210 ^{o}C), further mass losses and reductions in N-H/B-H modes coincided with increased modes for B=N–H, N=B–H, and B=N. Cumulatively, these results were consistent with the anticipated formation of PIB. Subsequent analyses of bulk AB between 25-130 ^{o}C using 2D-IR generally supported the above, but also found considerable evidence that highlighted the specific importance of the –BH_3 side of the AB. Strong correlations determined an order of precedence for the spectral changes, with initial reductions in N-B-H modes attributed to cleavage of the B-N. Importantly, the next step was identified as the formation of tetragonal B-N, which occurred entirely synchronously with reductions in –BH_3 but before subsequent formation of –BH_2. This was believed to fundamentally evidence the occurrence of homopolar (B-H$^{\delta-}$···H$^{\delta-}$-B) interactions, since the formation of tetragonal B-N is indicative of the key intermediate DADB whereas –BH_2 occurs after release of H_2. Furthermore, the corresponding changes for –NH_3 and –NH_2 were either substantially weaker or entirely absent; again underscoring the importance of the former side of AB during release reactions. Although such homopolar (B-H$^{\delta-}$···H$^{\delta-}$-B) interactions have been proposed before based on deuterium labelled experiments, their evidence is predicated on the absence of hydrogen exchange during both storage and release. This result appears to be the first spectroscopic evidence that confirms the existence of these homopolar (B-H$^{\delta-}$···H$^{\delta-}$-B) interactions without the possibility of hydrogen exchange.

In contrast, the analysis of AB/TA(L) was mostly compromised by the observed degradation of AB/TA(L) during storage (t ≈ 2 months) prior to experimentation. The explanation and discussion of this ambient temperature dehydrogenation has been given in detail in the preceding section. Nevertheless, in these experiments the degradation was seen to selectively affect the –BH_3 functionality of AB, which evidenced the similarly larger reactivity of –BH_3 within nanoconfined AB (identically to that discussed above for bulk AB). In agreement with

similar supports in literature, the reaction of nanoconfined AB with the surface of TA(L) was evidenced to form B-O functionality. This was further shown by the detection of a band in the stretching region of 2D-IR plots that did not correlate with surrounding N-H modes, leading to the proposed presence of B-OH modes. Nevertheless, in spite of the degradation and aside from the nominal result above, the analysis of AB/TA(L) also exposed several insufficiencies of the 2D-IR technique. The highly convoluted spectra of AB/TA(L) hindered confident assignment such that although strong correlations were seen during analysis, these could not be meaningfully interpreted. This represents a substantial weakness of 2D-IR in the analysis of complex materials and this research instead recommends further studies employ similar 2D-NMR analyses which should be able to better interrogate complex materials.

5.2 Recommendations for Future Work

Based on the programme of research, experimental results and subsequent conclusions presented in the preceding chapters, a number of areas were identified for further research. The recommendation of these areas was based on unexplained observations and/or results that offered exploitable opportunities if further developed, as discussed herein.

5.2.1 Carboxylate Functionalised Titania Aerogels

During the preparation of titania aerogels, it was discovered that solvent extraction with liquid (LCO_2) or supercritical carbon dioxide (SCO_2) resulted in the formation of surface carboxylates on the incipient TA(L) and TA(S) respectively. Whilst the formation of such surface species on titania has been extensively reported in other fields, their occurrence during preparation of aerogels by solvent extraction with LCO_2/SCO_2 is unreported. Previously, the functionalisation of the surface of titania with carboxylates has been achieved by the inclusion of carboxylic acids (*e.g.* formic acid, acetic acid) in solution during preparation (Nolan, Seery and Pillai, 2009)(Vasconcelos *et al.*, 2011)(Qu *et al.*, 2010). These functionalised surfaces resulted in distinct material properties compared to unmodified titania, which lead to better performance in applications such as photocatalysis, water purification, selective adsorption and gas sensing. To reiterate, the formation of such carboxylate functionalised titania by solvent extraction is unreported in literature. Nevertheless, this research demonstrated the (to the author's knowledge) novel formation of these species from the presumed reaction of surface hydroxyls (Ti-OH) and LCO_2/SCO_2, advised by similar reactions in literature (Sakakura, Choi and Yasuda, 2007). This discovery represents a distinctly different preparation route toward carboxylate functionalised titania surfaces that offer further advantages based on their additional identity as aerogel materials.

5.2.2 **Surface Acidity/Basicity of Surface Carboxylates**

Expanding on the above, this research speculated that the carboxylate functionality formed at the surface of TA(L)/TA(S) were surface bicarbonates in the bidentate bridging mode (Sakakura, Choi and Yasuda, 2007)(Mino, Spoto and Ferrari, 2014). These surface species were evidenced to strongly destabilise nanoconfined AB and greatly accelerated the release of hydrogen from AB/TA(L). Highly similar release characteristics have been reported for nanoconfined AB/Carbon (Moussa *et al.*, 2012), where the effect was attributed to the strong acidity of surface carboxyls (-COOH). This appeared to suggest the bicarbonate functionality of AB/TA(L) offered similar acidity to the surface carboxyls in AB/Carbon, however this is at odds with their speculated identity as bicarbonates (which are typically limited to weak acidity). It was conceived that the amphoteric nature of bicarbonates meant they were able to mediate proton transfer between the constituent $-NH_3$ and $-BH_3$ moieties of AB to slowly release H_2 at ambient temperature. In order to resolve this uncertainty, TA(L) and TA(S) materials should be further studied by temperature programmed desorption using ammonia (NH_3-TPD) and carbon dioxide (CO_2-TPD) probes. This would decisively quantify the nature of the carboxylate surface by evaluating the presence and strength of acidic and basic sites respectively which in turn would clarify the reason(s) for such strongly accelerated hydrogen release within nanoconfined AB/TA(L).

5.2.3 **Preparation of Monolithic AB/Titania Aerogels**

Aside from their precise surface functionality, this research demonstrated the preparation of titania aerogels with remarkable properties. In particular, the preparation of monolithic aerogels prepared with SCO_2, namely TA(S,M), offered significantly higher surface areas, pore volumes and pore sizes than the aforementioned TA(L). Nevertheless, the preparation of AB/TA(L) with LCO_2 was pursued based on time constraints and previous experiences highlighting the minimisation of premature thermolysis of AB. However, current understanding in literature predicts that if nanoconfined AB could be prepared into a support with better surface properties, this would likely realise subsequent improvements to hydrogen release (Rueda, Sanz-moral and Martín, 2018). On this basis, an alternative method of preparation was conceived whereby extraction would be conducted using LCO_2 (minimising thermolysis of AB) with the final depressurisation using SCO_2 (preventing pore collapse). When this method is coupled with the monolithic method the resulting aerogel, referred to as TA(L-S,M), is anticipated to realise similar surface properties as TA(S,M). Hence, further research might pursue the preparation and characterisation of TA(L-S,M), as well as subsequent testing of nanoconfined AB/TA(L-S,M) to verify hypothesised improvements to hydrogen release.

5.2.4 **Preparation of Nanoconfined AB/Silica-Titania Aerogels**

Another fundamental finding from this research was that the nanoconfinement of AB within TA(L) resulted in substantially different hydrogen release compared to bulk AB. The cause of such accelerated release was suggested to involve the interaction of nanoconfined AB with aforementioned surface bicarbonates on TA(L). Whilst this lead to remarkable acceleration in the release of hydrogen at ambient temperatures, the extent of this destabilisation was excessive and resulted in gradual loss of hydrogen during storage (necessarily challenging the application of AB/TA(L) as a candidate storage material). In contrast, nanoconfinement of AB within silica aerogels has been demonstrated to offer more moderate destabilisation (as reviewed in Table 4.17) that allowed controlled release upon heating (Rueda *et al.*, 2017). Furthermore, such silica aerogels generally offered better surface properties including surface area, larger pore volume, and narrower pore size distributions (as seen in Table 2.3).

On this basis, it was conceived that the nanoconfinement of AB within mixed silica-titania aerogels (AB/STA) might exhibit the relative advantages of both titania and silica aerogels. The preparation of such mixed silica-titania aerogels (STA) has been extensively reported in literature (Lu *et al.*, 2009) (Bonelli *et al.*, 2007) (Navarrete, Lopez and Gomez, 1996), where the resulting aerogels exhibited materials properties between those of silica and titania (Ingemar Odenbrand, Brandin and Busca, 1992). Plausibly, when prepared with a low titania content (*e.g.* Ti ≤ 10 wt%), the predominance of silica within the aerogel network (Si-O-Si) would facilitate improved surface properties, whilst the inclusion of titania (Si-O-Ti) would accelerate the release of hydrogen. However, the limited availability of titania would limit the formation of surface bicarbonates, and so reduce the magnitude of destabilisation. This might provide an opportunity to tailor the destabilisation of nanoconfined AB such that sufficient stability is achieved during storage as well as accelerated release upon heating. As such, the preparation of nanoconfined AB/STA (Ti ≈ 1-20 wt%) should be experimentally explored to establish if such advantageous effects can be realised.

References

Aguado-Serrano, J. and Rojas-Cervantes, M. L. (2006) 'Titania aerogels Influence of synthesis parameters on textural , crystalline , and surface acid properties', *Microporous and Mesoporous Materials*, 88, pp. 205–213. doi: 10.1016/j.micromeso.2005.09.011.

Akbayrak, S., Gençturk, S., *et al.* (2014) 'Rhodium(0) nanoparticles supported on nanotitania as highly active catalyst in hydrogen generation from the hydrolysis of ammonia borane', *RSC Advances*, 4, pp. 13742–13748. doi: 10.1039/c4ra00469h.

Akbayrak, S., Tanyıldızı, S., *et al.* (2014) 'Ruthenium (0) nanoparticles supported on nanotitania as highly active and reusable catalyst in hydrogen generation from the hydrolysis of ammonia borane', *International Journal of Hydrogen Energy*, 39(18), pp. 9628–9637. doi: 10.1016/j.ijhydene.2014.04.091.

Akbayrak, S. and Ozkar, S. (2018) 'Ammonia borane as hydrogen storage materials', *International Journal of Hydrogen Energy*, 43, pp. 18592–18606. doi: 10.1016/j.ijhydene.2018.02.190.

Al-kukhun, A., Hwang, H. T. and Varma, A. (2012) 'Mechanistic studies of ammonia borane dehydrogenation', *International Journal of Hydrogen Energy*. Elsevier Ltd, 38(1), pp. 169–179. doi: 10.1016/j.ijhydene.2012.09.161.

Alipour, J., Shoushtari, A. M. and Kaflou, A. (2015) 'Ammonia borane confined by poly(methyl methacrylate)/multiwall carbon nanotube nanofiber composite , as a polymeric hydrogen storage material', *Journal of Material Science*, 50, pp. 3110–3117. doi: 10.1007/s10853-015-8871-x.

Andersson, J. and Grönkvist, S. (2019) 'Large-scale storage of hydrogen', *International Journal of Hydrogen Energy*, 44(23), pp. 11901–11919. doi: 10.1016/j.ijhydene.2019.03.063.

Apostolou, D. and Enevoldsen, P. (2019) 'The past, present and potential of hydrogen as a multifunctional storage application for wind power', *Renewable and Sustainable Energy Reviews*. Elsevier Ltd, 112, pp. 917–929. doi: 10.1016/j.rser.2019.06.049.

Armstrong, G. and Kailas, L. (2017) 'Hyphenated analytical techniques for materials characterisation', *European Journal of Physics*. IOP Publishing, 38(5). doi: 10.1088/1361-6404/aa7e93.

ASTM (2010) 'E967 – 18 Standard Test Method for Temperature Calibration of Differential Scanning Calorimeters and Differential Thermal Analyzers 1'. doi: 10.1520/E0967-08.2.

ASTM (2014) 'E968-02 Standard Practice for Heat Flow Calibration of Differential Scanning Calorimeters'. doi: 10.1520/E0968-02R14.2.

ASTM (2015) *Standard Test Method for Kinetic Parameters for Thermally Unstable Materials by Differential Scanning Calorimetry Using the Kissinger Method*. doi: 10.1520/E2890-12.2.

ASTM (2018a) *Standard Test Method for Decomposition Kinetics by Thermogravimetry Using the Ozawa/Flynn/Wall Method*, *ASTM E1641 - 18*. Available at: https://www.astm.org/Standards/E1641.htm (Accessed: 26 June 2019).

ASTM (2018b) 'Standard Test Method for Mass Scale Calibration of Thermogravimetric Analyzers (E2040-08)', pp. 1–3. doi: 10.1520/E2040-08R14.2.

ASTM (2018c) *Standard Test Method for Temperature Calibration of Thermogravimetric Analyzers (E1582-17)*. doi: 10.1520/E1582-17.2.

Autrey, T. *et al.* (2004) 'Chemical hydrogen storage in nano-structured materials. Control of hydrogen release and reactivity from ammonia borane complexes', *ACS Div. Fuel Chem. Prepr.*, 49, pp. 150–151.

Autrey, T., Bowden, M. and Karkamkar, A. (2011) 'Control of hydrogen release and uptake in amine borane molecular complexes: Thermodynamics of ammonia borane, ammonium borohydride, and the diammoniate of diborane', *Faraday Discussions*, 151, pp. 157–169. doi: 10.1039/c0fd00015a.

Ayen, R. J. *et al.* (1988) 'Metal Oxide Aerogel Preparation by Supercritical Extraction', pp. 157–198.

Babenko, V. *et al.* (2017) 'Time dependent decomposition of ammonia borane for the controlled production of 2D hexagonal boron nitride', *Scientific Reports*, 7, pp. 1–12. doi: 10.1038/s41598-017-14663-8.

Bagheri, S. *et al.* (2014) 'Titanium Dioxide as a Catalyst Support in Heterogeneous Catalysis', *The Scientific World Journal*, pp. 1–21.

Baier, M. J., Ramachandran, P. V. and Son, S. F. (2019) 'Characterization of the Hypergolic Ignition Delay of Ammonia Borane', *Journal of Propulsion and Power*, 35, pp. 182–189. doi: 10.2514/1.b37075.

Baitalow, F. *et al.* (2002) 'Thermal decomposition of BNH compounds investigated by using combined thermoanalytical methods', *Thermochimica Acta*, 391, pp. 159–168. doi: 10.1016/S0040-6031(02)00173-9.

Baitalow, F. *et al.* (2006) 'Thermal decomposition of ammonia – borane under pressures up to 600 bar', c, pp. 121–125. doi: 10.1016/j.tca.2005.07.002.

Ball, M. and Weeda, M. (2015) 'The hydrogen economy - Vision or reality?', *International Journal of Hydrogen Energy*. Elsevier Ltd, 40(25), pp. 7903–7919. doi: 10.1016/j.ijhydene.2015.04.032.

Barth, A. (2007) 'Infrared spectroscopy of proteins', *Biochimica et Biophysica Acta*, 1767, pp. 1073–1101. doi: 10.1016/j.bbabio.2007.06.004.

Barthelemy, H., Weber, M. and Barbier, F. (2017) 'Hydrogen storage: Recent improvements and industrial perspectives', *International Journal of Hydrogen Energy*. Elsevier Ltd, 42(11), pp. 7254–7262. doi: 10.1016/j.ijhydene.2016.03.178.

Bastos-Neto, M. *et al.* (2012) 'Assessment of hydrogen storage by physisorption in porous materials', *Energy and Environmental Science*, 5, pp. 8294–8303. doi: 10.1039/c2ee22037g.

Baumann, J., Baitalow, F. and Wolf, G. (2005) 'Thermal decomposition of polymeric aminoborane (H2BNH2)x under hydrogen release', *Thermochimica Acta*, 430, pp. 9–14. doi: 10.1016/j.tca.2004.12.002.

Bennoua, S. *et al.* (2015) 'Role of hydrogen in resolving electricity grid issues', *International Journal of Hydrogen Energy*, 40(23), pp. 7231–7245. doi: 10.1016/j.ijhydene.2015.03.137.

Benzouaa, R. *et al.* (2010) 'Thermochimica Acta Metal chloride-doped ammonia borane thermolysis : Positive effect on induction period as well as hydrogen and borazine release', *Thermochimica Acta*. Elsevier B.V., 509, pp. 81–86. doi: 10.1016/j.tca.2010.06.007.

Berthier, J. (2013) 'Micro-Drops and Digital Microfluidics: Chapter 2 - Theory of Wetting', *Micro and Nano Technologies*, pp. 7–73. doi: 10.1016/B978-1-4557-2550-2.00002-X.

Bonelli, B. *et al.* (2007) 'Study of the surface acidity of TiO2/SiO2 catalysts by means of FTIR measurements of CO and NH3 adsorption', *Journal of Catalysis*, 246, pp. 293–300. doi: 10.1016/j.jcat.2006.12.015.

Bowden, M. *et al.* (2006) 'Mechanistic studies of hydrogen release from solid amine borane materials', *Materials Research Society Symposium Proceedings*, 927, pp. 9–14. doi: 10.1557/proc-0927-ee02-04.

Bowden, M. and Autrey, T. (2011) 'Characterization and mechanistic studies of the dehydrogenation of NHxBHx materials', *Current Opinion in Solid State & Materials Science*. Elsevier Ltd, 15, pp. 73–79. doi: 10.1016/j.cossms.2011.01.005.

Brown, L. B., Anderson, A. M. and Carroll, M. K. (2012) 'Fabrication of titania and titania-silica aerogels using rapid supercritical extraction', *J Sol-Gel Sci Technol*, 62, pp. 404–413. doi: 10.1007/s10971-012-2741-7.

BSI (2016) 'BS ISO 15901-1 : 2016 - Evaluation of pore size distribution and porosity of solid materials by mercury porosimetry and gas adsorption', (1).

Budrugeac, P., Segal, E. and Popescu, C. (2003) 'Some remarks

on the use of isothermal thermogravimetric data for the evaluation of kinetic parameters. Applications for degradation of polymeric materials', *Journal of Applied Polymer Science*, 89, pp. 355–360. doi: 10.1002/app.11852.

Bui, M. *et al.* (2018) 'Carbon capture and storage (CCS): The way forward', *Energy and Environmental Science*, 11, pp. 1062–1176. doi: 10.1039/c7ee02342a.

Cai, Y. and Feng, Y. P. (2016) 'Review on charge transfer and chemical activity of TiO2: Mechanism and applications', *Progress in Surface Science*. Elsevier Ltd, 91, pp. 183–202. doi: 10.1016/j.progsurf.2016.11.001.

Calzada, M. L. *et al.* (2002) 'Thermal-Decomposition Chemistry of Modified Lead-Titanate Aquo-Diol Gels Used for the Preparation of Thin Films', *Journal of Sol-Gel Science and Technology*, 23, pp. 221–230.

Campbell, L. K., Na, B. K. and Ko, E. I. (1992) 'Synthesis and Characterization of Titania Aerogels', *Chem. Mater.*, 4, pp. 1329–1333. doi: 10.1021/cm00024a037.

CarbonBrief (2019) *Reduction in UK Emissions, Analysis: Why the UK's CO2 emissions have fallen 38% since 1990*. Available at: https://www.carbonbrief.org/analysis-why-the-uks-co2-emissions-have-fallen-38-since-1990 (Accessed: 7 March 2020).

Carre, A., Roger, F. and Varinot, C. (1992) 'Study of Acid/Base Properties of Oxide, Oxide Glass, and Glass-Ceramic Surfaces', *Journal of Colloid and Interface Science*, 154, pp. 174–183.

Cerhová, M. *et al.* (2018) 'The Journal of Supercritical Fluids Preparation of nanocrystalline TiO2 monoliths by using modified supercritical carbon dioxide', *The Journal of Supercritical Fluids*, 137, pp. 93–100. doi: 10.1016/j.supflu.2018.02.001.

Chen, X. *et al.* (2011) 'Experimental and Computational Study of the Formation Mechanism', *Journal of the American Chemical Society*, 133, pp. 14172–14175. doi: 10.1021/ja203648w.

Chen, X. *et al.* (2012) 'Large-scale and facile preparation of pure ammonia borane through displacement reactions', *Chemistry - A European Journal*, 18(38), pp. 11994–11999. doi: 10.1002/chem.201201342.

Choi, H. *et al.* (2018) 'Synthesis of High Surface Area - TiO2 Aerogel Support with Pt Nanoparticle Catalyst and CO Oxidation Study', *Catal Lett*. Springer US, 148, p. 1504. doi: 10.1007/s10562-018-2355-y.

Choi, Y. J. *et al.* (2012) 'Hydrogen Storage Properties of New Hydrogen-Rich BH3NH3-Metal Hydride (TiH2, ZrH2, MgH2, and/or CaH2) Composite Systems', *Journal of Physical Chemistry C*, 116, p. 8349–8358. doi: 10.1021/jp210460w.

Crabtree, R. H. *et al.* (1996) 'A New Intermolecular Interaction: Unconventional Hydrogen Bonds with Element-Hydride Bonds as Proton Acceptor', *Accounts of Chemical Research*, 29, pp. 348–354. doi: 10.1021/ar950150s.

Custelcean, R. and Dreger, Z. A. (2003) 'Dihydrogen Bonding under High Pressure : A Raman Study of BH3NH3 Molecular Crystal', *J. Phys. Chem. B*, 107, pp. 9231–9235.

Dagan, G. and Tomkiewicz, M. (1994) 'Preparation and characterization of TiO2 aerogels for use as photocatalysts', *Journal of Non-Crystalline Solids*, 175, pp. 294–302.

Dampc, M. *et al.* (2011) 'Ionization and ionic fragmentation of tetrahydrofuran molecules by electron', *Journal of Physics B: Atomic, Molecular and Optical Physics*, 44, pp. 1–7. doi: 10.1088/0953-4075/44/5/055206.

DBEIS (2018) *Energy consumption in the UK*, *National Statistics*.

DBEIS (2019) *Final UK greenhouse gas emissions national statistics: 1990-2017*, *National Statistics*.

Debecker, D. P. *et al.* (2018) 'Aerosol processing: A wind of innovation in the field of advanced heterogeneous catalysts', *Chemical Society Reviews*, 47, pp. 4112–4155. doi: 10.1039/c7cs00697g.

Demirci, U. B. (2017a) 'Ammonia borane, a material with exceptional properties for chemical hydrogen storage', *International Journal of Hydrogen Energy*. Elsevier Ltd, 42(15), pp. 9978–10013. doi: 10.1016/j.ijhydene.2017.01.154.

Demirci, U. B. (2017b) 'Ammonia borane, a material with exceptional properties for chemical hydrogen storage', *International Journal of Hydrogen Energy*. Elsevier Ltd, 42(15), pp. 9978–10013. doi: 10.1016/j.ijhydene.2017.01.154.

Department for Transport (2018) *The Road to Zero*. London.

Desario, P. A. *et al.* (2019) 'Applied Catalysis B : Environmental Low-temperature CO oxidation at persistent low-valent Cu nanoparticles on TiO2 aerogels', *Applied Catalysis B: Environmental*. Elsevier, 252, pp. 205–213. doi: 10.1016/j.apcatb.2019.03.073.

Dillen, J. and Verhoeven, P. (2003) 'The end of a 30-year-old controversy? A computational study of the B-N stretching frequency of BH3-NH3 in the solid state', *Journal of Physical Chemistry A*, 107(14), pp. 2570–2577. doi: 10.1021/jp027240g.

Dincer, I. and Acar, C. (2014) 'Review and evaluation of hydrogen production methods for better sustainability', *International Journal of Hydrogen Energy*. Elsevier Ltd, 40(34), pp. 11094–11111. doi: 10.1016/j.ijhydene.2014.12.035.

EPA (2008) *CO2 Emissions from Production of H2 during Steam Reformation*, *Technical support document for hydrogen production: Proposed rule for mandatory reporting of greenhouse gases*. Available at: https://www.epa.gov/sites/production/files/2015-02/documents/subpartp-tsd_hydrogenproduction.pdf (Accessed: 25 September 2019).

EU (2018) 'Directive (EU) 2018/2001 of the European Parliament and of the Council', *Official Journal of the European Union*, 328, pp. 82–209.

Fang, Z. *et al.* (2011) 'Facile solid-phase synthesis of the diammoniate of diborane and its thermal decomposition behavior', *Phys. Chem. Chem. Phys.*, 13, pp. 7508–7513. doi: 10.1039/c1cp00018g.

Feaver, A. *et al.* (2007) 'Coherent Carbon Cryogel - Ammonia Borane Nanocomposites for H2 Storage', *Journal of Physical Chemistry B*, 111(26), pp. 7469–7472. doi: 10.1021/jp072448t.

Frattini, D. *et al.* (2016) 'A system approach in energy evaluation of different renewable energies sources integration in ammonia production plants', *Renewable Energy*, 99, pp. 472–482. doi: 10.1016/j.renene.2016.07.040.

Frueh, S. *et al.* (2011) 'Pyrolytic decomposition of ammonia borane to boron nitride', *Inorganic Chemistry*, 50(3), pp. 783–792. doi: 10.1021/ic101020k.

Gadipelli, S. *et al.* (2012) 'Nanoconfinement and Catalytic Dehydrogenation of Ammonia Borane by', *International Journal of Hydrogen Energy*, 37, pp. 6043–6047. doi: 10.1002/chem.201100090.

Galwey, A. K. and Brown, M. E. (2002) 'Application of the arrhenius equation to solid state kinetics: Can this be justified?', *Thermochimica Acta*, 386, pp. 91–98. doi: 10.1016/S0040-6031(01)00769-9.

Gangal, A. C. *et al.* (2012) 'Study of kinetics and thermal decomposition of ammonia borane in presence of silicon nanoparticles', *International Journal of Hydrogen Energy*. Elsevier Ltd, 37, pp. 6741–6748. doi: 10.1016/j.ijhydene.2012.01.017.

Gangal, A. C. and Sharma, P. (2013) 'Kinetic Analysis and Modeling of Thermal', *Int. J. Chem. Kinet.*, 45, pp. 452–461. doi: 10.1002/kin.20781.

Geanangel, R. A. and Rabalais, J. W. (1985) 'Evidence from Mass Spectra and X-ray Photoelectron Spectra Concerning the Structure of Poly(aminoborane)', *Inorganica Chimica Acta*, 97, pp. 59–64.

Gridwatch (2019) *G.B. National Grid Status*, *GridWatch Database*. Available at: https://www.gridwatch.templar.co.uk/ (Accessed: 25 September 2019).

Gur, T. M. (2018) 'Review of electrical energy storage technologies, materials and systems: challenges and prospects for large-scale grid storage', *Energy & Environmental Science*, 11, pp. 2696–2767. doi: 10.1039/c8ee01419a.

Gutowska, A. *et al.* (2005) 'Nanoscaffold Mediates Hydrogen Release and the Reactivity of Ammonia Borane**', *Angew.*

Chem. Int. Ed, 44, pp. 3578–3582. doi: 10.1002/anie.200462602.

Hache, E. (2018) 'Do renewable energies improve energy security in the long run?', *International Economics*, 156, pp. 127–135. doi: 10.1016/j.inteco.2018.01.005.

Hanaor, D. *et al.* (2011) 'Anodic Aqueous Electrophoretic Deposition of Titanium Dioxide Using Carboxylic Acids as Dispersing Agents', *Journal of the European Ceramic Society*, 31(6), pp. 1041–1047.

Harrington, P. de B., Urbas, A. and Tandler, P. J. (2000) 'Two-dimensional correlation analysis', *Chemometrics and Intelligent Laboratory Systems*, 50, pp. 149–174. doi: 10.1016/S0169-7439(99)00062-3.

He, T. *et al.* (2009) 'Nanosized Co- and Ni-Catalyzed Ammonia Borane for Hydrogen', *Chem. Mater.*, 21, pp. 2315–2318.

He, T. *et al.* (2011) 'Quasi in situ Mössbauer and XAS studies on FeB nanoalloy for heterogeneous catalytic dehydrogenation of ammonia borane', *Catalysis Today*. Elsevier B.V., 170, pp. 69–75. doi: 10.1016/j.cattod.2011.02.041.

Heldebrant, D. J. *et al.* (2008) 'Synthesis of ammonia borane for hydrogen storage applications', *Energy & Environmental Science*, 1, pp. 156–160. doi: 10.1039/b808865a.

Henderson, M. A. (1998) 'Evidence for bicarbonate formation on vacuum annealed TiO2(110) resulting from a precursor-mediated interaction', *Surface Science*, 400, pp. 203–219.

Hess, N. J. *et al.* (2008) 'Spectroscopic studies of the phase transition in ammonia borane: Raman spectroscopy of single crystal NH3BH3 as a function of temperature from 88to330K', *The Journal of Chemical Physics*, 128(3), p. 034508. doi: 10.1063/1.2820768.

Hiden Analytical (2018) *Relative Sensitivity: RS Measurements of Gases*, *Gas Analysis*. Available at: https://www.hiden.de/wp-content/uploads/pdf/RS_Measurement_of_Gases_-_Hiden_Analytical_App_Note_282.pdf (Accessed: 25 September 2019).

de Hoffman, E. and Stroobant, V. (2007) *Mass Spectrometry: Principles and Applications*. 3rd Ed., *Methods in Molecular Biology*. 3rd Ed. Brussels: John Wiley & Sons, Ltd. doi: 10.1007/978-1-4939-7877-9_17.

Holladay, J. D. *et al.* (2009) 'An overview of hydrogen production technologies', *Catalysis Today*, 139(4), pp. 244–260. doi: 10.1016/j.cattod.2008.08.039.

Hook, M., Sivertssen, A. and Aleklett, K. (2010) 'Validity of the Fossil Fuel Production Outlooks in the IPCC Emission Scenarios', *Natural Resources Research*, 19(2). doi: 10.1007/s11053-010-9113-1.

Huang, Y. *et al.* (2014) 'Experimental verification of the high pressure crystal structures in NH3BH3', *Journal of Chemical Physics*, 140(1–7). doi: 10.1063/1.4884819.

Ingemar Odenbrand, C. U., Brandin, J. G. M. and Busca, G. (1992) 'Surface Acidity of Silica-Titania Mixed Oxides: A FT-IR Study of the Adsorption of Pivalonitrile', *Journal of Catalysis*, 135, pp. 505–517.

IPCC (2007) 'Changes in Atmospheric Constituents and in Radiative Forcing. In: Climate Change 2007: The Physical Science Basis. Contribution of Working Group I to the Fourth Assessment Report of the Intergovernmental Panel on Climate Change', in Solomon, S. et al. (eds). Cambridge: Cambridge University Press.

IPCC (2018) *Global Warming of 1.5C*, *Special Report*. Available at: https://www.ipcc.ch/sr15/ (Accessed: 25 September 2019).

Iswar, S. *et al.* (2017) 'Effect of aging on silica aerogel properties', *Microporous and Mesoporous Materials*. Elsevier Ltd, 241, pp. 293–302. doi: 10.1016/j.micromeso.2016.11.037.

Jash, P., Meaux, K. and Trenary, M. (2012) 'Transmission Infrared Spectroscopy of Ammonia Borane', *Journal of Undergraduate Research*, 5(1), pp. 1–5.

Jianxin, P. and Yigang, L. (2009) 'Estimation of the surface tension of liquid carbon dioxide', *Physics and Chemistry of Liquids*, 47(3), pp. 267–273. doi: 10.1080/00319100701824389.

Kang, B. X. *et al.* (2008) 'Ammonia Borane Destabilized by Lithium Hydride : An Advanced On-Board Hydrogen Storage Material', *Adv. Mater.*, 20, pp. 2756–2759. doi: 10.1002/adma.200702958.

Kang, X. *et al.* (2009) 'Promoted hydrogen release from ammonia borane by mechanically milling with magnesium hydride : a new destabilizing approach', *Phys. Chem. Chem. Phys*, 11, pp. 2507–2513. doi: 10.1039/b820401b.

Kapdan, I. K. and Kargi, F. (2006) 'Bio-hydrogen production from waste materials', *Enzyme and Microbial Technology*, 38, pp. 569–582. doi: 10.1016/j.enzmictec.2005.09.015.

Khalily, M. A. *et al.* (2016) 'Facile Synthesis of Three-Dimensional Pt-TiO 2 Nano-networks : A Highly Active Catalyst for the Hydrolytic Dehydrogenation of Ammonia – Borane Angewandte', *Angew. Chem. Int. Ed.*, 55, pp. 12257–12261. doi: 10.1002/anie.201605577.

Kobayashi, T. *et al.* (2014) 'Mechanism of Solid-State Thermolysis of Ammonia Borane : A 15N NMR Study Using Fast Magic-Angle Spinning and Dynamic Nuclear Polarization', *Journal of Physical Chemistry C*, 118, p. 19548–19555. doi: 10.1021/jp504328x.

Komova, O. V *et al.* (2011) 'Low Temperature Decomposition of Ammonia Borane in the Presence of Titania', *Inorganic Materials*, 47(10), pp. 1011–1106. doi: 10.1134/S0020168511100116.

Komova, O. V *et al.* (2013) 'Improved low-temperature hydrogen generation from NH3BH3 and TiO2 composites pretreated with water', *International Journal of Hydrogen Energy*. Elsevier Ltd, 38, pp. 6442–6449. doi: 10.1016/j.ijhydene.2013.03.074.

Kondrat'Ev, Y. V. *et al.* (2015) 'Sublimation and thermal decomposition of ammonia borane: Competitive processes controlled by pressure', *Thermochimica Acta*. Elsevier B.V., 622, pp. 64–71. doi: 10.1016/j.tca.2015.08.021.

Kong, Y., Shen, X. and Cui, S. (2013) 'Preparation and thermal treatment of titania aerogels', *Int. J. Nanomanufacturing*, 9, pp. 253–260.

Kong, Y., Shen, X. and Cui, S. (2014) 'Direct synthesis of anatase TiO2 aerogel resistant to high temperature under supercritical ethanol', *Materials Letters*. Elsevier, 117, pp. 192–194. doi: 10.1016/j.matlet.2013.12.004.

Kostka, J. F. *et al.* (2012) 'Concentration-dependent dehydrogenation of ammonia-borane/triglyme mixtures', *European Journal of Inorganic Chemistry*, 1, pp. 49–54. doi: 10.1002/ejic.201100795.

Kulkarni, S. A. (1999) 'Intramolecular dihydrogen bonding in main group elements. Connection with dehydrogenation reactions', *Journal of Physical Chemistry A*, 103, pp. 9330–9335. doi: 10.1021/jp992206w.

Kurajica, S. *et al.* (2017) 'The utilization of modified alkoxide as a precursor for solvothermal synthesis of nanocrystalline titania', *Materials Chemistry and Physics*, 196, pp. 194–204. doi: 10.1016/j.matchemphys.2017.04.064.

Lai, S. *et al.* (2012) 'Hydrogen release from ammonia borane embedded in mesoporous silica scaffolds : SBA-15 and MCM-41', *International Journal of Hydrogen Energy*. Elsevier, 37, pp. 14393–14404. doi: 10.1016/j.ijhydene.2012.07.033.

Lang, J. and Huot, J. (2011) 'A new approach to the processing of metal hydrides', *Journal of Alloys and Compounds*, 509(3), pp. 18–22. doi: 10.1016/j.jallcom.2010.09.173.

Leng, Y. (2013) *Materials Characterization: Introduction to Microscopic and Spectroscopic Methods, Second Edition*. 2nd Ed. Wiley VCH.

Lermontov, S. A. *et al.* (2018) 'An approach for highly transparent titania aerogels preparation', *Materials Letters*. Elsevier B.V., 215, pp. 19–22. doi: 10.1016/j.matlet.2017.12.031.

Li, Zhu, *et al.* (2010) 'Ammonia Borane Confined by a Metal-Organic Framework for Chemical Hydrogen Storage: Enhancing Kinetics and Eliminating Ammonia', *Journal of the American Chemical Society*, 132, pp. 1490–1491.

Li, Guo, *et al.* (2010) 'Platinum Nanoparticle Functionalized CNTs as Nanoscaffolds and Catalysts To Enhance the Dehydrogenation of Ammonia-Borane', *Journal of Physical Chemistry C*, 114, pp. 21885–21890.

Li, B. L. *et al.* (2009) 'Lithium-Catalyzed Dehydrogenation of Ammonia Borane within Mesoporous Carbon Framework

for Chemical Hydrogen Storage', *Advanced Functional Materials*, 19, pp. 265–271. doi: 10.1002/adfm.200801111.

Li, H. *et al.* (2014) 'Ammonia borane, past as prolog', *Journal of Organometallic Chemistry*. Elsevier B.V, 751, pp. 60–66. doi: 10.1016/j.jorganchem.2013.08.044.

Li, J. *et al.* (2010) 'Preparation of Polyborazylene-Derived Bulk Boron Nitride with Tunable Properties by Warm-Pressing and Pressureless Pyrolysis', *Chem. Mater.*, 22, pp. 2920–2929. doi: 10.1021/cm902972p.

Li, X., Zeng, C. and Fan, G. (2015a) 'Magnetic RuCo nanoparticles supported on two-dimensional titanium carbide as highly active catalysts for the hydrolysis of ammonia borane', *International Journal of Hydrogen Energy*. Elsevier Ltd, 40, pp. 9217–9224. doi: 10.1016/j.ijhydene.2015.05.168.

Li, X., Zeng, C. and Fan, G. (2015b) 'Ultrafast hydrogen generation from the hydrolysis of ammonia borane catalyzed by highly efficient bimetallic RuNi nanoparticles stabilized on Ti3C2 X2 (X=OH and/or F)', *International Journal of Hydrogen Energy*. Elsevier Ltd, 40, pp. 3883–3891. doi: 10.1016/j.ijhydene.2015.01.122.

Li, Z. *et al.* (2015) 'Improved thermal dehydrogenation of ammonia borane by MOF-5', *RSC Advances*. Royal Society of Chemistry, 5, pp. 10746–10750. doi: 10.1039/c4ra13280g.

Lloyd, L. (2011) *Fundamentals of Applied Catalysis: Handbook of Industrial Catalysts*. Edited by M. V. Twigg and M. S. Spencer. Springer.

Lovins, A. B. (2017) 'Reliably integrating variable renewables: Moving grid flexibility resources from models to results', *Electricity Journal*. Elsevier, 30(10), pp. 58–63. doi: 10.1016/j.tej.2017.11.006.

Lu, J. *et al.* (2009) 'Surface Acidity and Properties of TiO2/SiO2 Catalysts Prepared by Atomic Layer Deposition: UV-visible Diffuse Reflectance , DRIFTS , and Visible Raman Spectroscopy Studies', *J. Phys. Chem. C*, 113, pp. 12412–12418.

Lv, M., Qin, G. and Wei, W. (2013) 'Preparation and Characterization TiO2 Aerogel Fibers', *Materials Science Forum*, 744, pp. 434–437. doi: 10.4028/www.scientific.net/MSF.743-744.434.

Ma, Y. *et al.* (2017) 'Ruthenium nanoparticles supported on TiO2(B) nanotubes : Effective catalysts in hydrogen evolution from the hydrolysis of ammonia borane', *Journal of Alloys and Compounds*. Elsevier B.V, 708, pp. 270–277. doi: 10.1016/j.jallcom.2017.02.239.

Madarász, J., Brăileanu, A. and Pokol, G. (2008) 'Comprehensive evolved gas analysis of amorphous precursors for S-doped titania by in situ TG-FTIR and TG/DTA-MS Part 1. Precursor from thiourea and titanium(IV)-isopropoxide', *Journal of Analytical and Applied Pyrolysis*, 82, pp. 292–297. doi: 10.1016/j.jaap.2008.05.003.

Maleki, H. (2016) 'Recent advances in aerogels for environmental remediation applications: A review', *Chemical Engineering Journal*. Elsevier B.V., 300, pp. 98–118. doi: 10.1016/j.cej.2016.04.098.

Maleki, M. *et al.* (2016) 'Three-dimensionally interconnected porous boron nitride foam derived from polymeric foams', *RSC Advances*. Royal Society of Chemistry, 6, pp. 51426–51434. doi: 10.1039/c6ra07751j.

Mamleev, V. *et al.* (2004) 'Three model-free methods for calculation of activation energy in TG', *Journal of Thermal Analysis and Calorimetry*, 78, pp. 1009–1027. doi: 10.1007/s10973-005-0467-0.

Manriquez, M. E. *et al.* (2004) 'Preparation of TiO2–ZrO2 mixed oxides with controlled acid-basic properties', *Journal of Molecular Catalysis A*, 220, pp. 229–237. doi: 10.1016/j.molcata.2004.06.003.

Matus, M. H. *et al.* (2007) 'Reliable predictions of the thermochemistry of boron-nitrogen hydrogen storage compounds: BxNxHy, x = 2, 3', *Journal of Physical Chemistry A*, 111, pp. 4411–4421. doi: 10.1021/jp070931y.

Mcgrail, B. P. *et al.* (2009) 'Energy Procedia Water Reactivity in the Liquid and Supercritical CO2 Phase: Has Half the Story Been Neglected?', *Energy Procedia*. Elsevier, 1, pp. 3415–3419. doi: 10.1016/j.egypro.2009.02.131.

McWhorter, S. *et al.* (2012) 'Moderate temperature dense phase hydrogen storage materials within the US department of energy (DOE) H2 storage program: Trends toward future development', *Crystals*, 2, pp. 413–445. doi: 10.3390/cryst2020413.

Merino, G., Bakhmutov, V. I. and Vela, A. (2002) 'Do Cooperative Proton - Hydride Interactions Explain the Gas-Solid Structural Difference', *Journal of Physical Chemistry A*, 62, pp. 8491–8494. doi: 10.1021/jp026087n.

Mino, L., Spoto, G. and Ferrari, A. M. (2014) 'CO2 Capture by TiO2 Anatase Surfaces: A Combined DFT and FTIR Study', *J. Phys. Chem. C*, 118, pp. 25016–25026. doi: 10.1021/jp507443k.

Moireau, M.-C. and Veillard, A. (1968) 'Quantum mechanical calculations on barriers to internal rotation', *Theoretica Chimica Acta*, 11, pp. 344–357. doi: 10.1007/bf00568790.

Moliner, R., Lázaro, M. J. and Suelves, I. (2016) 'Analysis of the strategies for bridging the gap towards the Hydrogen Economy', *International Journal of Hydrogen Energy*, 41(43), pp. 19500–19508. doi: 10.1016/j.ijhydene.2016.06.202.

Montoya, I. A. *et al.* (1992) 'On the effects of the sol-gel synthesis parameters on textural and structural characteristics of T i O 2', 15, pp. 207–217.

Moon, O. M. *et al.* (2004) 'Temperature effect on structural properties of boron oxide thin films deposited by MOCVD method', *Thin Solid Films*, 465, pp. 164–169. doi: 10.1016/j.tsf.2004.05.107.

Moradi, R. and Groth, K. M. (2019) 'ScienceDirect Hydrogen storage and delivery : Review of the state of the art technologies and risk and reliability analysis', *International Journal of Hydrogen Energy*. Elsevier Ltd, (xxxx). doi: 10.1016/j.ijhydene.2019.03.041.

Moran, P. D. *et al.* (1998) 'Vibrational Spectra and Molecular Association of Titanium Tetraisopropoxide', *Inorg. Chem.*, 37, pp. 2741–2748. doi: 10.1021/ic9709436.

Morgan, E., Manwell, J. and McGowan, J. (2014) 'Wind-powered ammonia fuel production for remote islands: A case study', *Renewable Energy*, 72, pp. 51–61. doi: 10.1016/j.renene.2014.06.034.

Mori, K., Miyawaki, K. and Yamashita, H. (2016) 'Ru and RuNi Nanoparticles on TiO2 Support as Extremely Active Catalysts for Hydrogen Production from Ammonia Borane', *ACS Catalysis*, 6, p. 3128–3135. doi: 10.1021/acscatal.6b00715.

Moury, R. *et al.* (2012) 'Hydrazine borane: synthesis, characterization, and application prospects in chemical hydrogen storage', *Phys. Chem. Chem. Phys*, 14, pp. 1768–1777. doi: 10.1039/c2cp23403c.

Moussa, G. *et al.* (2012) 'Room-temperature hydrogen release from activated carbon-confined ammonia borane', *International Journal of Hydrogen Energy*. Elsevier Ltd, 37, pp. 13437–13445. doi: 10.1016/j.ijhydene.2012.06.086.

Moussaoui, R., Elghniji, K. and Elaloui, E. (2017) 'Sol-gel synthesis of highly TiO2 aerogel photocatalyst via high temperature supercritical drying', *Journal of Saudi Chemical Society*, 21, pp. 751–760. doi: 10.1016/j.jscs.2017.04.001.

Nakagawa, Y. *et al.* (2014) 'Ammonia borane-metal alanate composites: Hydrogen desorption properties and decomposition processes', *RSC Advances*, 4, pp. 20626–20631. doi: 10.1039/c4ra02476a.

Nathanson, A. S. *et al.* (2015) 'Ammonia borane–polyethylene oxide composite materials for solid hydrogen storage', *Journal of Materials Chemistry A*. Royal Society of Chemistry, 3, pp. 3683–3691. doi: 10.1039/C4TA06657J.

National Grid (2018) *Future Energy Scenarios*, *Fes Document*. Available at: http://fes.nationalgrid.com/fes-document/ (Accessed: 25 September 2019).

Navarrete, J., Lopez, T. and Gomez, R. (1996) 'Surface Acidity of Sulfated TiO2-SiO2 Sol-Gels', *Langmuir*, 12, pp. 4385–4390. doi: 10.1021/la950927q.

Neiner, D. *et al.* (2009) 'Promotion of hydrogen release from ammonia borane with mechanically activated hexagonal boron nitride', *Journal of Physical Chemistry C*, 113, pp. 1098–1103. doi: 10.1021/jp8087385.

Ng, L. V. and Mccormick, A. V (1996) 'Acidic Sol-Gel Polymerization of TEOS: Effect of Solution Composition on Cyclization and Bimolecular Condensation Rates', *J. Phys.*

Chem., (100), pp. 12517–12531. doi: 10.1021/jp960089o.

Nguyen, M. T. *et al.* (2007) 'Molecular mechanism for H2 release from BH3NH4, including the catalytic role of the lewis acid BH3', *Journal of Physical Chemistry A*, 111, pp. 679–690. doi: 10.1021/jp066175y.

Nguyen, V. S. *et al.* (2007) 'Computational study of the release of H2 from ammonia borane dimer (BH3NH3)2 and its ion pair isomers', *Journal of Physical Chemistry A*, 111, pp. 8844–8856. doi: 10.1021/jp0732007.

Nguyen, V. S. *et al.* (2008) 'Reactions of diborane with ammonia and ammonia borane: Catalytic effects for multiple pathways for hydrogen release', *Journal of Physical Chemistry A*, 112, pp. 9946–9954. doi: 10.1021/jp804714r.

Niaz, S., Manzoor, T. and Pandith, A. H. (2015) 'Hydrogen storage: Materials, methods and perspectives', *Renewable and Sustainable Energy Reviews*, 50, pp. 457–469. doi: 10.1016/j.rser.2015.05.011.

Nikolaidis, P. and Poullikkas, A. (2017) 'A comparative overview of hydrogen production processes', *Renewable and Sustainable Energy Reviews*. Elsevier, 67, pp. 597–611. doi: 10.1016/j.rser.2016.09.044.

Nirmala, R. *et al.* (2012) 'Electrospun nickel doped titanium dioxide nanofibers as an effective photocatalyst for the hydrolytic dehydrogenation of ammonia borane', *International Journal of Hydrogen Energy*. Elsevier Ltd, 37, pp. 10036–10045. doi: 10.1016/j.ijhydene.2012.03.164.

NIST (2019) *Mass Fragmentation Pattern of 2-Propanol*, *NIST Chemistry Webbook*. Available at: https://webbook.nist.gov/cgi/cbook.cgi?ID=C67630&Mask=200 (Accessed: 12 April 2020).

Noda, I. (2015) 'Techniques of two-dimensional (2D) correlation spectroscopy useful in life science research', *Biomedical Spectroscopy and Imaging*, 4, pp. 109–127. doi: 10.3233/bsi-150105.

Noda, I. and Ozaki, Y. (2004) *Two-dimensional Correlation Spectroscopy – Applications in Vibrational and Optical Spectroscopy*. John Wiley & Sons, Ltd.

Nolan, N. T., Seery, M. K. and Pillai, S. C. (2009) 'Spectroscopic Investigation of the Anatase-to-Rutile Transformation of Sol-Gel-Synthesized TiO2 Photocatalysts', *J. Phys. Chem. C*, 113, pp. 16151–16157.

Oi, L. E. *et al.* (2016) 'Recent advances of titanium dioxide (TiO2) for green organic synthesis', *RSC Advances*. Royal Society of Chemistry, 6, pp. 108741–108754. doi: 10.1039/c6ra22894a.

ONS (2018) *UK Population*, *Overview of the UK population: November 2018*. Available at: https://www.ons.gov.uk/peoplepopulationandcommunity/populationandmigration/populationprojections/bulletins/nationalpopulationprojections/2015 (Accessed: 25 September 2019).

OPEC (2018) *Proven Oil Reserves in 2018*, *OPEC Share of World Oil Reserves, 2018*. Available at: https://www.opec.org/opec_web/en/data_graphs/330.htm (Accessed: 7 March 2020).

Pajonk, G. M. (1991) 'Aerogel Catalysts', 72, pp. 217–266.

Palmer, D. A. (1983) 'The Chemistry of Metal Carbonato and Carbon Dioxide Complexes', *Chem. Rev.*, 83, pp. 651–731. doi: 10.1021/cr00058a004.

Palumbo, O. *et al.* (2010) 'Decomposition of NH3BH3 at sub-ambient pressures: A combined thermogravimetry-differential thermal analysis-mass spectrometry study', *Journal of Power Sources*, 195, pp. 1615–1618. doi: 10.1016/j.jpowsour.2009.09.042.

Pan, C. *et al.* (2017) 'Tuning/exploiting Strong Metal-Support Interaction (SMSI) in Heterogeneous Catalysis', *Journal of the Taiwan Institute of Chemical Engineers*. Elsevier B.V., 74, pp. 154–186. doi: 10.1016/j.jtice.2017.02.012.

Paolone, A. *et al.* (2009) 'Absence of the Structural Phase Transition in Ammonia Borane Dispersed in Mesoporous Silica : Evidence of Novel Thermodynamic Properties', *J. Phys. Chem*, 113(24), pp. 10319–10321.

Patel, N., Kale, A. and Miotello, A. (2012) 'Improved dehydrogenation of ammonia borane over Co-P-B coating on Ni: A single catalyst for both hydrolysis and thermolysis', *Applied Catalysis B: Environmental*. Elsevier B.V., 111–112, pp. 178–184. doi: 10.1016/j.apcatb.2011.09.032.

Penner, G. H., Chang, Y. C. P. and Hutzal, J. (1999) 'A Deuterium NMR Spectroscopic Study of Solid BH 3 NH 3', *Inorganic Chemistry*, 38, pp. 2868–2873. doi: 10.1021/ic981370f.

Penner, S. S. and Chang, P. (1978) 'On the determination of log-normal particle size distributions using half widths and detectabilities of scattered laser power', *Journal of Quantitative Spectroscopy & Radiative Transfer*, 20, pp. 447–460.

Petit, J. and Demirci, U. B. (2018) 'Mechanistic Insights into Dehydrogenation of Partially Deuterated Ammonia Borane NH3BD3 Being Heating to 200 °C', *Inorganic Chemistry*. American Chemical Society, 58, pp. 489–494. doi: 10.1021/acs.inorgchem.8b02721.

Petit, J., Miele, P. and Demirci, U. B. (2016) 'Ammonia borane for solid-state chemical hydrogen storage : Different samples with different thermal behaviors', *International Journal of Hydrogen Energy*. Elsevier Ltd, 41, pp. 15462–15470. doi: 10.1016/j.ijhydene.2016.06.097.

Qu, Q. *et al.* (2010) 'Chemically Binding Carboxylic Acids onto TiO2 Nanoparticles with Adjustable Coverage by Solvothermal Strategy', *Langmuir*, 26(12), pp. 9539–9546. doi: 10.1021/la100121n.

Qu, X. *et al.* (2019) 'The hydrolysis of ammonia borane catalyzed by NiCoP/OPC-300 nanocatalysts: high selectivity and efficiency, and mechanism', *Green Chemistry*. Royal Society of Chemistry, 21, pp. 850–860. doi: 10.1039/c8gc03536a.

Rafael, O. *et al.* (2015) 'Design of multicomponent aerogels and their performance in photocatalytic hydrogen production', *Catalysis Today*. Elsevier B.V., 246, pp. 101–107. doi: 10.1016/j.cattod.2014.08.028.

Raj, K. J. A. and Viswanathan, B. (2009) 'Effect of surface area , pore volume and particle size of P25 titania on the phase transformation of anatase to rutile', *Indian Journal of Chemistry*, 48, pp. 1378–1382.

Rakap, M. (2014) 'Hydrogen generation from the hydrolytic dehydrogenation of ammonia borane using electrolessly deposited cobalt e phosphorus as reusable and cost-effective catalyst', *Journal of Power Sources*. Elsevier B.V, 265, pp. 50–56. doi: 10.1016/j.jpowsour.2014.04.117.

Ramachandran, P. V. and Gagare, P. D. (2007) 'Preparation of Ammonia Borane in High Yield and Purity , Methanolysis , and Regeneration', *Inorganic Chemistry*, 46, pp. 7810–7817. doi: 10.1021/ic700772a.

Rassat, S. D. *et al.* (2010) 'Thermal stability of ammonia borane: A case study for exothermic hydrogen storage materials', *Energy and Fuels*, 24, pp. 2596–2606. doi: 10.1021/ef901430a.

Ren, J. *et al.* (2017) 'Current research trends and perspectives on materials-based hydrogen storage solutions: A critical review', *International Journal of Hydrogen Energy*. Elsevier Ltd, 42(1), pp. 289–311. doi: 10.1016/j.ijhydene.2016.11.195.

Rossin, A. and Peruzzini, M. (2016) 'Ammonia-Borane and Amine-Borane Dehydrogenation Mediated by Complex Metal Hydrides', *Chemical Reviews*, 116(15), pp. 8848–8872. doi: 10.1021/acs.chemrev.6b00043.

Rouquerol, J., Llewellyn, P. and Rouquerol, F. (2007) 'Is the BET equation applicable to microporous adsorbents ?', *Studies in Surface Science and Catalysis*, 160, pp. 49–56.

Roy, B., Manna, J., *et al.* (2018) 'An in situ study on the solid state decomposition of ammonia borane: unmitigated by-product suppression by a naturally abundant layered clay mineral', *Inorganic Chemistry Frontiers*. Royal Society of Chemistry, 5, pp. 301–309. doi: 10.1039/c7qi00682a.

Roy, B., Hajari, A., Kumar, V., *et al.* (2018) 'Kinetic model analysis and mechanistic correlation of ammonia borane thermolysis under dynamic heating conditions', *International Journal of Hydrogen Energy*. Elsevier Ltd, 43, pp. 10386–10395. doi: 10.1016/j.ijhydene.2018.04.124.

Roy, B., Hajari, A., Manna, J., *et al.* (2018) 'Supported ammonia borane decomposition through enhanced homopolar B–B coupling', *Dalton Transactions*. Royal Society of Chemistry, 47, pp. 6570–6579. doi: 10.1039/c8dt00789f.

Ruban, A. *et al.* (1997) 'Surface electronic structure and reactivity of transition and noble metals', *Journal of*

Molecular Catalysis A: Chemical, 115, pp. 421–429. doi: 10.1016/S1381-1169(96)00348-2.

Rueda, M. *et al.* (2014) 'Production of silica aerogel microparticles loaded with ammonia borane by batch and semicontinuous supercritical drying techniques', *Journal of Supercritical Fluids*. Elsevier B.V., 92, pp. 299–310. doi: 10.1016/j.supflu.2014.06.012.

Rueda, M. *et al.* (2017) 'Improvement of the kinetics of hydrogen release from ammonia borane confined in silica aerogel', *Microporous and Mesoporous Materials*, 237, pp. 189–200. doi: 10.1016/j.micromeso.2016.09.030.

Rueda, M., Sanz-moral, L. M. and Martín, Á. (2018) 'The Journal of Supercritical Fluids Innovative methods to enhance the properties of solid hydrogen storage materials based on hydrides through nanocon fi nement : A review', *The Journal of Supercritical Fluids*. Elsevier, 141, pp. 198–217. doi: 10.1016/j.supflu.2018.02.010.

Sadrieyeh, S. and Malekfar, R. (2017) 'The effects of hydrolysis level on structural properties of titania aerogels', *Journal of Non-Crystalline Solids*. Elsevier B.V., 457, pp. 175–179. doi: 10.1016/j.jnoncrysol.2016.11.031.

Sakakura, T., Choi, J. and Yasuda, H. (2007) 'Transformation of Carbon Dioxide', *Chem. Rev.*, 107, pp. 2365–2387.

Salameh, C. *et al.* (2018) 'Robust 3D Boron Nitride Nanoscaffolds for Remarkable Hydrogen Storage Capacity from Ammonia Borane', *Energy Technology*, 6, pp. 570–577. doi: 10.1002/ente.201700618.

Salles, V. and Bernard, S. (2016) 'A Review on the Preparation of Borazine-derived Boron Nitride Nanoparticles and Nanopolyhedrons by Spray-pyrolysis and Annealing Process', *Nanomaterials and Nanotechnology*, 6, pp. 1–13. doi: 10.5772/62161.

Sanyal, U. *et al.* (2011) 'Hydrolysis of Ammonia Borane as a Hydrogen Source : Fundamental Issues and Potential Solutions Towards Implementation', *ChemSusChem*, 4, pp. 1731–1739. doi: 10.1002/cssc.201100318.

Schneider, M. and Baiker, A. (1997) 'Review: Titania-based aerogels', *Catalysis Today*, 35, pp. 339–365.

Sepehri, S. *et al.* (2007) 'Spectroscopic Studies of Dehydrogenation of Ammonia Borane in Carbon Cryogel', *J. Phys. Chem. B*, 111, pp. 14285–14289. doi: 10.1021/jp077057t.

Sepehri, S. and Cao, G. (2009) 'Influence of Surface Chemistry on Dehydrogenation in Carbon Cryogel Ammonia Borane Nanocomposites', *European Journal of Inorganic Chemistry*, pp. 599–603. doi: 10.1002/ejic.200800814.

Sepehri, S., Garcia, B. B. and Cao, G. (2008) 'Tuning dehydrogenation temperature of carbon – ammonia borane nanocomposites', *J. Mater. Chem.*, 18, pp. 4034–4037. doi: 10.1039/b808511k.

Shafeeyan, M. S. *et al.* (2010) 'A review on surface modification of activated carbon for carbon dioxide adsorption', *Journal of Analytical and Applied Pyrolysis*. Elsevier B.V., 89(2), pp. 143–151. doi: 10.1016/j.jaap.2010.07.006.

Shaulov, Y. K., Shmyreva, G. O. and Tubyanskaya, V. S. (1966) 'Heat of combustion of borine ammoniate', *Zh. Fiz. Khim.*, 40, pp. 122–124.

Shaw, W. J. *et al.* (2010) 'Characterization of a new phase of ammonia borane', *Energy and Environmental Science*, 3, pp. 796–804. doi: 10.1039/b914338f.

Shi, H. *et al.* (2014) 'Catalytic solvent regeneration using hot water during amine based CO2 capture process', *Energy Procedia*. Elsevier B.V., 63, pp. 266–272. doi: 10.1016/j.egypro.2014.11.028.

Shimoyama, Y. *et al.* (2010) 'Chemical Engineering Research and Design Drying processes for preparation of titania aerogel using supercritical carbon dioxide', *Chemical Engineering Research and Design*. Institution of Chemical Engineers, 88, pp. 1427–1431. doi: 10.1016/j.cherd.2010.02.018.

Si, X. *et al.* (2011) 'Improved hydrogen desorption properties of ammonia borane by Ni-modified metal-organic frameworks', *International Journal of Hydrogen Energy*. Elsevier Ltd, 36(11), pp. 6698–6704. doi: 10.1016/j.ijhydene.2011.02.102.

Sigma-Aldrich (2018a) *Borane-Ammonia Complex (97%)*.

Sigma-Aldrich (2018b) *Borane-Ammonia Complex (97%), Product Specification Sheet*. Available at: https://www.sigmaaldrich.com/Graphics/COfAInfo/SigmaSAPQM/SPEC/68/682098/682098-BULK_____ALDRICH__.pdf (Accessed: 25 September 2019).

Simagina, V. I. *et al.* (2017) 'Experimental and modeling study of ammonia borane-based hydrogen storage systems', *Chemical Engineering Journal*. Elsevier B.V., 329, pp. 156–164. Available at: http://dx.doi.org/10.1016/j.cej.2017.05.005.

Simonsen, M. E. and Søgaard, E. G. (2010) 'cluster formation and properties of the resulting products Sol – gel reactions of titanium alkoxides and water : influence of pH and alkoxy group on cluster formation and properties of the resulting products', *Journal of Sol-Gel Science and Technology*, 53, pp. 485–497. doi: 10.1007/s10971-009-2121-0.

Smirnova, I. and Gurikov, P. (2018) 'The Journal of Supercritical Fluids Aerogel production : Current status , research directions , and future opportunities', *The Journal of Supercritical Fluids*. Elsevier, 134, pp. 228–233. doi: 10.1016/j.supflu.2017.12.037.

Soetaert, W. and Vandamme, E. J. (2009) *Biofuels*. John Wiley & Sons, Ltd.

Speight, J. G. (2019) *10 - Energy Security and the Environment*. 2nd Editio, *Natural Gas*. 2nd Editio. doi: 10.1016/b978-0-12-809570-6.00010-2.

Stengl, V., Bakardjieva, S. and Szatmary, L. (2006) 'Titania aerogel prepared by low temperature supercritical drying', *Microporous and Mesoporous Materials*, 91, pp. 1–6. doi: 10.1016/j.micromeso.2005.10.046.

Stephens, F. H., Pons, V. and Baker, R. T. (2007) 'Ammonia-borane: the hydrogen source par excellence?', *Dalton Transactions*, 2, pp. 2613–2626. doi: 10.1039/b703053c.

Storozhenko, P. A. *et al.* (2005) 'No Title', *Russ. J. Inorg. Chem.*, 50, pp. 980–985.

Stuart, B. H. (2004) *Infrared Spectroscopy: Fundamentals and Applications*, *Infrared Spectroscopy: Fundamentals and Applications*. doi: 10.1002/0470011149.

Summerscales, O. T. and Gordon, J. C. (2013) 'Regeneration of ammonia borane from spent fuel materials', *Dalton Transactions*, 42, pp. 10075–10084. doi: 10.1039/c3dt50475a.

Sun, W., Li, H. and Wang, Y. (2015) 'Graphene-supported nickel chloride and cobalt chloride nanoparticles as highly efficient catalysts for dehydrogenation of ammonia borane', *International Journal of Hydrogen Energy*. Elsevier Ltd, 40, pp. 15389–15397. doi: 10.1016/j.ijhydene.2015.09.088.

Sutton, A. D. (2014) 'Regeneration of Ammonia Borane', *Science*, 331, pp. 1426–1429. doi: 10.1126/science.1199003.

Tang, Z. *et al.* (2012) 'Graphene Oxide Based Recyclable Dehydrogenation of Ammonia Borane within a Hybrid Nanostructure', *Journal of the American Chemical Society*, 134, p. 5464−5467. doi: 10.1021/ja300003t.

Thommes, M. *et al.* (2015) 'Physisorption of gases, with special reference to the evaluation of surface area and pore size distribution (IUPAC Technical Report)', *Pure Appl. Chem.*, 87, pp. 1051–1069. doi: 10.1515/pac-2014-1117.

Tonbul, Y., Akbayrak, S. and Ozkar, S. (2016) 'Palladium (0) nanoparticles supported on ceria: Highly active and reusable catalyst in hydrogen generation from the hydrolysis of ammonia borane', *International Journal of Hydrogen Energy*, 41, pp. 11154–11162. doi: 10.1016/j.ijhydene.2016.04.058.

Torrente-murciano, T. E. B. L. (2016) 'H2 Production via Ammonia Decomposition Using Non-Noble Metal Catalyst : A Review', *Top Catal*. Springer US, 59, pp. 1438–1457. doi: 10.1007/s11244-016-0653-4.

UN (1998) *Kyoto Protocol to the United Nations Framework Convention on Climate Change*. Kyoto. doi: 10.2307/2998044.

UN (2010) *Report of the Conference of the Parties on its fifteenth session, held in Copenhagen from 7 to 19 December 2009*. Copenhagen.

UN (2015) *Paris Agreement*. Paris.

Urban, P. L., Chen, Y. and Wang, Y. (2016) *Time-Resolved Mass Spectrometry: From Concept to Applications*. Wiley VCH. doi: 10.1002/9781118887332.

US DOE (2017) *Technical Targets*, *DOE Technical Targets for Onboard Hydrogen Storage for Light-Duty Vehicles*. Available at: https://www.energy.gov/eere/fuelcells/doe-technical-targets-onboard-hydrogen-storage-light-duty-vehicles (Accessed: 25 September 2019).

US DOE (2019) *Hydrogen Storage*, *Challenges during Hydrogen Storage*. Available at: https://www.energy.gov/eere/fuelcells/hydrogen-storage-challenges (Accessed: 25 September 2019).

Vakulchuk, R., Overland, I. and Scholten, D. (2020) 'Renewable energy and geopolitics: A review', *Renewable and Sustainable Energy Reviews*. Elsevier Ltd, 122. doi: 10.1016/j.rser.2019.109547.

Vareda, J. P., Lamy-Mendes, A. and Durães, L. (2018) 'A reconsideration on the definition of the term aerogel based on current drying trends', *Microporous and Mesoporous Materials*, 258, pp. 211–216. doi: 10.1016/j.micromeso.2017.09.016.

Vasconcelos, D. C. L. *et al.* (2011) 'Infrared Spectroscopy of Titania Sol-Gel Coatings on 316L Stainless Steel', *Materials Sciences and Applications*, 2, pp. 1375–1382. doi: 10.4236/msa.2011.210186.

Virga, E. *et al.* (2018) 'Wettability of Amphoteric Surfaces: The Effect of pH and Ionic Strength on Surface Ionization and Wetting', *Langmuir*, 34, pp. 15174–15180. doi: 10.1021/acs.langmuir.8b02875.

Wahab, M. A., Zhao, H. and Yao, X. D. (2012) 'Nano-confined ammonia borane for chemical hydrogen storage', *Frontiers of Chemical Science and Engineering*, 6(1), pp. 27–33. doi: 10.1007/s11705-011-1171-3.

Wang, C. *et al.* (2018) 'Cu/Ni nanoparticles supported on TiO2(B) nanotubes as hydrogen generation photocatalysts via hydrolysis of ammonia borane', *Inorganic Chemistry Frontiers*. Royal Society of Chemistry, 5, pp. 2038–2044. doi: 10.1039/c8qi00492g.

Wang, C. and Lin, J. (2008) 'Surface nature of nanoparticle zinc-titanium oxide aerogel catalysts', 254, pp. 4500–4507. doi: 10.1016/j.apsusc.2008.01.024.

Wang, L. *et al.* (2009) 'Xe NMR Investigation of Ammonia Borane in Mesoporous Silica', *J. Phys. Chem*, 113, pp. 6485–6490.

Wietelmann, U., Felderhoff, M. and Rittmeyer, P. (2016) *Hydrides*, *Uhlmann's Encyclopedia of Industrial Chemistry*.

Williams, D. and Fleming, I. (2007) *Spectroscopic Methods in Organic Chemistry*. McGraw-Hill.

Wohlfarth, C. (2016) *Surface tension of tetrahydrofuran. In: Lechner M.D. (eds) Surface Tension of Pure Liquids and Binary Liquid Mixtures. Landolt-Börnstein - Group IV Physical Chemistry (Numerical Data and Functional Relationships in Science and Technology)*. Berlin, Heidelberg: Springer.

Wolf, G. *et al.* (2000) 'Calorimetric process monitoring of thermal decomposition of B-N-H compounds', *Thermochimica Acta*, 343, pp. 19–25. doi: 10.1016/s0040-6031(99)00365-2.

Wolstenholme, D. J. *et al.* (2012) 'Thermal desorption of hydrogen from ammonia borane : unexpected role of homopolar interactions', *ChemComm*, 48, pp. 2597–2599. doi: 10.1039/c2cc16111g.

Wood, G. E. *et al.* (2017) 'In situ gas analysis during the growth of hexagonal boron nitride from ammonia borane', *Materials Research Express*. IOP Publishing, 4. doi: 10.1088/2053-1591/aa9a7f.

World Bank (2018) *GDP per Capita of the UK*, *GDP per capita (Current US$)*. Available at: https://data.worldbank.org/indicator/ny.gdp.pcap.cd (Accessed: 25 September 2019).

Xu, B. *et al.* (2016) 'Structures, preparation and applications of titanium suboxides', *RSC Advances*. Royal Society of Chemistry, 6, pp. 79706–79722. doi: 10.1039/C6RA14507H.

Yakub, I. (2018) *Nitric Oxide Reduction with Hydrogen over Carbon-Supported Copper-Iron Oxides Catalysts*. University of Sheffield.

Yamada, O. (2006) 'Generation of hydrogen gas by reforming biomass with superheated steam', *Thin Solid Films*, 509(1–2), pp. 207–211. doi: 10.1016/j.tsf.2005.09.174.

Yang, Z. *et al.* (2017) 'Improved hydrogen release from ammonia borane confined in microporous carbon with narrow pore size distribution', *Journal of Materials Chemistry A*. Royal Society of Chemistry, 5, pp. 15395–15400. doi: 10.1039/c7ta02461d.

Yousef, A., Barakat, N. A. M. and Yong, H. Y. (2013) 'Electrospun Cu-doped titania nanofibers for photocatalytic hydrolysis of ammonia borane', *Applied Catalysis A: General*. Elsevier B.V., 467, pp. 98–106. doi: 10.1016/j.apcata.2013.07.019.

Zapata-Escobar, A. D. *et al.* (2016) 'On the nature of the trimer, tetramer, and pentamer of ammonia borane', *Theoretical Chemistry Accounts*. Springer Berlin Heidelberg, 135, pp. 94–106. doi: 10.1007/s00214-016-1853-5.

Zhan, W., Zhu, Q. and Xu, Q. (2016) 'Dehydrogenation of Ammonia Borane by Metal Nanoparticle Catalysts'. doi: 10.1021/acscatal.6b02209.

Zhang, F. *et al.* (2016) 'The survey of key technologies in hydrogen energy storage', *International Journal of Hydrogen Energy*. Elsevier Ltd, 41(33), pp. 14535–14552. doi: 10.1016/j.ijhydene.2016.05.293.

Zhang, J. *et al.* (2011) 'Calorimetric and Microscopic Studies on the Noncatalytic Hydrothermolysis of Ammonia Borane', *Industrial & Engineering Chemistry Research*, 50, pp. 10407–10413. doi: 10.1021/ie200878u.

Zhao, B. J. *et al.* (2010) 'Soft Hydrogen Storage Material: Poly(methyl acrylate)-Confined Ammonia Borane with Controllable Dehydrogenation', *Advanced Materials*, 22, pp. 394–397. doi: 10.1002/adma.200902174.

Zhong, R. *et al.* (2012) 'Improved Hydrogen Release from Ammonia – Borane with ZIF-8', *Inorganic Chemistry*, 51, pp. 2728–2730. doi: 10.1021/ic202562b.

Zhou, Q. and Xu, C. (2017) 'Stratified nanoporous PtTi alloys for hydrolysis of ammonia borane', *Journal of Colloid And Interface Science*. Elsevier Inc., 496, pp. 235–242. doi: 10.1016/j.jcis.2017.02.030.

Zielinski, T. J. *et al.* (2005) 'Quantum States of Atoms and Molecules', *J. Chem. Educ.*, 82(12), p. 1880. doi: 10.1021/ed082p1880.2.

Zirakjou, A., Aghdam, R. M. and Soorbaghi, F. P. (2015) 'Synthesis and Characterization of Monolithic Titania/nanoclay Nanocomposite Aerogels', *Procedia Materials Science*. Elsevier B.V., 11, pp. 548–552. doi: 10.1016/j.mspro.2015.11.054.

Zou, C. *et al.* (2014) 'Fabrication and properties of borazine derived boron nitride matrix wave-transparent composites reinforced by 2.5 dimensional fabric of Si–N–O fibers', *Materials Science & Engineering A*. Elsevier, 620, pp. 420–427. doi: 10.1016/j.msea.2014.10.046.

Zou, S., Tao, Z. and Chen, J. (2011) 'Preparation of Ammonia Borane with Ammonia Complex and the Study of Hydrogen Desorption Performance', *Chem. Eur. J*, 69, pp. 2117–2122.

Zu, G. *et al.* (2015) 'The Journal of Supercritical Fluids Heat-resistant , strong titania aerogels achieved by supercritical deposition', *The Journal of Supercritical Fluids*. Elsevier B.V., 106, pp. 145–151. doi: 10.1016/j.supflu.2015.06.001.